2012

Risk of well integrity failure due sustained casing pressure

Koray Kinik

Louisiana State University and Agricultural and Mechanical College, kkinik1@lsu.edu

RISK OF WELL INTEGRITY FAILURE DUE SUSTAINED CASING PRESSURE

A Thesis

Submitted to the Graduate Faculty of the
Louisiana State University and
Agricultural and Mechanical College
in partial fulfillment of the
requirements for the degree of
Master of Science in Petroleum Engineering

in

Department of Petroleum Engineering

by
Koray Kinik
B.S., Middle East Technical University, 2007
May 2012

ACKNOWLEDGEMENTS

TABLE OF CONTENTS

ABBREVIATIONS

$\bar{E}$	Expected value sign	
API	American Petroleum Institute	
CDF	Cumulative density distribution	
CFL	Crome free lignosulfonate	
CMC	Carboxyl methyl cellulose	
CNL	Compensated neutron log	
CSS	Casing shoe strength	
CTIP	cement top inflow performance	
CTOP	cement top outflow performance	
DIL	Dual induction log	
ECD	Equivalent circulating density	
EOS	Equation of State	
FBP	Formation breakdown pressure	
FIT	Formation integrity test	
FST	Formation stability test	
FVF	Formation volume factor	rb/bbl
GR	Gamma Ray log	
HPHT	High temperature high pressure	
HPWBM	High performance water base mud	
ID	Inner diameter	
IO	Internal olefin	
LAO	Linear alpha olefin	
LDT	Litho density log	
LOT	Leak off test	
LSS	Log spaced sonic log	
MLE	Maximum likelihood estimator	
MWD	Measurement while drilling	
OBM	Oil base mud	
OD	Outer diameter	
PDC	Poly diamond crystalline	
PDF	Probability density function	
PHPA	Partially hydrolyzed ploy acrylamide	
POOH	Pull out of hole	
PVT	Pressure volume temperature	
P-ρ-T	Pressure-density-temperature	
QRA	Quantitative risk analysis	
RIH	Run in hole	
ROP	Rate of Penetration	
TD	Total depth	ft

TVD	True vertical depth	
UCS	Uniaxial compressive strength	MPa
WBM	Water base mud	

NOMENCLATURE

ΔP_{gel}	total pressure differential due to mud thixotropy	psig
Δt_0	static time before mud gel measurement at time 0th	s
Δt_1	static time before mud gel measurement at time 1st	s
$\Delta t_{1/2}$	time lap between time 0th and equilibrium	s
Δt_s	static non-circulating time	min
$\Delta \sigma_T$	total pressure differential due to thermal effects	psig
μ_o	correlation constant in eqn 4.16	cp
A_p	cross sectional area of annulus	ft^2
B_o	formation volume factor	rb/stb
c_o	compressibility of oil	1/psi
c_{p-f}	formation specific heat capacity	btu/lb-^{o}F
c_{p-fl}	specific heat capacity of fluid	btu/lb-^{o}F
c_{p-m}	mud heat capacity	btu/lb-^{o}F
D	depth, true vertical	ft
d_{ci}	diameter, casing inner	ft
d_{EP}	equiperiphery diameter	ft
d_{pi}	diameter, pipe inner	ft
d_{po}	diameter, pipe outer	ft
d_{to}	diameter, tubing outer	ft
D_{TOC}	depth from surface to top of cement	ft
d_w	diameter, wellbore	ft
E	Young's modulus of elasticity	psi
e	eccentricity	
f'	friction factor	
f_0	oil content of mud	
f_s	solid content of mud	
f_w	water ratio of mud	
g	earth gravitational constant	ft/s^2
G_T	geothermal gradient	^{o}F/100ft
H_L	liquid holdup	
H_{LLS}	liquid holdup in liquid slug	
h_p	overall heat transfer coefficient across drillpipe	BTU/ft^2-^{o}F-hr
k_e	earth formation thermal conductivity	btu/hr-ft-^{o}F
k_{eff}	effective permeability	md
k_m	thermal conductivity of the mud	btu/hr-ft-^{o}F
L	length	ft
L_{cell}	length of discritized cell	ft
L_{LF}	length of liquid film	ft
$L_{mud-exp}$	length of gas-cur mud	ft

L_{SU}	length of slug unit	ft
M	mass of fluid in one foot long well	lb
m	mass flow rate	lb/hr
m_g	gas mass influx rate	lb/s
n'	fluid index in power law rheological model	
N_{RB}	bubble Reynold's number	
$^o\theta$	hole inclination	^{o}
P_b	bubble point pressure	psi
P_{hyd}	hydrostatic pressure	psi
$P_{LOP\text{-}surface}$	surface leak off pressure	psi
P_p	pore pressure	psi
P_r	reduced pressure	unitless
P_{sc}	pseudo critical pressure	
P_w	wellbore pressure	psi
Q	heat influx per unit length	Btu/ft-hr
q_g	gas flow rate	scf/D
q_{pump}	pump rate during the circulation before leak off test	gpm
r	radius	ft
R_{so}	oil solution gas oil ratio	scf/stb
R_{sob}	oils solution gas oil ratio at bubble point	scf/stb
R_{swp}	water solution gas oil ratio	scf/stb
r_w	wellbore radius	ft
S_3	least principle stress	psi
S_{max}	maximum horizontal in situ stress	psi
S_{min}	minimum horizontal in situ stress	psi
T	temperature	^oF
T_0	surface earth temperature	^oF
t_D	dimensionless time	unitless
T_D	dimensionless temperature	unitless
T_{ei}	formation static temperature bottom-hole	^oF
T_f	formation temperature	^oF
T_{inlet}	inlet mud temperature (steady state flowing)	^oF
T_{outlet}	outlet mud temperature (steady state flowing)	^oF
t_p	circulation time before pump stop	hr
T_r	reduced temperature	unitless
t_r	gas residence time in mud	s
T_{sc}	pseudo critical temperature	
T_{ws}	transient wellbore mud temperature	^oF
U	overall heat transfer coefficient across wellbore	btu/hr-ft^2-^oF
v	poisson's ratio	unitless
v_E	expanding gas velocity ratio	

v_{gLS}	in-situ gas velocity in liquid slug	ft/s
v_{gTB}	in-situ gas velocity in Taylor bubble	ft/s
v_{LLS}	in-situ liquid velocity in liquid slug	ft/s
v_{LTB}	in-situ liquid velocity in liquid film	ft/s
$V_{L\text{-}unloaded}$	unloaded liquid volume	ft^3
v_m	mixture velocity	ft/s
$v_{o\infty}$	single bubble slip velocity	ft/s
v_s	gas rise velocity	ft/s
v_{Sg}	superficial gas velocity	ft/s
V_{sh}	cumulative clay content	%
v_{SL}	superficial liquid velocity	ft/s
v_{TB}	Taylor bubble transitional velocity	ft/s
z	number of discritized cell	
Z	gas deviation factor	
α	correlation constant in eqn 4.15	
α_T	thermal expansion coefficient	$^{\circ}c^{-1}$
γ	shear rate (=rpm·1.703)	s^{-1}
γ_g	gas specific gravity	
ε	pipe wall roughness	ft
ρ_f	formation density	lb/ft^3
ρ_g	gas density	lb/ft^3
ρ_L	liquid density	lb/ft^3
ρ_{LS}	liquid slug density	lb/ft^3
ρ_m	mud density	lb/ft^3
ρ_o	oil density	lb/ft^3
ρ_{oi}	oil density at reference conditions	lb/ft^3
ρ_{TP}	two-phase mixture density	lb/ft^3
σ_L	liquid surface tension	dynes/cm^2
σ_{max}	maximum matrix stress	psi
σ_{min}	minimum matrix stress	psi
σ_{Θ}	effective hoop stress	psi
τ_0	gel strength at time 0th	lb/100ft^2
τ_1	gel strength at time 1st	lb/100ft^2
τ_{10sec}	10 sec gel strength (=1.06· Θ_n)	lb/100ft^2
τ_{30min}	30 min gel strength (=1.06· Θ_n)	lb/100ft^2
$\tau_{\infty N}$	shear stress at n rpm steady state (=5.077· Θ_n)	dynes/cm^2
τ_y	yield stress	lb/100ft^2
Φ	porosity	unitless
θ_N	fann35 dial reading	$^{\circ}$ deflection
θ_o	equation constant in eqn 4.17	

LIST OF TABLES

LIST OF FIGURES

ABSTRACT

Sustained casing pressure (SCP) is considered a well integrity problem. The approach of this study is to look at SCP as environmental risk due hydrocarbon release. Currently, the risk is qualified by the value of surface pressure (P_{csg}) that may cause failure of casing head. However, the resulting rate of gas emission to the atmosphere is not considered. Also not considered is a possibility of breaching the casing shoe due transmission of P_{csg} downhole.

The objective of this study is to develop methods for maximum possible air emission rates (MER) and risk of subsurface well integrity failure due SCP. Mathematical models and software are developed for computing MER, casing shoe strength (CSS) determined by leak-off test (LOT), and casing shoe pressure load resulting from SCP (SCP_d). The models are used to find controlling parameters, identify the best and least-desirable scenarios, and assess environmental risk.

It is concluded that emission potential of SCP wells with high wellhead pressure (P_{csg}) can be quite small. The CSS model study reveals the importance of data recorded from LOT; particularly the time after circulation was stopped – the non-circulation time (Δt_s). Ignoring Δt_s would result in underestimation of the ultimate CSS. The error is caused by the cumulative effect of thermally induced rock stresses, which strongly depend on Δt_s. The study displayed SCP_d being controlled by the annular fluid properties which are subject to change in long time through mud aging; and mostly being overestimated.

Comparison of surface versus subsurface failure scenarios yielded cases where the casing shoe demonstrates more restrictive failure criterion (CSS) than the burst rating of wellhead (MAWOP). Risk of casing shoe breaching (R_K) is quantified using the CSS and SCP_d models and application of risk analysis technique (QRA). The CSS distribution followed log-normal trend due the effect of Δt_s, while the SCP_d distribution maybe of various shapes dependent on the annular fluid size and properties that are not well known. Possible scenarios of casing shoe breaching are statistically tested as a hypothesis of two means. The study produced engrossingly variant outcomes, R_K changing from 1 to 80 percent.

.

1. INTRODUCTION – SUSTAINED CASING PRESSURE PROBLEM

Well-head pressure (P_{csg}) is the undesired accumulation of pressure in any casing annuli of producing or abandoned wells. Excessive P_{csg} constitutes potential environmental risk of well integrity failure. Source of the P_{csg} may vary [1]. It may result from expansion of the wellbore fluids caused by the differential temperature between the static and producing conditions defined as thermally induced well-head pressure. Another source, operator induced well-head pressure is the pressure imposed by the operator on a casing annulus for various purposes, such as gas lift or thermal management. If the P_{csg} results from a leak in any of the pressure containment barriers it is called sustained casing pressure (SCP).

SCP has two potential sources. Firstly, P_{csg} may be due internal integrity failure, *i.e.* pressure communication between tubing and casing or between casing strings. This is a frequent cause of SCP and approximately 9 of 10 incidents in the Gulf of Mexico (GOM) are due internal integrity failure [2]. Secondly, P_{csg} may be due external integrity failure, *i.e.* gas migration through damaged cement sheath. Remediation of external integrity failure is more difficult and less than half of the operations are successful [2]. Industry recommended practices recognize the difference between casing pressures that are thermally induced, operator induced or due internal integrity failure and those resulting from gas migration [1]. In this study, we address SCP due external integrity failure.

Sustained casing pressure (SCP) is identified as the casing pressure that returns after bleed off, thus, resulting from a continuing gas migration. MMS/BOEMRE 30 CFR Part-250 [3] provides criteria for monitoring and testing of wells with sustained casing pressure. Also, the American Petroleum Institute (API) Recommended Practice 90 Annular Casing Pressure Management for Offshore Wells [1] provides guidelines for managing annular casing pressure and identifies different levels of environmental risk. At present, the SCP risk is identified using the well-head failure scenario.

In the United States, MMS/BOEMRE requires that casing pressure in the fixed platform wells must be monitored on a regular basis. A bleed-off – build-up (B-B) test must be performed if P_{csg} is greater than 100 psig [3]. In Canada, Energy and Utilities Board (EUB) regulates SCP using the flowing bleed-down pressure and the increase of P_{csg} during the shut-in period [4]. If flowing pressure is greater than 1,400 kPa, or increases more than 42 psig during test shut in period, the SCP is considered to constitute high risk. In Norway, NORSOK Standard D-010 Well Integrity in Drilling and Well Operations [5] regulates SCP using an arbitrary sub-surface failure criterion. If P_{csg} is greater than 7,000 kPa for any intermediate casing, SCP is considered high risk.

Monitoring of P_{csg} is different in fixed-platform versus subsea wells. For fixed platform wells, each non-structural casing string is equipped with gauge and the pressure in each annulus can be monitored

monthly from taps or flanges installed directly on the wellhead. For subsea wells, pressure in the innermost tubing-casing annulus can be monitored. However, other annuli are hydraulically isolated after the casing strings have been landed in the wellhead. Thus it is a technical challenge to monitor the pressures in subsea well-heads.

The API Recommended Practice 90 identifies environmental risk of SCP based on the magnitude of P_{csg} and its comparison with the maximum allowable well-head operating pressure (MAWOP) [1]. If any P_{csg} is greater than 100 psig or exceeds the casing's minimum internal yield pressure (MIYP), a B-B test must be performed. A flowchart demonstrating the risk-rating logic is shown in Fig. 1.1.
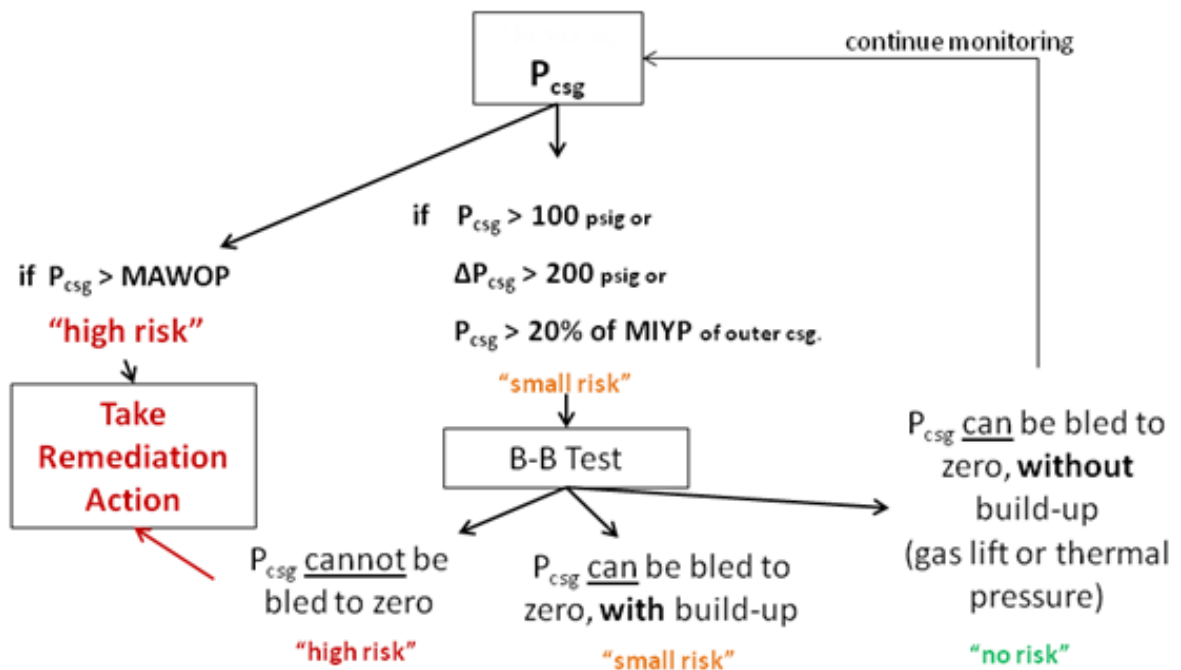
Fig. 1.1-Current identification of SCP risk [1]

The B-B test is performed by bleeding off the wellhead pressure through a one-half inch needle valve, followed by a 24 hour shut-in period. Based on the outcome, the environmental risk is categorized as none, small or high. If the pressure cannot be bled off within 24 hours, the risk is considered high. Else if it is bled to zero but builds back up when shut in, the risk is considered small. If no build up is observed, the P_{csg} is not considered due SCP constituting no risk. The three cases are shown on a qualitative B-B test chart in Fig. 1.2.
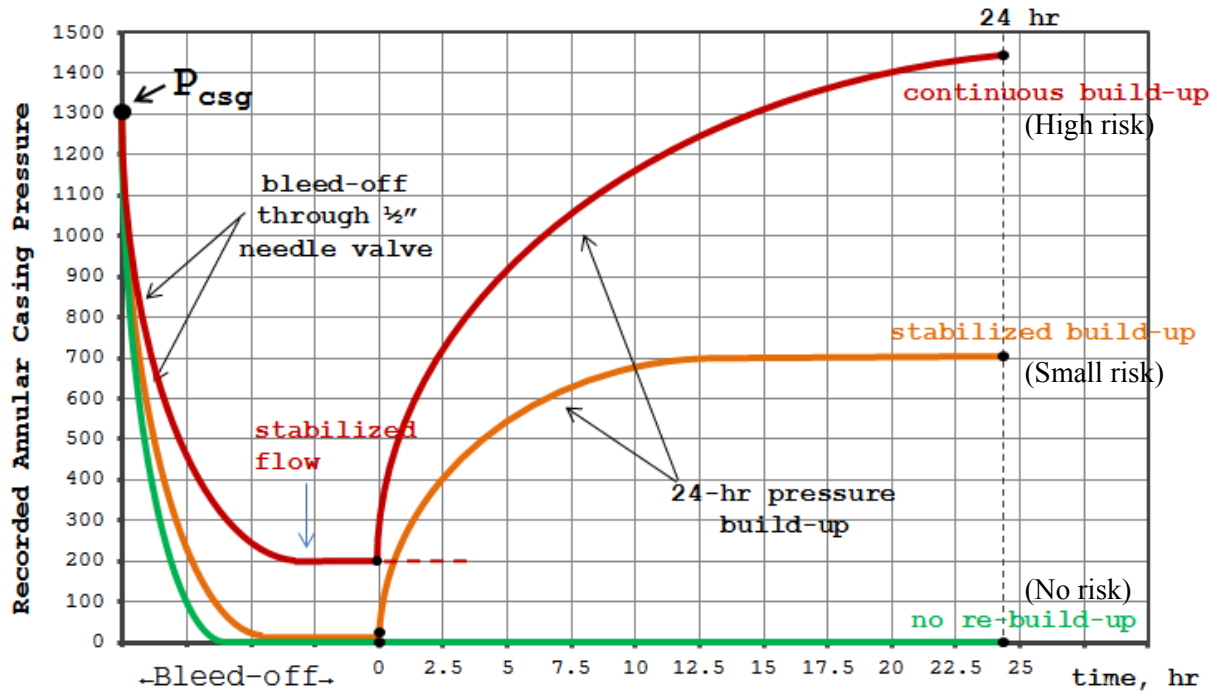
Fig. 1.2-Possible outcomes in a B-B test

SCP is not a static problem [1]. It may escalate over time as a result of factors such as deterioration of the cement sheath, damage to primary cement caused by mechanical shock impacts during tripping, thermal cracking, or dissolution of cement in acidic formation brine. Several case studies have reported initially problem-free wells developing sustained casing pressure over time [6].

Current regulatory control considers surface failure by comparing P_{csg} with MAWOP. But it does not present any methodologies to quantify the environmental risk in case of failure. Risk assessment is left to the operator's judgment on case-by-case evaluation [1].

2. WELL INTEGRITY FAILURE DUE SUSTAINED CASING PRESSURE

Release of reservoir hydrocarbons, possibly natural gas, into the environment can occur due to gas migration through leaking cement in producing or idle wells. Generally, emission rates of hazardous substances and criteria pollutants into the ambient air are difficult to quantify without special monitoring equipment. Methods have been published to calculate or estimate the emission rates for specific equipment and processes for variety of industries in SPE Monograph Volume 18 [7].

U.S. EPA AP-42, Compilation of Air Pollution Emission Factors, Vol.1 contains emission factors for stationary point and area sources [8] (Oil and gas wells are considered as stationary source, since their location is known.) EPA-450/2-88-006a "Toxic Air Pollutant Emission Factors – A Compilation for Selected Air Toxic Compounds and Sources" is a document that lists the emission factor database for variety of stationary point sources. However, there is no quantitative methodology regarding possible air emissions from wells with SCP. Thus, calculation of emission rates requires correct modeling of gas migration. In this study, a mathematical model and software have been developed to calculate maximum air emission rate.

As discussed above, present regulations consider the environmental risk of SCP based on the surface failure scenario. However, the well-head may not necessarily be the weakest barrier of the well's integrity system. A subsurface barrier may be the first to fail in response to the pressure build up due gas migration. Typically, the formation below a casing shoe is the weakest point in the annulus and its pressure limitation is termed here as casing shoe strength (CSS). If the well-head pressure increases high enough to create a downhole pressure exceeding the CSS, the formation below the casing shoe would fail. In this case, the gas would breach the casing shoe and flow into the outer annulus or rock causing an underground blowout [9]. Environmental consequences of an underground blowout may be catastrophic [10]. Migrating gas may also charge the shallower formations causing unexpected abnormal pressures or polluting the fresh water aquifers [10]. Consequently, the possibility of subsurface failure should also be considered. API Recommended Practice 90 defines the property of casing that can be used to determine the critical conditions for surface failure as,

$$P_{csg} > MAWOP \qquad\qquad 2.1$$

where,

P_{csg} =   casing well-head pressure at surface, psi

MAWOP =   maximum allowable well-head operating pressure, psi

MAWOP is calculated considering the collapse of the inner tubular and bursting the outer tubular [1]. It equals either 50% of MIYP of the pipe body for the casing being evaluated, or 80% of MIYP of the pipe body of the next outer casing, or 75% of collapse rating of the inner tubular pipe body, whichever is smaller. For the outermost casing, MAWOP is the lesser value of 30% of MIYP of the pipe body for the casing or production riser being evaluated or 75% of inner tubular pipe body collapse rating. The critical condition for the subsurface failure has not been defined by the regulations to date. Here, the critical condition is proposed to be,

$$P_{csg} > CSS \cdot SF - P_{hyd}$$ 2.2

where,

P_{hyd} =   hydrostatic pressure of the mud column above cement top outside casing, psi

SF =   safety factor that can be estimated from the kick margin value

CSS =   casing shoe strength, psi

The B-B test analysis model presented by Xu. *et al.* [11] provides reasonable estimate of the downhole pressure due SCP (SCP_d), given as,

$$SCP_d = P_{csg} + P_{hyd}$$ 2.3

In this study, the model is used to compare critical condition for the casing head failure – defined by eqn.2.1 with those for casing shoe failure –eqn.2.2, for two example wells, Study Well (See Fig. 3.22) and Well KH-9.

Table 2-1- Comparison of Surface vs. Subsurface Integrity Failure for GoM Well*

Annulus		MIYP	Collapse	MAWOP (eqn.2.1)	Critical P_{csg}* (eqn.2.2)
		psig	psig	psig	psig
A	9 5/8", 53.5#, Q-125	12,390	8,440	N/A	N/A [1]
B	13 5/8", 88.2#, Q-125	10,030	4,800	4,168	3,569
C	18 5/8", 136#, N-80	5,210	2,480	1,276	1,424
D	24", 256#, Gr.B	1,595	742	478	558

*SF = 1.0

---

[1] Pressure in the A annulus is not considered as sustained casing pressure (See Section 1)

The calculated critical values of well-head pressures that cause surface and subsurface failure in the Study Well are shown in Table 2-1. In annuli C and D, the critical P_{csg} from eqn.2.1 is smaller than that from eqn.2.2. Thus, wellhead failure criterion is more restrictive than the subsurface failure. However, for annulus B, the subsurface failure criterion (3,569 psi) is more restrictive than surface failure (4,168 psig). In other words, a continuous buildup of P_{csg} in annulus B would cause the casing shoe to fail first.

Comparison of the critical well-head pressures for the surface and subsurface failure in Well KH-9 has been performed by Ameen,S. (2012) [12]. Well KH-9 is a 9,895 ft vertical well located in KhorMor field in Kirkuk. The surface, upper and lower intermediate and production intervals were drilled with 9, 10.5, 14 and 17.6 ppg water base muds, respectively. All annuli were cemented to the surface, except the 7" production liner. The 7" liner was hanged at 6,778 ft with 195 ft cement overlap with the 9-5/8" casing. Therefore, annulus B form the first pressure containment barrier protecting the tubing at the surface. The well configuration and drilling data are presented in APPENDIX A. In Table 2-2 shown the critical pressures for the surface and subsurface failure of Well KH-9.

Table 2-2-Comparison of MAWOP and SCP_d inWell KH-9*

Annulus		MIYP	Collapse	MAWOP	Critical P_{csg}*
		psig	psig	psig	psig
A	7", 29#, L-80	8,160	7,020	N/A	N/A
B	9-5/8", 53.5#, P-110	10,900	7,930	N/A	N/A [1]
C	13-3/8", 68#, K-55	3,450	1,950	1,725	3,206
D	20", 133#, K-55	3,060	1,500	918	1,344

*SF = 1.0

In this example, the well-head forms a weaker pressure containment barrier, *i.e.* if P_{csg} increases due gas migration exceeding the well's pressure limitations, the well is expected to fail at the surface. This result is mainly due the practice of cementing the annuli to the surface. This action noticeably reduces the risk of subsurface failure, however limits the SCP remediation options over the life time of the well [13]. Consequently, calculation of MAWOP has been defined based on arbitrary numbers set based on industry experience. The critical condition for the casing shoe failure is set with no safety margin making the comparison somewhat biased towards the surface-failure scenario. Moreover, flow potential of the well in case of a well-head failure is not considered. In this study, mathematical model and software are presented to calculate the maximum emission rate from the failed well-head.

---

[1] The 7" liner is hanged to the 9 5/8" casing at 6,680 ft (See Fig.A.1)

2.1. Case Histories of Well Integrity Failure due Sustained Casing Pressure

US Department of Interior Mineral Management Services (MMS/BOEMRE) has created a database for the well integrity failure incidents including surface and subsurface failures due external gas migration, as well as tubing leaks, thermally induced pressures and gas lift [2]. Several case history examples are presented here in order to provide better understanding of the potential well integrity failure problem caused by sustained casing pressure, as follows.

Case 1 is loss of subsurface well integrity in Sahara Desert near the community Rhourde Nouss, Algeria, where an underground blowout was initiated due SCP between the 9 $^5/_8$ and 13 $^3/_8$ " casings. The migrating gas cratered a water well 127 meters away, and small fires around the well, as shown in Fig. 2.1. Temperature and noise logs confirmed continuous flow of gas from the formation at 12,230 ft into a lost circulation zone at 5,570 ft, below the casing shoe at 2,343 ft.

Fig. 2.1-Migration of gas to surface from failued casing shoe [14]

Case 2 is loss of surface well integrity due build up of pressure at the B annulus on a fixed platform GOM well [15]. The well developed SCP 6 years after the wells were completed. Two years after departure granted by MMS, the surface integrity was lost between the production and surface casings. The well flowed for 46 days releasing 66 MMscf gas and 3,200 bbl condensate until it was blowout was eventually killed by a relief well.

Case 3 is an example of well integrity loss during drilling in a 300 ft .water depth where external gas migration. Minimum of 100 MMscfD was estimated to flow, which nearly resulted the loss of the platform [14].

Fig. 2.2-Loss of subsurface well integrity in offshore well [14]

Case 4 is loss of subsurface well integrity in Grand Isle Block 90, Well C-7ST OCSG 4003 in 2002 [16]. Gas channeling following the primary cementing operation resulted build up of pressure at the conductor-surface casing annulus. The buildup of annular pressure, which initially was 580 psig, eventually caused breaching of the 16" conductor at 1,200 ft and resulted flow of gas to the surface.

3. UNCONTROLLED EMISSION RATE FROM OPEN SCP WELL

In this study, the mathematical model and software used to calculate the maximum gas rate into the atmosphere from a failed wellhead due to sustained casing pressure were developed. Firstly, a description of the overall flow mechanism is presented, followed by descriptions of the sub-mechanisms involved. Secondly, a model algorithm is presented followed by a field case example.

Indeed, 'pressure communication between tubing and casing strings' is a more frequent cause of SCP and approximately 9 of 10 incidents are due to this so called 'internal integrity' failure [2]. However, it can often relatively easily be remediated by routine work-over operations [15]. Thus, analysis of the external integrity failure rather than internal integrity is the major focus of this study.

3.1.   Gas Flow in Open Annulus

In a well with sustained casing pressure (SCP), the wellhead pressure (P_{csg}) results from the system equilibrium. As the gas from the source formation is charged into the cement, accumulation of the gas above the mud column brings the system to the equilibrium. [17]. Components of a vertical well with P_{csg} are shown in Fig. 3.1.
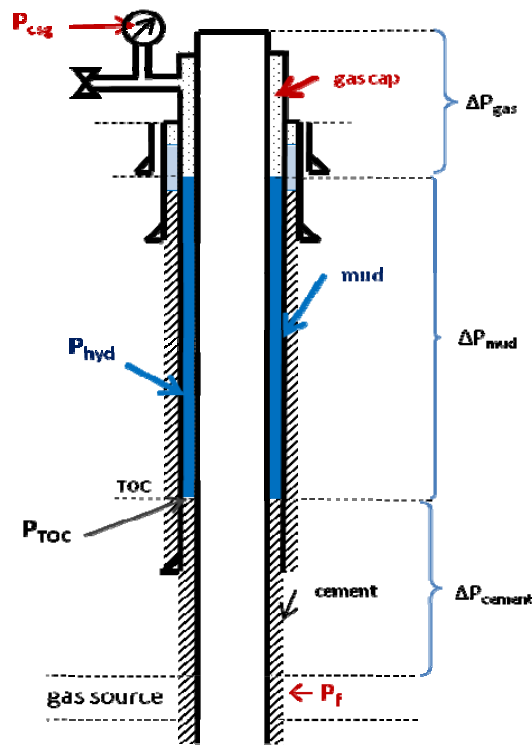
Fig. 3.1-Verticle well with equilibrium sustained casing pressure

In equilibrium, formation pressure (P_R) is balanced with P_{csg}, hydrostatic pressure created by the mud column (P_{hyd}) and hydrostatic pressure of the fluids inside the cement leak. If the cement leak is filled with gas, the pressure balance can be simplified as [17],

$$P_f \cong P_{TOC} = P_{csg} + P_{hyd}$$

3.1

In case of the casing well-head failure, $P_{csg} = 0$, *i.e.* an instant pressure imbalance is formed, which is the driving force for the gas flow. The resultant flow rate in such case depends on the total pressure drop downstream from the gas source as,

$$q_{gas} = f\left(P_f - \Delta P_{total}\right)$$

3.2

where,

$$\Delta P_{total} = \Delta P_{cement} + \Delta P_{mud} + \Delta P_{gas}$$

3.3

where,

ΔP_{cement}: frictional pressure loss through the cement sheath

ΔP_{hyd}: mud column hydrostatic pressure

ΔP_{gas}: frictional pressure loss through the gas column

In eqn.3.3 each term is a complex function of the model parameters controlling the flow mechanism. Therefore, calculation of the maximum gas rate requires mathematical definition of each component and coupling the components at the cement top using Nodal analysis. The well flow system comprises four nodes shown in Fig. 3.1: gas formation, cement, mud, and well-head. Graphical representation of the flow system performance is presented in Fig. 3.2. As shown, performance of the overall flow system can be expressed as two nodes coupled at the cement top. The bottom node is that the formation responses to pressure drop by delivering flow, and the upper node is that the pressure drop from the top of cement to the atmosphere. The approach is similar to the widely accepted IPR-TPR [1] performance analysis in gas well production design [18].

However, the complexity added by the flow in mud column requires a different mathematical modeling approach. These two nodes represent flow in the cement sheath and gas migration in a stagnant mud

---

[1](inflow performance relation – tubing performance relation)

column. The Cement Top Inflow Performance (CTIP) represents gas flow in the cement sheath and gas formation.

It depends solely on cement leak size and the reservoir pressure of gas bearing formation. Gas well testing theory provides mathematical description of flow from the formation to the top of cement [18]. The flow is a combination of radial and linear flow in series. In this study, the reservoir pressure (P_R) is assumed constant.

The Cement Top Outflow Performance (CTOP) represents gas migration upwards from the cement top through the mud column and the liquid-free annulus above free level of liquid. (When liquid unloading occurs, at high gas rates a narrow annulus and a liquid-gas mixture with higher average density could result in a significant pressure gradient that would add to the flowing pressures at the top of cement (TOC). At low gas rates, however, contribution of the pressure drop due to frictions above mud level become insignificant. Additional restriction to flow is the failed well-head. The restriction behavior of this component depends on the case by case well-head failure incident, thus in this study the well-head is assumed to form no restriction to flow.
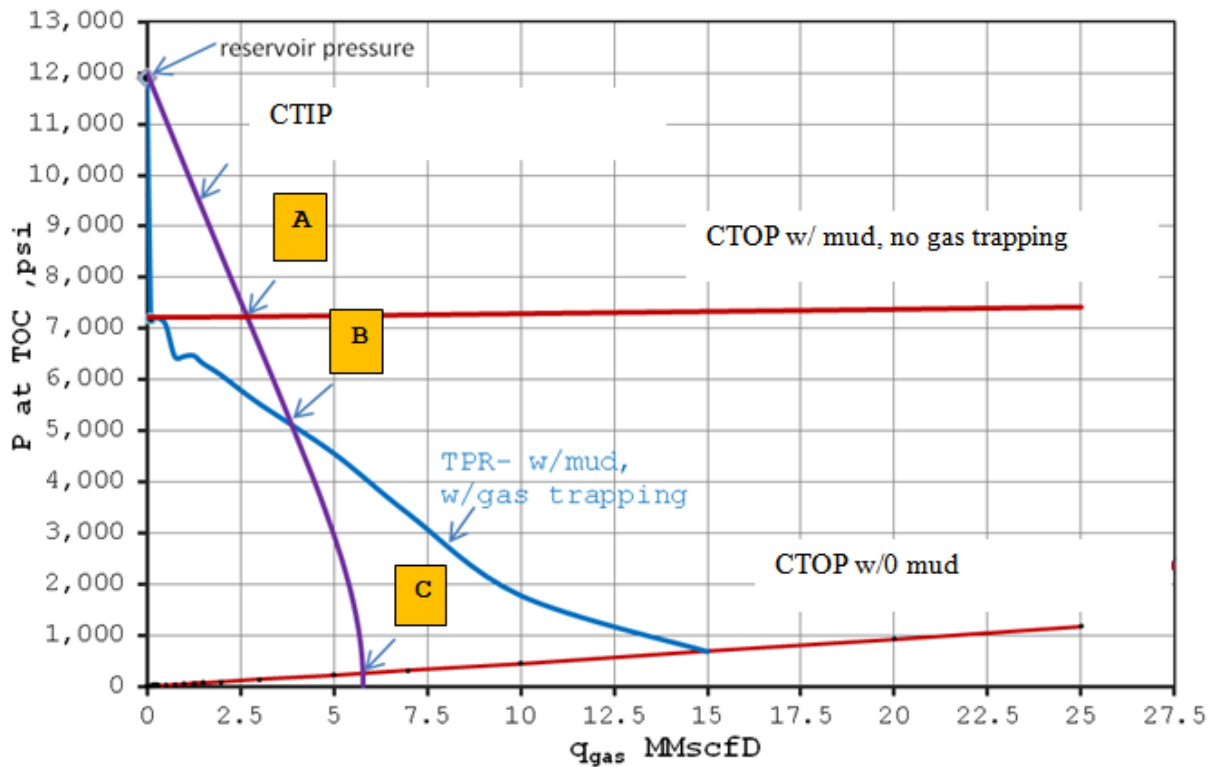
Fig. 3.2-System performance of SCP well

Mathematically, the maximum steady-state gas flow rate (q_g) is the common solution at the cement top. Graphically, the solution is the intercept of the CTIP and CTOP curves. Top cement inflow performance and cement top outflow performance curves are shown in Fig. 3.2.

Numerically, the system can be solved for the two mechanisms as a function of each other to converge on the coupling criteria. Coupling criteria in the Max Rate Model is the top of cement pressure (P_{TOC}). The developed software offers both options. It either constructs the complete CTIP-CTOP curves or converges on equilibrium q_g.

Major difference of a flow system that includes cement sheath and stagnant mud column from a conventional gas well testing is the various possible outcomes depending on the well configuration, condition of the mud and the cement sheath. Expansion of the mud due gas cutting may trigger liquid unloading from the annulus causing reduction in P_{TOC}. Depending on the combination of the configuration the system may equilibrate on various rates as shown in Fig. 3.2 as points A, B and C.

Complexity is added by liquid unloading phenomenon. Pressure differential between the reservoir pressure and P_{TOC} determines the rate through the cement sheath. Hydrostatic pressure created by the stagnant mud column controls P_{TOC}. As the gas is charged into the mud from the TOC, mud column expands and if its length exceeds the distance to the surface, liquid is unloaded. This phenomenon requires closer attention because reduction in P_{TOC} due liquid unloading may trigger an irreversible domino effect resulting AOF.

Possible scenarios are as follows. If the mud was not trapping any gas, and allowing the gas bubbles to migrate to the top with zero gas cutting, the mud column would not expand. With no expansion and unloading, q_g would be defined at point A in Fig. 3.2. Hence, mud rheology becomes the critical parameter since gas trapping is primarily controlled by the residence time of the gas in the mud. Gas residence time is a direct function of gas rise velocity in mud.

If gas trapping is considered, some mud is unloaded from the annulus until the system comes to a steady state flow, which yields the equilibrium rate shown at point B. Depending upon the leak size and formation pressure, complete unloading may occur. In such case the equilibrium rate, q_g, occurs at point C, which is the worst case scenario.

In this study, a comprehensive mathematical model and software for computing the equilibrium rate are developed. The following chapters present analytical formulations of the mechanisms involved in the unrestricted flow from well with failed wellhead.

3.2.   Flow through Cement

The Main purpose of a cementing operation is to permanently isolate the zones behind the casing string [6]. Two stage cementing, or annular intervention actions are essentially performed to guarantee or remediate this function [19]. However, a significant number of wells experience late gas migration during their life time.

Although cement itself is almost impermeable, micro cracks form in time due to chemical effects, mechanical impacts or temperature variations [20]. Nazridoust *et al.* (2006) [21] used effective permeability concept to model gas flow through cement micro cracks. Representation of the cement sheath as a porous medium with an 'effective permeability' was also proposed by Duan,S. (2000) [22] . Al-Hussainy *et al.* (1966) [23] introduced equation for linear real gas flow in porous medium as,

$$q_g \int_0^L dx = 0.006328 \; \frac{k_{eff} A_p T_{sc}}{P_{sc} T} \int_{P_1}^{P_2} \frac{P}{\mu(P)Z(P)} dP \qquad\qquad 3.4$$

where,

q_g =	gas rate, scf/D
k_{eff} =	cement effective permeability, md
A_p =	annular flow area, ft^2
T_{sc} =	standard temperature, °R
P_{sc} =	standard pressure, psia

The integral in 3.4 defines pseudo pressure property of natural gas defined as,

$$m(P) = 2 \int_{P_b}^{P} \frac{P}{\mu(P)Z(P)} dP \qquad\qquad 3.5$$

A real gas pseudo pressure solution was presented by Al-Hussainy *et al.* as,

$$q_g = 0.003164 \cdot \frac{k_{eff} A_p T_{sc} [m(P_f) - m(P_{ws})]}{P_{sc} \cdot T_{ws} \cdot L_c} \qquad\qquad 3.6$$

where,

L_c =	cement sheath length, ft
T_{ws} =	temperature at the top of cement, °F

The following assumptions are made for modeling gas flow through cement:

- diameter of the cement sheath is small compared to its length;

13

- there is a single-phase flow of gas in cement leak;

- capillary pressures and gas hydrostatic pressure are ignored;

- gas flow rate at cement top is constant and continuous;

- mass flow rate of gas is constant throughout mud column.

In this study, real gas flow equation given by eqn.3.6 is used to model the flow through the cement sheath.

3.2.1. Flow through Stagnant Mud Column

Flow of gas starts at the cement top, and ends at the top of the mud column. Kulkarni *et al.* [24] suggested that the cement/mud interface can be represented as single orifice. Driven by the buoyancy forces, gas bubbles move upwards by slippage [25]. As gas bubbles rise upward in stagnant mud, mud is displaced creating local flow around the bubbles.

Modeling of gas flow with single bubble approach however considers only infinite medium and disregards size and shape of bubbles. During unrestricted flow, gas is introduced from the interface continuously. The rate of gas flow and the void space occupied by the gas determine distribution of the bubbles in the annulus, liquid holdup and the flow regimes [26].

Multiphase flow approach is considered in this study to model gas flow through stagnant mud column. Mass transfer between the gas and liquid phases is ignored. Phases are assumed immiscible. Mud is assumed non-Newtonian water based mud. Well is assumed vertical.

Gas is highly compressible and expands as the ambient pressure decreases. Therefore its velocity increases as it rises in the annulus. Superficial velocities of gas and liquid at depth z, which assume one phase occupies the entire flow area, A_p, are given by,

$$v_{SL}(z) = \frac{q_L(z)}{A_p}$$ 3.7

$$v_{Sg}(z) = \frac{q_g(z)}{A_p}$$ 3.8

where $q_g(z)$ is gas flow rate at depth z. Therefore, time and space averaged velocity of gas at depth z is calculated by,

$$v_g(z) = \frac{v_{Sg}(z)}{1 - H_L(z)}$$ 3.9

where $H_L(z)$ is the in-situ volume fraction of the liquid, known as liquid holdup. $H_L(z)$ is flow regime dependent and must be determined from empirical or mechanistic models. Calculation of the gas rise velocity is further discussed in following sections.

Ansari *et al* [27]. presented mechanistic model for vertical flow in pipes and used equivalent diameter concept to estimate pressure gradient in annulus. Hasan and Kabir [28] presented mechanistic model for flow in annulus based on experiments with air and water. In their model for bubble flow, liquid holdup is calculated assuming pipe-flow. For slug flow, drift flux model is applied, assuming single-phase slugs of water and gas.

Caetao *et al.* [29] presented mechanistic model for vertical upward flow in concentric and fully eccentric annuli. Pressure at depth z, $P(z)$, is the sum of elevation, friction and acceleration terms from surface to z, given as,

$$P\left(z_{TC}\right) = \int_0^{z_{TC}} \left[\left(\frac{dP}{dz}\right)_{el} + \left(\frac{dP}{dz}\right)_f + \left(\frac{dP}{dz}\right)_{acc}\right] \cdot dz \qquad\qquad 3.10$$

As the acceleration term is small it is ignored in this study. Elevation and friction terms are strong functions of flow regime and friction factor. For steady state gas flow rate, q_g, pressure gradient is determined at each depth z and numerically integrated over the length of liquid column. In this study, Caetao *et al.* [29] mechanistic model is used to determine flow regime transitions and to calculate pressure gradient for bubble and slug flow regimes. For annular flow, liquid film thickness is assumed zero, and single phase flow of gas-liquid mixture is assumed.

3.2.1.1. Flow Regime Transition Criteria

Bubble/slug flow transition. Caetano *et al.* [29] observed substantial differences in the flow regimes in wellbores and annuli. Annular eccentricity plays a role on the flow regime such that the small bubbles and larger size bubbles, so called cap bubbles tend to flow through the widest gap in the cross section [28]. Effect of this phenomenon makes difference in slow liquid rates, since it creates void fraction heterogeneity throughout the area. Depending on the relation between superficial gas velocity, v_{Sg}, and superficial liquid velocity, v_{SL}, flow pattern changes [27].

Shoham *et al.* [25] described characteristics of flow regimes. Bubble flow is characterized by homogenously distributed discrete bubbles moving upwards in zigzag motion in continuous liquid phase. Bubble flow is observed at low liquid rates and low gas rates, and slippage is observed between phases. Slug flow is observed at higher gas rates. Slug flow is characterized by bullet shape gas pocket called Taylor bubbles which occupies almost the entire cross sectional area, followed by a slug of liquid. At

higher gas-flow rates, churn flow is observed. Churn flow is characterized by chaotic slugs with no clear boundaries. At higher gas rate transition to annular flow is observed. Annular flow is characterized by a fast moving continuous gas core and slow moving liquid film around the pipe wall. Dispersed bubble flow occurs at very high liquid rates and low gas rates, with no observed slippage. Flow regimes in eccentric and concentric annuli are shown in Fig. 3.3. In this study, only bubble, slug and annular flow regimes are considered.
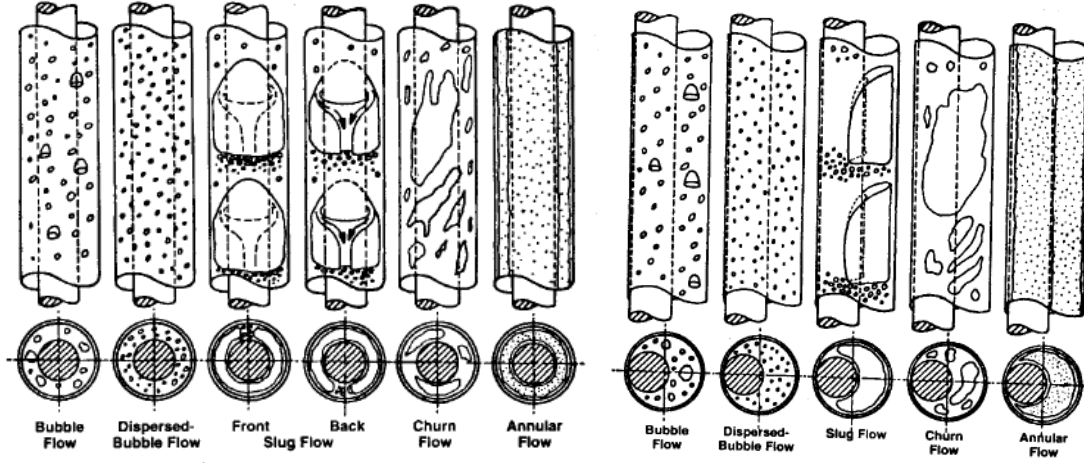
Fig. 3.3-Flow regimes in vertical concentric annulus (left), in eccentric annulus (right), (Caetano *et al.*,1992) [29]

For bubble/slug flow transition, Taitel *et al.* [30] model is modified for experimental gas void-fraction values. Transition to slug flow is observed to occur at gas void fractions above 0.20 in concentric annuli and 0.15 in fully eccentric annuli. Modification of Taitel *et al.* [30] model by use of gas void fractions yields superficial gas velocities above which transition to slug flow at low liquid rates will occur are given as,

$$v_{sg}(z) = \frac{v_{SL}(z)}{4.0} + 0.306 \cdot \left[\frac{\left[\rho_L - \rho_g(z)\right] \cdot g \cdot \sigma_L}{\rho_L^2} \right]^{\frac{1}{4}} \qquad 3.11$$

$$v_{sg}(z) = \frac{v_{SL}(z)}{5.67} + 0.230 \cdot \left[\frac{\left[\rho_L - \rho_g(z)\right] \cdot g \cdot \sigma_L}{\rho_L^2} \right]^{\frac{1}{4}} \qquad 3.12$$

where $v_{Sg}(z)$ and $v_{SL}(z)$ are gas and liquid superficial velocities, in fully concentric annuli and fully eccentric annuli respectively.

Slug/annular flow transition. Transition to annular flow is defined by minimum gas velocity to lift the largest liquid droplet upwards in a gas core. The balance between gravity and drag forces gives the critical superficial gas velocity for the transition from slug flow to annular flow [30] as,

$$v_{Sg} = 3.1 \left[\frac{(\rho_L - \rho_g)g\sigma_L}{\rho_g^2} \right]^{1/4}$$

3.13

3.2.1.2. Pressure Gradient above Top of Cement

Bubble flow. The cement top pressure profile given by eqn.3.10 strongly depends on the flow regimes. In the bubble flow regime, mechanistic model presented by Caetao et al. [29] is used to determine pressure gradient as,

$$\left(\frac{dP}{dL} \right)_{el}\bigg|_z = \rho_{TP}(z) \cdot g$$

3.14

where g is the gravitational constant and $\rho_{TP}(z)$ is the two-phase mixture density. In the bubble flow, the drift flux approach assumes homogeneously distributed discrete bubbles and considers slippage. So the mixture density is,

$$\rho_{TP}(z) = \rho_L \cdot H_L(z) + \rho_g(z) \cdot [1 - H_L(z)]$$

3.15

In eqn.3.15, ρ_L and ρ_g are the liquid and gas densities at depth z, respectively. $H_L(z)$ is the in-situ liquid holdup, calculated implicitly from the equation,

$$H_L^{n+2} - H_L^{n+1} + \frac{(v_{SL} + v_{Sg})H_L}{1.53 \left[\frac{(\rho_L - \rho_g)g\sigma_L}{\rho_L^2} \right]^{1/4}} - \frac{v_{SL}}{1.53 \left[\frac{(\rho_L - \rho_g)g\sigma_L}{\rho_L^2} \right]^{1/4}} = 0$$

3.16

where n is the bubble swarm index, experimentally determined as 0.5.

The friction component in eqn.3.10 is given as,

$$\left(\frac{dP}{dL} \right)_f\bigg|_z = \frac{4 \cdot f'}{d_{ci} - d_{to}} \cdot \rho_{TP}(z) \cdot \frac{v_m(z)^2}{2}$$

3.17

where $v_m(z)$ is the mixture velocity, for bubble flow given by,

3.18

$$v_m(z) = v_{SL}(z) + v_{Sg}(z)$$

and f' is the Fanning friction factor for non-Newtonian flow in annuli. Friction factor for laminar flow in eccentric annuli is calculated by numerical model developed by Haciislamoglu and Langlinais [31], and for turbulent flow, method suggested by Brill and Mukherjee [26] is considered (See APPENDIX D).

Slug Flow. Caetano *et al.* [29] developed mechanistic hydrodynamic model for slug flow in annuli. In Fig. 3.4 physics of fully developed slug flow is shown. Iterative procedure on film thickness is required as described below.

Pressure gradient at depth *z* in eqn.3.10 is given as,

$$\left(\frac{dP}{dL}\right)_{el}\bigg|_z = \rho_{LS}(z)\cdot g\cdot\left(\frac{L_{LS}(z)}{L_{su}(z)}\right)$$

3.19

where ρ_{LS} is the slip density for the gas/liquid mixture in the liquid slug.
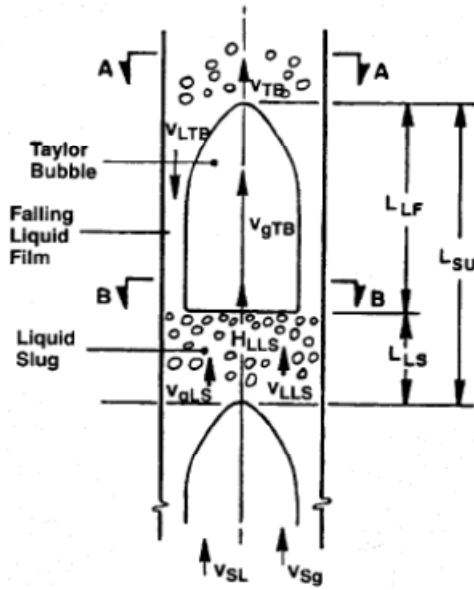
v_{SL} = superficial liquid velocity, m/s
v_{Sg} = superficial gas velocity, m/s
v_{LLS} = in-situ liquid velocity in liquid slug, m/s
v_{gLS} = in-situ gas velocity in liquid slug, m/s
v_{LTB} = in-situ liquid velocity in liquid film, m/s
v_{gTB} = in-situ gas velocity in Taylor bubble, m/s
v_{TB} = Taylor bubble transitional velocity, m/s
H_{LLS} = liquid holdup in liquid slug
L_{LS} = length of liquid slug, m
L_{LF} = length of liquid film, m
L_{SU} = length of slug unit, m
δ = film thickness, m

Fig. 3.4 Fully developed slug flow (Caetano *et al.*,1992) [29]

Friction component in eqn.3.10 is given by,

$$\left(\frac{dP}{dL}\right)_f\bigg|_z = \frac{2f'}{d_{ci} - d_{to}}\cdot\rho_{LS}(z)\cdot\left[v_{Sg}(z) + v_{SL}(z)\right]^2\cdot\left(\frac{L_{LS}(z)}{L_{su}(z)}\right)$$

3.20

where *f'* is the Fanning friction factor for non-Newtonian flow in annuli, calculated by the methodology described in APPENDIX D. Net upward liquid velocity in a stagnant mud column is zero. Hence, energy needed to accelerate the liquid film is negligible. Therefore, the acceleration component of eqn.3.10 for slug flow yields,

$$\left(\frac{dP}{dL}\right)_{acc}\bigg|_z = 0$$

3.21

Solution of the lengths, velocities and holdup parameters given in equations 3.19 through 3.21 is described in APPENDIX C. Mass balance on liquid phases in slug and film zone must be satisfied for a film thickness, δ. Thus, iterative procedure on δ is necessary to solve for v_{LTB}, v_{LLS} and H_{LTB}.

Annular Flow. If the superficial gas velocity exceeds the critical value for slug/annular transition, gas forms a continuous core and the liquid phase forms liquid films on the surface of the inner and outer casing faces, as shown in Fig. 3.5. In this study, liquid rate is assumed zero, the gas flow occupies the entire cross sectional area and the liquid film thicknesses is assumed to zero.
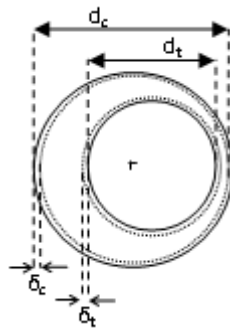
Fig. 3.5-Annular two phase flow in eccentric annulus

The liquid holdup is considered in the mixture density computation. The elevation term in eqn.3.10 is given as,

$$\left(\frac{dP}{dL}\right)_{el}\bigg|_{z} = \rho_{TP}(z) \cdot g \qquad\qquad 3.22$$

Friction component in eqn.3.10 is given as,

$$\left(\frac{dP}{dL}\right)_{f}\bigg|_{z} = \frac{2 \cdot f' \cdot \rho_{TP}(z) \cdot v_{g}(z)^{2}}{d_{c} - d_{t}} \qquad\qquad 3.23$$

where calculation of Fanning friction factor, f' is described in APPENDIX D.

3.2.1.3. Liquid Unloading due Gas Expansion

When gas emits from the mud/cement interface, mud level in the annulus rises because of the additional volume occupied by the migrating gas. Total volume of the 'gas-cut mud' in the steady state flow condition is the summation of the liquid and gas volumes. Gas is compressible and the pressure in a gas bubble is equal to the ambient pressure, resulting in expansion of the gas bubbles. The total volume of liquid in the mixture column is,

$$V_L = \int_{z=0}^{D} V_L(z) \cdot dz \qquad\qquad 3.24$$

where $V_L(z)$ is the liquid volume in a computation cell z, given as,

$$V_L(z) = L_{cell}(z) \cdot A_p \cdot H_L(z) \qquad\qquad 3.25$$

where,

$L_{cell}(z) =$ length of computation cell of annulus at depth z, ft

$A_p =$ cross sectional flow area, ft^2

Likewise, the total volume of gas in the mixture column is,

$$V_g = \int_{z=0}^{D} V_g(z) \cdot dz \qquad\qquad 3.26$$

where $V_g(z)$ is the gas volume in a computation cell of annulus at depth z, given as,

$$V_g(z) = q_g(z) \cdot t_r(z) \qquad\qquad 3.27$$

where $q_g(z)$ is the gas flow rate, and $t_r(z)$ is the gas residence time in cell of annulus at depth z. Gas flow rate at is given as,

$$q_g(z) = \frac{\dot{m}_g}{\rho_g(z)} \qquad\qquad 3.28$$

where $\dot{m}_g$ is steady state gas mass flow rate, in lb/s, and ρ_g is the gas density in cell of annulus at depth z, in lb/ft^3. Gas density can be calculated using real gas law. The residence time of gas in cell of annulus at depth z, in ft/s, is given as,

$$t_r(z)\Big|_{z_1}^{z_2} = \int_{z_1}^{z_2} \frac{dz}{v_s(z)} \qquad\qquad 3.29$$

where z_1 to z_2 are the depths of the bottom and tops of the computation cell, respectively. Gas residence time, $t_r(z)$, depends on the flow regime, mud properties and well-bore geometry. In eqn.3.29, $v_s(z)$ is the gas rise velocity at depth z. Calculation of $v_s(z)$ is discussed in the following section in detail. Combination of eqn 3.26 to 3.28 gives,

$$V_g = \dot{m}_g \cdot \int_{z=0}^{D} \frac{t_r(z)}{\rho_g(z)} \cdot dz \qquad\qquad 3.30$$

The total length of the gas-cut mud (expanded mud length) is,

$$L_{m-exp} = \frac{V_g + V_L}{A_p} \qquad\qquad 3.31$$

Depending on the length of the expanded mud column, there are three possible cases. In case (a), L_{m-exp} is shorter than annulus above the cement top. It does not exceed the depth from surface to the top (D_{TOC}), so no liquid unloading occurs. In case (b), L_{m-exp} exceeds D_{TOC} ,thus some liquid is pushed out of the annulus at the surface - a typical case observed in sustained casing pressure testing when the casing head valve is opened for bleed-off [2]. Case (c) may occur at relatively high gas rates where at some depth along the mud column transition to annular flow occurs. This is defined as the point above which all liquid is mixed with gas and only the mixture flows. Slug/annular transition criterion is given by eqn.3.13. Determination of this point is critical also for required pump rate calculations in dynamic kill operations in blowouts [32].

For case a, volume of the unloaded liquid ($V_{L-unloaded}$) is zero, as given in eqn.3.33. For case b, $V_{L-unloaded}$ is,

$$V_{L-unloaded} = \int_{z=0}^{(L_{m-exp}-D_{TOC})} V_L(z) \qquad \text{if} \qquad L_{m-exp} > D_{TOC} \qquad\qquad 3.32$$

$$\qquad\qquad 3.33$$

$$V_{L-unloaded} = 0 \quad \text{if} \qquad L_{m-exp} < D_{TOC}$$

If liquid unloading occurs, reduction in the hydrostatic pressure must be calculated and a new top of cement pressure (P_{TOC}) must be calculated accordingly. Then a new steady state mass rate must be calculated. Computation algorithm is described in Section 3.3.

Prior to well-head failure	After well-head failure		
No gas flow	Gas flow - Case (a)	Gas flow - Case (b)	Gas flow - Case (c)
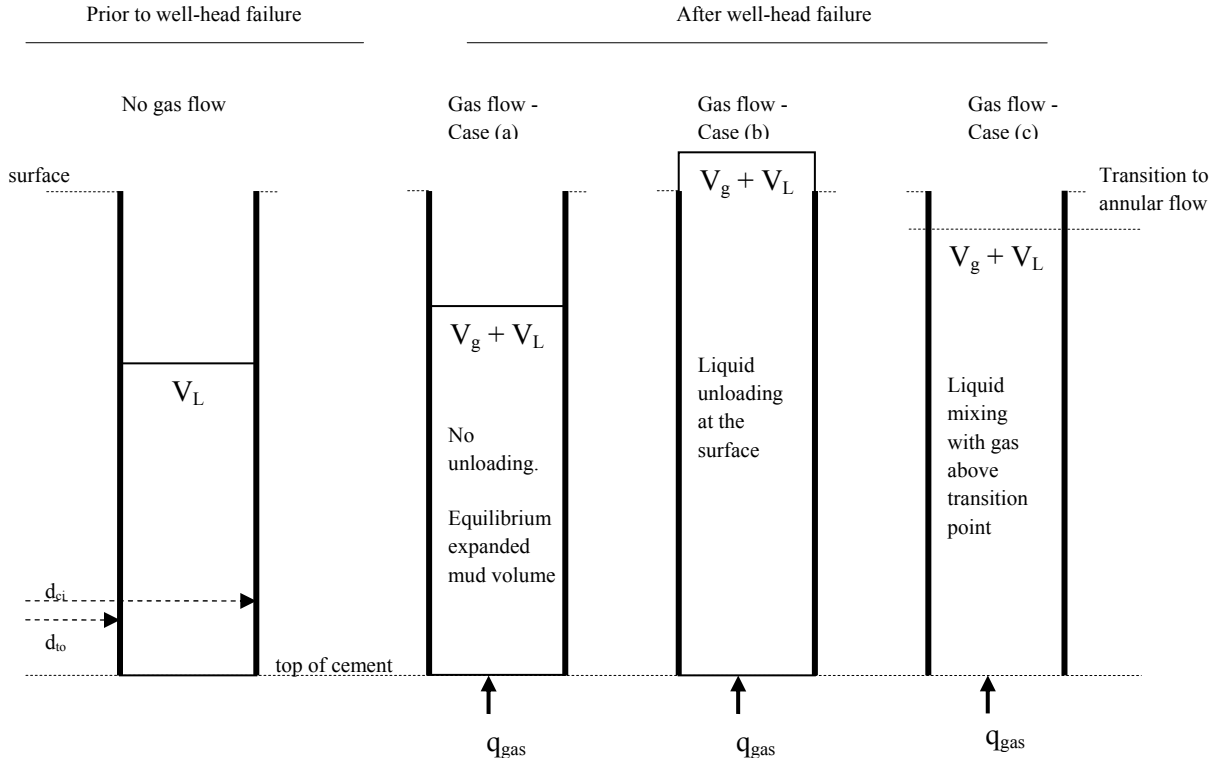
Fig. 3.6- Liquid unloading after well-head failure

3.2.1.4. Gas Rise Velocity

Physical mechanism of gas bubbles motion is complex and involves effects of fluids properties. The overall rise velocity of the swarm gas bubbles depend on the size and shape distribution of bubbles, density difference between the phases, viscosity, interfacial tension and flow regime as well as local temperature and pressure (Kulkami *et al.*, 2005) [33]. Typically, for flow systems composed of gas and liquid the two phases are assumed insoluble. Harmathy (1960) [34] expressed the bubble rise velocity for a single bubble in a stagnant medium as,

$$\mathbf{v_{0\infty}} = \mathbf{1.53}\left[\frac{\mathbf{g}(\boldsymbol{\rho}_L - \boldsymbol{\rho}_g)\boldsymbol{\sigma}_L}{\boldsymbol{\rho}_L^2}\right]^{0.25}$$

3.34

where $v_{0\infty}$ in m/s , ρ is the density in kg/m^3 and σ is the interfacial tension in kg/s^2.

In a stagnant liquid column, velocity inlet of the liquid phase is zero, thus gas flows by displacing the liquid, which causes an increase in the gross volume of the liquid column.

Rodrigue *et al.* (2004) [35] observed that in Newtonian liquids, gas bubble rise velocity linearly increases with bubble volume and decreases with viscosity. In Non-Newtonian liquids, on the other hand, rise

velocity does not seem to follow straight forward relation to bubble size, but tend to show abrupt changes due to change in dominant parameters such as viscous forces and flow regime. Transition to turbulent flow causes zigzag motion of bubbles which increases their overall residence time in liquid and increase the gas concentration. Therefore, behavior of large bubbles or swarm of bubbles are different than of a single bubble. In Fig. 3.7 shown the rise velocity of a bubble vs. its size during its motion. The trend of bubble rise velocity vs. bubble size changes at a critical bubble size where the regime transition occurs.

Akthar *et al.* (2007) [36] performed CFD analysis to analyze bubble flow path instability. He modeled the behavior of continuous chain of bubbles and bubble swarms, and validated results of the numerical simulations with experimental data. He observed that above certain superficial gas velocities, coalescence of bubbles increase the residence time of the flowing gas in the liquid column.

Urseanu, M.I., (2000) [37] studied bubble rise in stagnant liquids and proposed that bubble size vs. rise velocity relation works against forming of bubble swarm. A bubble expands thus rises faster as it rises upwards making the following bubble not possible to coalescence with it.
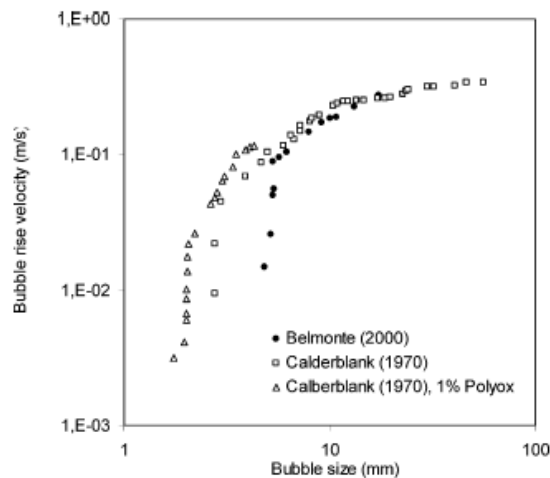
Fig. 3.7-Effect of bubble size on bubble rise velocity (Kulkarni *et al.*, 2005) [24]

However, as a bubble expands, it either breaks down into smaller bubbles resulting in a sudden drop in velocity, or as the trailing bubble in the group is sucked by the vortex created by the leading bubble. Zuber and Hench (1962) [38] modified the Harmathy's equation by implementing a correlation factor to account for the hindering effect of the swarm of bubbles as a function of liquid holdup. Slip velocity is calculated by,

$$1.53\left[\frac{g(\rho_L - \rho_g)\sigma}{\rho_L^2}\right]^{0.25}(1-\alpha)^{0.5}\sin\theta = \frac{v_{Sg}}{\alpha} - 1.2v_m \qquad 3.35$$

where v_{Sg} is the superficial gas velocity, m/s, v_m is the mixture velocity in m/s, and θ is the hole deviation. Since v_{Sg} is a function of α, iterative solution is required.

Kulkarni et al. [24] studied effect of temperature on bubble rise velocity. While decreasing the buoyancy force on the bubble by decreasing the liquid density, temperature also makes increasing effect on gas volume, thus as shown in Fig. 3.8 direct relation of rise velocity to temperature is not possible. In this study, heat exchange between the bubbles and liquid column is neglected. Luo (1997) [39] studied the effect of pressure on bubble rise velocity and observed reducing effect as shown in Fig. 3.9.

Rader, Bourgoyne and Ward (1975) [40] experimentally determined the factors affecting the bubble rise velocity during a well control operation and introduced correlation which holds for annular spaces with inner diameters from 0.2 to 7.94 inch, outer diameters from 0.58 to 9.58 inch, and viscosities from 1 to 1,050 cp for Newtonian fluids and yield points from 1.3 to 129 lb/100 ft^2 and plastic viscosities from 11 to 111 cp for Non-Newtonian fluids.
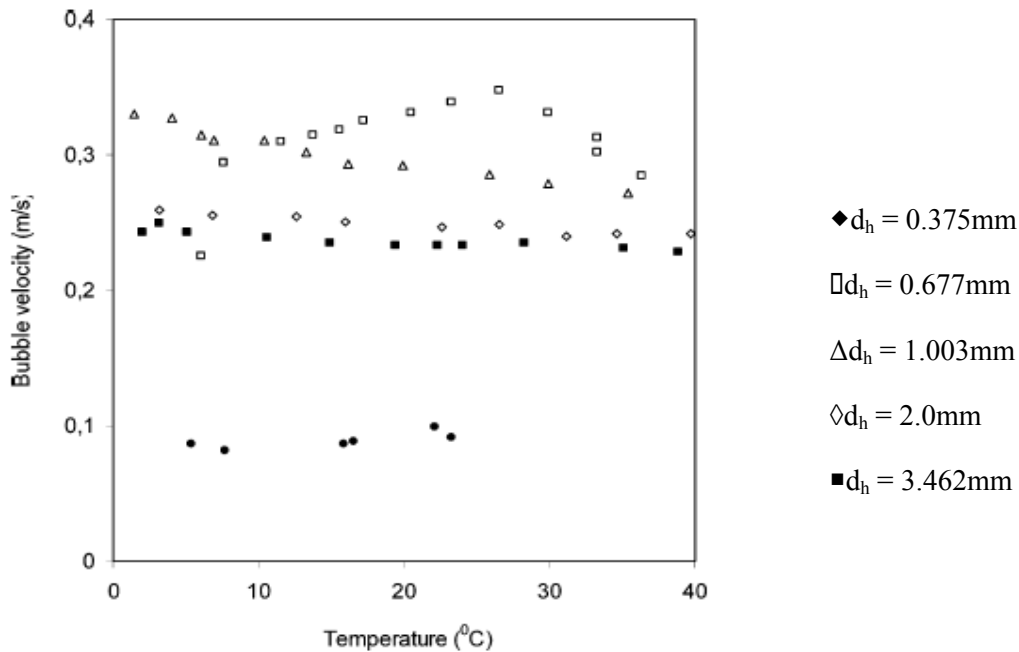
Fig. 3.8-Experimental data on temperature effect on bubble rise velocity (Kulkarni et al., 2005) [24]

They used water, $ZnCl_2$, and guargum as liquid and methane, pentane and air as gas phase. They studied the sensitivity of the correlation to annular geometry, liquid viscosity, gas and liquid densities, length of the gas bubble, interfacial tension and annulus eccentricity.
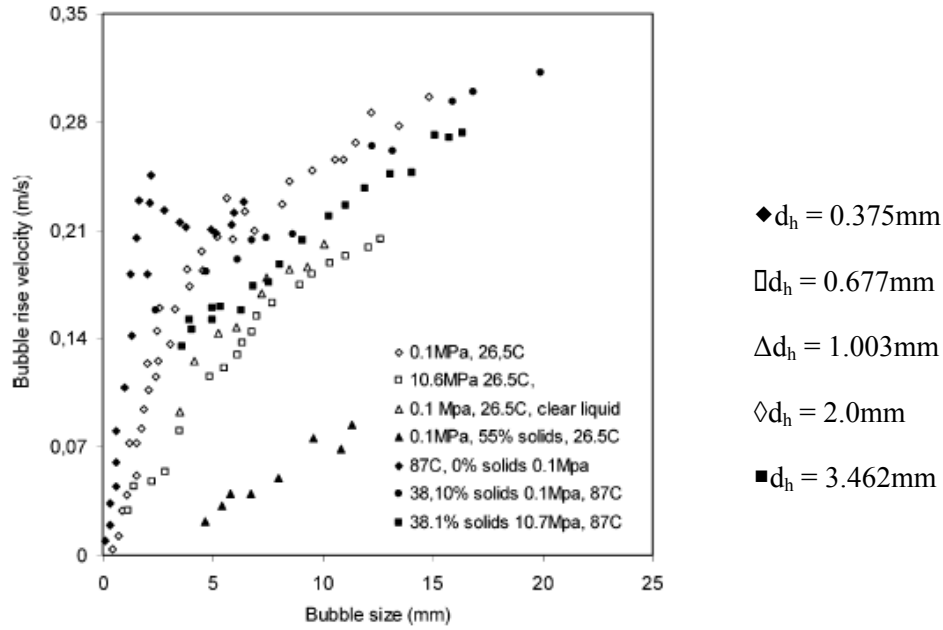
Fig. 3.9-Effect of external pressure on bubble rise velocity (right) (Luo *et al.*, 1997) [39]

Resultantly they observed that bubble length, interfacial tension and eccentricity have negligible impact on the bubble rise velocity, whereas the others have significant impact. Modification of Dumitrescu's [41] equation to determine the bubble rise velocity in the annulus in light of the experimental data gives,

$$\overline{v_s} = 10 \cdot C_1 \sqrt{F_g} \cdot C_2 \cdot C_3 \cdot \sqrt{\frac{(r_c + r_t)(\rho_L - \rho_g)}{\rho_L}}$$ 3.36

where the term $C_1 \sqrt{F_g}$ accounts for the viscous effects, which can be correlated with bubble-Reynold's number, as shown in Fig. 3.10.
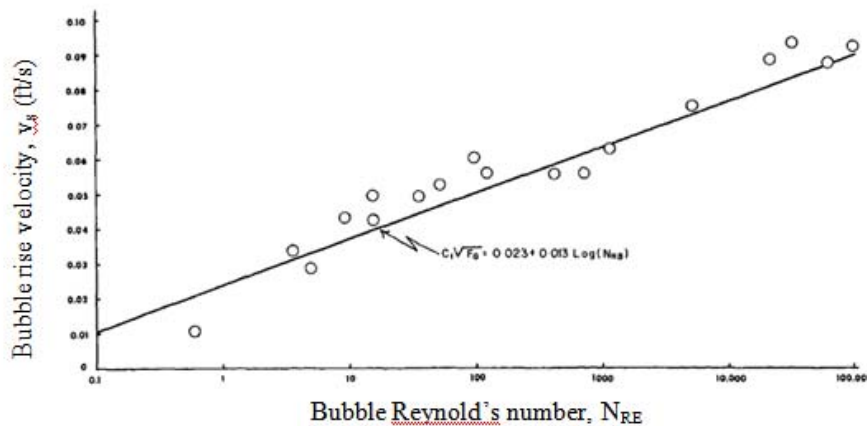
Fig. 3.10-Bubble rise velocity coefficient $C_1\sqrt{F}$ vs. bubble Reynold's number (Rader, *et al.*, 1975) [40]

25

where Bubble Reynold's number is given by,

$$N_{RB} = \frac{928\rho_L v_s d_e}{\mu_p}$$

3.37

where μ_p is the plastic viscosity, cp, and can be obtained from 600 and 300 rpm viscometer readings, ρ_L is liquid density in ppg, v_s is the velocity of the bubble in ft/s, de is the equivalent diameter in inch. The correlation constant C_2 accounts for the effect of the liquid velocity which can be correlated to liquid/gas velocity as shown in Fig. 3.11. C_3 accounts for the effect of bubble expansion on bubble rise velocity which can be correlated to v_E/v_B, where v_E is the expanding gas velocity ratio, as shown in Fig. 3.12.
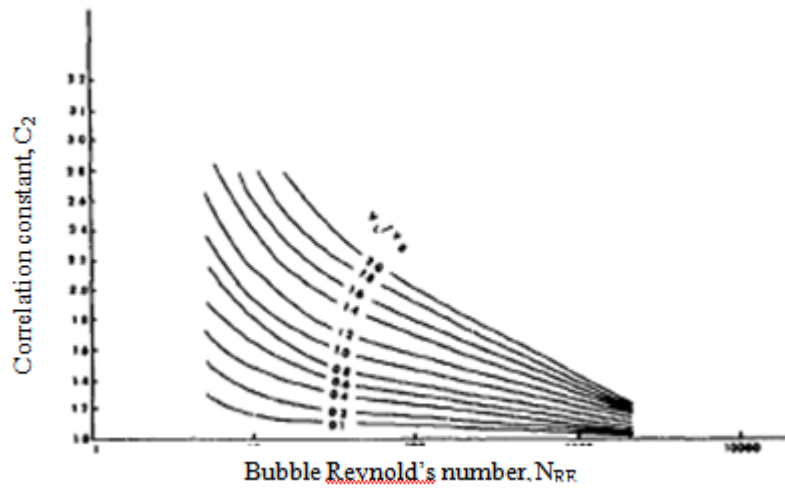
Fig. 3.11-Bubble rise velocity coefficient, C_2 for an annulus (Rader, *et al.*, 1975) [40]
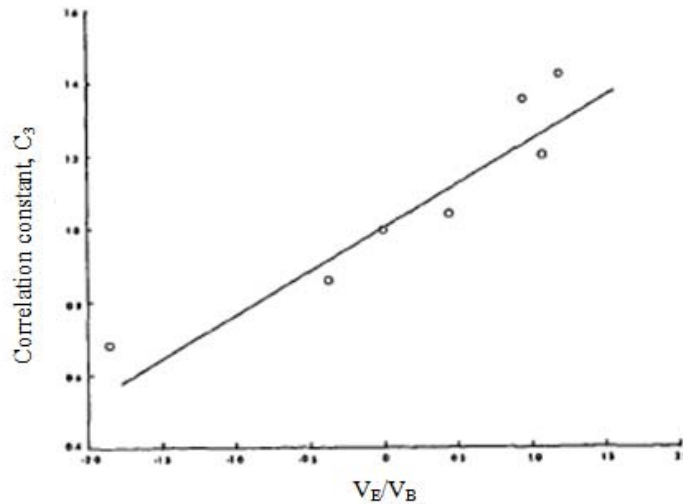
Fig. 3.12-Bubble rise velocity coefficient, C_3 for an annulus (Rader, *et al.*, 1975) [40]

In this study, we consider the flow of gas through a static mud column with low liquid-to-gas velocity ratios. Thus, the gas rise velocity calculation method proposed by Rader *et al.* [40] is employed. The effects which makes values of the liquid flow velocity are considered to be negligible for a static mud column, which makes values of constants C_2 and C_3 equal to unity. Casairego (1987) [42] simplified the correlation for gas flow through a static column of Non-Newtonian mud in annulus as,

$$v_s = (0.163 + 0.092\, log\, N_{RB}) \cdot (d_{ci} + d_{to})^{0.5} \cdot \left(\frac{\rho_L - \rho_g}{\rho_L} \right)^{0.5}$$

3.38

for 1< N_{RB} < 100,000.

3.3.   Maximum Emission Rate Model

3.3.1.   Model Algorithm

Mathematical model and software has been developed to calculate the maximum gas flow rate from a well with failed well-head. The following assumptions have been made:

- Inflow pressure of the gas source formation is not affected by emission rate;
- Flowing hydrocarbon is in dry gas phase;
- Gas flow is steady state;
- Top of cement is above the shoe of outer casing and the well is vertical;
- Mud in the annulus is homogeneous, with known properties;
- Mud plastic viscosity and surface tension does not change with temperature;
- Heat transfer due to flowing gas from the reservoir is neglected;
- Temperature profile of the mud is in equilibrium with the geothermal gradient;
- There is no leak in inner/outer casings;
- Gas migration flowpath is contained by the casing-casing annulus;
- For water based mud, mud is incompressible and gas solubility is neglected;
- Annular flow above cement top can be discretized into large number of cells with all properties constant within each cell;
- Within each discritized cell, gas rise velocity is assumed constant;

The Maximum Emission Rate (MER) software offers two solution options. One is to construct so called IPR-TPR curves to determine q_g graphically. The other is convergence on q_g, which is the faster option in terms of simulation time. The MER model allows computation of the SCP Well System performance

plotted in Fig. 3.2. The plot can be used to find the MER value graphically. It could also be used to analyze options for SCP control and to study effects of the system parameters.

As shown in Fig. 3.1, the MER value is the intercept of the cement top inflow performance (CTIP) and cement top outflow performance (CTOP) plots. The MER model also allows direct calculation of the maximum rate by solving numerically the equation,

$$P_{CTIP}(q_g) - P_{CTOP}(q_g) = 0 \qquad\qquad 3.39$$

where P_{CTIP} and P_{CTOP} are the system inflow and outflow performance relationships, respectively.

The input parameters used in the model are summarized in Table 3-1.

Table 3-1-Input paramaters for Maximum Emission Rate Model

Data	Source of Data
Pressure of the gas source, P_R	Sustained Casing Pressure Test data and its interpretation using Xu.model [17]
Effective permeability, k_{eff}	
Length of cement sheath, L_c	
Length of mud column (initially), L_m	
Annular geometry, d_{ci}, d_{ti}	Well program and/or Post drilling report
Depth to top of cement, D_{TOC}	
Mud density, ρ_m	
Fann-35 readings, $\theta_{3\ to\ 600}$	
Interfacial tension, σ_L	
Eccentricity, e	Assumed
Casing wall roughness, ε	
Gas gravity, γ_g	

After the well's casing head fails, the top pressure instantly drops from its shut-in value (SCP$_{max}$) to zero (atmospheric pressure). The system becomes imbalanced and a transient (unsteady-state) flow of gas begins. During the flow, gas rate increases to its asymptotic maximum value of the steady-state flow. The MER model, however, does not determine the transient flow and it does not consider time. To determine the steady state flow equilibrium gas rate the model simulates a series of steady state flows in several steps.

In the example shown in Fig. 3.14, steady state gas flow rate is calculated for initial pressure drop at the cement top - points A-B [P_R-P_{TOC}(t=0)] from 12,000 psi (A) to 7,000 psi (point B), giving q_g(C) =2.5 MMscfD. In the next step a 2.5 MMscfD rate is used to calculate the corresponding top of cement pressure, P_{TOC}(t=1) = 5,800 psig (point D) and so on until the rates and pressures converge. The computation algorithm is shown in Fig. 3.13.
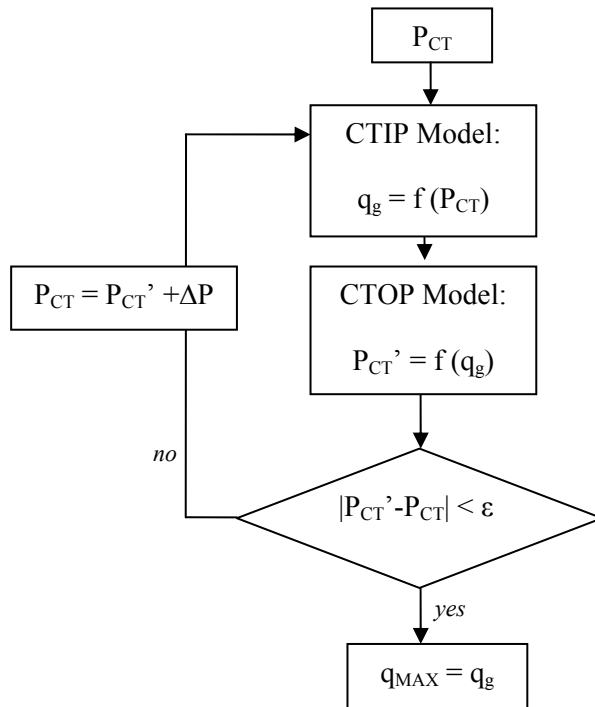
Fig. 3.13- General algorithm of MER model

The CTOP model calculates the cement top pressure for a given steady state gas flow rate, q_g. Pressure at the cement top (P_{CT}) is,

$$P_{CT} = \sum_{z=0}^{N} \left[\left(\frac{dP}{dL} \right)_{el} + \left(\frac{dP}{dL} \right)_z \right] L_{cell}(z)$$

3.40

The elevation and friction terms of the numerical integration are calculated for liquid and gas two-phase flow, as presented in section 3.2.1.2. The initial guess for the CTOP model is the gas flow rate calculated by the CTIP model for the initial mud column in the annulus (point B in Fig. 3.14). The model algorithm is shown in Fig. 3.15.
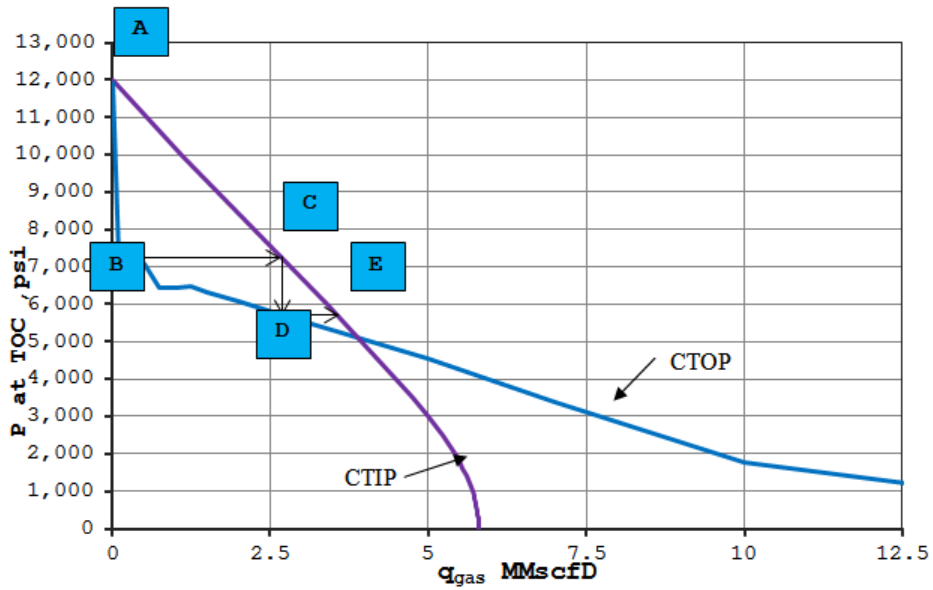
Fig. 3.14-Flow performance (nodal) analysis of CSP well with open casing head
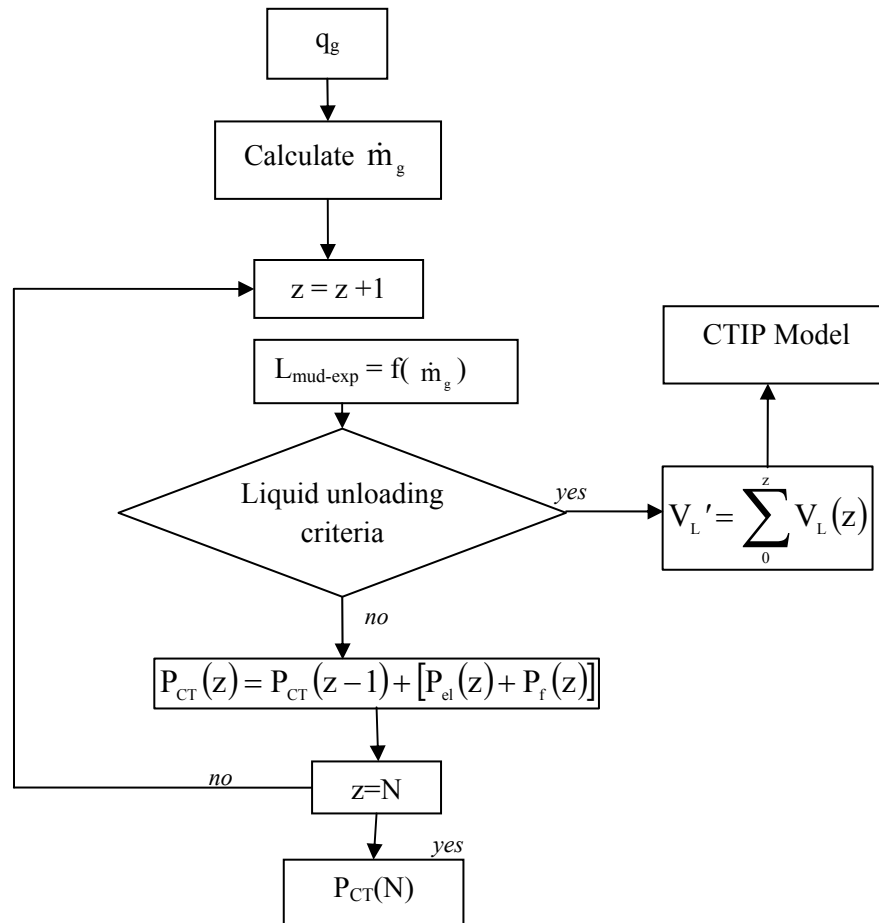
Fig. 3.15-Model algorithm for CTOP model

The volume of liquid in each cell, $V_L(z)$, is assumed equal and constant. Gas mass flow rate is assumed constant at any point along the mud column. The total gas mass in cell z depends on the residence time of gas in the cell, $t_r(z)$, as given in eqn.3.30. Volume of gas in each cell, $V_g(z)$, varies as a function of the gas mass and the pressure in the cell and calculated by eqn.3.30. The residence time is a function of cell length, $L_{cell}(z)$, and calculated by eqn.3.29. Therefore, iterative solution is required to compute $t_r(z)$, $V_g(z)$, and $L_{cell}(z)$ in each discritized cell. The computation algorithm is shown in Fig. 3.16.

The initial guess for the cell length calculation is the length of discritized cell of the initial mud column. In the algorithm shown in Fig. 3.16 gas mass influx rate, $\dot{m}_g$, is constant. Starting from the cement top, the total length of the gas cut mud column, $L_{mud-exp}$, is calculated by numerical integration.
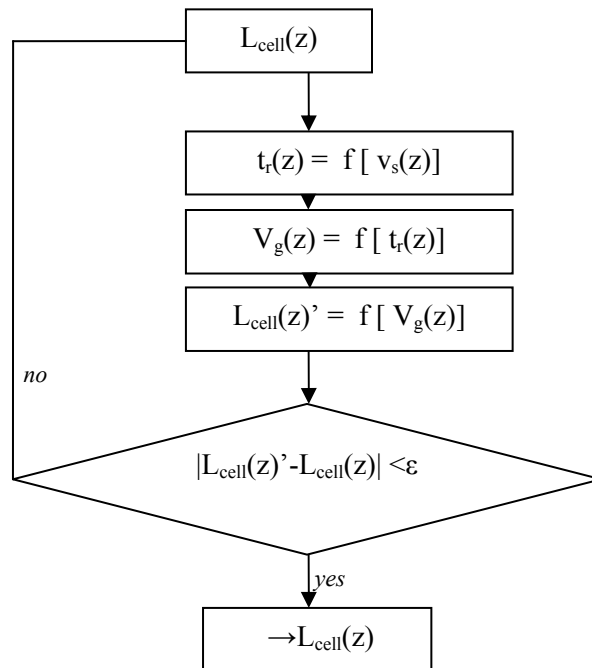
Fig. 3.16-Computation algorithm of cell length

If the gas flow rate is high, the mud column length may exceed the surface, or transition to annular flow may occur resulting liquid unloading, as shown in Fig. 3.6. In such a case the MER algorithm must be reset for new total liquid volume, V_L. The numerical integration for $L_{mud-exp}$ is shown in Fig. 3.17. The algorithm calculates the length of gas cut mud column for a steady state gas flow rate, q_g.

Fig. 3.18and Fig. 3.19 show the cement top pressures (P_{CT}), gas flow rates (q_g), total liquid volumes (V_L), and gas cut mud lengths ($L_{mud-exp}$) calculated by the CTOP model $vs.$ number of iterative steps from an example application of the model.

31

In Fig. 3.18, decrease in P_{CT} and accordingly, increase in q_g can be observed. In Fig. 3.19, at 4th iteration the length of gas cut mud column exceeds the surface, thus liquid unloading occurs. The drop in liquid volume due unloading can be observed.

In Fig. 3.20 shown the CTIP-CTOP system performance plot. The cement-top pressure (P_{CT}) values calculated by the CTOP model are used to calculate the gas flow rates at each iterative step. Eventually the algorithm converges to the solution of the two systems, CTIP and CTOP. As discussed, the convergence point at which the coupling criteria is satisfied is the maximum emission rate, q_{MAX}.
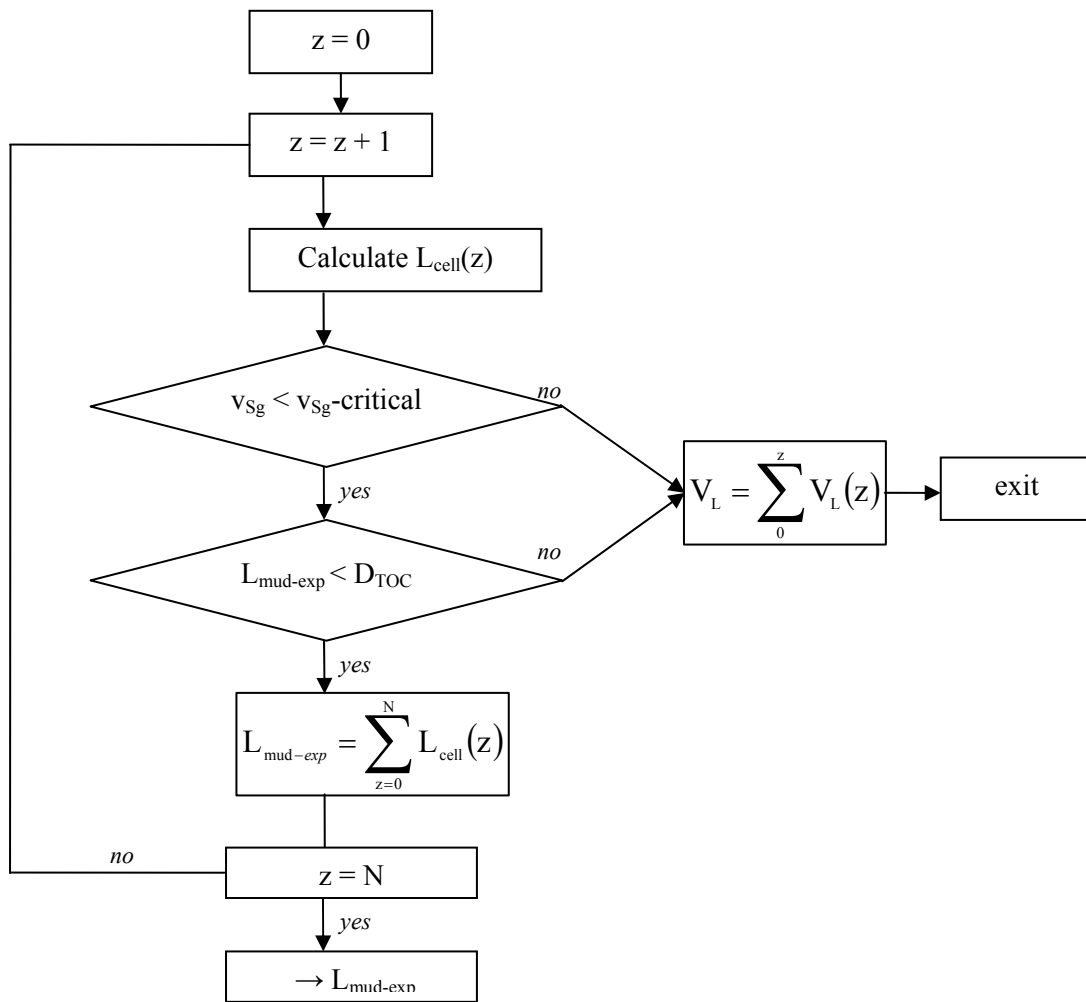
Fig. 3.17-Numerical integration for calculation of gas cut mud length
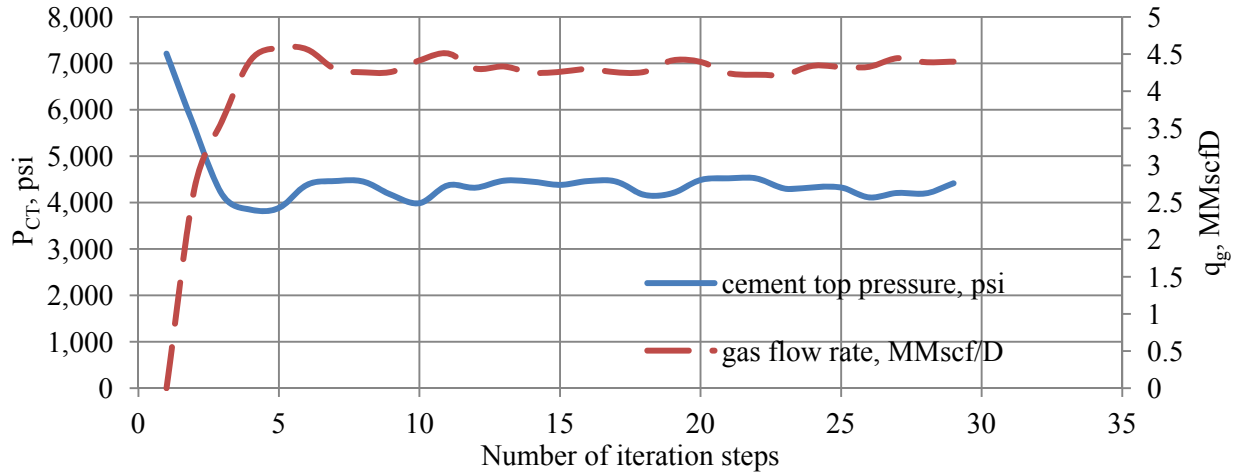
Fig. 3.18-Calculated cement top pressure and gas flow rates *vs.* number of iterations
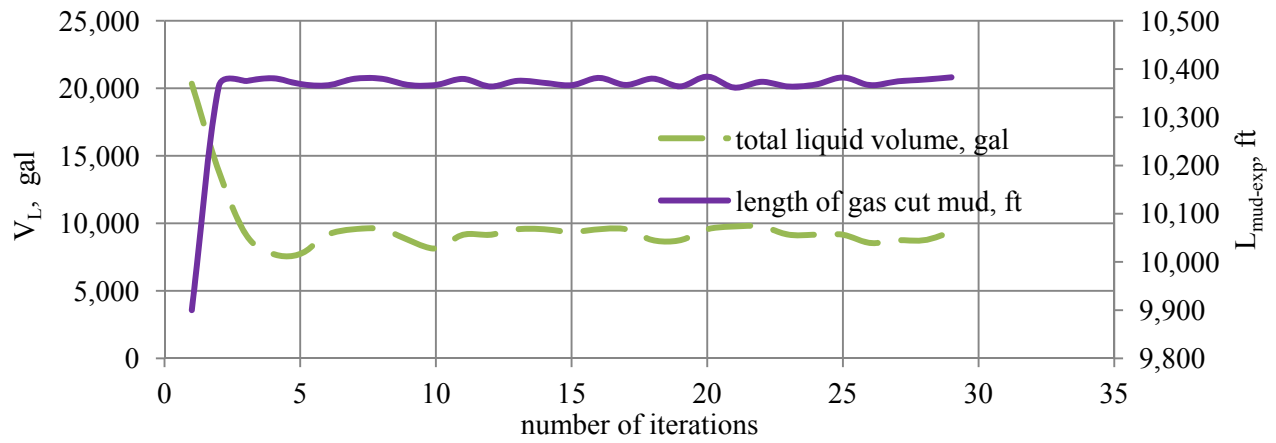
Fig. 3.19- Calculated liquid volume and gas cut mud length vs. number of iterations
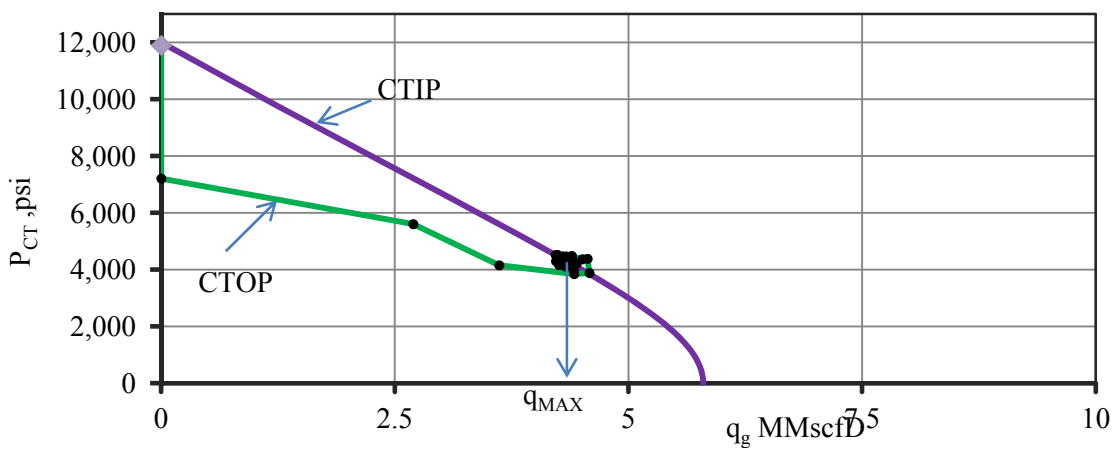
Fig. 3.20 Computation of equilibrium steady state flow rate from a well with failed well head

3.3.2. Maximum Rate Software Interface

The Maximum Emission Rate software (MER) runs on visual basic platform. In Fig. 3.21 shown is the software interface. The well configuration and mud parameters are entered to the input boxes described in Fig. 3.21. The simulation controls, *i.e.* relaxation factors, number of solution cells and selection of solution method are selected from the user box that opens from the 'initialize' button. The program also shows the residuals calculated throughout the computation process. This allows the user to track the convergence process. The output is shown on the right hand side of the screen.

The output includes P_{CT}, q_g, V_L, V_g, $L_{mud\text{-}exp}$, and the CPU time. The control buttons and input boxes are labeled on Fig. 3.19, and explained as follows.
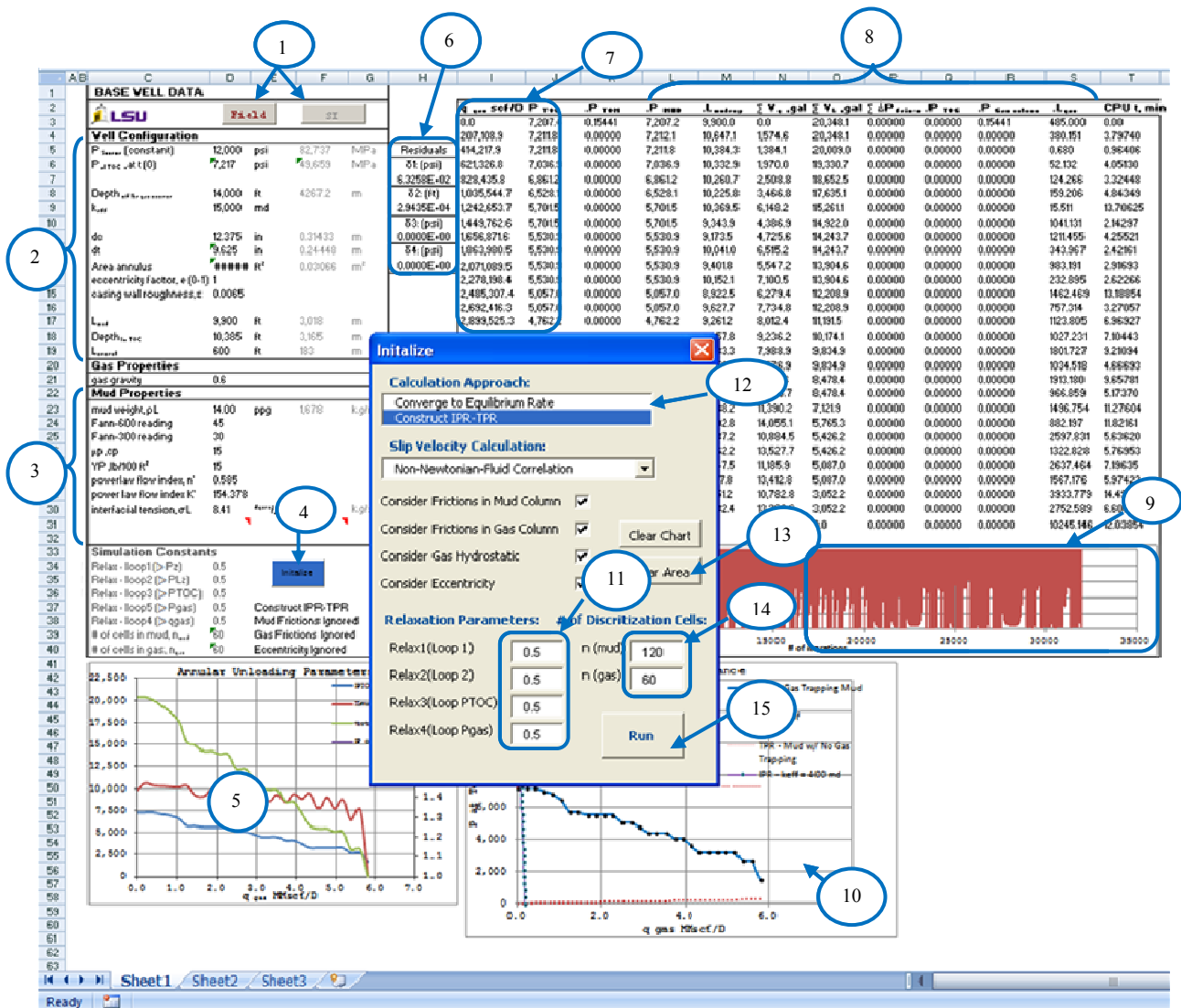
Fig. 3.21-Maximum Rate Software Interface

34

1. Selection of field or SI unit systems. The program automatically converts the units from field to SI, vice versa;

2. Input boxes for well configuration data;

3. Input boxes for mud data;

4. 'Initialize' button. Opens the simulation initialization form computation options;

5. Plot of liquid, gas and gas cut mud volume vs. q_g;

6. Residuals of the iterative cycles described Residuals are dynamically activated during simulation;

7. P_{TOC} vs. q_g simulation output graph;

8. List of simulation outputs at timesteps. Includes V_g, V_L, $L_{mud-exp}$. It is plotted to allow the user to see the progress of the factors at each time-steps;

9. Residuals vs. number of iterations. Plotted to allow the user to see the convergence process;

10. System flow performance curves. The plot is the final output of the simulation and allows the user to analyze the flow potential of the system;

11. Relaxation parameters, which are entered to control the speed of the convergence of the iterations;

12. Selection of solution method. Available options are: IPR-TPR analysis, and direct convergence on the equilibrium rate;

13. 'Clear' button. Cleans the table labeled with (7) and (8) before a new simulation;

14. Input boxes for number of discritization cells for the simulation;

15. 'Run' button. Initiates the simulation for the data entered in boxes labeled with (2) and (3) and simulation parameters entered in input boxes (11) and (14).

Relaxation factor is used for increasing the convergence speed of an algorithm, or make a divergent solution to converge. It is recommended to enter small relaxation factors for the P_{CT} , *i.e.* 0.1, since the system is sensitive to pressure increments. Small relaxation factors increase the computational processing time (CPU time), however, are often required for the MER model to converge on q_{MAX}. Number of computation cells can be entered any integer from 20 to 500. If the number is small, however, the precision of the liquid unloading depth will be less. The reason is that when liquid unloading occurs in a computation cell, the program assumes the entire liquid volume in the particular cell is removed.

3.3.3. Study of Gas Emission Rate from SCP Well

The Maximum emission rate (MER) software was used to study various scenarios of gas emissions from the annulus B (production/intermediate casing) of Study Well. Study Well is a hypothetical well

generated by modifying several properties of an 18,834 ft GoM well,[1]. The structure and mechanical components of Study Well were considered constant while varying other properties in theoretical "experiments". This approach is similar to carrying physical experiments in an actual well. The schematic of Study Well is shown in Fig. 3.22. The B annulus has casing pressure (P_{csg}) of 3,355 psig. Xu [17] model has been used to determine parameters k_{eff}, P_R, L_c, and L_m. (The model simulates the bleed-off and build-up data of a sustained casing pressure (B-B) test and the model parameters have been found by iterative matching the B-B test data with the model).

The input data of the annulus B of Study Well is summarized in Table 3-2.

Table 3-2-Control parameters of Annulus B at Study Well

Data	
Well-head pressure, P_{csg}	3,355 psi
Pressure of the gas source, P_R	8,000 psi
Effective permeability, k_{eff}	1,200 md
Length of cement sheath, L_c	1,400 ft
Length of mud column (initially), L_m	9,900 ft
Annular geometry, d_{ci}, d_{ti}	12.375 x 9.625 in
Depth to top of cement, D_{TOC}	10,385 ft
Mud density, ρ_m	9 ppg
Fann-35 readings, θ_{300} / θ_{600}	30/45
Interfacial tension, σ_L	8.41 $^{dynes}/_{cm}$
Eccentricity, e	0.5
Casing wall roughness, ε	0.0065 in
Gas gravity, γ_g	0.6

3.3.3.1. High Risk Scenario Study

This study demonstrates a 'high risk' Case 1 with high P_{csg} and large cement leak size. Mud density in the annulus above the cement top is assumed 9 ppg – the minimum practical density of the WBM left in the annulus after the cementing operation. A low-density mud may constitute higher risk of complete liquid unloading from the annulus by allowing greater gas expansion so the unloading criteria are met at greater

---

[1] In Section 6.2.2, detailed information about Study Well is presented including drilling, leak-off test, and geological data.
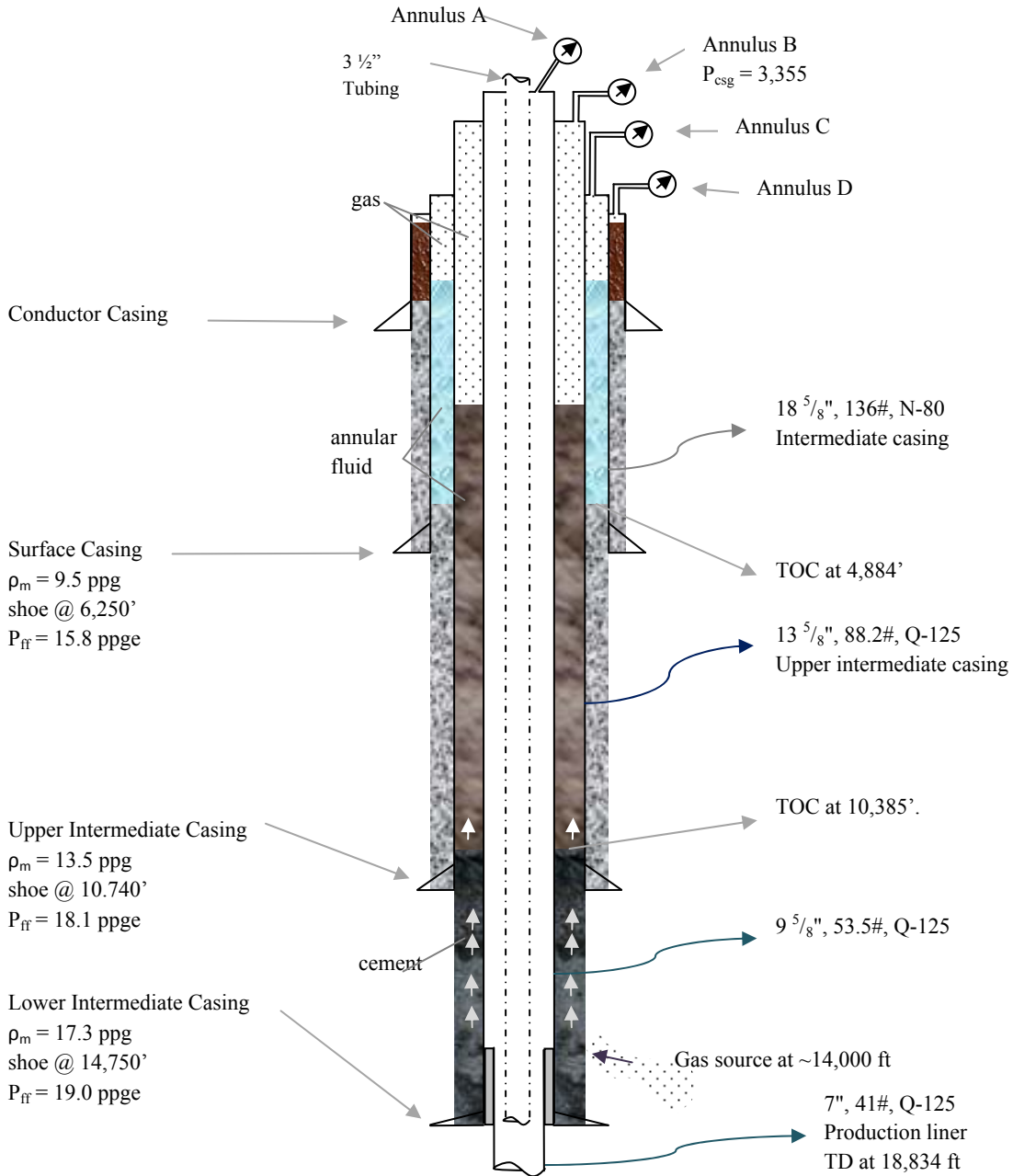
Fig. 3.22-Well schematics of Study Well

depths. The maximum allowable well-head operating pressure (MAWOP) of annulus B of the 9-5/8 Q-125 and 13-5/8 Q-125 casings is 4,168 psi. The sustained casing pressure (P_{csg}= 3,355 psig) is 80% of the MAWOP and is considered a high surface failure risk according to the MMS regulations . Also, the cement sheath is assumed to have high equivalent permeability and short length (k_{eff} = 1,200 md, L_c=1,400 ft), which constitutes a high flow potential [22].

Fig. 3.23 shows the annular system flow performance of this well. Initially, the top of cement pressure (P_{TOC}) is equal to the reservoir pressure of 8,000 psi (gas column's hydrostatic inside the cement sheath is neglected in this model). As the casing head fails, the well-head pressure (P_{csg}=3,355 psi) is removed, causing P_{TOC} to reduce to 4,665 psi. The dashed line (B) is CTOP –for fricitionless gas migration in the mud column and no liquid unloading regardless of the gas flow rate.

The intercept point with CTIP indicates of 0.65 MMscfD. The actual CTOP plot demonstrates the flow performance of the well considering friction and unloading. In this case, qg is calculated 0.67 MmscfD. The bottom line represents the "absolute open flow" (AOF) performance of the well with no mud column.
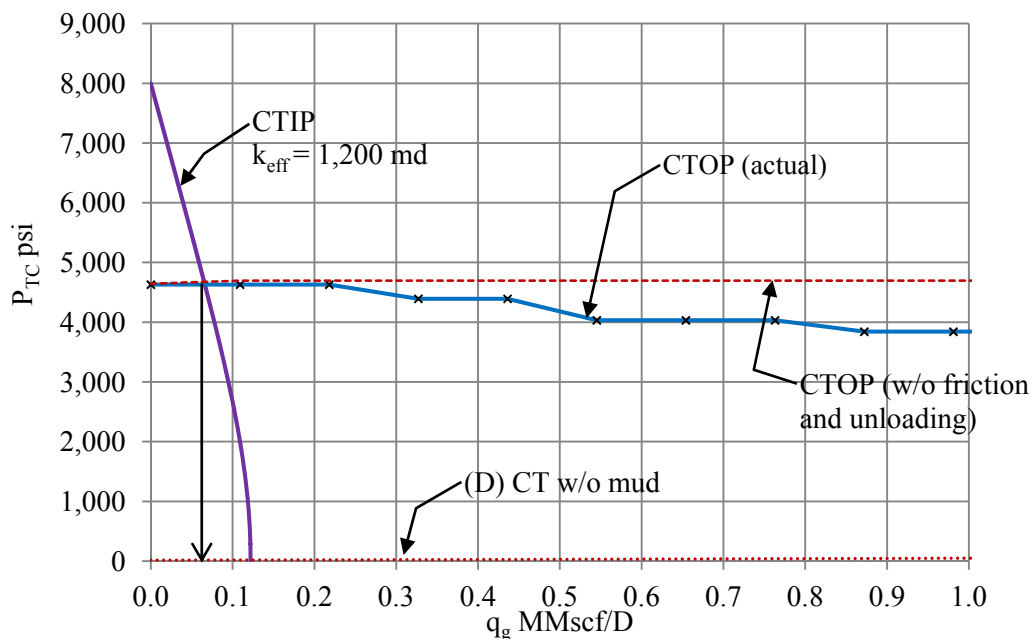
Fig. 3.23-Flow performance analysis of study well for Case 1

In this case, the only pressure loss is due friction of single phase gas flow in the annulus, and q_g is 1.12 MMscf/D- almost twice of that with the mud column. The analysis shows that with thin low-density mud the unloading is minimal and hydrostatic pressure of the mud column acts as a pressure containment barrier and prevents AOF.

As discussed above the cement leak permeability and its length control the CTIP relationship. The annular mud thixotropy and the initial length of the mud column control the CTIP relationship by providing restriction to the flow.

3.3.3.2. Effect of SCP Well Parameters on Gas Emission Rate

We analyze the effect of four parameters: cement leak size, initial mud column density and length above the cement top (maximum value of SCP), and mud rheology (plastic viscosity). Other parameters of the well system are considered constant- shown in Table 3-3.

Table 3-3-Constant well-system parameters of Case 1

Data	
Pressure of the gas source, P_R	8,000 psi
Annular geometry, d_{ci}, d_{ti}	12.375 x 9.625 in
Length of cement sheath, L_c	1,400 ft
Depth to top of cement, D_{TOC}	10,385 ft
Interfacial tension, σ_L	8.41 $^{dynes}/_{cm}$
Eccentricity, e	0.5
Casing wall roughness, ε	0.0065 in
Gas gravity, γ_g	0.6

Also, Table 3-4 is a matrix of the simulation experiments for the assumed values of control parameters. Results of Experiment 1 in Fig. 3.24 show that small leaks with heavy mud drastically reduce emission rate. Moreover, mud density effect alone is negligible comparing to the effect of leak size. Also the liquid unloading effect seems not dependent on mud density-the reduction of pressure due unloading is the same for the same increase of emission rate.

Table 3-4-Matrix of elements of Case 1

Parameter	Experiement#1	Experiement#2	Experiement#3
Leak size, md	1,200 / 12,000	1,200 / 12,000	1,200 / 12,000
Mud density, ppg	9 / 12 / 13	9	9
Plastic viscosity, cp	15	15	5 / 15 / 20
Mud column length, ft	10,000	1,000/3,000/5,000/10,000	10,000

The irregularities in the flow performance plots results from abrupt transitions from slug flow regime to annular flow regime in the annular column. The transition between slug and annular flow regimes. However, there is no widely accepted slug/churn and churn/annular transition criteria in the literature [25] and for simplicity, churn flow is not considered in the model.

Fig. 3.25 depicts sensitivity of the SCP well flow system to the initial length of the mud column in the annulus (L_{mud}). As shown, with small amounts of mud (L_{mud} = 1,000 ft) and large leak sizes (k_{eff}=12,000 md), a complete unloading of the annulus may occur, and AOF is the equilibrium gas flow rate. Again, the leak size dominates the process- for small leak (k_{eff}=1,200 md), regardless of L_{mud}, q_g does not exceed 0.13 MMscf/D.
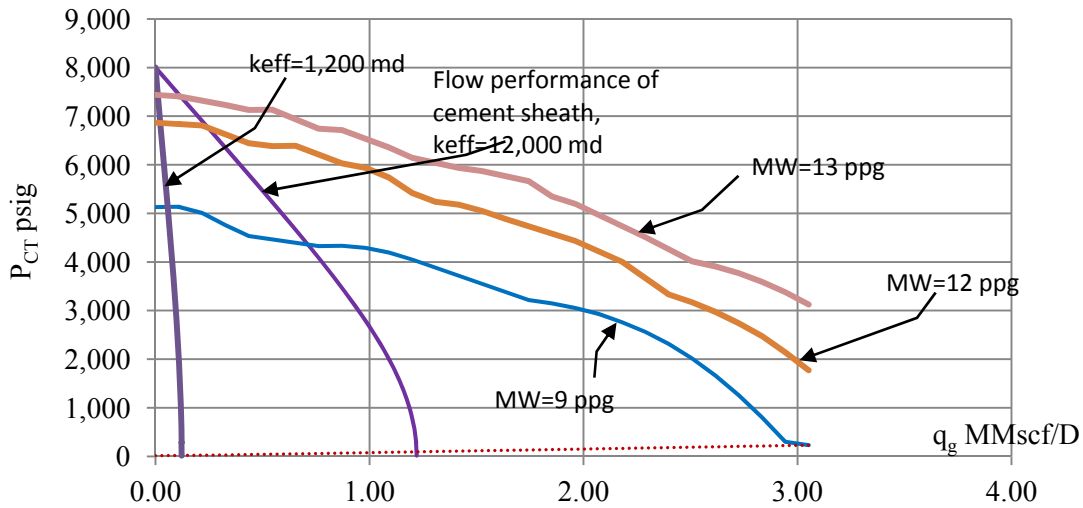
Fig. 3.24-effect of mud density and leak size on gas emission- Experiment 1
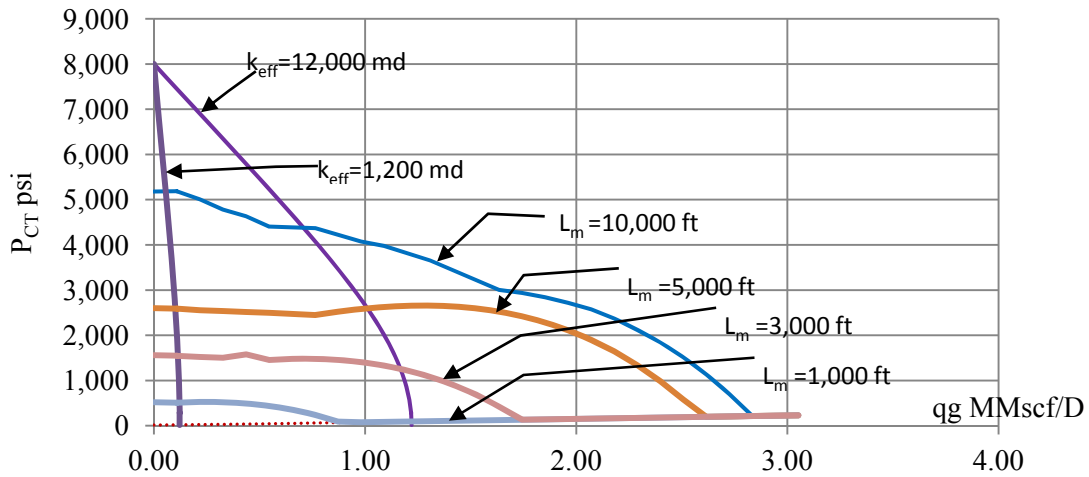
Fig. 3.25- Effect of mud column length and leak size on gas emission-Experiment 2

Unlike in experiment 1, liquid unloading strongly depends on the length of mud column. The CTOP plots clearly demonstrate the effect like the annulus is filled with mud columns merely expand in the annulus

with increasing gas rates (flat sections of the CTOP plots) until the rates exceed a critical value that triggers liquid unloading (sloping down sections of CTOP plots).

A lack of sensitivity of the SCP well flow system to plastic viscosity is demonstrated in Fig. 3.25. The CTOP plots are almost the same varying gas flow rates (q_g). No significant difference of the emission rate is observed. Moreover, liquid unloading appears not dependent on plastic viscosity that solely controls gas residence time, *i.e.* gas trapping and liquid expansion. This surprisingly small effect may be caused by the absence of other rheological and thixotrophic parameters in this model (such as yield stress and gel strength).
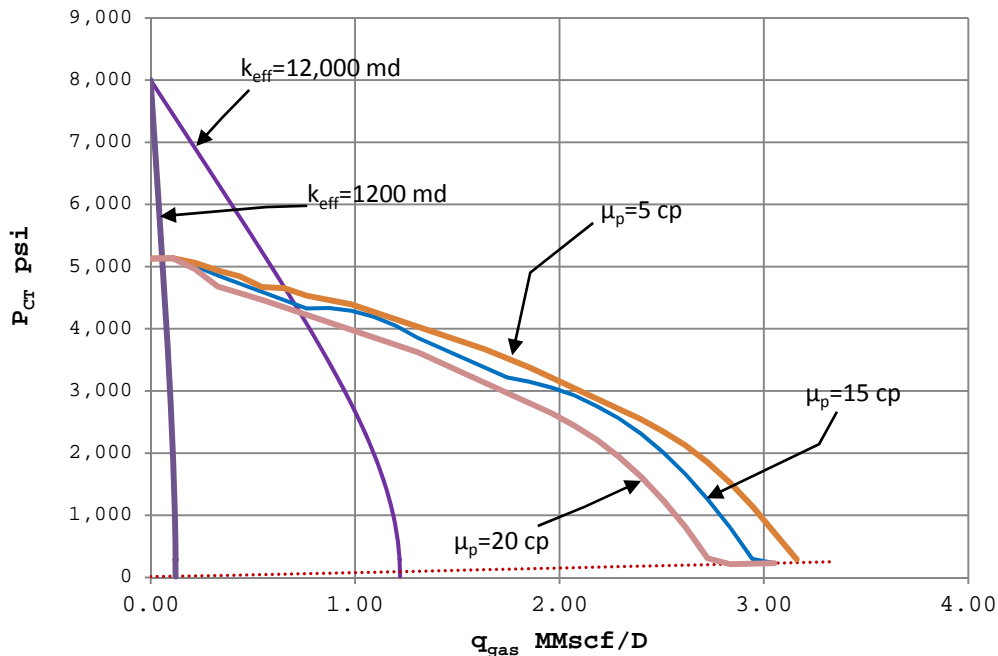
Fig. 3.26- effect of mud rheology and leak size on gas emission –Experiment 3

In all, this study shows that the maximum gas emission rate is mostly controlled by the leak size, *i.e.* permeability of the cement sheath. The smallest rate may result from high hydrostatic pressure of the mud column. (Both the mud density and column length contribute to the hydrostatic pressure.) The hydrostatic pressure of the initial height of the mud column involves no gas cutting.

Assuming the same gas source formation and the cement leak size, the results of this study can be summarized in two most important conclusions:

1. When the SCP annulus is only partially filled with heavy mud, gas emission rate to atmosphere can be estimated from a simple formula describing only flow in cement for hydrostatic pressure of the mud (CTIP relationship) at the cement top.

2. For the mud-filled annulus, the simplified approach would give under-estimation of gas rate and the proposed model should be used.

4. CASING SHOE STRENGTH DETERMINATION

4.1. Definition of Casing Shoe Strength

As shown in eqn.2.2 finding subsurface failure of a well due to sustained casing pressure requires knowledge of casing shoe strength (CSS) at the casing depth. Determination of CSS is already a part of designing drilling and well completion operation. As pore pressure defines the lower limit of mud density, fracture pressure gives the upper limit. Planning of mud weight window, decisions for casing setting depths for the next interval, calculation of kick tolerances and design of fracture operations all require accurate knowledge of the maximum pressure that the casing shoe would withstand. In order to understand the mechanism of CSS, a brief description of rock mechanics principles of wellbore breakdown is presented, below.

4.1.1. Mechanical Description of Casing Shoe Strength

Rock mechanics describes how a particular mass of rock responds to stress at particular conditions such as overburden, pore pressure and temperature changes. In geology setting with minimal tectonic activity and chemical changes, weight of the overburden and reservoir pressure mainly create the in situ stresses. When a well is drilled, the rock matrix is replaced by the drilling fluid, and the initial stress distribution is altered. The stress distribution around a wellbore in an isotropic, elastic medium is shown in Fig. 4.1.
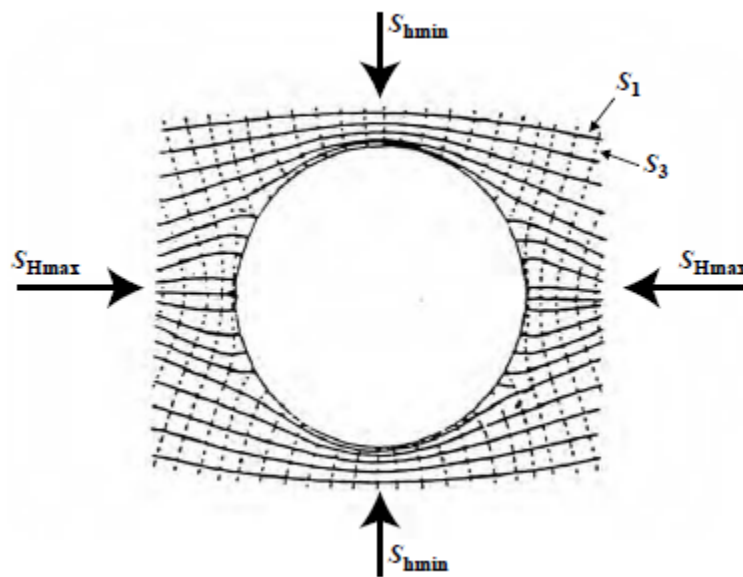
Fig. 4.1-Components of a geomechanical model to describe near wellbore stresses (top view) [43]

Stress distribution around the casing shoe is described by six components. Various methods have been developed for determination of minimum and maximum in situ stress. The methods are summarized in Table 4-1.

Table 4-1-Components of a geomechanical model

Component	Source
Rock Strength (UCS)	Core analysis, logs, cuttings, wellbore failure analysis
Overburden Stress (S_v)	Density and/or sonic logs
Pore Pressure (P_p)	MWD, sonic/resistivity/density logs, seismic
Min. Horizontal Stress (S_{min})	Leak off Test, XLOT, minifracs
Max. Horizontal Stress (S_{max})	Wellbore failure analysis, lab measurements, dipole sonic scanner
S_{max} Orientation	Image/caliper log, fault analysis

Stress distribution model can be simplified by making these assumptions,

- wellbore is parallel to one of the in situ principle stresses, ideally vertical

- depth of interest is not under the effect of extreme abnormal pore pressures

- formation is not composed of unconsolidated shallow sand

- rock is a homogeneous isotropic material, *i.e.* heterogeneity is ignored

The horizontal in situ stresses (S_{min} and S_{max}) and the pore pressure (P_p) create a compressive hoop stress concentration around the wellbore [44], opposing fracture initiation. For a non-penetrating fluid this hoop stress ($S_{\theta\theta}$) is given in cylindrical coordinates as [43],

$$S_{\theta\theta} = \frac{\sigma_{max} + \sigma_{min}}{2}\left(1 + \frac{r_w^2}{r^2}\right) - \frac{\sigma_{max} - \sigma_{min}}{2}\left(1 + \frac{3r_w^4}{r^4}\right)\cos 2\theta + P_p \qquad 4.1$$

where
r : radius
r_w : wellbore radius
θ : stress orientation angle (measured from the azimuth of S_{max})

The wellbore pressure (P_w) creates a tensile hoop stress, in the opposite direction of the compressive stress, given as [43],

$$S_\theta = -\frac{r_w^2}{r^2}\left(P_w - P_p\right) \qquad 4.2$$

(Compression is assumed positive, and tension is assumed negative.) The summation of tensile and compressive stresses at orientation angle θ and radius r gives the total hoop stress (S_θ) as,

$$S_\theta = -\frac{r_w^2}{r^2}\left(P_w - P_p\right) + \frac{\sigma_{max} + \sigma_{min}}{2}\left(1 + \frac{r_w^2}{r^2}\right) - \frac{\sigma_{max} - \sigma_{min}}{2}\left(1 + \frac{3r_w^4}{r^4}\right)cos\ 2\theta + P_p \qquad 4.3$$

The total hoop stress (S_θ) can be related to the effective hoop stress (σ_θ) as,

$$S_\theta = \sigma_\theta + \alpha_p P_p \qquad 4.4$$

where α_p is the Biot's constant.

The CSS property can be defined as the maximum wellbore pressure that open-hole below the casing shoe can withstand, *i.e.* at which fracture initiates. For an intact, linear elastic rock and non-penetrating fluid, wellbore breakdown occurs when the effective hoop stress equals the tensile strength of the rock (-T). The fracture initiates perpendicular to the minimum horizontal stress; at wellbore wall ($r=r_w$) and at an orientation perpendicular to the minimum stress ($\theta=0°$), eqn.4.3 reduces to [43],

$$\sigma_\theta = -P_w + P_p + 3\sigma_{min} - \sigma_{max} = -T \qquad 4.5$$

Rearrangement of eqn.4.5 gives the wellbore pressure at which the wellbore breakdown will occur, given as,

$$P_w = 3\sigma_{min} - \sigma_{max} + P_p + T \qquad 4.6$$

Note that eqn.4.7 assumes no pore pressure increase in the rock matrix near the wellbore wall, i.e. the effect of pore deformation on the principle stresses is neglected. Also, the actual wellbore breakdown pressures deviate from the theoretical value calculated by eqn.4.7 in the presence of natural fractures, drilling induced fractures, non-linear rock properties or thermally induced rock stresses [45]. In this study, wellbore is assumed intact, and filter cake is assumed ideal, i.e. zero filtrate invasion. No plastic zones are considered, reverse faulting or tectonically active environments are not considered, and the well is assumed located in a normal fault regime environment. Consequently, initiation of vertical fracture is the main focus [43].

Besides mechanistic calculation of the least principle stress based on log, seismic and core data, direct field measurement methods are conducted to back calculate the least principle stress. These methods involve imposing deformation incrementally to rock limitations, which are called formation strength tests (FST).

4.1.2.   Measurement of Casing Shoe Strength by Formation Strength Tests

Various types of formation strength tests (FST) are performed to verify the strength of the cement bond and rock, such as formation integrity test (FIT), leak off test (LOT), or extended leak off test (XLOT). They are performed to determine the pressure limitations of the wellbore, kick tolerance and casing setting depths in order to safely drill the next section of the well. After casing is run and cemented; the cement plug, shoe and a short section of open hole are drilled and the open hole is pressurized at very slow constant rate and pressure response of the formation is analyzed to determine the least principle stress. A leak off test pressure response chart is shown in Fig. 4.2.
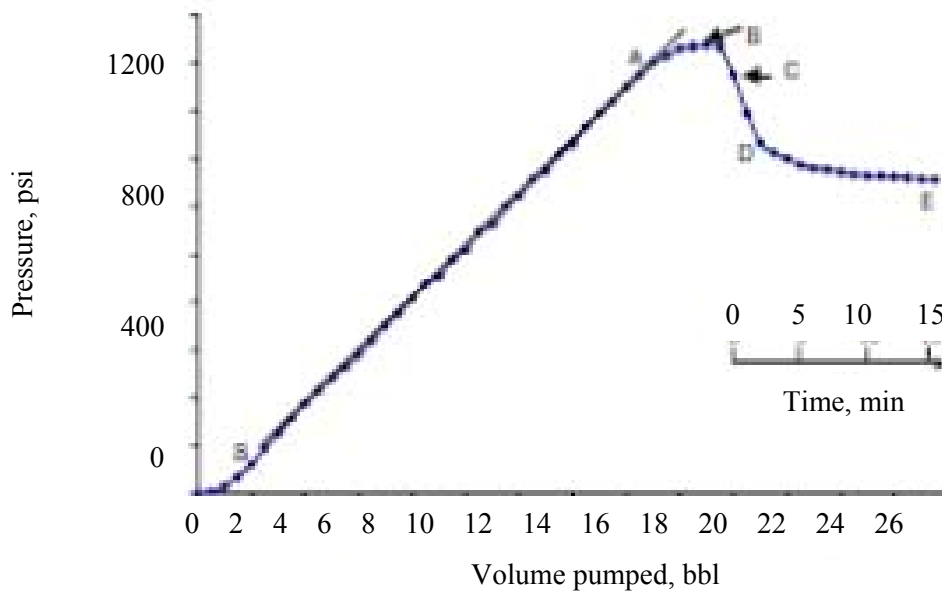
Fig. 4.2-Pressure response chart in typical leak off test [46]

In the initial section of formation integrity test (FIT), the wellbore strength is 'verified' to withstand a certain value of bottom-hole pressure and the test is stopped with the system still being within elastic compression state. This corresponds to the straight line between points S and A in Fig. 4.2.

In a leak-off test (LOT), the well is pressurized until the first sign of wellbore failure occurs, which is identified by a deviation from the linear response. This is the 'leak off pressure' at the surface, shown with point A. If the pumping is continued, fracture growth occurs, from points A to B in Fig. 4.2. At point B pumping is ceased, and the section C-D-E is the pressure fall-off due to filtration [46]. An extended leak off test (XLOT) has been also developed to determine the integrity of shallow casing shoes and its interpretation is more complex [46]. The operational practices of LOT and XLOT are similar [45].

In case of an intact rock, i.e. leak-off from initial fracture, the wellbore breakdown pressure given by eqn.4.5 is equal to the leak-off pressure. In this study, only leak-off test is considered. During LOT, injection is ceased at the leak off pressure (point A in Fig. 4.2). This pressure recorded at the surface is the 'surface leak off pressure' ($P_{LOT-surface}$). A conventional practice to calculate the casing shoe strength (CSS) is to add $P_{LOT-surface}$ to the hydrostatic pressure of the mud column from surface to the casing shoe to calculate CSS, as in the equation 4.7.

$$CSS = P_{LOT-surface} + 0.052 \cdot TVD \cdot \rho_{mud-surface}$$

4.7

However, conventional calculation of CSS solely based on $P_{LOT-surface}$ and surface mud weight is inaccurate. Oort et al . [47] demonstrated the discrepancy between the calculated downhole pressures during a leak off test and measured by MWD (measurement while drilling) tools as shown in Fig. 4.24.

4.1.3. Shortcomings of Conventional Testing of CSS

Conventional CSS calculation is inaccurate as it ignores effects of several factors. First, only part of pressure measured at the surface is transmitted to the casing shoe depth because of gellation. Second, hydrostatic pressure calculation based on surface density does not consider variations in mud density at elevated pressure and temperatures. Third, temperature difference between mud and formation may significantly change the minimum horizontal in-situ stress, S_{min}. Forth, mud invasion properties, and chemical alteration of wellbore with mud filtration may cause discrepancy in measured formation fracture pressures.

The contributions made by each of these factors, however, can be calculated based on commonly available data from drilling reports, mud reports and offset data, within an acceptable margin of uncertainty. Thus, a more precise determination of CSS from LOT accounting for the effects of mud compressibility, thixotropy and change in rock thermal stresses would require new mathematical formulation.

Each effect can be described as an additional term. In LOT, bottom-hole pressure is the summation of the surface leak off pressure ($P_{LOT-surface}$), hydrostatic pressure of the compressible mud column in the drill string (P_{hyd}) and pressure loss due friction resistance of thixotrophic mud (P_{gel}). Also, an additional rock stress rock stress ($\Delta\sigma_T$) caused by the temperature difference between the mud and the formation must be considered. Consequently, CSS can be described as,

$$CSS = \left(P_{LOT-surface} - \Delta P_{gel}\right) + P_{hyd} - \Delta\sigma_T$$

4.8

where

$P_{LOT\text{-}surface}$ = observed leak off pressure at the surface, psig

P_{hyd} = hydrostatic pressure of compressible mud column, psi

ΔP_{gel} = pressure loss due to resistance of thixotrophic mud to pressure transmission, psig

$\Delta \sigma_T$ = thermally induced stress due to mud-formation temperature difference, psig

In Chapter 4.2, below, each term in eqn.4.8 is discussed and described mathematically. Then, the CSS computation model is validated with field or laboratory data.

4.2. Factors Considered in Casing Shoe Strength Calculations

4.2.1. Hydrostatic Pressure Transmission Downhole

Calculation of hydrostatic pressures (P_{hyd}) using the surface mud density and disregarding the downhole effect of temperature and pressure variations result in underestimation of downhole pressures. Field data from HTHP wells showed static downhole pressure variations up to 1.5 ppge both for oil base and water base muds with densities up to 18 ppg, at temperatures 400 ^{o}F and pressures 15,000 psig [48]. Babu presented emprical method to calculate the density of oil and water base mud and he noticed that the oil base mud (OBM) density change with temperature and pressure is greater than that for the water based mud (WBM) [49]. For example, in a 25,000 ft well, density variation was 0.62 ppge for 17.6 ppg OBM and 0.34 ppge for 17.8 ppg WBM for temperatures 300 ^{o}F.

Hydrostatic pressure depends on mud density, which is function of pressure (P) and temperature (T). Bland,R. *et al.* [50] discussed mud density variation at bottom-hole temperature and pressures in the context of HPHT drilling fluid challenges, and showed that density of 18.2 ppg mud can increase to 18.6 ppg at 30,000 ft true vertical depth. Hydrostatic pressure of a column of mud with density $\rho_m(P,T)$ at depth D can be calculated by eqn.4.9. Common industry practice is to make density correction for every 100 ft [50].

$$P_{hyd} = 0.052 \cdot \int_0^D \rho_m \left[P(z), T(z) \right] \cdot dz \qquad\qquad 4.9$$

The integration of eqn.4.9 involves iterative solution. Mud is a composition of water, oil and solid phases and each phase react to imposed P and T based on its own material properties. Compositional mud density model is widely accepted method used in majority of software and proved to estimate densities accurately [51], [52]. In this study, mud density is calculated by compositional model at each cell of the discritized mud column.

4.2.1.1. Mud Density Model at Elevated Temperature and Pressure

At downhole conditions, mud weight changes predominantly due to compression or expansion of its phases with increased temperature and pressure. Compositional model developed by Hoberock *et al.* [52] considers the P-ρ-T behavior of each phase given as,

$$\rho_{mud}(P,T,z) = \frac{f_o \rho_{oi} + f_w \rho_{wi} + f_s \rho_{si}}{1 + f_o\left(\dfrac{\rho_{oi}}{\rho_o(z)} - 1\right) + f_w\left(\dfrac{\rho_{wi}}{\rho_w(z)} - 1\right)} \qquad 4.10$$

where f_0, f_w, f_s are the oil, water and solid fractions of mud, respectively. ρ_{oi} and ρ_{wi} are the oil and water densities at surface pressure and temperature, respectively; ρ_o and ρ_w are the oil and water densities at depth, respectively. As compaction of solid content is small comparing oil and water phases, the effect of solid component of the mud is assumed to be negligible.

Hoberock *et al.* [53] used Redlich-Kwong EOS and assumed composition of diesel oil to calculate gas free diesel oil densities. However, in case of presence of gas in mud, this assumption does not hold. On a rig site various types of degassing equipment continuously removes the gas from mud. However, the removal is not complete - especially from OBM. White *et al.* [54] studied mud density variations due to gas cutting and found that dissolved gas must be considered. Drilling fluid usually contain some gas due to routine drilling operation. The gas in the porous medium of the formation continuously enters the drilling fluid as new rock is drilled, which is also called 'background gas'. Also, additional gas can enter the mud due to pressure drop when pumping stops, which is also called 'connection gas'. In case of abnormally pressured formations, gas units may increase above background gas value, resulting in gas cutting of the mud, which is also called 'drilled show' [55].

Moreover, in extreme cases such as a well control situation, if uncontrolled, expansion of the bubbles can trigger a domino effect of irreducible reduction in the bottom-hole pressure eventually resulting a blow-out [9]. In this study, the effect of dissolved gas (R_{so}) is considered in the oil and water P-ρ-T calculations.

The mud density model takes P,T and R_{so} data input, and calculates ρ_o and ρ_w for known mud composition (f_0, f_w, f_s) as explained in Appendix E.1.5 and E.2.4. Inputs are obtained from routine field measurements and readily available on well site such as retort analysis and mud balance. For a gas-free oil, the zero R_{so} input should be entered. Moreover, if the retort analysis is not available, the software calculates a default composition. For WBM, water-barite mixture is assumed and their fractions are calculated for known mud weight. For OBM, oil-water-barite mixture is assumed and their fractions are calculated considering the minimum API recommendations for oil-water ratio for oil based muds.

Table 4-2- Correlations used for calculation of P-ρ-T properties

Property	Correlation used
Gas solubility in oil or synthetic phase	O'Bryan et al. correlation [56]
Bubble point pressure	Standing correlation [57]
Oil formation volume factor below bubble point	Van Slyke et al. correlation [58]
Oil formation volume factor above bubble point	Standing correlation [59]
Oil compressibility below bubble point	McCain et al. correlation [60]
Oil compressibility above bubble point	Vazques Begg's correlation [61]
Water solution gas oil ratio	McCain correlation [62]
Water formation volume factor	McCain correlation [62]
Water compressibility	Meehan correlation [63]
Gas PVT properties	Dranchuk and Abou Kassem EOS [64]

The P-ρ-T correlations summarized in Table 4-2 [except for gas solubility, R_{sob}] have been derived for reservoir oils. These correlations are strong functions of gas solubility (See Appendix E.1). For gas solubility, correlation developed specifically for diesel and mineral oils is considered [56].

O'Bryan et al. [65] presented correlation to calculate gas solubility (R_{sob}) in Diesel oil No.2, and two commonly used mineral oils Conoco LVL and Exxon Chemicals Mentor 28 as given in equation E.1 in Appendix E.1.1. To calculate oil density, first R_{sob} is calculated, then correlations summarized in Table 4-2 are used to calculate oil density for P, T and R_{so}. Computation of mud density at each depth of iteration is shown in Fig. 4.3.

Inputs:	P(z) , T(z) , f_o, f_w, f_s	
Step 1	Calculate gas solubility in oil, R_{sob}	(Eqn. E.1)
Step 2	Calculate bubble point pressure, P_b	(Eqn. E.8)
Step 3	Calculate oil compressibility, c_o	(Eqn. E.10-E.11)
Step 4	Calculate oil density, ρ_o	(Eqn. E.13)
Step 5	Calculate gas solubility in water, R_{sw}	(Eqn. E.19)
Step 6	Calculate water compressibility, c_w	(Eqn. E.27)
Step 7	Calculate mud density, ρ_m	(Eqn. 4.10)

Fig. 4.3-Calculation of mud density for P,T and R_{so}

4.2.1.2. Validation of Mud Density Model with Laboratory Data

The mud density model has been verified with laboratory data. Peters et al. [51] did laboratory experiements with 11 and 17 ppg Diesel and Mineral Oil's at ambient temperatures of 78, 200 and 350 °F and pressures up to 15,000 psig to using PVT cell to predict mud densities and observed good match with the compositonal model proposed by Hoberock et al. [52].

Compositions of the mud samples used by Peters *et al.* [51] and the default retort parameters used by the density model are shown in Table 4-3.

Table 4-3-Compositions of mud samples [51] used for model for validation

Composition	11 ppg OBM (Peters *et al.* [66])	11 ppg OBM (model)	17 ppg OBM (Peters *et al.* [66])	17 ppg OBM (model)
Oil	231 ml	220.5 ml	194.7 ml	178.5 ml
Organophilic clay	6.45 g		3 g	
Emulsifier	2 g		2 g	
Wetting agent	2 g		2 g	
Lime	2 g		2 g	
Water	63.2 ml	80.5 ml	25.3 ml	38.5 ml
$CaCl_2$	22.3 g	16.1 g	8.93 g	7.7 g
Barite	167.3 g	205.8 g	504.8 g	543.9 g
f_o	0.66	0.63	0.55	0.51
f_w	0.18	0.23	0.07	0.11
f_s	0.16	0.14	0.38	0.38
Density	11 ppg	11.00 ppg	17 ppg	17.00 ppg

The test data for 11 and 17 ppg diesel oil based mud samples is shown in Table 4-4. The data and densities calculated by the casing shoe strength software are in good aggreement, as shown in Fig. 4.4 below.

Table 4-4.Measured density of 11 and 17 pp Diesel Oil Base Muds [51]

		Measured Density	
T (°F)	P (psig)	11 ppg OBM	17 ppg OBM
78	14.7	11	17
	3,000	11.116	17.136
	6,000	11.218	17.258
	9,000	11.307	17.368
	12,000	11.387	17.468
	15,000	11.460	17.560
200	14.7	10.487	16.410
	3,000	10.630	16.596
	6,000	10.758	16.760
	9,000	10.867	16.901
	12,000	10.967	17.021
	15,000	11.057	17.128
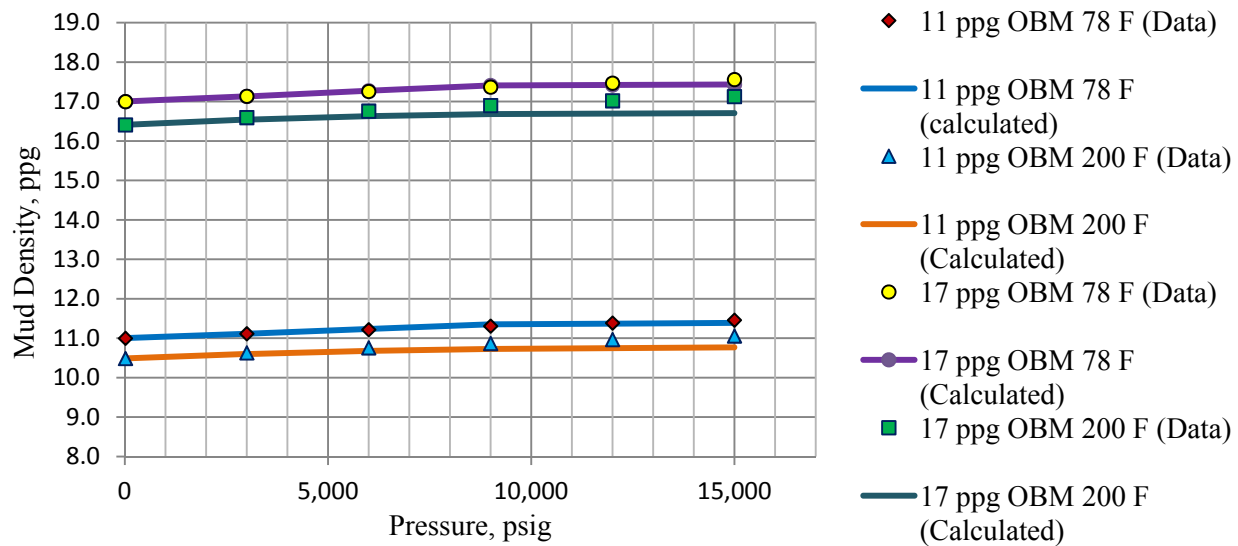
Fig. 4.4-Composite mud density model vs. experimental data of Peters *et al.* [51]

4.2.2. Effect of Mud Thixotropy on Pressure Transmission

During drilling, the mud flow is often interrupted by non-circulating periods of non-drilling activities [67]. At static conditions, drilling fluids exhibit time-dependent development of gel strength, which exceeds the value of yield stress, traditionally described with Bingham Plastic or Hersley-Bulkley models.

Yield stress inaccurately predicts the rheological behavior of the fluid in the ultra-low-shear rate region as it disregards thixotropy [68], which has been shown to be the key property controlling the barite sagging and pressure surges due transient gel breaking [69], [70]. Numerous authors addressed pressure surges at pump start ups and their effect on equivalent circulating density during drilling. Zoellner *et al.* [71] outlined the concept with several case studies and provided real-time downhole pressure data. Shown in Fig. 4.5 is stand pipe pressure recorded at a pump start up following a short non-circulating period. Note that a surge pressure of 174 psig to break the circulation was observed until the stand pipe pressure stabilized.

In LOT, pressure transmission is hampered by the friction force caused by the gel breaking of the overly structured fluid. The friction force counteracts the transmission of pressure applied from the surface. Therefore, the effect of thixotropy must be considered in the CSS model. Also, the shear rates since the injection rate is very small. At low shear rate is low mud gellation begins - a complex phenomenon depending on the structural network of the mud.

time. sec
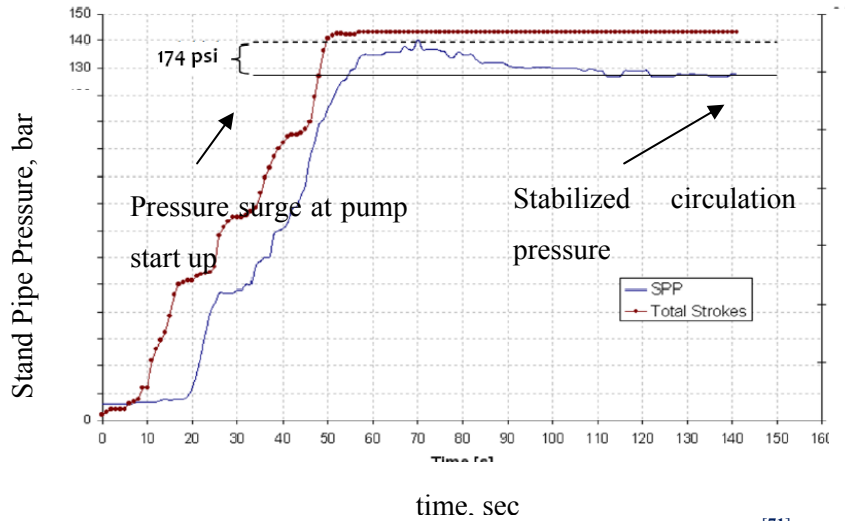
Fig. 4.5-Pressure surge observed durıng pump start-up [71]

4.2.2.1. Mud Thixotropy Effect at Low Shear Rates

The mechanism of thixtopy depends on the mud composition, *i.e.* content of solids, polymers and colloids in the water based mud (WBM); and fraction of the, continuous and emulsified phases in the oil based muds (OBM). The structure network of the system depends on time, temperature and shear rate. The chemical network in static conditions is also influenced by temperature. A common misconception is to confuse thixotropy with shear-thinning behavior. Shear-thinning is defined as the isothermal reversible decrease in viscosity for increasing shear rates, whereas thixotropy is the reversible reduction of viscosity with time at constant shear rate [72].

At steady-state low shearing rate, fluid compositional structure is in balance; part of the system is inactive because the energy input prevents building a structure, while other part is still active providing the shear stress response (τ) to that particular shear rate (γ). When the shear is reduced and kept constant, the structure comes to a new equilibrium [73]. At ultra low shear rates, fluid enters an 'unsteady-state' region where shear stresses do not follow behavior predicted by the Hersley-Buckley model. In other words, thixotropic behavior is 'activated', as shown in Fig. 4.6. Note that shear stress behaves differently at shear rates lower than 1.0 sec^{-1}, which means extrapolation of high shear rheology models would miscalculate the actual value of shear stress in that region.
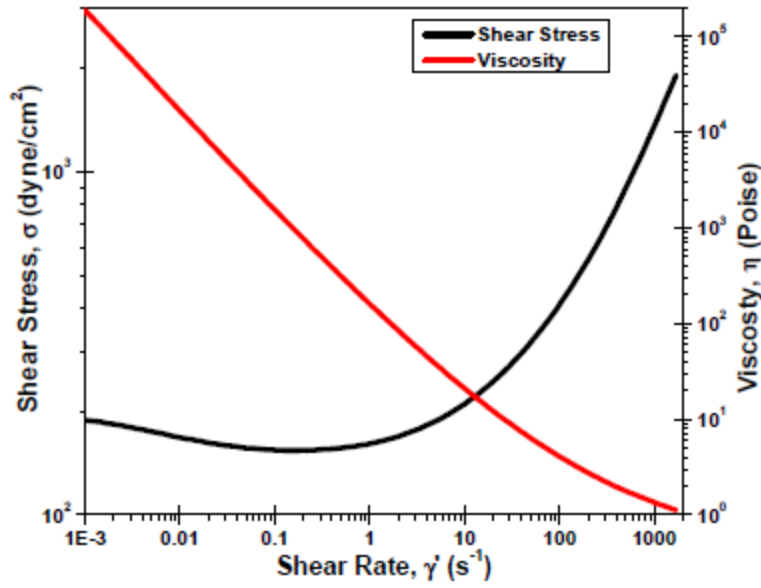
Fig. 4.6-Controlled rate flow data with Anton-Paar rheometer for 16 ppg WBM at 120°F [68]

Fig. 4.6 is from Maxey *et al.* (2007) [68], who studied the effects of thixotropy and yield stress on rheological measurements on two OBM's (14 ppg each) and two WBM's (10 and 16 ppg) at 120°F constant temperature using an Anton-Paar MCR301 stress controlled rheometer and OFI-900 viscometer for shear rates from 0.001 to 1,200 sec^{-1}, allowing 10 sec per data point. Mendes *et al.* [74] and Moller *et al.* [75] presented mathematical models to characterize shear stress of fluids in the ultra low shear rate region.

Furthermore, viscoelastic vs. viscoplastic behavior phenomenon makes the modeling efforts even more challenging, such that the fluid does not exhibit the same deflection response when the shear is incrementally increased or decreased, vice versa. In this study, the drilling fluid is assumed to be fully viscoelastic.

When the shearing stops, structural network immediately starts to build up as a function of time, resulting in gel strength which is needed to be broken to initiate the movement. Standard API practice is to measure the 10 sec, 10 min and 30 min gel strengths (lb/100ft[2]) to ensure that the mud does not have 'progressive' gels, but preferably have 'flat' gels [76]. The difference between the two types of gellation is the shape of the gel strength plot vs. time – flat, or steadily increasing.

Herzhaft *et al.* [70] examined build up of gel strength at low shear conditions with Fann-35 rheometer applying constant shear rate of 5.11 s^{-1} after various static times ('time of rest' in Fig. 4.7) following strong shearing on OBM samples. Note that each data point in Fig. 4.7 is taken individually, *i.e.* after re-shearing and resting for gel buildup.
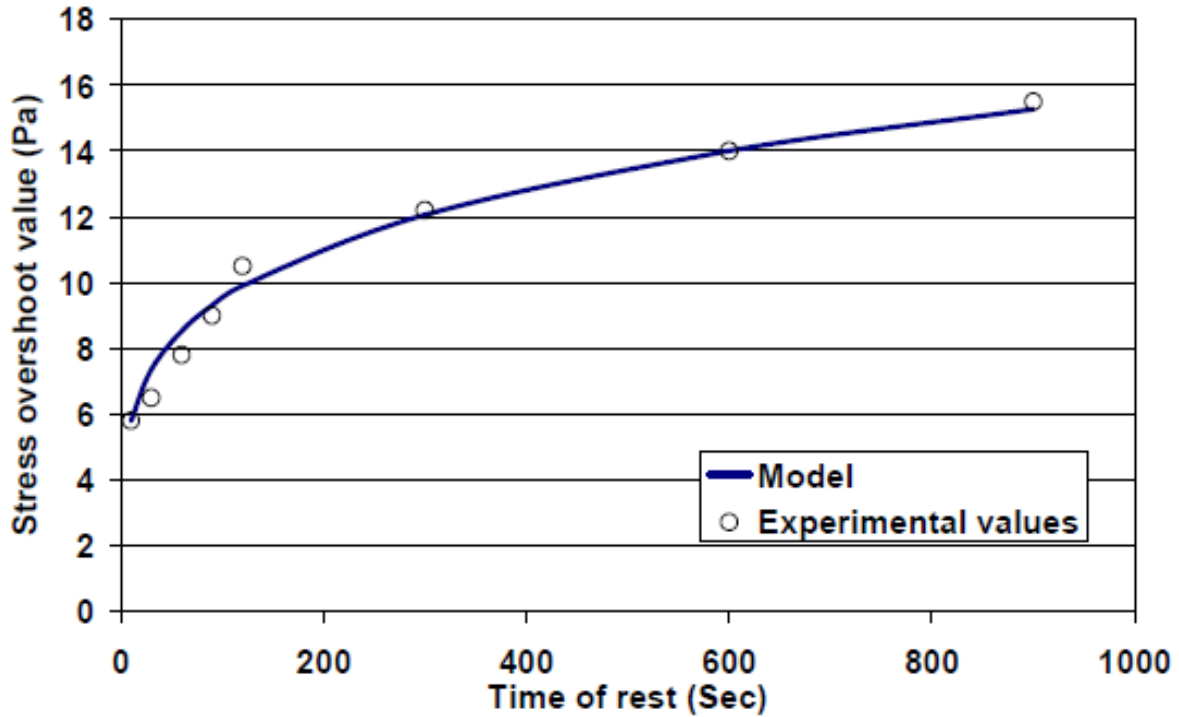
Fig. 4.7-Gellation of mud in time at low-shear of 5.11 s^{-1} [70]

Note that build up of thixotropy from the start of static time after strong shear and the moment that the measurement is taken cannot be measured continuously since measurement itself generates shear, which prohibits gel development. As the shear is started to be introduced to the mud after 10 sec, 10 min or 30 min rest periods, shear stress rapidly increases to a peak value, and as the constant shear rate is continued, the shear stress slowly decreases and converges to a plateau of τ_∞ value, which actually is the steady state equilibrium.

Knut *et al.* [67] examined gel breaking using water suspensions of Laponite clay and CMC using a Fann-35 rheometer and presented model to estimate pressure surges as a function of static time before shear. As the data demonstrates, the initial shear stress increases with time, *i.e.* the plot starts at higher values of shear stress; and as the 10.22 s^{-1} constant shear rate is applied shear stress response decreases until it converges to its equilibrium state, as shown in Fig. 4.8.

The developed mathematical model estimated pressure surges at pump start ups at 16,000ft wells drilled with WBM and OBM. They observed no significant discrepancy between OBM and WBM.
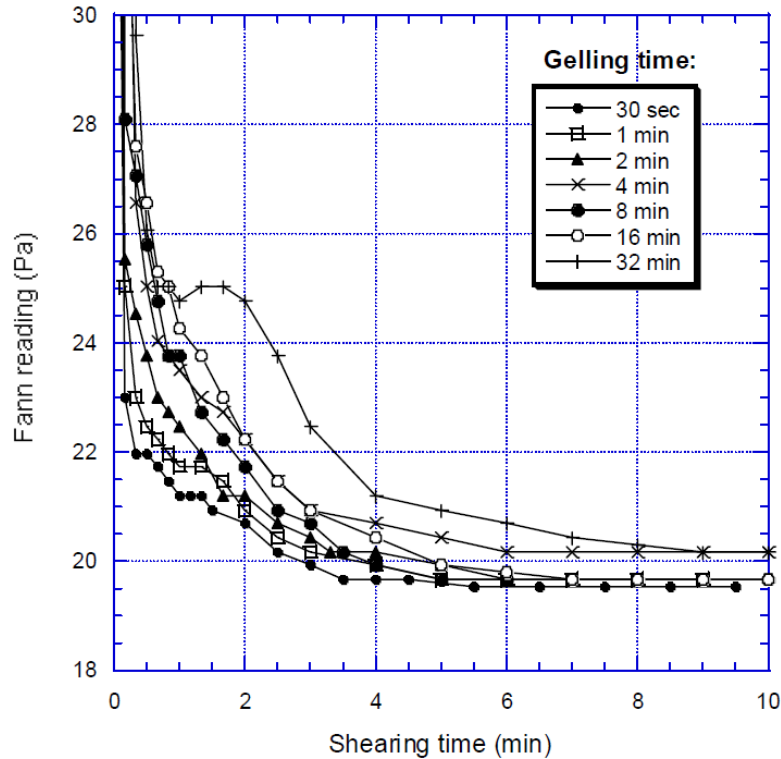
Fig. 4.8-Shear stress response at constant shear rate 10.22 s^{-1} after various static gelling times [67]

4.2.2.2. Effect of Temperature on Gel Strength

Effect of temperature on the rheological properties of mud has been investigated in mostly for the ECD estimati0ns in HPHT deep wells. However, little research has been published on temperature effect on thixotropy. No correlation models have been developed to to that would relate gel strengths to temperature for different mud composition, because of the structural complexity of drilling fluids [77].

Drilling mud composition is the key factor controlling the behavior of mud system at elevated temperatures. For example, an OBM and WBM give different responses to temperature differences. Therefore, temperature effect on mud rheological properties must be considered separately for WBM's and OBM's. Barlett et al. [77] performed laboratory experiments with WBM's with various concentrations of sodium and calcium montmorillonite, barite, NaOH and lignosulfonate at temperatures up to 350 $^{\circ}$F and clay concentrations up to 50 ppb using Fann-35 rheometer. He observed decrease in viscosity with temperature for higher clay concentrations. He also observed that at relatively lower clay concentrations at high temperatures viscosity starts to build up, as shown in Fig. 4.9.

He speculated that the physics behind the system's rebuilding of viscosity at high temperatures relates to the chemical alteration of working efficiency of lignosulfonate in conjunction with pH change.
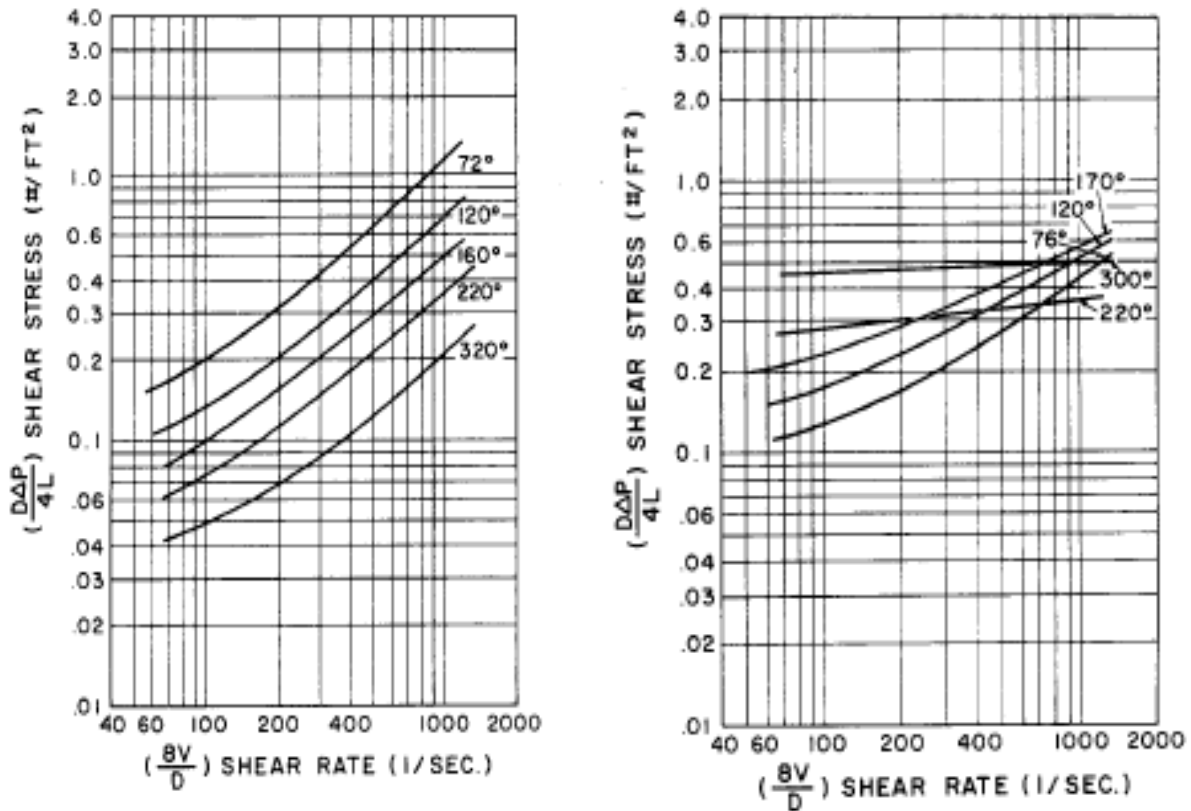
Fig. 4.9-Rheoplot of 25 ppb Na-Montmorillonite, 9 ppb lignosulfonate, ph=9 (left), and 21 ppb Na-Montmorillonite [77]

Dahab [78] made laboratory experiments with seawater-palygorskite and freshwater- palygorskite muds with fluid loss and pH control additives to study the effect of temperature, pH and clay concentration on thixotropy, effective viscosity and fluid loss. He observed strong increase of gel strength with temperature for freshwater muds and almost no effect for seawater muds.

Individual effect of temperature on polymers, the glycol's solubility, brine activity, solubility of the ions and their chemical reactivity with the other components, electrolytic properties of the clay and irreversible degradation of polymers at elevated temperatures add complexity to the overall system, prohibiting development of direct correlations to link thixotropy and temperature. Besides temperature's magnitude, it has been reported that the time period the mud has been exposed to the temperature also has significant effect on the resultant rheological behavior [79].

Deterioration of mud due to chemical instability at temperatures above the working margin has been studied primarily for development of geothermal mud system, and will be discussed further in detail in the 'mud aging' section. In conclusion, the CSS model does not consider temperature effect on gel strength of WBM.
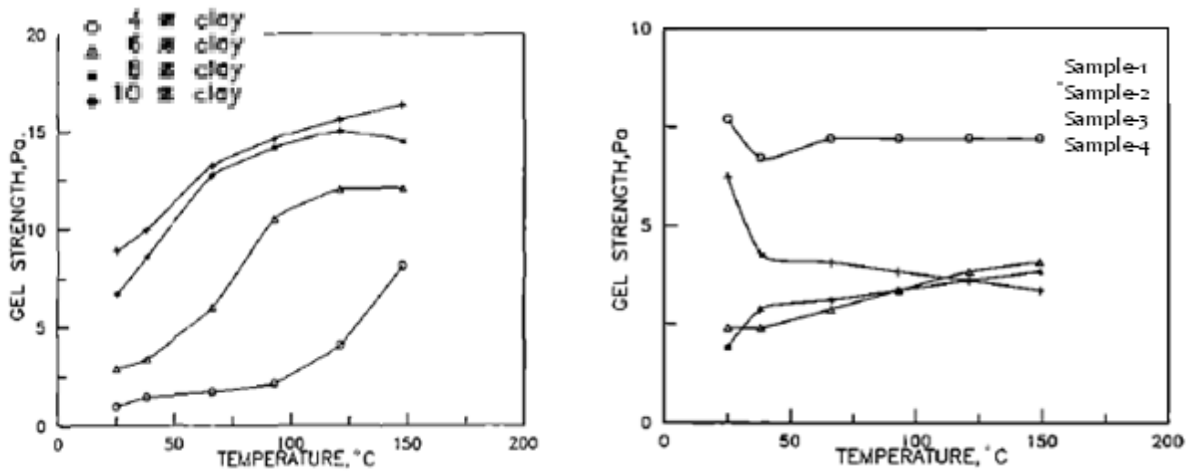
Fig. 4.10- Gel strength vs.temperature of palygorskite clay freshwater (left), and seawater (right) muds [78]

The oil based muds have been reported to be more stable at high temperatures [80]. McMordie made experiments with 17.5 ppg OBM mud and observed that the mud preserves its stability for temperatures up to 420 °F. Within the working margin, an OBM's viscosity and thixotropy is predominantly controlled by the viscosity of the chemical composition of its continuous phase [81]. Growcock *et al.* [82] made experiments with various 16.5 ppg synthetic based muds for temperatures up to 350 °F and observed continuous decrease in viscosity with temperature. In Fig. 4.11, shown change in apparent viscosities (at 100 s^{-1}) of various synthetic based muds by temperature.
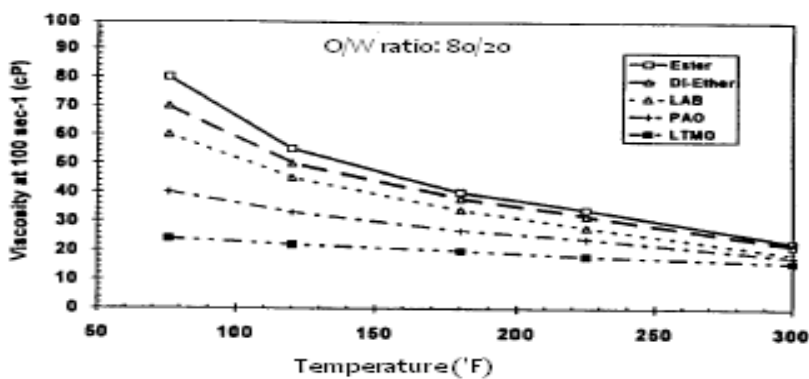
Fig. 4.11-Apparent viscosity of synthetic base muds at different temperatures [82]

Gandelman *et al.* [83] made laboratory experiments with Fann-75 rheometer to evaluate the freezing phenomena of synthetic based drilling fluids in deep water environments.

58

They developed correlation model to predict temperature and static time dependent thixotrophic properties and for low temperatures and high pressures (below 40°F and below 5,000 psi).

$$\tau_g = a \left(\frac{T}{277.6} \right)^b \left(\frac{t}{10} \right)^d \qquad 4.11$$

where τ_g is in Pa, t is static time in min., T is temperature in °K, and a, b and d are correlation constants

$a = 18.41 \, \text{Pa}$
$b = -6.7049$
$d = 0.13$

Politte *et al.* [84] performed experiments with 10 to 18 ppg Diesel oil no.2 OBM's using coaxial viscometer at pressures up to 15,000 psig and temperatures from 90 to 500 °F. He presented a correlation to predict the yield point of an OBM at elevated temperatures as for a reference temperature (T_o), valid for the range of temperatures the tests were performed.

$$\tau_y (T) = \tau_{yo} \cdot C_T \qquad 4.12$$

where,

τ_{y0} :   yield point at reference temperature, °F

$\tau_y(T)$:   yield point at temperature T, °F

C_T :   temperature correlation constant, given by,

$$C_T = \frac{B_0 + B_1 T^{-1} + B_2 T^{-2}}{B_0 + B_1 T_0^{-1} + B_2 T_0^{-2}} \qquad 4.13$$

$90 < T < 300 \; °F$
$B_0 = -0.186$
$B_1 = 145.054$
$B_2 = -3410.322$

In view of lacking research data, the correlation presented by Politte *et al.* [84] has been used to estimate the effect of temperature on thixotropy.

4.2.2.3. Thixotropy Effect Model

The Herzhaft *et al.* [70] study, discussed above, was used to develop a mathematical model that links the Fann-35 measurements to pressure gradient at ultra-low-shear-rate. The model was later verified with Haake RS150 rheometer measurements. Two Fann-35 gel peak measurements, τ_0 and τ_1, after two resting

times Δt_0 and Δt_1 (preferably at 10sec and 10min) are taken following mixing at high shear rate. The unitless model constant, n is,

$$n = 1 + \frac{ln\left(\dfrac{\tau_1}{\tau_0}\right)}{ln\left(\dfrac{\Delta t_1}{\Delta t_0}\right)}$$

4.14

where

Δt_0 :   resting time prior to the first gel measurement, sec

τ_0 :   gel measurement following a resting time of Δt_0 , lb/100ft^2

Δt_1 :   resting time prior to the second gel measurement, sec

τ_1 :   gel measurement following a resting time of Δt_1 , lb/100ft^2

α :   unitless model constant, which is,

$$\alpha = \frac{ln\ 2}{\dot{\gamma} \cdot \Delta t_{1/2}}$$

4.15

where

$\Delta t_{1/2}$:   half time needed for the shear stress to drop from its initial value at Δt_0, (τ_0) to its stabilized value (τ_∞) during the first gel strength measurement [1], s

γ :   the shear rate at which the gel measurements have been made [2], s^{-1}

Additional model parameters μ_0 and Θ_o are given as,

$$\mu_o = \frac{\tau_\infty}{\dot{\gamma}} - \left(\frac{1}{\alpha \dot{\gamma}}\right)^n \frac{\alpha \tau_1}{\Delta t_1^{n-1}}$$

4.16

$$\theta_o = \left(\frac{\mu_o}{\alpha \tau_1}\right)^{1/n} \Delta t_1^{1-1/n}$$

4.17

Finally, the pressure drop, (psi/ft) at pump start up prior to a non-circulating time period of Δt_s is given as,

$$\frac{\Delta P}{\Delta z} = \frac{2.777 \cdot \mu_0}{\alpha \cdot \theta_0 \cdot d_{pi}} \left(\frac{60 \cdot \Delta t_s}{\theta_o}\right)^{n-1}$$

4.18

where

d_{pi} :   pipe inner diameter, ft

---

[1] See Fig. 4.8

[2] for 3 rpm, $\gamma = 5.11$ s^{-1}

60

Δt_s :   non-circulating time before the leak off test, min

Consequently, pressure loss due to the resistance of gel strengths to the transmission of pressure from surface to the casing shoe in a leak of test is derived for OBM as,

$$\Delta P_{gel} = \int_{z=0}^{D} \Delta P_z = \frac{2.777 \cdot \mu_0}{\alpha \cdot \theta_0 \cdot d_{pi}} \left(\frac{60 \cdot \Delta t_s}{\theta_o} \right)^{n-1} \cdot \int_{z=0}^{D} C_T \left[T_{ws}(z) \right] \cdot dz \qquad 4.19$$

where

$T_{ws}(z)$: wellbore temperature at depth z, ^oF

D :   total depth, ft

C_T :   temperature function in eqn.4.13

For WBM, eqn.4.19 reduces to,

$$\Delta P_{gel} = \int_{z=0}^{D} \Delta P_z = \frac{2.777 \cdot \mu_0}{\alpha \cdot \theta_0 \cdot d_{pi}} \left(\frac{60 \cdot \Delta t_s}{\theta_o} \right)^{n-1} \cdot D \qquad 4.20$$

4.2.2.4. Validation of Thixotropy Effect Model with Field Data

Zoellner et al. [71] published the downhole pressure data from a well in Austria drilled with 9.5 ppg (τ_y=23 lb/100ft^2) mud from depths 4,317 to 6,312 ft. The data included measurements of a downhole pressure sensor (1 Hz data frequency) and the surface data of pressure surges to break the gel after static time periods from 4 to 25 minutes. In this 2,000 ft well section, mud weight was constant. The pump on/off data for different static (resting) time was matched using the thixotropy-effect model as shown in Fig. 4.12. The plot demonstrates a good agreement.
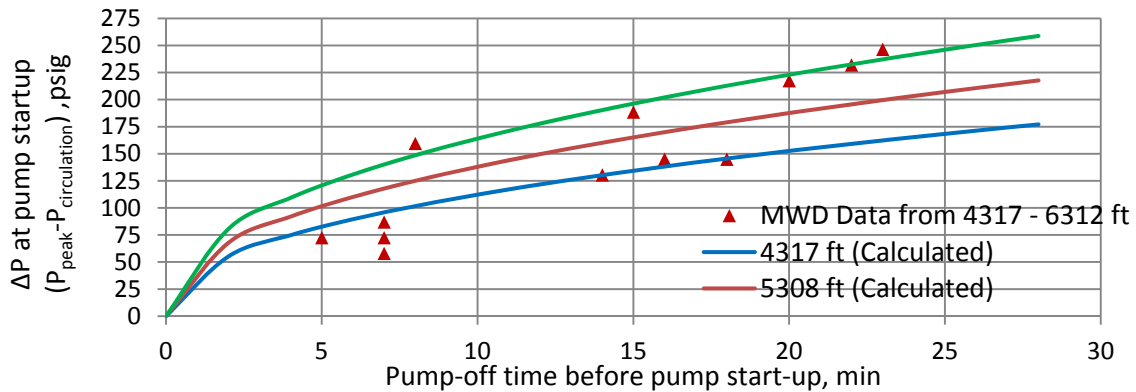
Fig. 4.12-Pressure surges at pump start-ups, model verification with field data, from Zoellner [71]

4.2.3. Effect of Drilling Fluid Temperature on Formation Strength

When a well is drilled, the stress distribution around the wellbore is altered due to the temperature variation. The responsive thermal effect depends on the thermoelastic behavior of the rock, filtration, and temperature difference between the mud and the rock. This is a time dependent effect, i.e. as the longer the cooler mud stays in contact with the rock, the more the temperature perturbation propagates away from the wellbore [43]. In this study, the rock temperature (T_{ei}) is assumed uniform, and filtration is not considered.

Perkins and Gonzales observed that mud temperatures below the rock temperature reduces fracture pressures [85]. A case study from North Sea was reported in which wellbore breakdown occurred due to circulation of cold mud [86]. When the circulation was stopped, mud temperature stabilized and compressive stress increased resulting the fractures to close and the lost mud to return as pit gain. A full scale field test has been performed by ChevronTexaco to investigate the effect of temperature on fracture gradient [87]. A series of leak-off tests have been performed with mud temperatures; cooled to 94 $^{\circ}$F, and heated up to 132 and 153 $^{\circ}$F. For +33°C mud-rock temperature difference, they observed approximately 145 psi increase in fracture gradient at 3,000 ft. Hettema et $al.$ [88] analyzed the effect of temperature change on formation strength while drilling.

During a leak off test, when the tensile stresses at any point on the wellbore wall exceeds the tensile strength of the rock, wellbore breakdown occurs, as given by eqn.4.5. In the case of an intact rock and symmetric loading, the minimum and maximum effective stresses can be assumed equal. Thus, the wellbore pressure at which the breakdown will occur is [43],

$$P_{w} = 2\sigma_{min} + P_{p} + T$$
4.21

The minimum horizontal effective stress (σ_{min}) can be related to elastic rock properties, pore pressure, overburden stress and thermal variations as [89],

$$\sigma_{min} = \frac{v}{1-v}(S_{v} - \alpha_{T}P_{p}) + \alpha_{p}P_{p} + \frac{E}{1-v^{2}}\varepsilon_{tect} + \frac{E\alpha_{T}\Delta T}{1-v} - P_{p}$$
4.22

where ε_{tect} is the strain coefficient for tectonic effects, and α_{p} is the poroelastic coefficient. Discussion of the elastic rock parameters Young's modulus (E), thermal expansion coefficient (α_{T}), Poisson's ratio (v), in conjunction with their determination methods are discussed in section 6.2.1.1 in detail.

The fourth term in eqn.4.22 accounts for the thermally induced stress for a temperature disturbance of the in situ rock temperature by ΔT [1]. Zoback [43] suggested that a mud cooler or hotter than the rock creates such disturbance at the wellbore wall. Consequently, the difference in the wellbore breakdown pressure due to the thermally induced rock stresses is,

$$\Delta \sigma_T = \frac{2 \cdot E \cdot \alpha_T}{(1-v)} \cdot \left(T_{ws} - T_{ei}\right) \qquad 4.23$$

where T_{ws} is the downhole mud temperature Δt_s after the circulation is stopped, T_{ei} is the geothermal earth temperature, E is Young's modulus, v is Poisson's ratio, and α_T is the formation's thermal expansion coefficient. Charlez [90] stated the α_T values in the range from 2.5 psi/°C to 52.2 psi/°C and Hettema *et al.* [88] presented its value in the range from 5 to 15 psi/°C for sandstone formations in GoM.

4.2.4. Effect of Non-circulating Time on Temperature Profile during Leak-off Test

Before LOT, the top and bottom cement plugs are drilled out, and the well is circulated for a sufficient time to remove all cuttings, check wellbore stability, and condition the mud, *i.e.* restore its chemical and physical properties that have been damaged by drilling the cement.

As a result of mud circulation, downhole temperature affects properties of drilling fluid, and the pressure profile. Therefore, knowledge of the temperature profile would improve the accuracy of the leak-off test analysis. If, MWD or LWD was available, bottom-hole mud temperature and pressure could be obtained by direct measurement. However, most cases direct measurement is not possible so the temperature profile must be calculated.

In the CSS model, we assume, that the well is circulated long enough for the wellbore temperature profile to come to steady state equilibrium for particular pump rate before the circulation stops. Then, the well's temperature increases until reaching geothermal gradient.

4.2.4.1. Model of Steady State Circulating Temperature

Raymond *et al.* [91] presented numerical methodology to estimate unsteady state and pseudo steady state circulating mud temperature profiles. Tragesser *et al.* [92] presented simplified methodology to calculate steady state circulating pipe and annulus temperature profiles. Keller *et al.* [93] presented numerical model describing two dimensional transient heat transfer to calculate wellbore temperature profile.

---

[1] Do not confuse with the rock tensile strength, T.

Holmes *et al.* [94] presented analytical solution of steady state heat transfer between the pipe, annulus and the wellbore, that fully estimates the steady state circulating mud temperature profiles. In this study analytical model proposed by Holmes *et al.* [94] is used due its simplicity. The model is presented below.

During the circulation downhole mud is cooler than the formation. The temperature difference between the mud and the formation generates heat flux that heats the mud, as shown in Fig. 4.13. In the model, the thermal diffusivity equation is solved by assuming zero heat convection and constant tank temperature [94]. Heat transfer between the annular fluid and the formation is approximated by steady-state linear heat transfer model and no heat generated by the bit is assumed. Also, formation temperature is constant at any point around the wellbore. The heat flux between the well annulus and the formation in differential form (Btu/hr) is,

$$dQ_{af} = 2\pi r_w U \cdot (T_{ws} - T_{ei}) dz$$

4.24

where

Q_{af} :   heat flux between the annulus and formation, Btu/hr

r_w :   wellbore radius, ft

U :   overall heat transfer coefficient across wellbore face, Btu/hr/ft^2/$^{\circ}$F

T_{ws} :   mud temperature in wellbore, $^{\circ}$F

T_{ei} :   formation temperature, $^{\circ}$F
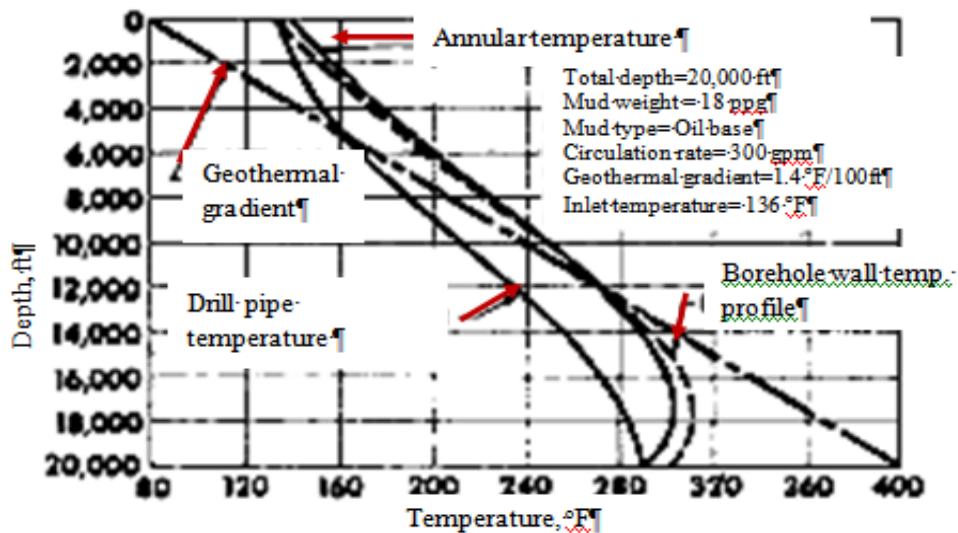
Fig. 4.13-Circulating mud temperature profiles in pipe, in annulus and geothermal gradient [91]

64

Likewise, the heat transfer between the pipe and the annulus is given as,

$$dQ_{pa} = \pi d_{pi} h_p \left(T_p - T_{ws}\right) dz \qquad 4.25$$

where

Q_{pa}:   heat flux between the pipe and annulus, Btu/hr

h_p :   overall heat transfer coefficient across drill pipe, Btu/hr/ft^2/^{o}F

T_p :   mud temperature in pipe, ^{o}F

d_{pi} :   pipe inner diameter, ft

Combining eqn. 4.24 and 4.25 yields the overall heat transfer through the annulus given as,

$$m \cdot c_{p-m} \cdot \frac{dT_{ws}}{dz} + \pi d_{pi} h_p \cdot \left(T_p - T_{ws}\right) = 2\pi r_w U \cdot \left(T_{ws} - T_{ei}\right) \qquad 4.26$$

where

c_{p-m} :   mud heat capacity, BTU/lb-^{o}F

m :   mass flow rate, lb/hr

Since the mud temperatures in pipe and annulus are equal at the bottom of the well, the following boundary conditions have been considered [94]:

For $z = 0$; $T_{pipe\ (z=0)} = T_{inlet}$

and $z = D$; $T_{pipe\ (z=D)} = T_{ws\ (z=D)}$

For these boundary conditions, integration constants for the steady state linear solution are given as,

$$K_1 = T_{inlet} - K_2 - T_s + GA \qquad 4.27$$

$$K_2 = \frac{GA - \left(T_{pi} - T_s + GA\right)e^{C_1 H} \cdot \left(1 - C_3\right)}{e^{C_2 H}\left(1 - C_4\right) - e^{C_1 H} \cdot \left(1 - C_3\right)} \qquad 4.28$$

Thus, steady state circulating mud temperature in the pipe and the annulus is given by 4.29 to 4.36 as follows.

$$T_{ws} = K_1 C_3 e^{c_1 x} + K_2 C_4 e^{c_2 x} + Gx + T_s \qquad 4.29$$

$$T_p = K_1 e^{c_1 x} + K_2 e^{c_2 x} + Gx + T_s - GA \qquad 4.30$$

where

$$C_1 = (B/2A)\left[1 + (1 + 4/B)^{1/2}\right]$$ <div align="right">4.31</div>

$$C_2 = (B/2A)\left[1 - (1 + 4/B)^{1/2}\right]$$ <div align="right">4.32</div>

$$C_3 = 1 + B/2\left[1 + (1 + 4/B)^{1/2}\right]$$ <div align="right">4.33</div>

$$C_4 = 1 + B/2\left[1 - (1 + 4/B)^{1/2}\right]$$ <div align="right">4.34</div>

$$A = mc_{p-m}/\pi d_{pi} h_p$$ <div align="right">4.35</div>

$$B = 2 r_w U/d_{pi} h_p$$ <div align="right">4.36</div>

where

T_s = surface earth temperature, ^oF

G_T = geothermal gradient, $^oF/ft$

4.2.4.2. Validation of the Steady State Model

Raymond, L.R. [91] proposed numerical method to estimate the wellbore temperatures for unsteady state and pseudo steady state conditions. He presented charts (verified with results from over 70 wells) for predicting steady state flowing bottom hole temperature (T_{BHF}) from a measured outlet temperature (T_{outlet}) [1], for constant inlet temperature (T_{inlet}) [2]. (He also observed that pipe and hole size had small effect on temperature profile, but depth and mud type played significant role.)

To validate the steady state model (based on Holmes et al. [94]) Raymond's results have been compared with the calculations made by the model, as shown in Fig.4.14 through Fig.4.17. Well configuration and mud properties are presented in Table 4-5. The comparison demonstrates excellent aggreement between the two models.

---

[1] Outlet temperature is taken from the flowline or possum belly.
[2] Inlet temperature is the suction tank fluid temperature.

Table 4-5: Well Configuration and Mud properties used for validation

Property	OBM		WBM	
	10.0 ppg	18.0 ppg	10.0 ppg	18.0 ppg
Retort oil content	0.64	0.49	0	0
Retort water content	0.26	0.10	0.94	0.63
Retort solid content	0.10	0.40	0.06	0.37
Mud thermal conductivity (BTU/ft-^{o}F-hr)	0.291	0.662	0.411	0.755
Mud heat capacity (BTU/lb-^{o}F)	0.559	0.310	0.948	0.312
Heat transfer coefficient	28.0			
Heat transfer coefficient	0.78			
Formation thermal conductivity	1	BTU/ft-^{o}F-hr		
Formation heat capacity	0.2	BTU/lb-^{o}F		
Formation density	165	lb/ft^3		
Mud inlet temperature (T_{inlet})	120	^{o}F		
Wellbore & pipe diameter	8.625	in	4.5	in
Casing shoe depth	15,000	ft		
Geothermal gradient	1.7	^{0}F /100 ft		
Surface earth temperature	80	^{0}F		

Table 4-6: Comparison of Circulating Mud temperatures calculated by Model vs. Raymond, L.R. [91]

	$\Delta T = T_{BHF} - T_{outlet}$, ^{o}F							
	Raymond,L.R. [91], ^{0}F			Steady State Model Results, ^{0}F				
Pump Rate :	200 gpm	300 gpm	400 gpm	200 gpm	300 gpm	400 gpm		
25,000	194	142	100	208.613	145.258	101.064	10.0ppg	OBM
20,000	131	84	61	135.057	85.658	55.098		
15,000	68	38	22	70.629	39.149	22.631		
10,000	25	9	3	23.200	10.574	5.216		
25,000	204	156	122	208.909	145.575	101.353	18.0ppg	
20,000	132	91	69	135.302	85.889	55.287		
15,000	80	47	31	70.800	39.282	22.726		
10,000	27	17	7	23.277	10.621	5.244		
25,000	168	103	68	159.128	96.642	59.880	10.0ppg	WBM
20,000	94	58	40	95.925	52.223	29.633		
15,000	40	20	13	45.202	21.192	10.581		
10,000	16	6	1	12.751	4.789	1.853		
25,000	149	100	72	148.613	87.447	52.797	18.0ppg	
20,000	90	54	37	88.112	46.352	25.554		
15,000	43	20	10	40.573	18.315	8.802		
10,000	10	3	0	11.076	3.955	1.400		

(Depth, ft — column at far left of data rows)
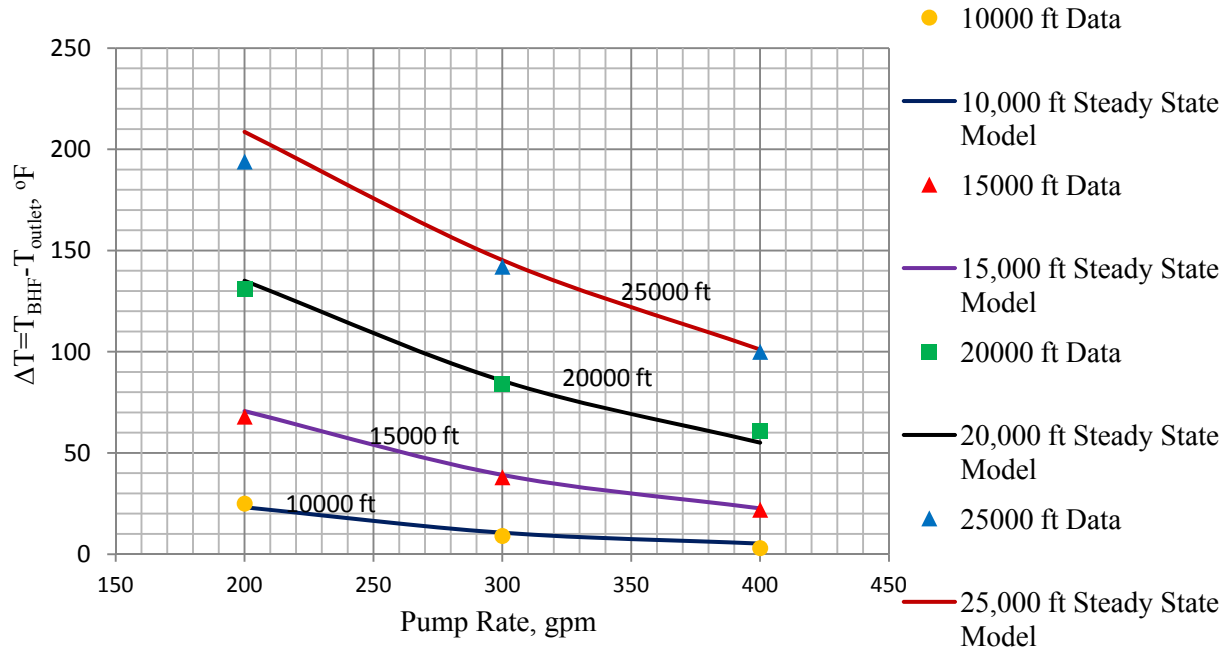
Fig.4.14-Circulating Temperatures for 10 ppg OBM- S-S model vs.Raymond,LR. [91]
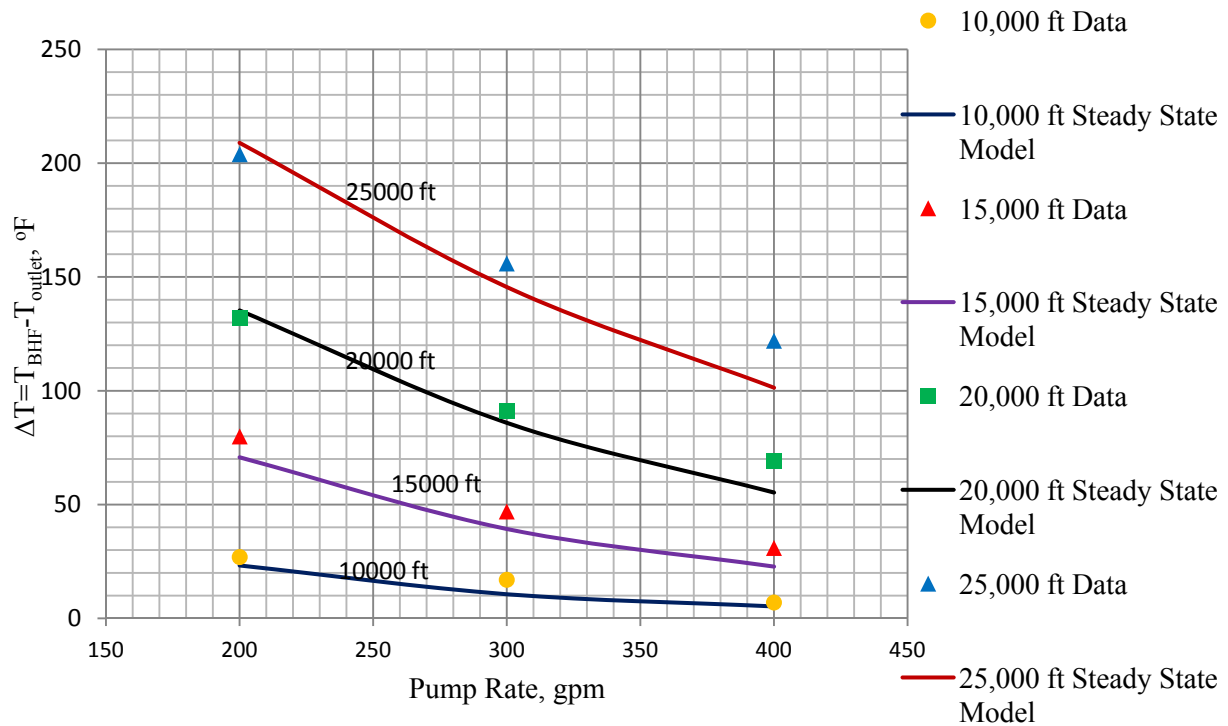
Fig.4.15-Circulating Temperatures for 18 ppg OBM,- S-S model vs.Raymond,LR. [91]
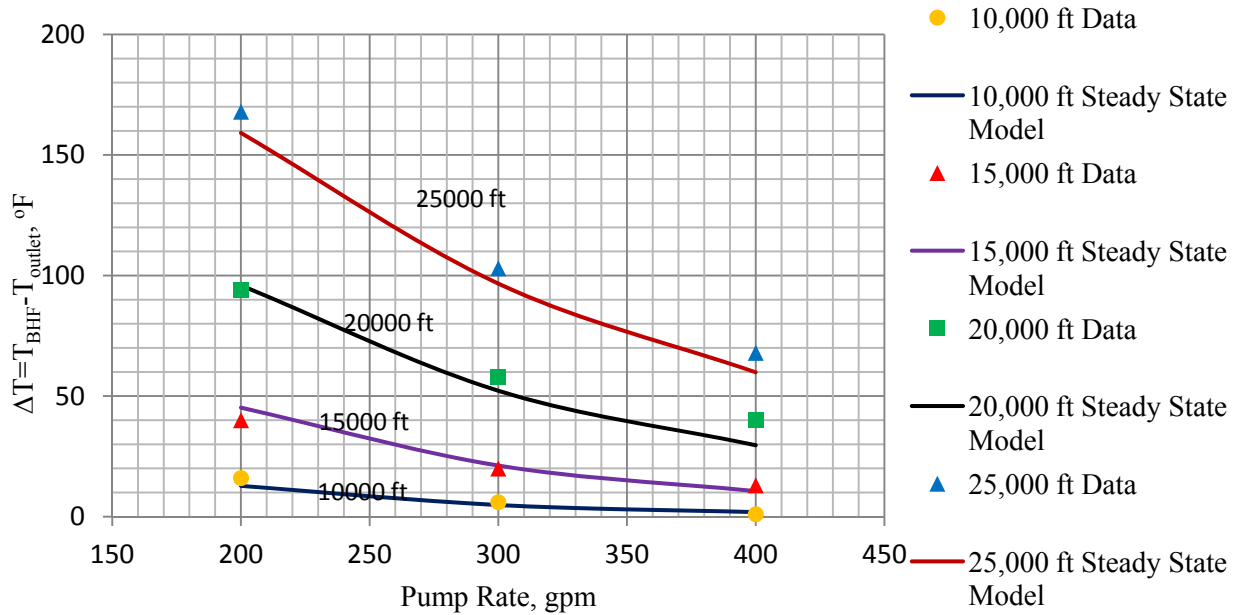
Fig.4.16-Circulating Temperatures for 10 ppg WBM- S-S model vs.Raymond,LR. [91]

The main reason of the difference in the circulating mud temperature profiles for the same density oil-base and water-based muds is the difference in their total heat capacities. OBM has more solids than WBM and specific heat of the weighting material (Barite-1.45 Btu/ft-^{o}F-hr) is smaller than that for water's (~1 Btu/ft-^{o}F). Therefore, OBM heats up faster than WBM. This has also been observed by other authors [91], [95]. The temperature profiles of 10 ppg and 18 ppg OBM and WBM in the 15,000 ft annulus are shown below.
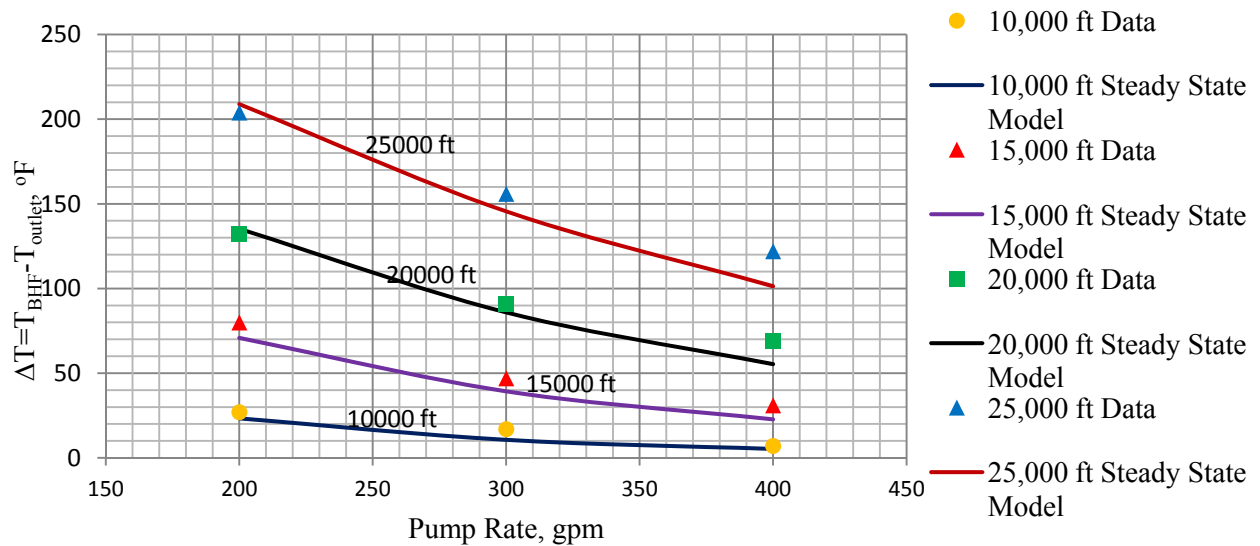
Fig.4.17-Circulating Temperatures for 18 ppg OBM- S-S model vs. Raymond,LR. [91]
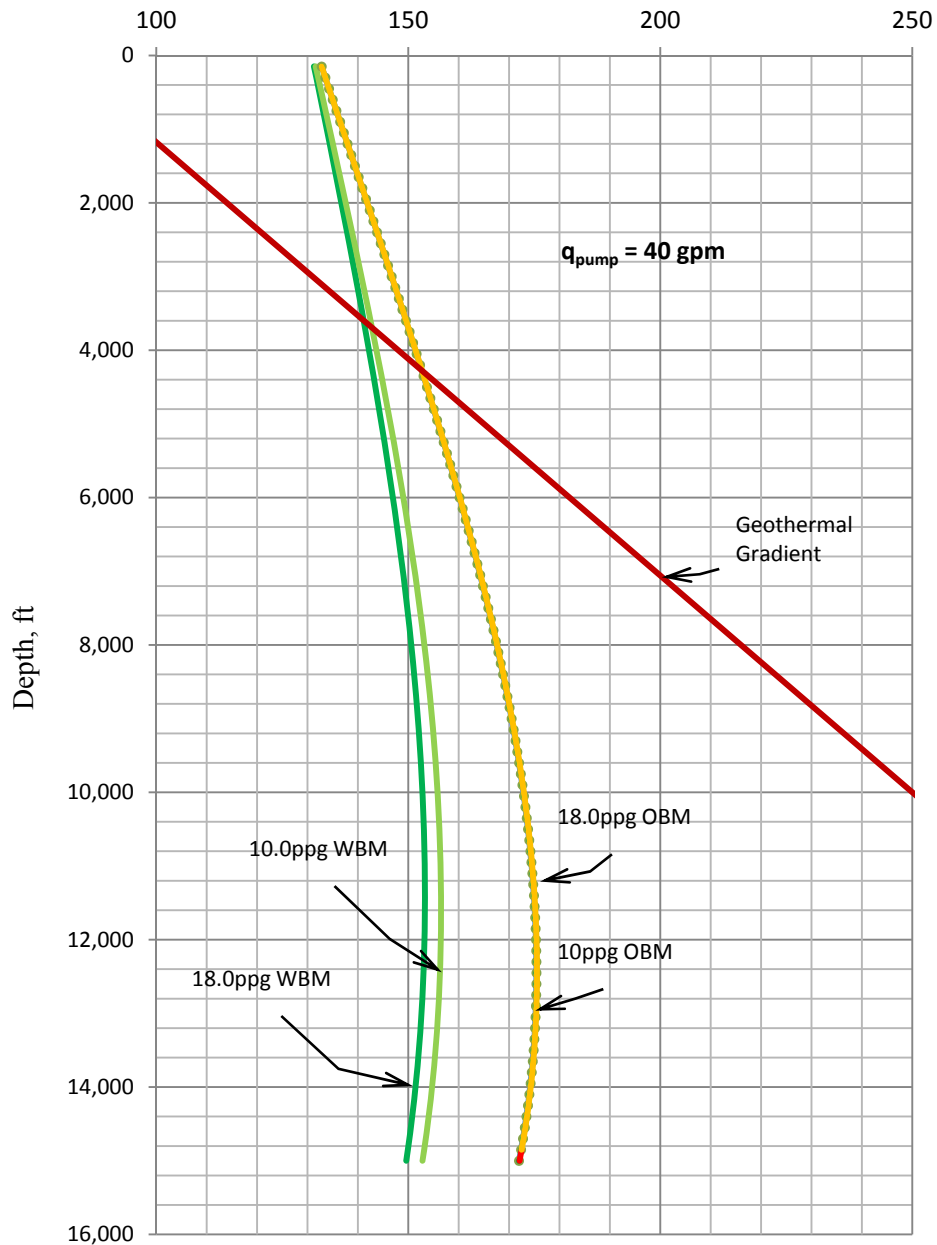
Fig. 4.18- Effect of mud type and density on circulating mud temperature in annulus

Pumping rate has significantly affects the steady-state circulating mud temperature downhole; as the mass flow rate decreases, heat transfer per unit time increases, so the mud temperature approaches the geothermal gradient, as shown in Fig. 4.19.

Circulating Mud Temperature, °F
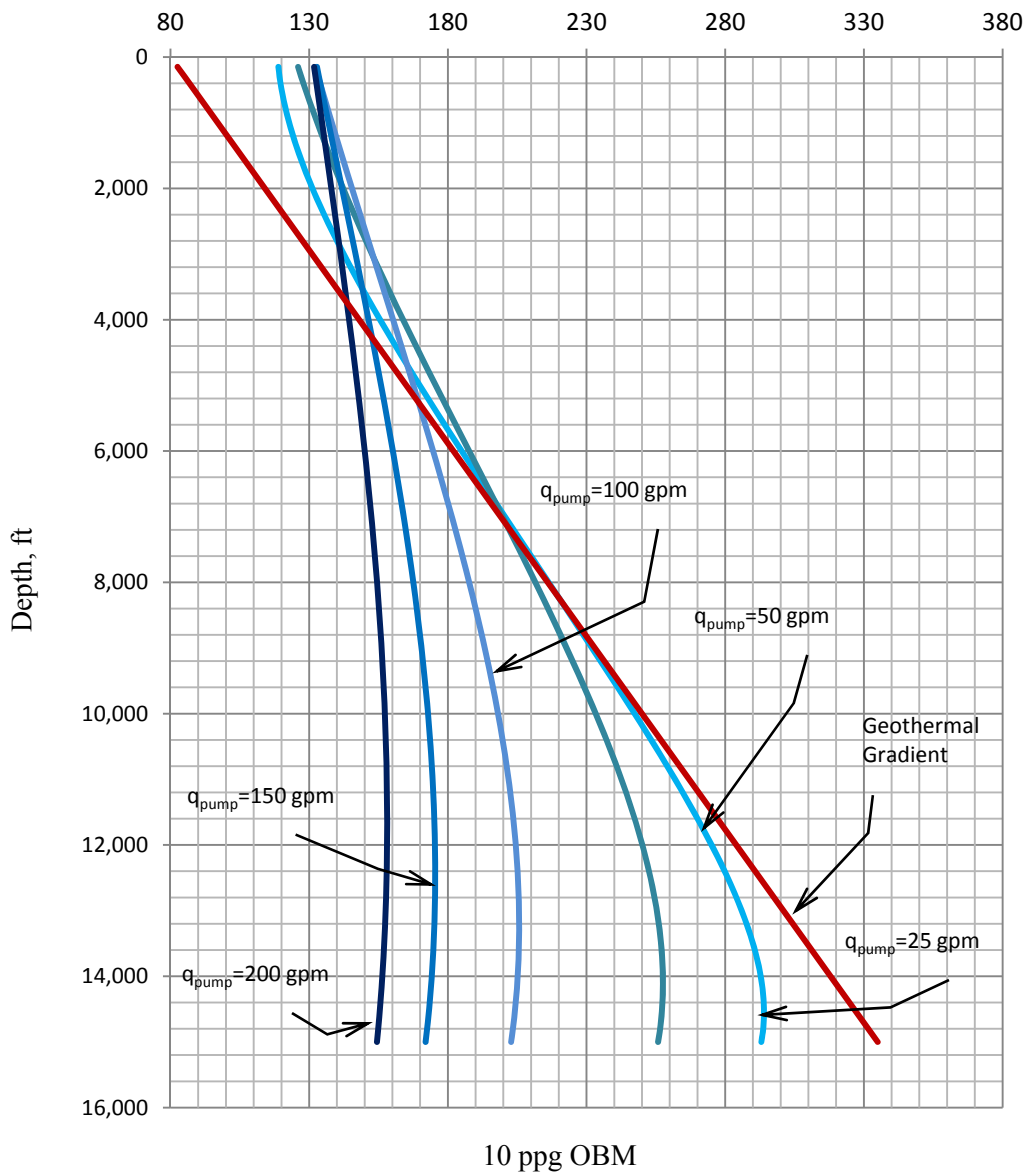
Fig. 4.19-Circulating mud temperature at various pumping rates for 10 ppg OBM

When the circulation stops, transient change of the downhole temperature begins that brings the mud in the well to geothermal conditions. At shallow depths, the mud in the well is cooled down while at greater depths it is heated up, as shown in Fig. 4.20.
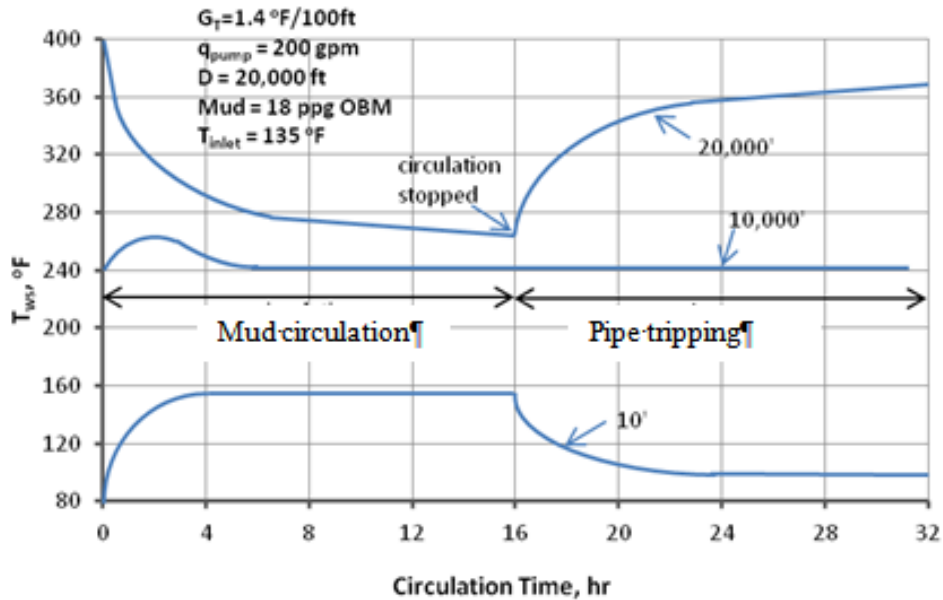
Fig. 4.20- Transient change of well temperature after circulation stops [91]

4.2.4.3. Transient Model of Well Temperature

Estimation of the well's temperature buildup during the static non-circulating time requires transient model. Dowdle and Cobb [96] employed the similarity between the welltesting pressure build up and static temperature build up and presented Horner solution to estimate the formation temperatures from well logs. Hasan and Kabir [97] developed mathematical model to use open hole temperature logs for estimating static formation temperature assuming that the circulating mud has negligible effect on the geothermal temperature around the wellbore since the mass of the mud is small compared to the rock mass. In this work, the log-linear approximation presented by Hasan and Kabir [97] has been adopted to estimate transient wellbore temperatures with satisfactory accuracy needed for this study. Heat transfer per unit time - unit length of the wellbore (Btu/ft-hr) is given as,

$$\frac{dQ}{dt} = Mc_{p-m} \frac{dT_{ws}}{dt} \qquad\qquad 4.37$$

where M is the mass of mud in one foot of well-bore (lb), c_{p-m} is the specific heat capacity of mud (BTU/lb-°F). The mass of the mud in the annulus is small compared to the mass of formation therefore the temperature within the wellbore radius is assumed to be constant. Heat influx, Q, decreases in time as the well temperature, T_{ws}, asymptotically approaches the rock temperature, T_{ei}.

In the calculations of temperature rise, at each time step Q is assumed constant as,

$$Q = -2\pi \left[\frac{r_w U k_e}{k_e + r_w U T_D} \right] (T_{ws} - T_{ei})$$

4.38

where

r_w :   wellbore radius, ft

U :   overall heat transfer coefficient, BTU/hr-ft^2-^{o}F

k_e :   formation thermal conductivity, BTU/hr-ft-^{o}F

T_D is dimensionless temperature, approximated by the equation [98],

$$T_D = \begin{cases} 1.1282\sqrt{t_D}\left(1 - 0.3\sqrt{t_D}\right), \text{ for } t_D < 1.5 \\ (0.4063 + 0.5\,ln\,t_D)\left[1 + \frac{0.6}{t_D}\right], \text{ for } t_D > 1.5 \end{cases}$$

4.39

where t_D is dimensionless circulation time is given by eqn 4.40.

$$t_{Dp} = \frac{k_m t_p}{\rho_{mud} c_{fl} r_w^2}$$

4.40

where

k_m :   thermal conductivity of the mud, BTU/hr-ft-^{o}F

c_{fl} :   fluid specific heat capacity, Btu/lb-^{o}F

The downhole mud temperature after a non-circulating time, Δt_s, can be explicitly calculated as,

$$T_{ws} = T_{ei} - B\left(T_{pD} + \Delta T_D\right) + \Delta T_D = -0.5B\,ln\left(\frac{t_p + \Delta t_s}{\Delta t_s}\right)$$

4.41

where

T_{ws} :   mud temperature after a period of Δt_D because the circulation is stopped, ^{o}F

T_{ei} :   formation static temperature bottomhole, ^{o}F

t_p :   circulation time before pump stop, hr, given by the formula,

$$t_p = \left(\frac{\left(d_{ci}^2 - d_{po}^2\right) - d_{pi}^2}{1,342 \cdot q_{pump}} \right) \cdot D$$

4.42

where

d_{pi} :   pipe inner diameter, ft

d_{po} :   pipe outer diameter, ft

d_{co} :   casing outer diameter, ft

q_{pump} : circulation rate, gpm

D :   depth, ft

The value of t_p is assumed one cycle of circulation time at q_{pump}. Δt_s is the non-circulating time, min, and q_{pump} is the pump rate during the circulation before leak off test, gpm. The correlation constant B is given by,

$$ B = \frac{M \cdot Q}{2\pi \cdot k_e} $$

4.43

where

M :   mass of fluid in one foot long well (including mud in pipe), lb

The initial value of T_{ws} (for Δt_s=0) is assumed the steady state circulation temperature. The value of T_{ws} in long time (for $\Delta t_s \rightarrow \infty$) is T_{ei}. Consequently, the initial and final values of the transient model are pre-known. Thermal conductivity of metals are high, and pipe and casing walls are relatively thin. Thus they provide negligible resistance to heat flow [99]. In the steady state and transient models convective heat transfer is neglected and overall heat transfer coefficients (U and h_p) are assumed constant.

4.2.4.4. Validation of Transient Model with Wireline Data

Shown in Fig. 4.21 is the increase of the wellbore temperature calculated with the transient model compared to data from the well logging tool in a 7,608 ft well (Dowdle,1975) [96].
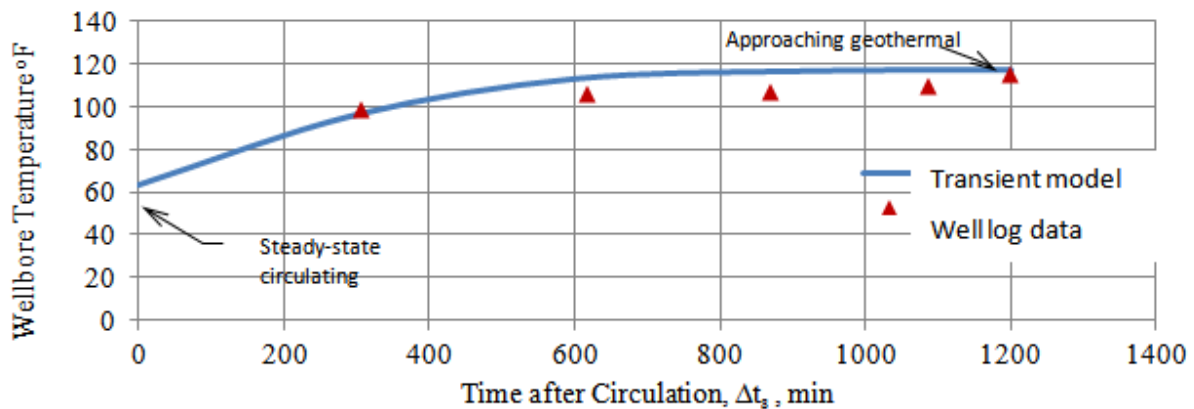
Fig. 4.21- Validation of transient wellbore temperature

A comparison of the calculated and measured temperature is also shown in Table 4-7. The initial temperature (63.2°F) was calculated from steady state model assuming 10 ppg OBM. The missing mud properties have been assumed assuming typical values.

Table 4-7- Comparison of wireline data [96] and transient model calculations of wellbore temperatures

Depth:	7,646 ft				
Drilling stopped :	22:00/2nd				
Circulation stopped:	2:30/ 3rd				
Circulation time:-	4-1/2 hrs				
Tool	Thermometer Depth, ft	Time off bottom	Time since circulation stopped, Δt_s, hr	Temperature, °F (Data)	Temperature, °F (Calculated)[*]
					63.2
Sonic	7,608	07:36/3rd	5:06	99	96.2
DIL	7,608	12:48/3rd	10:18	106	
FDC	7,620	14:29/3rd	14:29	107	112.9
SNP	7,620	20:37/3rd	18:07	110	116.5
Geothermal (T_{ei})				116	117.1

[*]For the calculations, 10 ppg OBM was assumed.

4.3. Model and Software for Casing Shoe Strength Determination

A complete mathematical model of CSS has been developed by substituting the terms in eqn.4.8 with partial models described in the proceeding chapters. The partial models have been adopted from literature with or without modification. The literature sources are shown in Table 4-8. All partial models, except for one have been validated using data published in other literature sources listed in Table 4-8.

Input parameters are:

Well configuration :   D, d_{ci}, d_{po}, d_{pi}

Mud data :   mud type, ρ_m at surface, Fann35 readings, retort analysis

Circulation data : Δt_s, q_{pump}, T_{inlet}, $P_{leak off-surface}$

Rock properties : T_0, G_T, α_T, E, v

Table 4-8-Literatue sources of partial models and validation

CSS Model's Components	Selected models	Sources of data for software validations
Mud density	Hoberock *et al.* compositional model [52]	Peters, *et al.*,1990 [51]
Pressure losses due to mud gellation	Herhaft *et al.* mathematical model [70]	Zoellner *et al.*, 2011 [71]
Effect of temperature on mud rheology	Politte correlation [84]	
Thermally induced rock stresses	Analytical relation from Zoback *et al.* [43]	
Steady state circulating mud temperature profile	Holmes *et al.* analytical model [94]	Raymond, L.R.1969 [91]
Transient wellbore temperature profile	Hasan and Kabir log-linear approximation [98]	Dowle, 1975 [96]
	Integrated CSS model and software	Oort *et al.*, 2007 [47]

Mud and formation thermal conductivities, heat transfer coefficients, heat capacities are automatically calculated as function of mud composition. If retort analysis data is not available, the software automatically calculates a default composition based on minimum oil-water ratio (O/W) requirements and assumes 20%weight $CaCl_2$ brine as the emulsified phase. The O/W requirement has been obtained from a drilling fluids company's engineering manual [100].

Depending on the user's preference, the software runs the model for a given non-circulating time (Δt_s) to calculate the CSS, or generates plots of the contributing factors (T_{ws}, ΔP_{gel}, $\Delta\sigma_T$, P_{hyd}, and CSS) vs. Δt_s for a series of given number and length of time-steps as shown in Fig.4.23.

Major assumptions considered by the model are as follows.

- Pump rate during circulation before the LOT is constant with steady state temperature profile;
- The PVT correlations are extrapolated for temperature and pressures exceeding their ranges;
- There is no alteration of gels at higher temperatures;
- Rock temperature around wellbore is geothermal;
- There is one value of heat transfer coefficient of the mud and formation along the wellbore (a typical assumption by various authors);
- Heat exchange due convection is neglected;
- Well is vertical, *i.e.* measured depth ≈ true vertical depth;
- There is no significant temperature effect on thixotropy of water-based muds;

- Thixotropy effect model is extrapolated for non-circulating time exceeding its range;
- There is no fluid loss during leak off test;

Computation algorithm of the model is presented in Fig. 4.22.

```
                        ┌────────────────────┐
                        │    Input data-     │
                        │   _____     │
                        └────────────────────┘
                                  │
          ┌───────────────────────────────────────────┐
          │ For Δt_s=0, calculate steady-state temp.   │
          │ profile: T_ws(q, z=0, Δz, 2Δz, .., D)      │
          │                                            │
          │                       (Section 4.2.4.1)    │
          └───────────────────────────────────────────┘

      ┌─────────────────────────────────────────────────┐
      │ For t_s = Δt_s, 2Δt_s, 2Δt_s…, calculate transient│
      │ temperature profiles:      (Section 4.2.4.3)     │
      │ T_ws(Δt_s, z=0, Δz, 2Δz, .., D)                  │
      └─────────────────────────────────────────────────┘
                                  │
          ┌────────────────────────────────────────┐
          │ For T_ws(Δt_s, D), calculate thermally   │
          │ induced stresses: Δσ_T(Δt_s)             │
          │              (Section 4.2.3)             │
          └────────────────────────────────────────┘
                                  │
              ┌──────────────────────────────────┐
              │ P(z=0) = P_leak-off surface       │
              └──────────────────────────────────┘

  ┌────────┐
  │ z+Δz   │
  └────────┘
                                  │
          ┌─────────────────────────────────────────────┐
          │ ρ_m(z,T_ws,P)        (Section 4.2.1.1)        │
          │                      (Section 4.2.2)          │
          │ ΔP_gel(T_ws)                                  │
          │                            (eqn. 4.8)         │
          │ P(z)= 0.052·ρ_m·Δz                            │
          └─────────────────────────────────────────────┘
                                  │
        yes          ╱ z < D ╲   no
           ┌────────<         >────────┐
                     ╲       ╱
                                  │
              ┌──────────────────────────────────┐
              │ CSS = P(z=D)-Δσ_T(Δt_s)           │
              └──────────────────────────────────┘
```

$P(z=0) = P_{\text{leak-off surface}}$

$z+\Delta z$

$\rho_m(z,T_{ws},P)$ (Section 4.2.1.1)

$\Delta P_{gel}(T_{ws})$ (Section 4.2.2)

(eqn. 4.8)

$P(z)= 0.052 \cdot \rho_m \cdot \Delta z$

$z < D$

$CSS = P(z=D) - \Delta\sigma_T(\Delta t_s)$

Fig. 4.22-Algorithm of CSS Model

4.3.1. Description of the CSS Software

A screenshot of the CSS software is shown in Fig.4.23. The locations to enter the input data, simulation options and the outputs are shown in the figure.
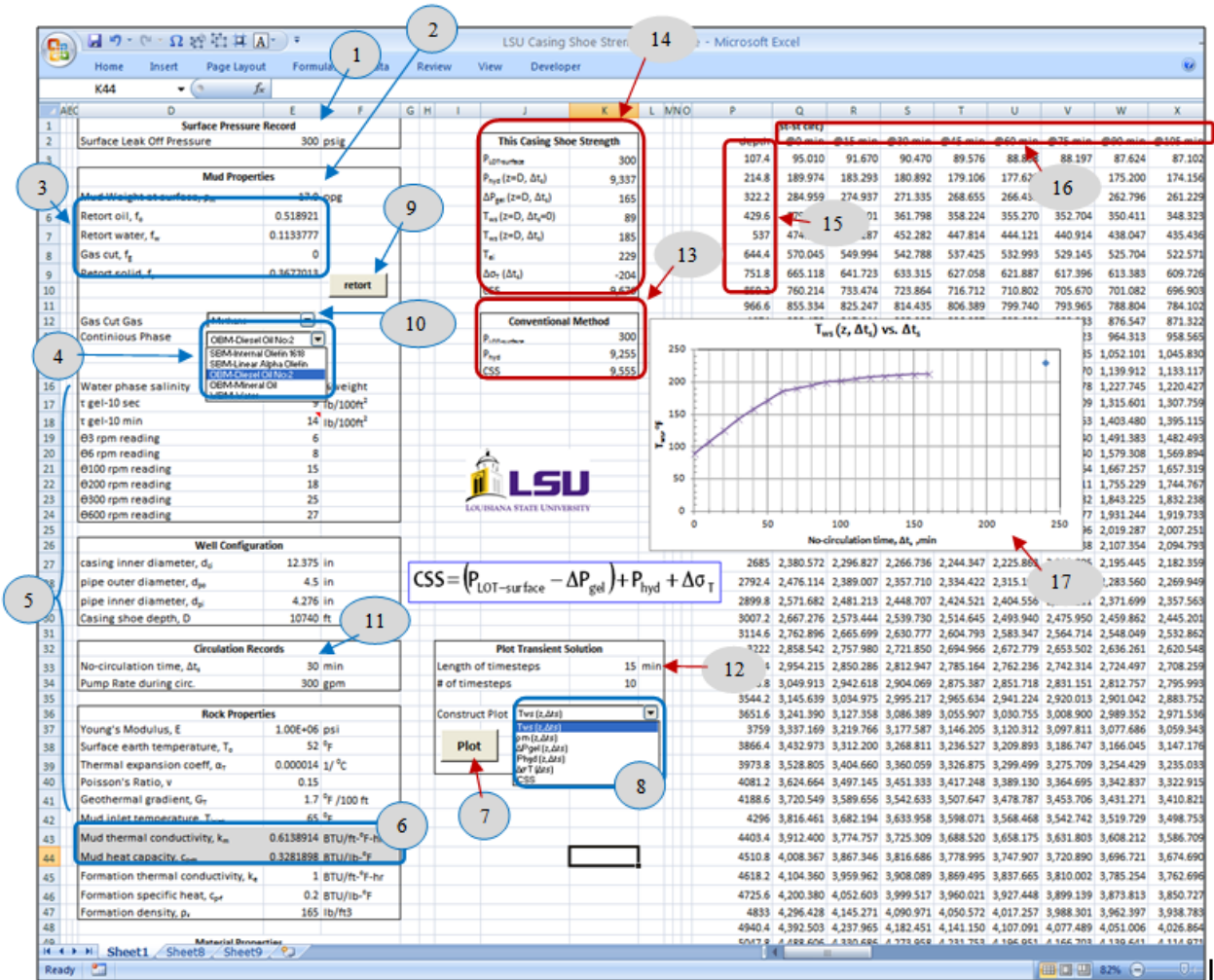
Fig.4.23-Screenshot of the CSS Software Interface

Inputs (blue)

1. Recorded surface leak off test ('Point A' in Fig. 4.2);

2. Surface mud density measurement;

3. Retort analysis section. Oil, water and solid contents are entered;

4. Selection of the continuous phase. Options are SBM (IO, LAO), OBM (Diesel oil, Mineral oil), WBM;

5. Input data of Mud rheology, well configuration, circulation records and rock properties;

6. Mud thermal conductivity, k_m, and heat capacity, $c_{p\text{-}m}$, (automatically calculated);

7. 'Plot' button. Runs the simulation for a series of Δt_s values defined by user (See item 9);

8. Selection of the component to be plotted as a function of Δt_s. Options are (T_{ws}, ρ_m, ΔP_{gel}, P_{hyd}, $\Delta\sigma_T$, CSS);

9. 'Retort' button. If retort data is not available, calculates a default composition (See page 76 for details).

10. Must be done before the simulation;

11. Selection of the type of dissolved gas. Options are methane, ethane CO_2. Required by the R_{sob} correlation (See Appendix E.2.1)

12. Non-circulating time, Δt_s ,min;

13. Outputs (red)

14. Selection of length and number of time-steps for the simulation;

15. Output of the conventional method;

16. CSS model output (calculated for single Δt_s value entered (label16));

17. Depth, ft;

18. Time-steps, min (X axis of the output plot);

19. Plot of the selected component vs. Δt_s (Y axis of the output plot);

4.3.2. Validation of CSS Model with Downhole PWD data

The CSS model has been verified with published downhole PWD data. Van Oort, E. *et al.* [47] investigated the discrepancy between the measured downhole pressures during a leak off test with pressures calculated from the cementing pump at the surface. He demonstrated the discrepancy of downhole pressures due to gellation of the mud and mud compressibility as shown in Fig. 4.24.

The test was performed on the casing shoe at 9,853' of 11-3/4" casing with 12.1 ppg mud in wellbore. Second, note that PWD tool measures the bottom-hole pressure in the wellbore, without correction for the thermally- induced rock stresses. Thus, in the CSS model validation example, thermal stress correction term has been subtracted to simulate the conditions of this test.

The input data is shown in the left column in Table 4-9. The input data in parentheses were obtained from the literature (Oort *et al*., 2007) [47] and the others were discerned from the published plots. In the right column is the comparison of the CSS's calculated conventionally, with the CSS model and measured with the PWD tool. The model provides sufficient match with the downhole measurements.
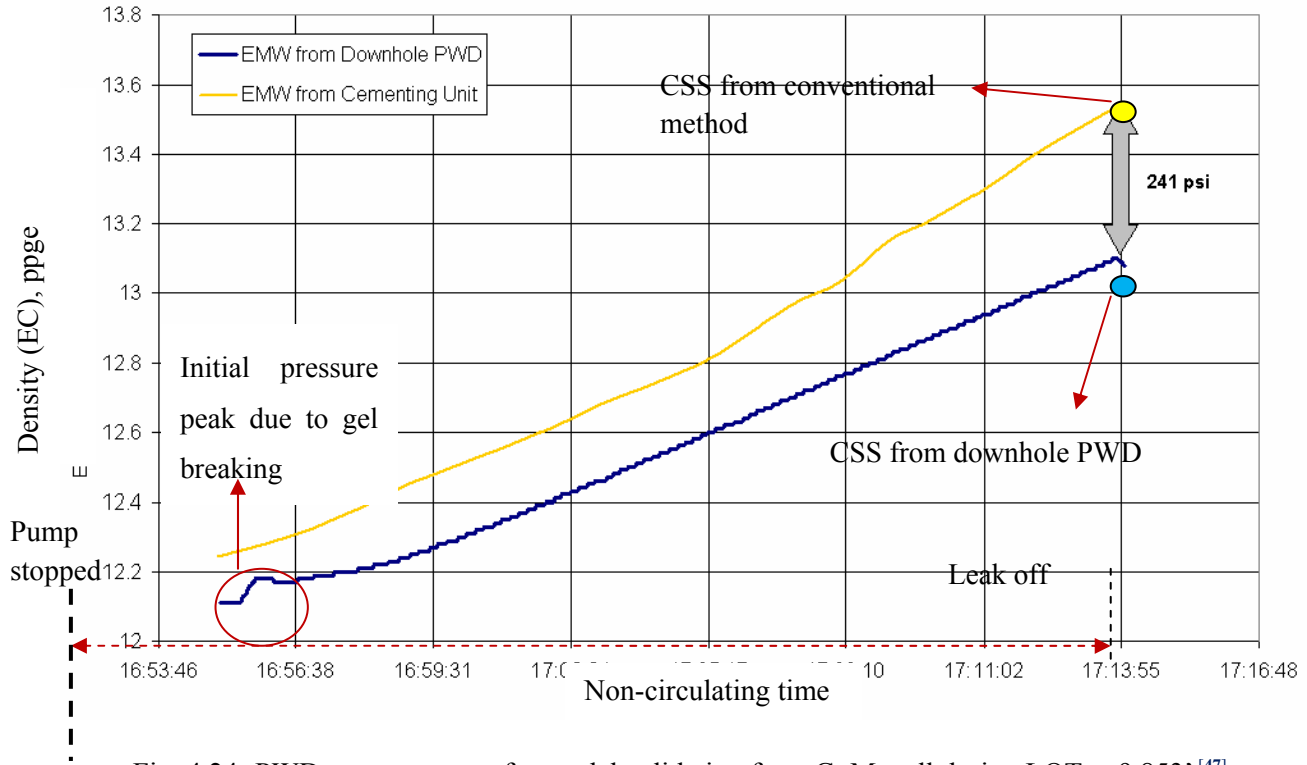
Fig. 4.24- PWD measurements for model validation from GoM well during LOT at 9,853' [47]

Table 4-9-Data summary for CSS model validation with PWD data

Inputs			CSS Model Results	
Geothermal Gradient, G_T	1.7	^{0}F /100 ft	P_{hyd} compressible	6,398 psi
Non-circulating time, Δt_s	30	min	P_{gel}	293 psig
Circulation rate, q_{pump}	1,225	gpm	T_{ws} at shoe at $\Delta t=0$ (st-st circ)	80.8 F
Inlet temperature, T_{inlet}	80	^{0}F	T_{ws} at shoe at $\Delta t=30$min	172 F
Casing ID, d_{ci}	(11.75)	in	T_{ei} earth temperature	219 F
Pipe OD, d_{po}	5	in	ΔT (T_{ws}-T_{ei})	-47
Pipe ID, d_{pi}	4.761	in	$\Delta\sigma_T$	-1,111 psi [*]
Casing Shoe Depth,D	(9,853)	ft	CSS (CSS model)	6,705 psi
τ gel-10-sec	18	lb/100ft^2		(= 13.08 ppge)
τ gel-10-min	25	lb/100ft^2	CSS (conventional)	6,953 psi
θ_3 rpm reading	8			(= 13.57 ppge)
Surface leak off pressure	(600)	psig	CSS (PWD data)	6,711 psi
Mud density at surface	(12.4)	Ppg (WBM)		(13.10 ppge)

[*]Note that $\Delta\sigma_T$ was not included in this example to simulate the conditions of the test.

4.3.3. Example of Casing Shoe Strength Prediction

The CSS software was used to calculate the casing shoe strength and evaluate its discrepancy with the conventional method. Configuration and operational data of an example well is summarized in Table 4-10. The calculations were done for multiple non-circulating times (Δt_s) to demonstrate the time effect. An example comparison of the results from CSS model and conventional method for Δt_s=30 min is shown in Table 4-11.

Table 4-10-Input parameters for example CSS prediction

Inputs (default parameters)					
Circulation rate, q_{pump}	500	gpm	Surface leak off pressure	1,465	psig
Casing ID, d_{ci}	12.375	in	Mud type	OBM	
Pipe OD, d_{po}	5	in	Mud density at surface, ρ_m	17.3	ppg
Pipe ID, d_{pi}	4.761	in	Inlet temperature, T_{inlet}	100	^0F
Casing Shoe Depth, D	14,830	ft	τ gel-10-sec	7	$lb/100ft^2$
Geothermal Gradient, G_T	1.6	^0F /100 ft	τ gel-10-min	11	$lb/100ft^2$
Young's modulus, E	$7 \cdot 10^5$	psi	θ_3 rpm reading	5	
Thermal expansion coefficient, α_T	$1.1 \cdot 10^{-5}$	$1/^0C$	f_o	0.52	
Poisson's ratio, v	0.15		f_w	0.10	
Non-circulating time, Δt_s	(30)	min	f_s	0.38	

Table 4-11-Comparison of CSS model and conventional method at Δt_s=30 min

Parameter	CSS Model	
Surface leak off pressure, psi	$P_{LOT\text{-}surface}$	1,465
Hydrostatic pressure of compressible mud, psi	P_{hyd}	13,972
Pressure loss due gellation, psi	ΔP_{gel}	181
S-S circulating bottom-hole temperature, ^oF	$T_{ws}(\Delta t_s=0)$	136
Static bottom-hole temperature at Δt_s, ^oF	T_{ws}	204
Geothermal temperature the casing shoe, ^oF	T_{ei}	317
Thermal stress correction, psi	$\Delta\sigma_T$	-1,138
Bottom-hole pressure, psi	P_{bh}	15,257
Casing shoe strength, psi	CSS	16,395
Parameter	Conventional Method	
Surface leak off pressure, psi	$P_{LOT\text{-}surface}$	1,465
Hydrostatic pressure, psi	P_{hyd}	13,341
Casing shoe strength, psi	CSS	14,806

The value of CSS calculated by conventional method (14,806 psi) is 548 psi (10.6%) lesser than that from the CSS model (16,395 psi). The discrepancy is a result of the overall contributions of the factors described in section 4.2: mud compressibility [P_{hyd} (model) - P_{hyd} (conventional)], gellation (ΔP_{gel}) and thermally induced rock stresses ($\Delta \sigma_T$).

4.3.4. Analysis of Contributing Factors

Fig. 4.25 shows casing shoe strength vs. Δt_s calculated by conventional method and the CSS model. Clearly, the conventional method underestimates CSS. Thermal effects dominate the trend and the error reduces with longer non-circulating time. It means, conventional CSS analysis requires delaying with the leak off test. However, from an operation cost standpoint this would not be convenient. A better option is to use the CSS model.
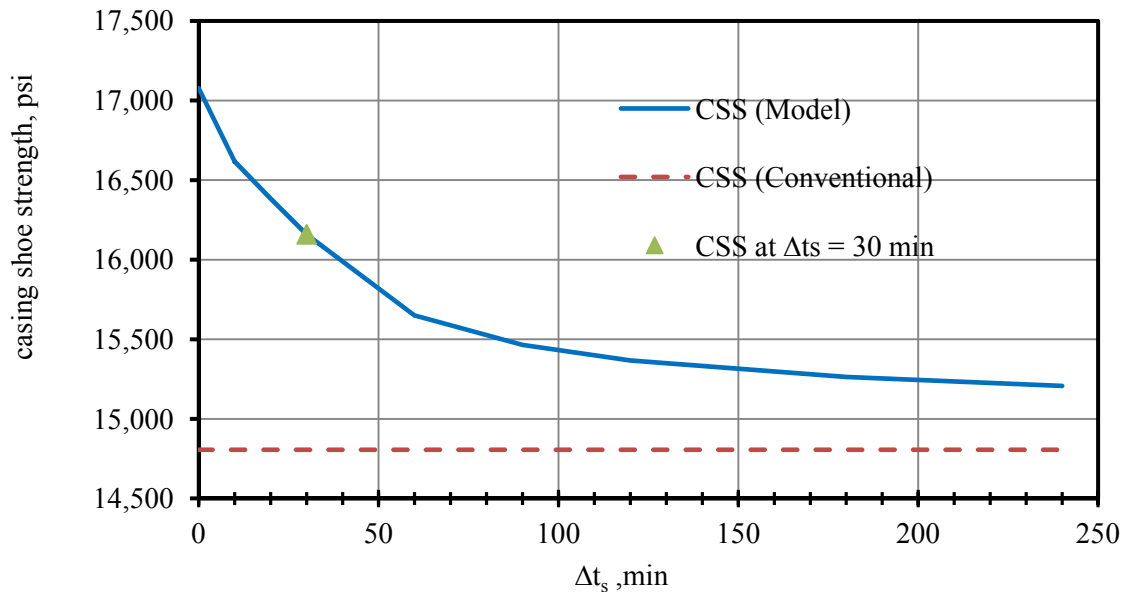
Fig. 4.25-CSS as a function of Δt_s: model vs. conventional

The discrepancy, discussed above strongly depends on mud temperature in the well T_{ws}. T_{ws} is a function of Δt_s, as discussed in section 4.2.4. As the well is left static, mud temperature increases due the heat exchange with the well-bore and approaches the geothermal gradient (T_{ei}). Fig. 4.26 shows temperature build-up as a function of Δt_s. Since the build-up of mud temperature is a function of heat exchange (See section 4.2.4.3), the temperature increase is relatively rapid in early time.
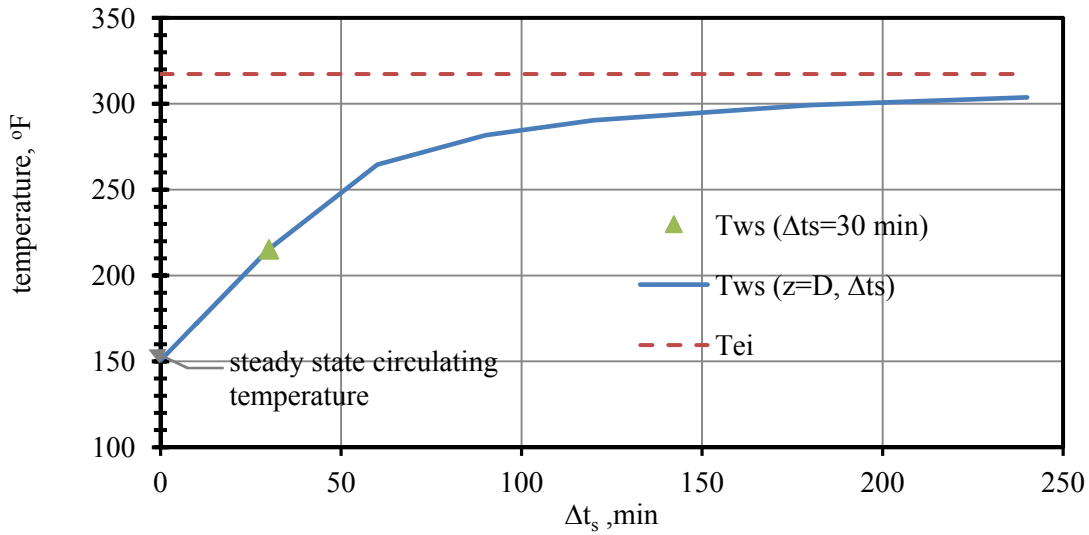
Fig. 4.26-Temperature build-up during non-circulating time

Hydrostatic pressure calculated at Δt_s =30 min by the CSS model (13,972 psi) was 631 psi (4.7%) greater than it was from the conventional method (13,341). Conventional method calculates the mud hydrostatic pressure assuming constant mud density at any depth and equal to its surface density. However, in this example 52% of the mud is diesel oil, which is highly compressible, thus mud density is greater at depth. Therefore, disregarding mud compressibility results in underestimation of the hydrostatic pressure at the casing shoe. Fig. 4.27 shows hydrostatic pressure as a function of Δt_s calculated by conventional method and the CSS model. There is a considerable 600 psi difference that does not change with time.
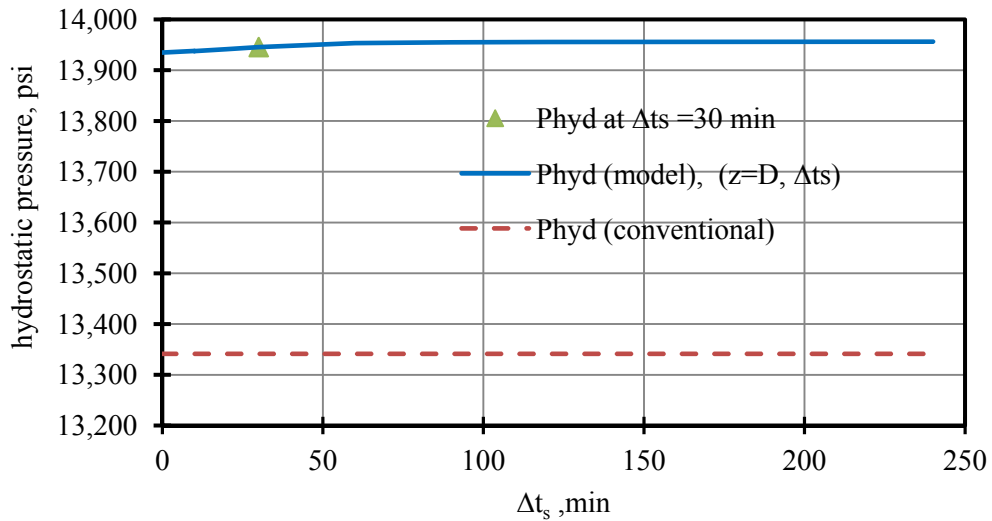
Fig. 4.27-Hydrostatic pressure as a function of Δt_s

In the conventional method, the surface leak off pressure ($P_{LOT-surface}$) is assumed to be transmitted to the casing shoe without any pressure losses. However, mud gellation resists the transmission. At Δt_s=30 min, 12% of the surface pressure (181 psig) is lost due mud gellation. Therefore, ignoring the gellation effect overestimates the bottom-hole pressure. Fig. 4.28 shows pressure loss due mud gellation as a function of Δt_s. Note that ΔP_{gel} is also a function of T_{ws}, which has reducing effect on gels given by eqn.4.13.

Since the two factors-mud compressibility and gellation- have opposite effects on the bottom-hole pressure (P_{bh}). Their cumulative effect depends on mud type and thixotropy. For example WBM is less compressible than OBM, thus compressibility would have less effect on the P_{bh} miscalculation.
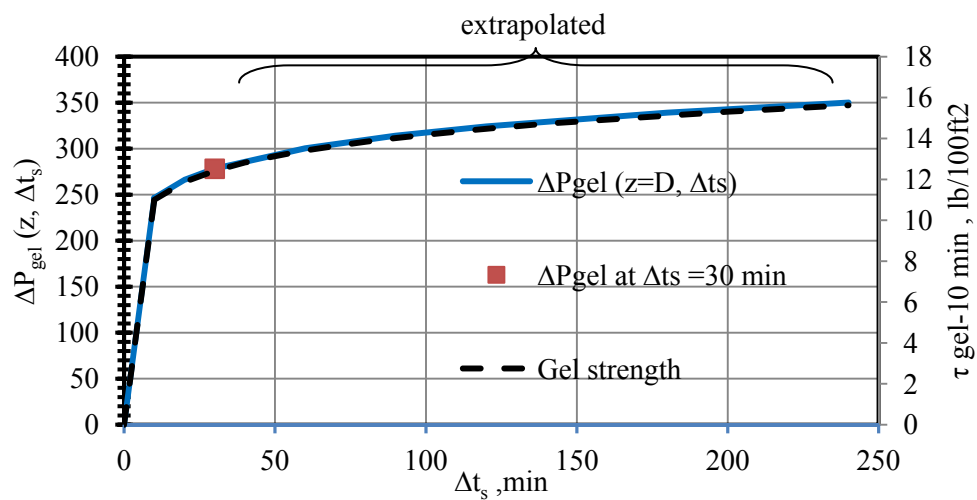
Fig. 4.28-Pressure loss due mud gellation as a function of Δt_s

The same example was repeated for the same density WBM at Δt_s =30 min giving a 598 psig difference comparing to 631 psi for OBM. Moreover, a mud with progressive gels would yield higher pressure losses, causing less of the surface pressure being transmitted to the casing shoe. (The same example was repeated for gel strengths $\tau_{gel-10-sec}$= 15 and $\tau_{gel-10-min}$=35 lb/100ft^2, resulting and Δt_s =30 min, 639 psig pressure loss as compared to 181 psig for OBM.

The conventional method considers the bottom-hole pressure at which the first indication of well-bore failure is observed at the surface as the "casing shoe strength". Such an approach 'measures' the CSS at the particular non-circulating time the test was performed and disregards the strengthening of the wellbore with temperature. If the mud is cooler than the rock, the rock fails at lower wellbore pressures, as discussed in section 4.2.3. In fact, the 'real' CSS is the 'undisturbed' CSS, $i.e.$ considering equilibrium with the geothermal gradient. Therefore, the last term ($\Delta \sigma_T$) in eqn.4.8 can be considered a correction accounting for thermal stresses.

Fig. 4.29 shows thermal stresses ($\Delta\sigma_T$) as a function of Δt_s. Note that $\Delta\sigma_T$ has negative sign because ΔT in eqn.4.23 is negative, *i.e.* mud temperature is smaller than that of the rock; and its magnitude decreases with Δt_s (heat exchange decreases with Δt_s,) *i.e.* mud temperature approaches the geothermal gradient. $\Delta\sigma_T$ has greater magnitude in early times, because the mud in the well is still cool, making the rock easier to fracture. Therefore in early times, CSS is underestimated more, *i.e.* more error is made.
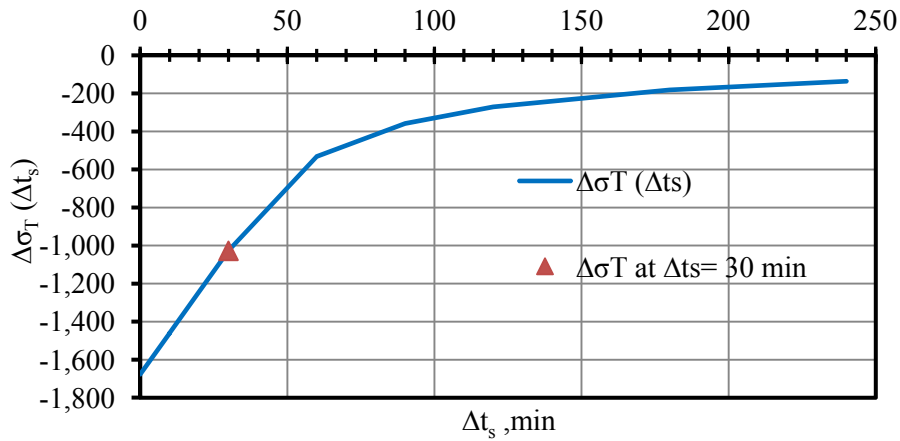
Fig. 4.29-Thermal stresses as a function of Δt_s

The factors, discussed above (mud compressibility, gellation and thermal stresses) are shown in Fig. 4.30 as a function of Δt_s. The plots show relative contributions of the factors to the difference between CSS's calculated by the conventional method and the CSS model. Note that the difference reduces with time (Fig. 4.25) so the contribution of thermal stress still dominates the effect in absolute terms.
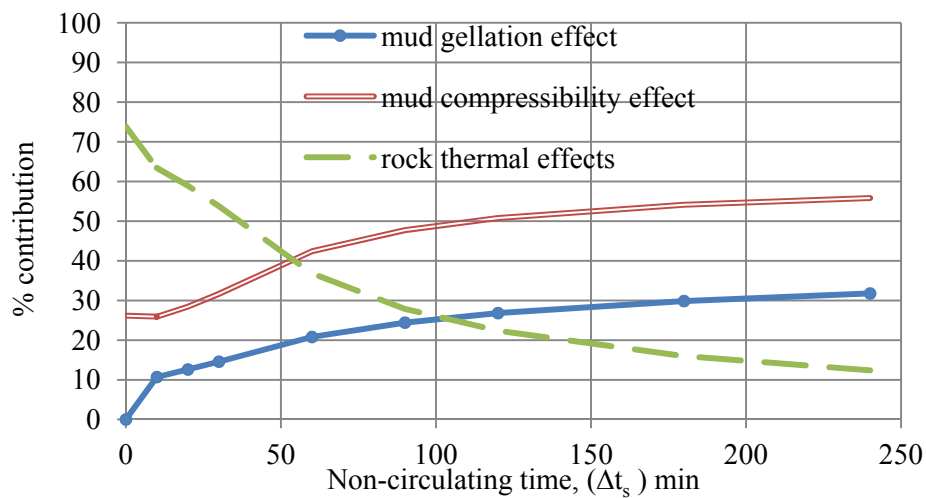
Fig. 4.30-Percent contributions of the factors to discrepancy in CSS calculation

As discussed in section 4.2.4.3, OBM heats up faster than WBM primarily because the overall heat capacity of OBM is smaller than that of WBM. To demonstrate the effect of mud type, CSS of the same well configuration is calculated as a function of Δt_s for the same density OBM and WBM, as shown in Fig. 4.31.
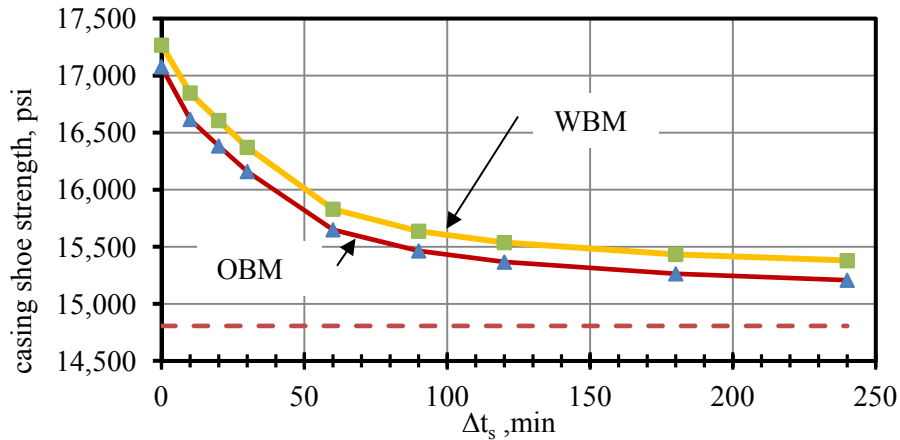
Fig. 4.31-Comparison of CSS calculated assuming OBM and WBM

The effect of progressive gels is shown in Fig. 4.32. Using the same well data and two values of CSS gel strengths: $\tau_{gel\text{-}10\text{-}sec}$= 12 and $\tau_{gel\text{-}10\text{-}min}$=35 lb/100ft^2. Note that at early Δt_s, thermal effects cause underestimation of the CSS, and at late Δt_s, thermal effects become less significant and ΔP_{gel} begins to dominate the discrepancy, resulting in overestimation of the CSS by the conventional method.
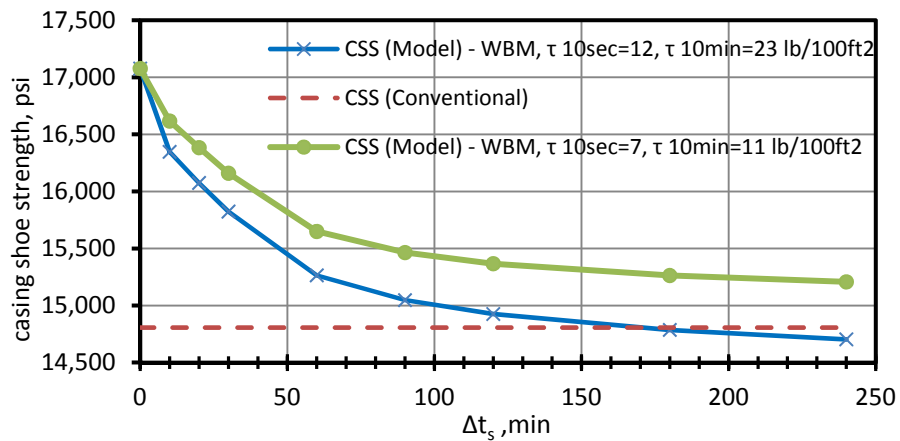
Fig. 4.32-Comparison of the effect of flat vs. progressive gels on CSS

Based on the analysis, above, the following conclusions can be made:

- CSS is almost always underestimated by the conventional method (eqn.4.7), except for the case of

late LOT and mud with progressive gels;

- CSS may be overestimated by conventional method only if non-circulating time is long <u>and</u> the mud has progressive gel strength;

- Mud thixtropy causes overestimation of CSS, whereas mud compressibility and rock thermal effects cause its underestimation;

- There are opposite effects of mud compressibility and thixotropy on bottom-hole pressure transmission.

- The effect of mud compressibility on the discrepancy is partially canceled out by the reverse effect of thixotropy;

- Using the MWD tool during LOT would improve CSS interpretation but still requires a correction for thermal stresses;

- Delaying LOT would improve CSS determination but is not practical so the model is needed.

5. SUBSURFACE WELL INTEGRITY FAILURE DUE SUSTAINED CASING PRESSURE

As discussed in section 2, well's casing shoe may be weaker subsurface pressure containment barrier compared to the well-head. (In Table 2-1 compared the critical conditions for surface vs. subsurface well integrity failures.) In the well with SCP the well-head pressure (P_{csg}) may increase over time due to deterioration of the cement sheath and gas channeling. This pressure is transmitted to the casing shoe through the mud column in the annulus (SCP_d). If SCP_d exceed the maximum pressure that the casing shoe could withstand (CSS), subsurface failure occurs. Critical condition is,

$$SCP_d > CSS/SF \qquad \text{5.1}$$

Model for calculation of CSS is presented in section 0. Prediction of the subsurface well integrity failure scenario requires also computation of all factors contributing to SCP_d.

5.1. Sustained Casing Pressure Transmission Downhole

It is common practice to calculate downhole pressure assuming that the entire surface pressure (P_{csg}) is transmitted to the bottom-hole, and the estimated mud density is homogeneously distributed along the annulus, as given in eqn.2.2. However, in section 4.2.2 it was shown that mud thixotropy opposes the pressure transmission so the surface pressure is partially lost. Also, in section 4.2.1 it was shown that ignoring mud compressibility causes underestimation of the hydrostatic pressure since mud density in the annulus is greater than its value measured at the surface. Therefore, SCP_d is given as,

$$SCP_d = P_{csg} - \varDelta P_{gel} + P_{hyd} \qquad \text{5.2}$$

The mathematical models presented in sections 4.2.2.3 and 4.2.1.1 employ calculations of the mud thixotrophic and compressibility effects, respectively. However, the annular SCP system is different to that in the leak off testing. Firstly, the annular fluid is shorter because the top of cement is above the casing shoe depth, and there is free liquid level below surface. Secondly, the temperature profile follows the geothermal gradient. Thirdly, the time periods regarding development of thixotropy are orders of magnitude greater compared to the non-circulating time in the leak off test. Thus, the long-time gellation effects must be considered.

In most cases, the annular fluid is the drilling mud that was left after cementing operation. Bull-heading lubrication of heavy completion brines to remove SCP is a common practice. However, it is not

recommended since it might increases SCP_d, endangering the subsurface integrity of the well [1]. In this study, the annular fluid is assumed the mud that was used during the drilling operation.

During cementing if the casing is not cemented to above the casing shoe, an open hole section is left. In this case, interaction of the mud with the pore fluids reduce the mud weight in time. Higher formation permeability or higher osmotic pressure difference results in faster exchange between the formation fluids and the mud [43]. In this study, the top of cement is assumed at above the depth casing shoe.

Mud aging is also a common reason of late mud density change. Mud aging may cause solid sag. Solids are suspended in a stagnant mud by gel strength. Oil and synthetic base mud gel strength is provided by emulsion of the brine in the continuous phase and addition of organophilic clays, whereas long chain polymers and hydrophilic clays provide the gels in water base mud. Gel strength is subject to changes in time due thermal degradation. The change in mud properties in long time is called aging. Hence, mud type plays crucial role in the aging process. Several studies have been made to investigate mud aging.

Annis [101] studied aging of bentonite muds with time and temperature up to 300 ^{o}F and observed increase in gels due flocculation. Mohammed S.A. [102] made laboratory experiments with water base mud using Fann-70 HTHP viscometer and dynamic roller oven to investigate mud aging at temperature of 490 ^{o}F, pressure of 10,000 psig and aging time of 30 days. He observed that gel strength at a given temperature exponentially increased with aging time. He also observed that 10 minute gel strengths doubled in 30 days aging time, as shown in Fig. 5.1.

Shokoya *et al.* [103] studied corrosiveness and rheology of water base mud under simulated downhole conditions using Fann-70 rheometer, flow loop and dynamic roller oven. They observed increase in effective and plastic viscosities with aging time. Exner [104] carried out investigation on mud aging and concluded that viscosity of most muds decrease with aging time, but gel strengths increased due flocullation. Makinde *et al.* [105] made experiments with aged 22.5 ppb bentonite freshwater base mud using Fann-800 HPHT rheometer to study mud aging. Fig. 5.2 shows their gel strength measurements at various aging times.

Pavel [106] studied high temperature mud aging and observed excessive gellation due bentonite flocculation, turning some samples into gel plugs. He concluded that gellation increases with temperature until a critical temperature above which the mud losses its thermal stability. Charlie [107] discussed increasing thermal stability of water base mud by adding oxygen scavengers and glycol based anti oxidants.
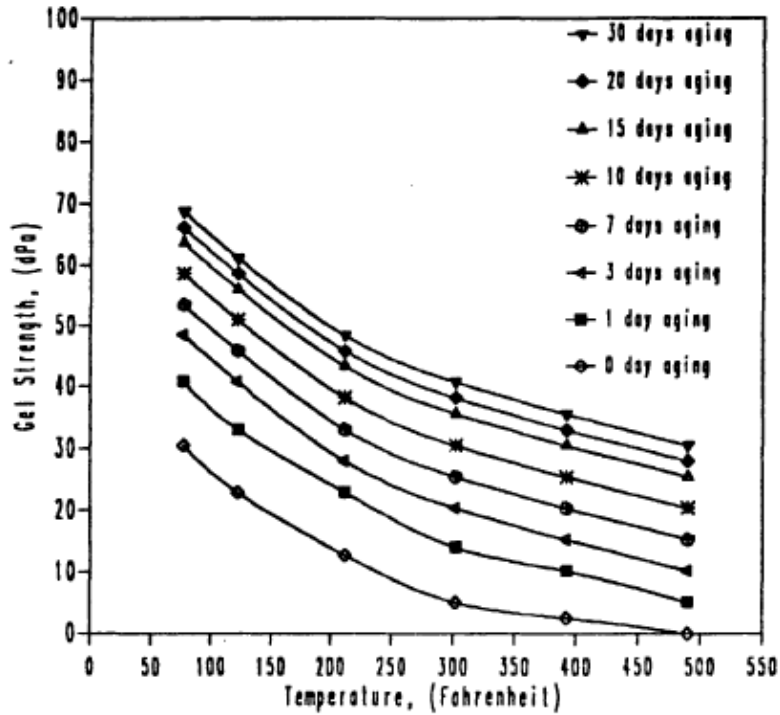
Fig. 5.1-10 minute gel strengths vs. time and temperature at 10,000 psig [102]
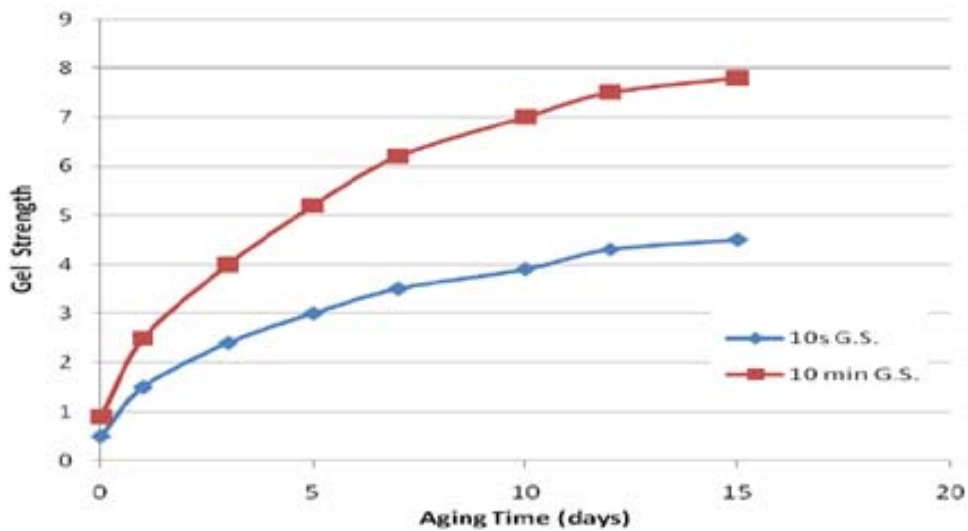
Fig. 5.2-Gel strength of freshwater-bentonite mud as a function of aging time [105]

Wysocki and Bielewicz et al. [108] studied the effect of bacterial degradation of polymers and suggested addition of biocide for prevention. Methven et al. [109] studied thermal stability of oil base muds and observed that they preserve their thermal stability up to noticeably higher temperatures than of water base muds. The following conclusions can be made based on the literature survey presented above:

90

1. Mud preserves its stability and its gel strength increases with increasing aging time as soon as it is not exposed to high temperatures exceeding its thermal limitation;

2. Presently, there are no application models quantitatively linking gel strengths to aging time since mud aging critically depends on the type and thermal stability of mud.

In this work, SCP_d model has been developed by considering mud compressibility and thixotropy as shown in eqn.5.2. Mud compressibility is considered in the hydrostatic pressure calculations of hydrostatic pressure using the mud density model presented in section 4.2.1.1. Due to the lack of quantitative models of long term mud gellation, thixotrophic effects are simulated by extrapolation of the model presented in section 4.2.2.3. Hydrostatic pressure of the gas column above the mud and inside the cement sheath is ignored. Gas dissolution in the mud is also ignored.

5.2.   Analysis of Critical Conditions for Casing Shoe Failure

The SCP_d model has been used to study casing shoe breaching of the B annulus in Study Well. Study Well is described in Fig. 3.22. For the purpose of the study, control parameters have been hypothetically modified while preserving other parameters and the well configuration. The configuration of the Study Well is given in Table 5-1.

Table 5-1-Parameters of the example well

Wellhead pressure, P_{csg}	4,168	psig
Cement sheath length, L_c	1,400	ft
Mud column length, L_m	9,900	ft
Annulus geometry, d_{ci}, d_{to}	12.375 x 9.625	in
Depth to top of cement, D_{TOC}	10,385	in
Mud density, ρ_m	14.0	ppg
Casing shoe strength, CSS[1]	11,120	psi

The values of control parameters, density, gel strength, and length of the mud column are given in Table 5-2. Hydrostatic pressure in the SCP_d model is calculated assuming oil base mud in the annulus, and the mud composition is described in section 0. Pressure loss due gellation (ΔP_{gel}) is calculated using 10-second and 10-minute gel strength values of 7 and 70 lb/100ft^2 at 10 hours.

---

[1] CSS was calculated by the model presented in section 0.

These values represent progressive gel strength, complacent with the observations made by several authors [101], [102]. The reservoir pressure was assumed unknown throughout the analysis. The comparison of the results obtained from SCP$_d$ model and the conventional method is shown in Table 5-2.

Table 5-2-Components of SCP$_d$ calculated by conventional method and SCP$_d$ model

Parameter	Conventional	SCP$_d$ model
P$_{hyd}$, psig	7,207	7,550
ΔP$_{gel}$ psi	0	2,860
SCP$_d$ psi	11,375	8,858

The results show that the model gives SCP$_d$ value much smaller than conventional computation. Pressure reduction of 2,860 psig was due mud thixotropy, and pressure increase 343 psi due compressibility. Therefore, the mud compressibility and thixotropy counteract. Compared to the CSS, the conventional method gives SCP$_d$ value calculated 256 psi greater then CSS. However the model yields SCP$_d$ value 2,262 psi smaller than CSS. Consequently, disregarding the mud compressibility and thixotropy effects would result in overestimation of the SCP$_d$ and a potentially false conclusion that the casing shoe failed.

A theoretical study is performed by hypothetically changing the control parameters, L$_m$, ρ_m, or $\tau_{gel-10min}$, while keeping all other properties in Table 5-1 constant. Table 5-3 is a matrix of the parameters used in the theoretical experiments with the SCP$_d$ model.

Table 5-3-Matrix of experiments with the SCP$_d$ model

Parameter	Experiment **A**	Experiment **B**	Experiment **C**
L$_m$,ft	9,900	9,900	100-10,300
$\tau_{gel-10min}$,lb/100ft^2	8 to 120	20	20
ρ_m ,ppg	14	9 to 16	14

In experiment **A**, the 10 minute gel strength ($\tau_{gel-10min}$) was varied from that to very progressive gels. The thixotropy effect model (See section 4.2.2.3) was extrapolated to calculate gel strength after 10-hour aging time, assuming $\tau_{gel-10sec}$= 7 lb/100ft^2. The 10-hour time represents long-term time effect since there is very small change of gel strength for longer times. The resulting values of SCP$_d$ are plotted in Fig. 5.3.
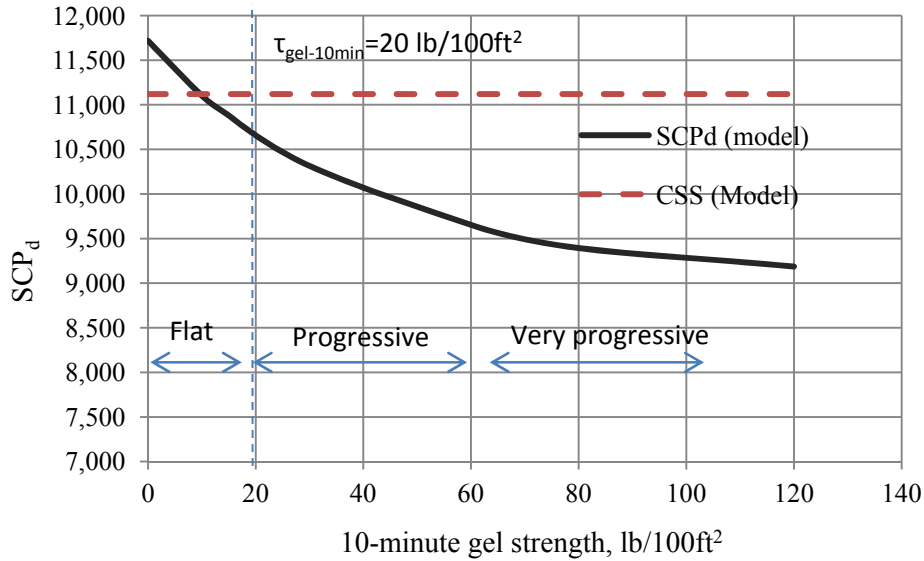
Fig. 5.3-Experiment **A** -Effect of gel strength on SCP_d at 10 hr aging time

It was observed that P_{csg} is poorly transmitted downhole for high values of gel strength. Also, for "flat" gels, (10-min gel strength values, smaller than 10 $lb/100ft^2$), SCP_d is greater than the CSS, since mud compressibility effect prevails resulting in greater hydrostatic pressure. It was also observed that significant part of the surface pressure is not transmitted downhole due mud thixotophy, even for mud with flat gels. Experiment **B** demonstrates the effect of mud density variation on SCP_d. In the experiment the SCP_d model was used to calculate downhole pressures for surface mud densities ranging from 9 to 16 ppg as shown in Fig. 5.4.
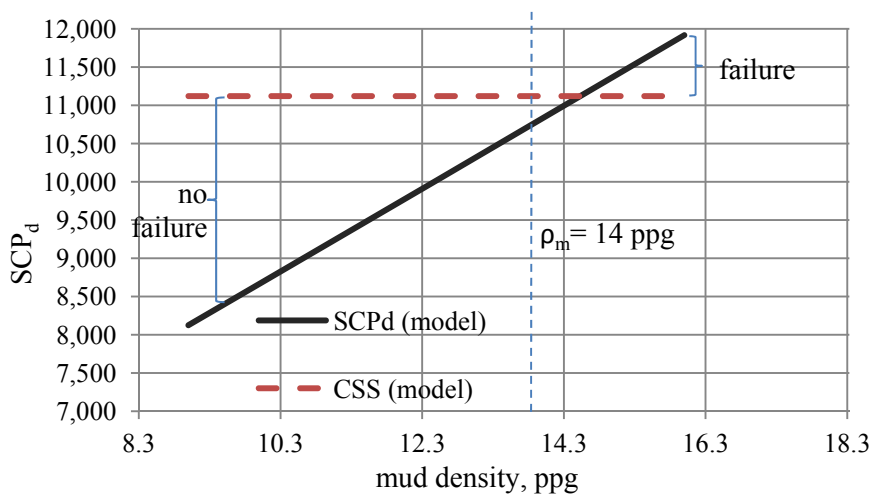
Fig. 5.4-Experiment **B**- Effect of mud density on SCP_d

It is clear that for ρ_m greater than 14.5 ppg, SCP_d would exceed CSS, resulting in subsurface failure. The actual mud density in the study well was 14 ppg so there would be no potential failure for the observed SCP, 4,168 psi. Experiment **C** demonstrates the effect of mud column length, L_m, that was changed from 100 to 10,300 ft.
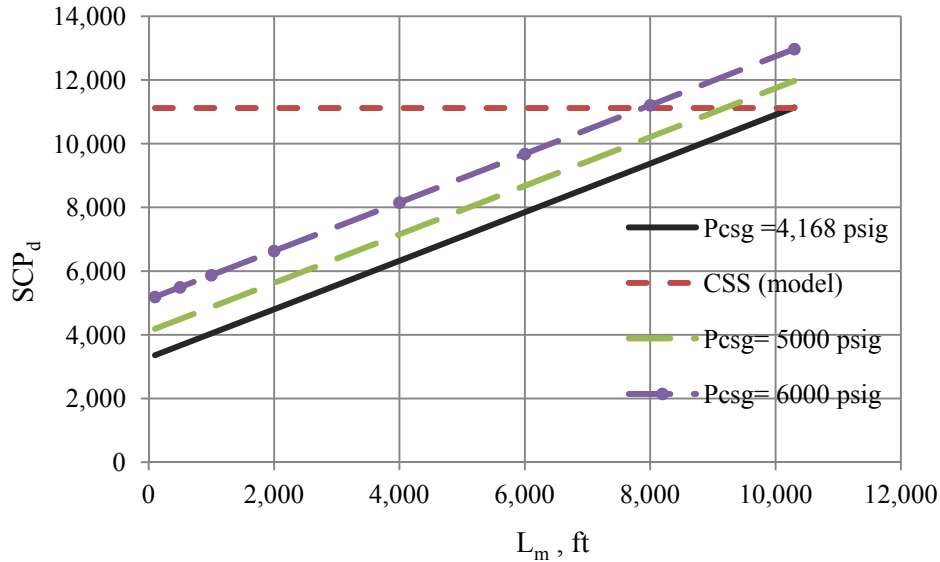
Fig. 5.5-Experiment **C**- Effect of of mud column length on SCP_d

The maximum L_m value is 10,385 ft since this is the depth to the top of cement. Thus, it was observed for P_{csg}= 4,168 psi filling the annulus up with 14 ppg mud would not cause casing shoe failure. However, for higher values of P_{csg}, pumping more mud to the annulus may breach the shoe.

Based on the example presented above, the following conclusions can be made:

1. Conventional method for prediction of casing shoe breaching in SCP well neglects mud compressibility and thixotropy gives mis-estimation of the critical value of SCP-critical. Considering mud compressibility decreases SCP-critical while inclusion of mud thixotropy increases SCP-critical. Typically the effect of mud gellation would prevail thus causing underestimation of SCP-critical with conventional method.

2. SCP_d increase with increasing mud density and column length, and decrease with mud thixotropy. For the same value of P_{csg} the maximum SCP_d is created when the annulus is filled up with high density mud having flat gels. The smallest SCP_d is created by a short column of low density mud with progressive gels.

3. As long as the mud preserves its thermal stability over time, the gel structure prevents the transmission of surface pressure to the casing shoe, and subsurface failure is prevented otherwise, mud thermal stability deteriorates, the gel strength is lost, and mud solids sagging reduces mud density. In the both cases above, mud aging would reduce SCP_d, thus reducing the risk of subsurface failure;

4. Approximate values of mud density and free level of liquid in the annulus are either readily available or obtained from SCP well testing (Xu. *et al,* 2000. [11]). However, mud thixotropy remains uncertain and gel strength may take a wide range of values depending on the mud composition and aging conditions.

6. PROBABILISTIC ASSESSMENT OF SUBSURFACE FAILURE DUE SCP

As discussed in section above, if the downhole pressure due sustained casing pressure (SCP_d) exceeds the casing shoe strength (CSS), subsurface failure occurs. The comparison of the critical conditions for the surface vs. subsurface failure considered values of SCP_d and CSS as deterministic magnitudes. However, these values are merely most likely estimates of probabilistic distributions, resulting from uncertainties of their controlling parameters. Consequently, the critical conditions of well integrity failure require a probabilistic approach to determine probability (or risk) of the failure occurrence.

6.1. Uncertainty Analysis Method

Quantitative risk assessment (QRA) provides powerful statistical technique to evaluate CSS uncertainty associated with the control parameters and their effect. Moos and Peska *et al.* [110] conducted comprehensive wellbore stability analysis using QRA. They calculated the probability density distribution of the required the wellbore collapse and lost circulation pressures.

Their work is an example of using QRA for drilling geomechanics design. Shown in Fig. 6.1 is the input probability density distributions for the mud density window, each defined by a minimum, maximum and mean value, and the output distribution of mud density associated with its input distributions - in-situ stresses, pore pressure and rock strength.

In the QRA terminology, uncertain variables are stochastic, while certain variables (with zero confidence interval) are deterministic. Statistical model relates dependent variables to independent variables. An experiment is a single run of the model based on a scenario, and a simulation cycle involves large number of experiments with the model parameters selected randomly from the 'pool' of their values. A 'bell curve' having some degree of "skewness" is generated as a result of the simulations, resulting in frequency or probability density function of the dependent variable.

The mean value of the bell-curve is the expected value of the dependent variable, while the confidence interval gives the upper and lower limits of the dispersion that measures uncertainty. Finally, an 'analysis' is the series of simulation cycles to evaluate the controlling parameters by computing sensitivity of the model to its parameters. In this section, the CSS and SCP_d models (from Sections 4.3 and 5.1) –describing the casing shoe-rock system, are analyzed using the QRA method.
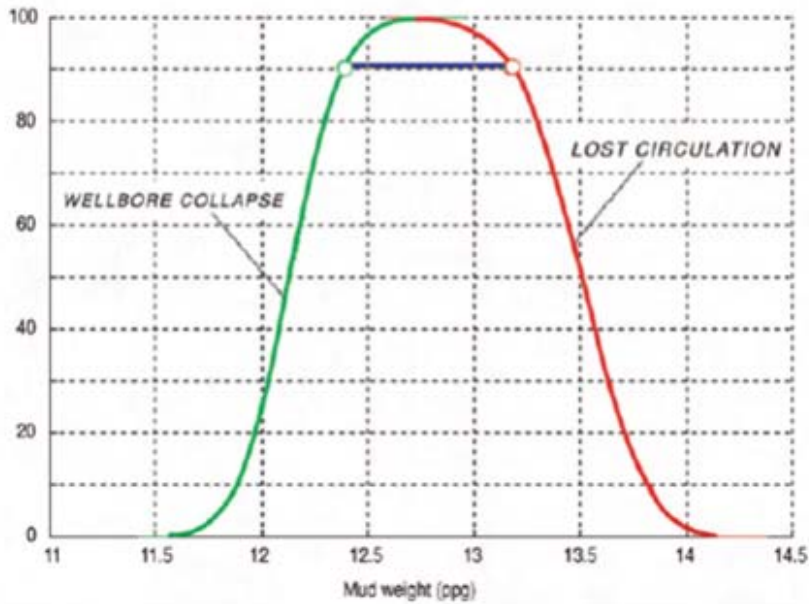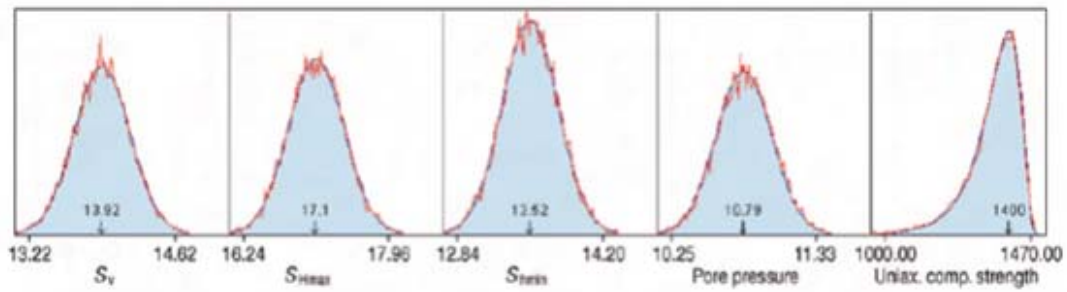
Fig. 6.1-Example application of QRA in geomechanics: Probability densities of input parameters defined by min-max and means (top), statistical analysis of wellbore stability for associated inputs (bottom) [110]

The QRA approach employs the Monte Carlo technique for the simulation experiments. The technique is used to simulate the uncertainty of the model input parameters shown in Table 6-1 and Table 6-8, for CSS and SCP_d models, respectively. Then, the output distribution resulting from each simulation cycle is matched with the best fit PDF plot. The best match is made by minimizing the root-mean square error (RMSErr), for the CSS distribution given as,

$$RMSErr = \sqrt{\frac{1}{n}\sum_{i=1}^{n}\left(f(CSS_i,\alpha) - CSS_i\right)^2}$$

6.1

where CSS_i is the casing shoe strength calculated by the model for a combination of input parameters, $f(CSS_i,\alpha)$ is the theoretical distribution function with one parameter, α, and n is the population size. The

value of α that minimizes the RMSErr is called the least squares fit. For normal distribution, for example, the parameter α is the standard deviation, σ.

6.2. Probabilistic Assessment of Casing Shoe Strength

The CSS mathematical model described in section 4 calculates casing shoe strength deterministically for known values of the system parameters: mud compressibility, thixtropy, well temperature profile, and thermal properties of mud and rock. However, the parameters' values are merely estimated so the resultant casing shoe strength is an estimate, too. Moreover, it is important to know which parameter mostly controls the risk of failure.

6.2.1. Probabilistic Formulation of CSS Uncertainty

Probabilistic formulation of CSS considers the CSS model parameters as statistical terms as,

$$\overline{E}(CSS) = \overline{E}\left[\left(P_{LOT-surface} - \Delta P_{gel}\right) + P_{hyd} - \Delta\sigma_T\right] \qquad 6.2$$

where, $\overline{E}$, is the expected value of CSS as a function of expected values of all input parameters in the deterministic model. The casing shoe strength calculation yields a statistical distribution resulting from the uncertain parameters - each having its own distributions. Thus, each term in eqn.6.2 can be expanded as follows.

$$\overline{E}(\Delta P_{gel}) = f_1\left[\overline{E}(\tau_{10\ min}), \overline{E}(\Delta t_s), \overline{E}(T_{ws})\right] \qquad 6.3$$

where,

$$\overline{E}(T_{ws}) = f_2\left[\overline{E}(\Delta t_s), \overline{E}(q_{pump}), \overline{E}(T_{inlet}), \overline{E}(T_o), \overline{E}(G_T)\right] \qquad 6.4$$

$$\overline{E}(P_{hyd}) = f_3\left[\overline{E}(T_{ws})\right] \qquad 6.5$$

$$\overline{E}(\Delta\sigma_T) = f_4\left[\overline{E}(E), \overline{E}(\alpha_T), \overline{E}(v), \overline{E}(T_{ws})\right] \qquad 6.6$$

where f_1, f_2, f_3, f_4 stand for the computation methodologies described in sections 4.2.2.3, 4.2.4.3, 4.2.1.1 and 4.2.3, respectively.

Minimum, maximum and mean values, and probability densities of the CSS model parameters must be determined in order to generate the population of the terms in equations 6.3 through 6.6. Distributed parameters of the casing shoe strength model are listed in Table 6-1. Note that availability of real-time measurement of downhole pressure-temperature data would significantly improve determination of the downhole parameters, and the casing shoe strength calculation. However, most wells are drilled without downhole data monitoring.

Table 6-1-Summary of distributed parameters of CSS Model

Non-circulating time, Δt_s
Circulation rate before the LOT, q_{pump}
Mud inlet temperature, T_{inlet}
Surface earth temperature, T_0
Geothermal gradient, G_T
Fann-35 gel measurements, $\tau_{10sec}/\tau_{10min}$
Young's modulus, $\mathbf{E}$
Poisson's ratio, v
Rock thermal expansion coefficient, α_T

Remaining parameters of the model; hole geometry (d_{ci}, d_{po}), recorded surface pressure ($P_{leakoff-surface}$), surface mud density ($\rho_{m-surface}$) are deterministically entered to the simulation, *i.e.* these recorded values are assumed to have no uncertainty. Operation data (q_{pump}, T_{inlet}, $\tau_{10sec}/\tau_{10min}$) are obtained from the drilling and mud reports.

Non-circulating time (Δt_s) is a distributed parameter because it is often not reported. It controls wellbore temperature that is the significant parameter since all terms of the CSS model either directly or indirectly depends on temperature. Geophysical data (T_0, G_T, $\mathbf{E}$, v, α_T) of the rock and mud properties are not available from the operation records, but can be estimated from the offset geophysical data. Mud parameters can be calculated from the mud composition. Bottom-hole temperature (T_{ws}) is not direct input, but it is calculated from the model.

A single QRA simulation algorithm is summarized Fig. 6.2. A software, @Risk for students has been used to perform the QRA simulations. @Risk is a commercial statistical analysis software package which is Visual Basic for Applications (VBA) compatible and widely used by the industry.

Define well configuration, mud type, formation and operational data (not distributed).

Assign min-max and mean values to distributed parameters in Table 6-1.

Use @Risk to generate distributions (Table 6-3, for example)

Randomly set distributed parameters values using @Risk.

Run CSS Model using VBA

Run Monte Carlo Iterations using @Risk

Save output in @Risk memory

Run @Risk to compute PDF of CSS output population

Fig. 6.2-Algorithm of single QRA simulation cycle

6.2.1.1. Uncertainty of CSS Model Parameters

Uncertainty in the distributed parameters results from measurement errors and missing data. Accuracy of the measurements may be affected by the testing conditions, or the time (temperature) delays of the measurements. Real time data recording in the recent years enabled direct monitoring of the well operations during and after the operation. For semi-submersible platforms, it has become a standard to record mud logging data and deliver to the central office for secondary monitoring [71]. However, for a majority of the onshore or jack-up operations, operation logs are not recorded in an automatic manner. Furthermore, old wells lack operational data, such as pump rate changes, pump startup-shut down times, mud properties and wellbore condition.

Circulation rate (q_{pump}) prior to leak off test is often not reported. However, it can be estimated based on depth and hole geometry. The minimum q_{pump} must be high enough to satisfy hole cleaning. Sifferman *et al.* [111] suggested minimum annular velocity of 50 ft/min for satisfactory cutting transport for a typical mud. The maximum q_{pump} must be low enough to prevent ECD to exceed fracture gradient [80]. Maximum pump horse power also sets an upper limit to q_{pump} [80]. Also, required q_{pump} to achieve the same annular velocity decreases by depth due to smaller cross sectional flow area.

Inlet mud temperature T_{inlet} is the temperature of the mud in the suction tank, thus its measurement is not accurate. Mud volume in the surface tanks is large compared to the mud volume in the well, thus temperature in the tanks require long circulation periods to heat up and long non-circulating periods to cool down [99]. The ambient air temperature and flowline mud temperature can be set as the minimum and maximum margins of T_{inlet}.

Mud gel strength (τ_{10sec}/ τ_{10min}) has a considerable uncertainty although recorded measurements are available. The reason is that gel strength is quite sensitive to chemical contaminations, in particular cement contamination and the leak off test is performed right after drilling the plugs and float shoe Besides, surface measurement may not totally reflect the downhole gel values.

Uncertainty of geophysical data predominantly stems from the accuracy of evaluation of geophysical well data and logs. If the rock elasticity data have been derived from logs, spatial variability causes uncertainty. If the data have been obtained by laboratory testing, formation heterogeneities prohibit representation of overall formation properties by single point tests.
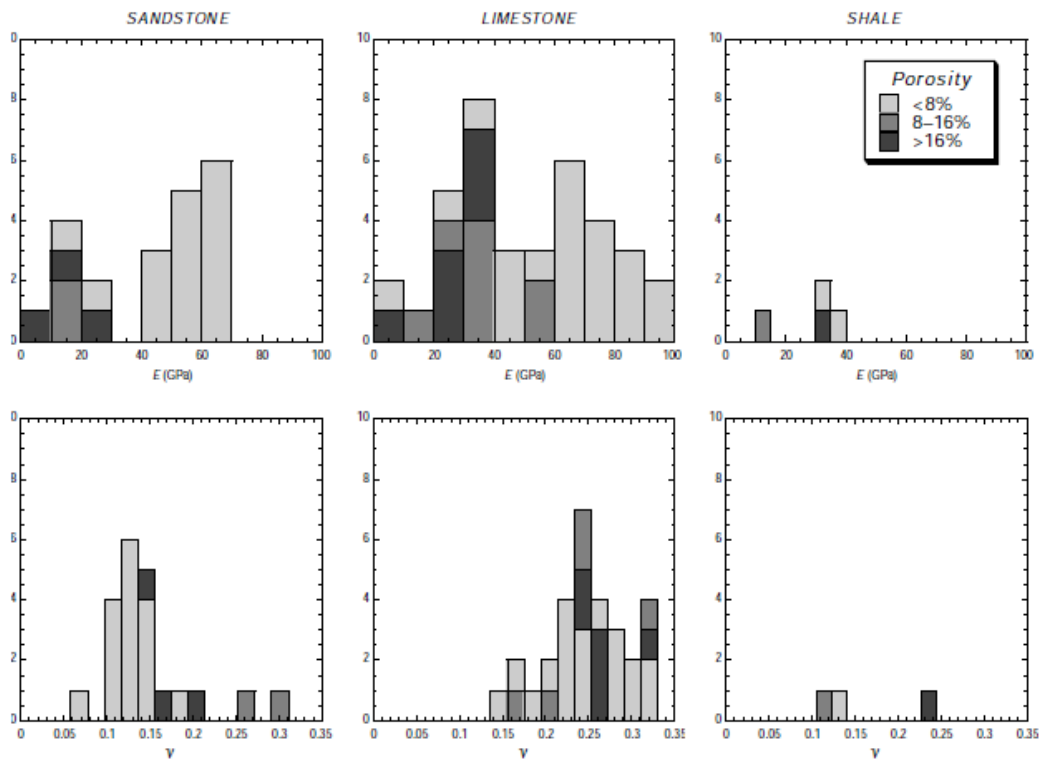
Fig. 6.3-Typical values of static measurements of Young's modulus (**E**) and Poisson's ratio (*v*) in shale, sandstone and siltstones [112]

Uncertainty of the elastic rock properties (from well logs and seismic measurements) comes from precision limitations of the equipment and formation heterogeneities. Spatial variability around the wellbore, on the other hand, contributes more uncertainty in core analysis as well as the uncertainty due to measurement errors in laboratory testing. Moreover, obtaining cores at overburden stress conditions and at downhole temperature and pressure is almost never possible. Thus, for the data from logs or seismics, core analysis, or extrapolated from offset wells the uncertainty is inevitable. Typical values of Young's modulus (**E**) and Poisson's ratio (*v*) from Lama and Vutukuri (1978) [112] and log-derived **E** and *v* measurements are shown in Fig. 6.3 and Fig. 6.4 respectively.

There are additional sources of uncertainty that could be further added to the analysis, such as,

- Effect of filtration on mud-rock heat exchange;
- Effect of filter cake on crack initialization;
- Effect of drilling induced micro fractures on wellbore stability;
- Interpretation of leak off pressure for shallow and unconsolidated formations or in tectonically active areas (T-fractures occurring due to high horizontal in situ stresses).
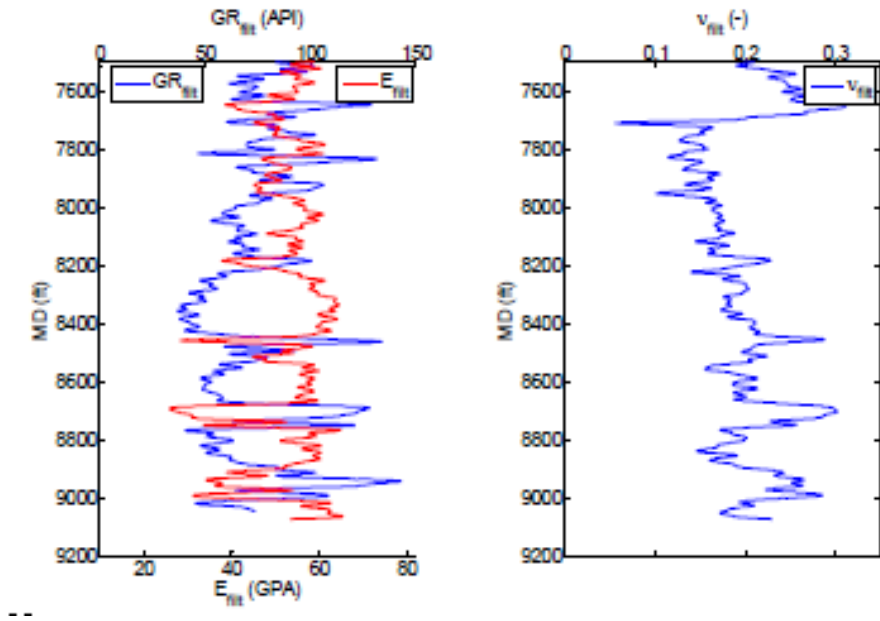
Fig. 6.4-Log derived Young's modulus with the gamma ray curve (left), Poisson's ratio from slow wave travel time plotted from the cross dipole log at 7500-9250 ft (right) [113]

6.2.2. Application of CSS Uncertainty Model to Study Well

The Study Well was drilled in 1993, located in offshore Texas [114]. The well was drilled to 18,834' total depth in 85 days, nearly all straight, in water depth of 85 ft on a fixed platform rig without any major troubles. Stratigraphy was predominated by Miocene shaly sandstones. Seawater-gel-CFL-PHPA drilling fluid system was used for surface and intermediate intervals, and freshwater-CFL-low lime system was used for the lower intermediate and production intervals.

Operations data presented here has been obtained from Study Well pre and post well reports. Daily operations summary provided hourly activity data providing critical information about the leak off testing, such as pre-leak off activity, circulation periods, wellbore stability problems, rate of penetration, formation rock, and mud properties such as density, gels and plastic viscosity and yield point.

Geophysical data presented here has been obtained primarily from the well log and core analysis data in addition to bit performance analysis from the study performed to diagnose poor PDC performance in deep, overpressured shales by Smith,J.R.(1998) [114]. Estimations of rock elastic parameters (E, v, α_t) have been made using literature data (*e.g.* Lama and Vutukuri, 1978 [112]) presenting statistical correlations relating travel time of compressional waves along the wellbore wall, density and porosity measurements, and the rock parameters, as discussed in APPENDIX G.

In this study we use the Study Well's basic data and assign uncertainties to the distributed parameters in Table 6-1. Then, we perform QRA analysis of CSS for all three sections of the well. As discussed above (Fig. 6.2), probability distribution function (PDF) of the control parameters are generated based on their minimum, maximum and most likely values, and the expected skewness of the distributions. In particular, formation strength parameters ar e entered as normal distributions between the lower and upper limits based on the rock type, porosity, sonic travel time from logs and silica content as discussed in APPENDIX F. The analysis starts from the production section of the well and proceeds upwards.

6.2.2.1. Uncertainty Analysis of CSS at 14,830' (second intermediate hole)

The Well's second intermediate hole was drilled with 12 $\frac{1}{4}$" PDCs from 10,754 to 14,830' with freshwater system. No significant wellbore stability problems were encountered except excessive hole enlargement problems and slow ROP below 16,800'. Large splintery shales over shakers observed which indicates sloughing, as well as tight spots below 13,800' to TD. Hi-vis pills were pumped for enhanced hole cleaning. Circulation was stopped every 10 stands when RIH. 9 $\frac{5}{8}$" liner run in and cemented, followed by 3-hr circulation and LOT performed at 14,830' at recorded operation time of 1.5 hours.

Mud density in hole was 17.3 ppg and surface leak off pressure recorded was 1,465 psig, which reportedly corresponded to 19.2 ppge fracture gradient. Summary of the reported drilling data of the interval is shown in Table 6-2.

Table 6-2-Drilling Data from Production Section of Study Well

Operation Data	Second intermediate interval (casing shoe at 14,830')		
Hole geometry	12 $^1/_4$" hole – 9 $^5/_8$" Q125		
Drilled interval	10,754 (top)	14,830 (bottom)	ft
Mud Specification	13.5	17.3	ppg
Mud Gel Strengths (10 min)	15	35	lb/100ft^2
Mud Gel Strengths (30 min)	30	50	lb/100ft^2
Mud Plastic Viscosity	22	31	cp
Mud Yield Point	6	20	lb/100ft^2
Mud API Fluid loss (HPHT)	10	25	cc/30min
Mud MBT	27	35	ppb
Circulation time before LOT		180	min
Recorded ρ_m in wellbore at LOT		17.3	ppg
Recorded surface LOP		1,465	psig
Recorded operation time for LOT, Δt_s		90	min
Reported CSS (eq.density/pressure)		19.2 / 14,806	ppge/psi

It is a common practice to circulate the well at least one bottoms-up cycle to assure hole cleaning and condition the mud [115]. 180 min of circulation has been reported before the LOT, followed by 90 min total operation time for LOT. The total operation time includes establishment of the high pressure lines to the cementing pump, opening the choke manifold safety valve, closing the BOP pipe rams, pressurizing the closed system by slow rate injection, performing LOT, shutting-in for pressure decline, and assembling the lines to resume drilling[1]. Therefore based on the industry practice, a delay of 10 to 60 min (Δt_s) between stopping the pumps and the reported total operation time for the LOT is assumed (Smith,J.R., personal communication). Surface earth temperature (T_0) and geothermal gradient (G_T) are estimated addressing the database published by the Department of Interior (2010) [116] that includes data from 108 wells in Judge Digby Field, Louisiana. The input distributions for QRA of CSS at 14,830' are shown in Table 6-3.

---

[1] Note that in this study only LOT from the pipe is considered.

The 10 minute gel strength ($\tau_{gel\text{-}10min}$) was entered as triangular distribution to prevent random selection of too low values since the thixotropy effect model described in section 4.2.2.3 cannot return numeric results for $\tau_{gel\text{-}10min}$ values smaller than $\tau_{gel\text{-}10sec}$ values.

The distribution of the geomechanical parameters ($\mathbf{E}$, v, α_T) are estimated considering the reported cutting analysis, wireline log and core analysis data. Wireline openhole logging (DIL/LLS/LDT/CNL/GR)[1] was run by Schlumberger from 14,843' to the next casing shoe at 10,740'.A summary of the formation characteristics from wireline log interpretation is shown in Table F.2.

Sidewall cores also has been taken in this interval. Summary of the subsurface core data is shown in Table F.1.The XRD mineralogy data presented Table F.1 was used to estimate α_T. Acoustic travel time and effective porosity data listed Table F.2 were used to estimate $\mathbf{E}$, v using statistical correlations presented by Lama and Vutukuri [112] (See APPENDIX G).

QRA was performed to generate the CSS distribution at 14,830'. In each experiment, a set of distributed parameters randomly selected from their pools were used to calculate CSS using the deterministic model. Calculated distribution of CSS is defined with P_5, P_{50} and P_{95} statistics (with 5%, 50% and 95% probabilities, respectively). In this study the CSS window has been defined with 90% confidence interval (CI), thus P_5 and P_{95} refer to the lower and upper limits, respectively. P_{50} is the median of the distribution, the CSS value that divides the CSS bell curve into two equal areas.
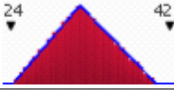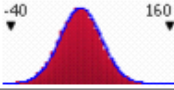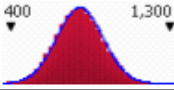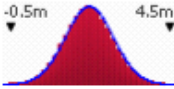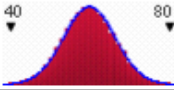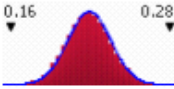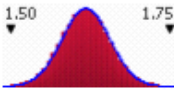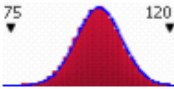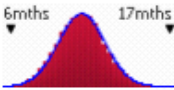
For large size of sample size, i.e. large number of Monte Carlo experiments, the P_{50} value approaches to the value calculated by the deterministic model. Mode is the measure of central tendency, *i.e.* the CSS value at which the PDF function has its maximum value. Mode is also referred as the most frequent observation throughout the simulation. For an unbiased distribution, such as normal distribution, mode, median and mean values are approximately equal.

Output probability density distribution of CSS is shown in Fig. 6.5. The CSS distribution was best-fitted using theoretical model of log-normal distribution. Note a very small discrepancy between the empirical and theoretical distributions.

---

[1] See Abbreviations for the log types.

Table 6-3- Input data distributions for CSS analysis at 14,830 ft

Performed By: kkinik1				
Date: Friday, March 09, 2012 4:49:52 PM				
Name	Graph	5%	Mean	95%
10 min gel strength	24 ▼ 42 ▼	27.28056	32.33333	37.54296
No-circulation time, min	-40 ▼ 160 ▼	10.37117	50.01205	89.31569
Circulation rate, gpm	400 ▼ 1,300 ▼	599.2431	800.0419	1000.588
Young's Modulus, psi	-0.5m ▼ 4.5m ▼	8.47E+05	2.00E+06	3.15E+06
Surface earth temperature, oF	40 ▼ 80 ▼	50.10839	60.00005	69.86418
Rock Poisson's ratio	0.16 ▼ 0.28 ▼	0.1951882	0.2200007	0.2446509
Geothermal gradient, F/100ft	1.50 ▼ 1.75 ▼	1.562218	1.619997	1.67749
Mud inlet temperature, Tinlet / Rock Properties	75 ▼ 120 ▼	90.13069	99.99863	109.8282
Rock thermal expansion coefficient, 1/C	6mths ▼ 17mths ▼	8.52136E-06	1.10001E-05	1.34667E-05

Log-normal distribution is defined with parameters mean value (μ) and standard deviation (σ). As shown in Fig. 6.5, the distribution is skewed to the left, *i.e.* it is asymmetric. As the skewness of a log-normal distribution is greater, the difference between the mean, median is greater. According to the central limit theorem, expected value of the sample, **E**(CSS), approximates the population mean, μ(CSS), for large population size, n. [117] Thus, in this analysis the mean value of the output CSS distribution, μ(CSS), was considered as the measure for comparison with the conventional method.

The CSS values were distributed with mean value 16,476 psi, with 90% confidence interval between 15,367 and 19,490 psi, and standard deviation 1,382 psi. CSS was calculated 14,806 psi with the conventional method. Conclusively, the mean CSS at 14,830' has been 1,670 psig (11.2%) greater than CSS calculated by the conventional method.

Fit Comparison for PDF of CSS at 14,830' (Model)
RiskPearson5(3.1881,3664.5,RiskShift(14792.9))
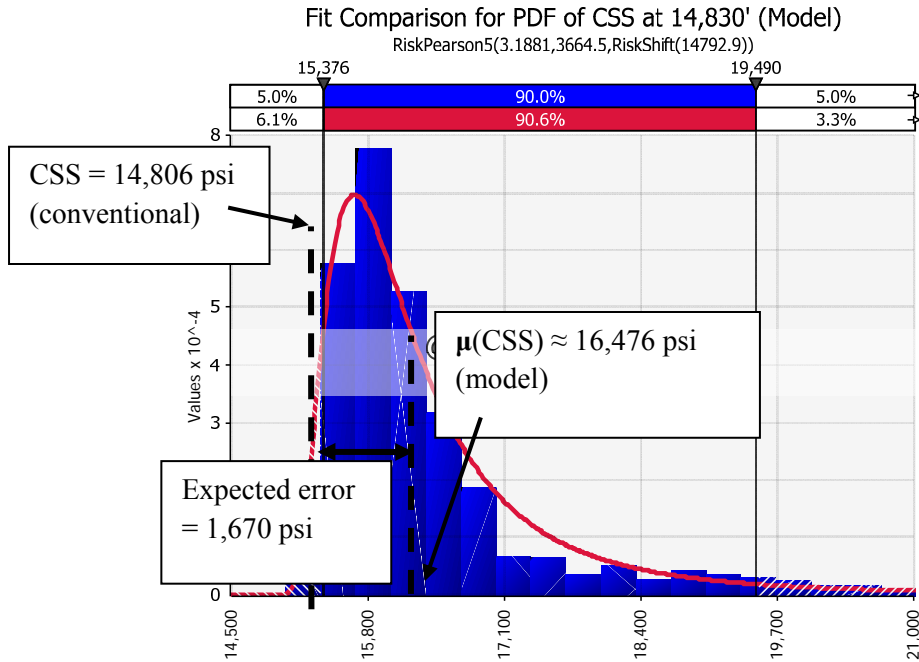
Fig. 6.5- PDF of CSS at 14,830 ft

Casing shoe strength sensitivity has been tested in 63,000 experiments. Shown in Fig. 6.6 is a Pareto plot of the distributed parameters from Table 6-1 -on the X axis, the parameters, and on the Y-axis, their contribution on the CSS uncertainty. For example, 21% of the CSS uncertainty at 14,830' was due the Young's modulus distribution.
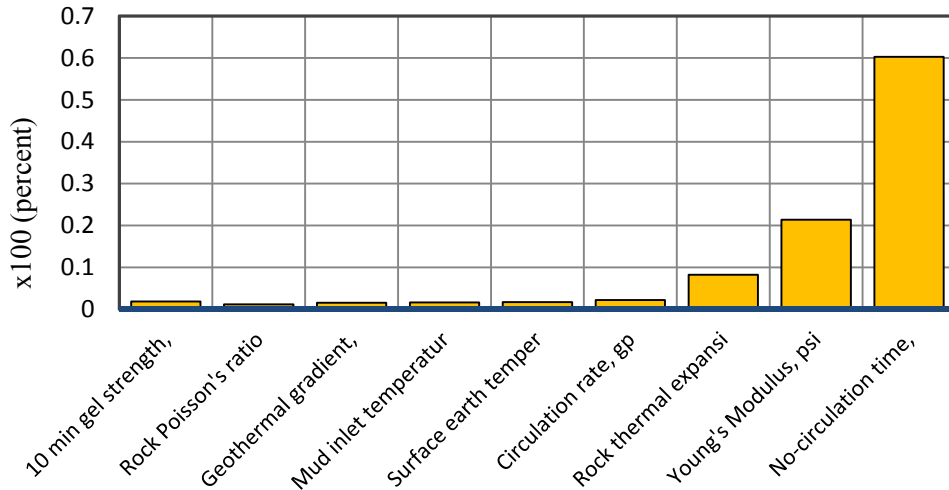
Fig. 6.6- Pareto plot of CSS sensitivity at 14,830 ft

CSS sensitivity to Δt_s, α_T, and **E** is noticeably higher than other parameters, i.e. the CSS value at 14,830 ft is controlled by Δt_s, α_T, and **E**. Contribution of other parameters v, $\tau_{gel-10min}$, G_T, T_{inlet}, T_o, and q_{pump} is below 5%, critical limit of significance. Thus, the CSS uncertainty at 14,830' is solely controlled by Δt_s, α_T, and **E** – included in the thermal effect term in eqn.4.8.

6.2.2.2. Uncertainty Analysis of CSS at 10,740' (first intermediate hole)

The first intermediate hole section was drilled from the 18 $^5/_8$ casing shoe at 6,235' to 10,750' with 9.5 to 12.8 ppg seawater-polymer based mud with Soltex (shale stabilizer). Directional survey indicated nearly vertical well. Large section of sloughing shale was drilled with frequent washouts and requirement of reaming. Eventually with the help of hi-vis pills hole cleaning was successful, and the recorded leak off test pressure was equal to that estimated from the offset wells. Summary of the well, formation and operation data is shown in Table 6-4.

Table 6-4- Drilling data from 2nd Intermediate Section of Study Well

Operation Data	First Intermediate Section (casing shoe at 10,740 ft)		
Hole geometry	16" hole – 13-5/8" 88.2 ppf Q125		
Drilled interval	from 6,235'	to 10,754'	
Mud Specification	9.0	12.8	ppg
Mud Gel Strengths (10 min)	9	25	lb/100ft^2
Mud Gel Strengths (30 min)	12	34	lb/100ft^2
Mud Plastic Viscosity	5	25	cp
Mud Yield Point	4	30	lb/100ft^2
Mud API Fluid loss (HPHT)	6	35	cc/30min
Mud MBT	20	33	ppb
Circulation time before LOT		60	min
Recorded ρ_m in wellbore at LOT		12.8	ppg
Recorded surface LOT pressure		3,000	psig
Recorded operation time for LOT		60	min
Reported CSS (eq,density/ pressure)		18.2 /10,177	ppge/psi

The minimum, maximum and most likely values of Δt_s were kept identical to the analysis of CSS at 14,830 ft (See Table 6-3), since the leak off test was performed with the same rig equipment and under similar operation conditions (surface lines, BOP, cementing unit).

Distributions of the surface earth temperature and geothermal gradient is also identical to the production hole section since they do not depend on depth. As a well gets deeper, the ratio of mud volume in the well

to the total mud volume on surface increases. Also, geothermal temperatures increase somewhat linearly. Therefore, the outlet mud temperature is expected to be greater.

The distribution of T_{inlet} was estimated by considering the subsurface mud volume and well depth. Young's modulus has not been quantitatively related to depth. However, increasing horizontal stresses with depth tend to increase **E**. Yet, **E** is a strong function of rock type. Casing shoes at 14,830' and 10,740' have been set in the same geological section that was composed of Miocene shaly sandstone. Therefore, distribution of **E** at 10,740' was generated with the expected value smaller than that at 14,830'. Thermal expansion coefficient of the rock is a strong function of its quartz content. The XRD data from cores at 13,078' (See Table F.1) was extrapolated to estimate α_T. Approximately the same distribution was generated for α_T. The input values of the distributed parameters are shown in Table 6-5.

Table 6-5- Input data distributions for CSS analysis at 10,740 ft

Performed By: kkinik1				
Date: Friday, March 09, 2012 9:28:22 PM				
Name	Graph	5%	Mean	95%
No-circulation time, min	-60 ⋯ 140	10.47724	49.99216	89.4558
Circulation rate, gpm	400 ⋯ 1,300	698.1944	899.8832	1100.052
Young's Modulus, psi	-0.5m ⋯ 3.5m	6.77E+05	1.50E+06	2.32E+06
Surface earth temperature, oF	35 ⋯ 80	50.08896	59.99501	69.8273
Rock Poisson's ratio	0.15 ⋯ 0.25	0.1753133	0.1999982	0.2246535
Mud inlet temperature, oF	75 ⋯ 120	85.0969	95.00313	104.8601
10 min gel strength, lb/100ft2	10 ⋯ 40	17.8158	24.99976	32.12147
Geothermal gradient, F/100ft	1.50 ⋯ 1.80	1.562326	1.620028	1.677532
Rock thermal expansion coefficient, 1/C	4mths ⋯ 16mths	7.367E-06	9.9995E-06	1.2628E-05

The QRA of CSS at 10,740' required 63,000 simulation experiments, - running the CSS model. The resultant probability density distribution of CSS is shown in Fig. 6.7.
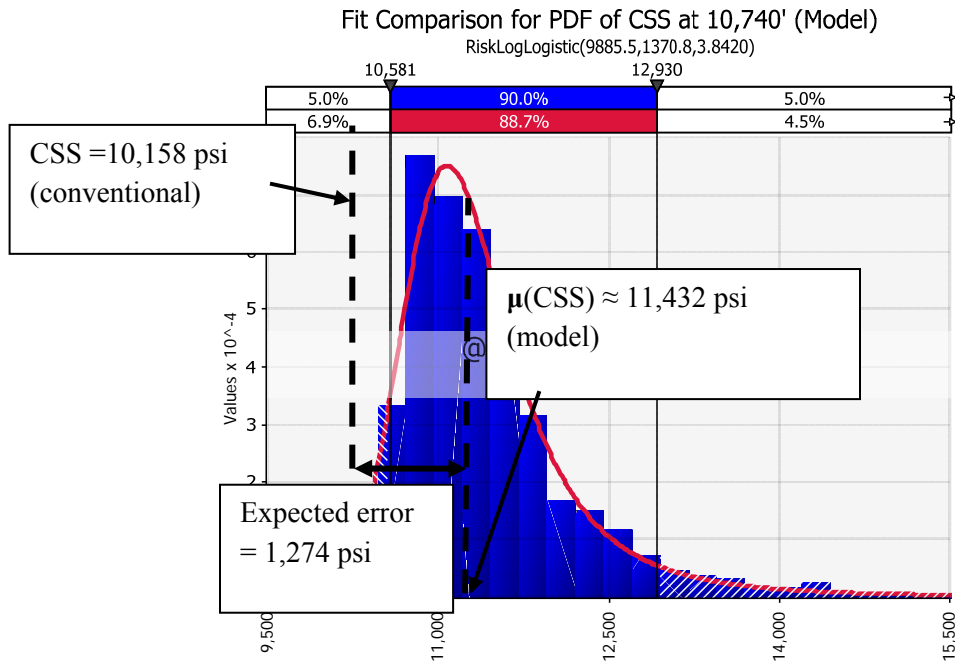
Fig. 6.7- PDF of CSS at 10,740 ft

Again, the CSS are log-normally distributed with mean value 11,432 psi, standard deviation 805 psi, and the 90% confidence interval from 10,581 psi to 12,930 psi. The CSS value calculated conventionally is 10,158 psi resulting in the 1,274 psig (12.7%) underestimation with the conventional method.
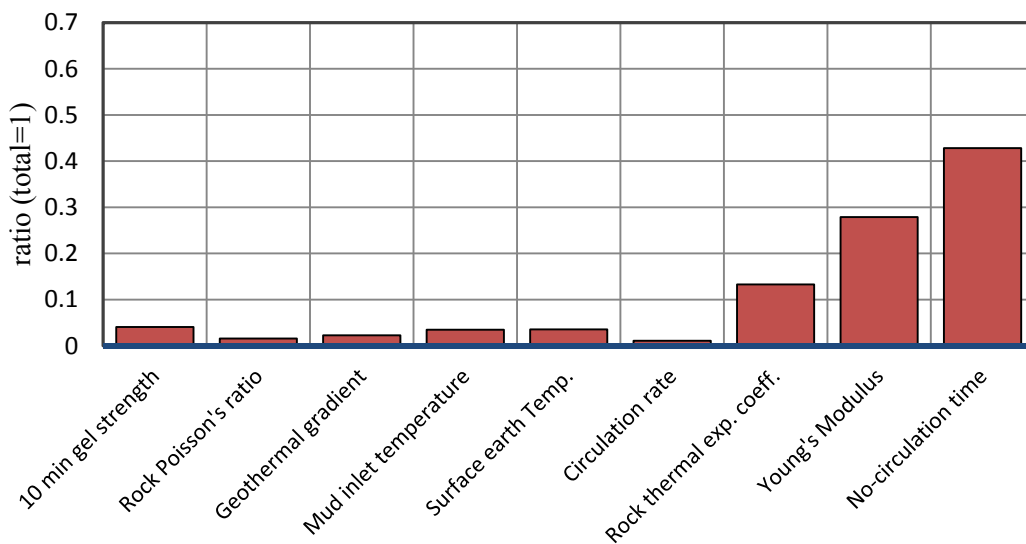
Fig. 6.8- Pareto plot of CSS sensitivity at 10,740 ft

110

Relative contributions of the distributed parameters are depicted with Pareto plot in Fig. 6.8. Again, the dominating effects result from Young's modulus, coefficient of thermal expansion, and non-circulating time variations. Effects of other parameters (ν, $\tau_{gel-10min}$, G_T, T_{inlet}, T_o, and q_{pump}) are below 5%, and are insignificant.

6.2.2.3. Uncertainty Analysis of CSS at 6,250' (surface hole)

The surface hole section was drilled from the 24" casing shoe at 1,209 to 6,250 ft with 8.9 to 9.4 ppg seawater-polymer mud system. Directional survey indicated maximum 1.0 degree inclination. Bit balling was reported due to sticky formation. LOT was performed with 9.2 ppg mud in hole; the reported surface pressure was 1,740 psig and the calculated CSS was 14.5 ppge, smaller than expected value from offset data, 15.4 ppge.
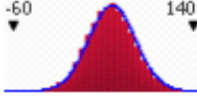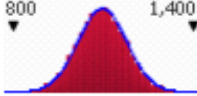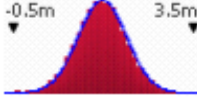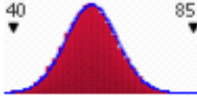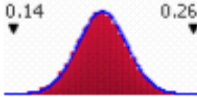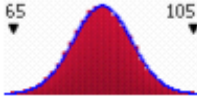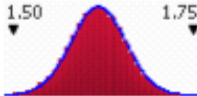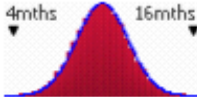
No wireline or core analysis data is available for the formation at this casing shoe depth. However, the records in the drilling report, notes on ROP, bit balling and hole enlargement incidents, and the geophysical data suggest occurrence of a massive Miocene shale section in this interval. There was also strong indication that the formation was made of sticky to hard shale rocks. The total LOT time per the drilling report was 30 min, following a 60 min circulation. Drilling data for this well section is shown in Table 6-6.

Table 6-6- Drilling data from First Intermediate Section of Study Well

Operation Data	Surface Section (casing shoe at 6,250 ft)		
Hole geometry	22" hole – 18-$^5/_8$" N-80		
Depth	1,209 ft (top)	6,250 ft (bottom)	
Density	8.9	9.5	ppg
Mud Gel Strengths (10 min)	11	26	lb/100ft^2
Mud Gel Strengths (30 min)	12	27	lb/100ft^2
Mud Plastic Viscosity	4	5	cp
Mud Yield Point	16	40	lb/100ft^2
Mud API Fluid loss (HPHT)	28	68	ml/30min
Mud MBT	23	32	ppb
Circulation time before LOT		60	min
Recorded ρ_m in wellbore at LOT		9.2	ppg
Recorded surface LOP		1,740	psig
Recorded operation time for LOT		30	min
Reported CSS (eq.density		14.5/ 4,730	ppge/psi

The distribution of non-circulating time (Δt_s) at 6,250 ft was generated identical to that of it at 10,740 ft since the operational conditions for the leak-off testing (BOP stack, surface lines, etc.) are identical. The distribution of circulating rate (q_{pump}), however, was described with a greater mean value since the flow area in this section was greater, requiring higher pump rates to satisfy hole cleaning. The casing shoes at 6,250 ft and 10,740 ft were reported to have been set in a massive, Miocene shaly sandstone formation. Thus, the rock parameters, Young's modulus (**E**), Poisson's ratio (v) and thermal expansion coefficient (α_T) were assumed similar at the two depths, and their input distributions at 6,250 ft were set the same as they are at 10,740 ft.

Table 6-7- Input data distributions for CSS analysis at at 6,250 ft

Performed By: kkinik1				
Date: Friday, March 09, 2012 11:28:19 PM				
Name	Graph	5%	Mean	95%
No-circulation time, min		10.33128	49.99843	89.35982
Circulation rate, gpm		976.4607	1100.021	1222.648
Young's Modulus, psi		6.78E+05	1.50E+06	2.32E+06
Surface earth temperature, oF		50.07483	60.00364	69.86769
Rock Poisson's ratio		0.1753225	0.1999945	0.2245379
Mud inlet temperature, oF		75.12113	85.00137	94.8551
10 min gel strength, lb/100ft2		13.27316	19.00022	24.71046
Geothermal gradient, F/100ft		1.562382	1.620018	1.677265
Rock thermal expansion coefficient, 1/C		7.3536E-06	1.0001E-05	1.2624E-05

The total hole volume at 6,250 ft was smaller than that of it at 10,740 ft. Therefore the volume of mud heated by the rock during the circulation is greater, thus steady state tank temperature is expected to be

smaller during drilling of the shallower sections of a well [99]. Mud inlet temperature (T_i) in this section was assumed approximately 10 $^\circ$F smaller than that of it at 10,740 ft. Since the volume of mud in the hole is smaller compared to that in the surface tanks at shallower depths, the change in mud properties due to chemical contaminations will be less. Therefore, at 6,250 ft, distribution of 10 min gel strength ($\tau_{gel-10min}$) was generated with a relatively smaller value than that of it at 10,740 ft. No changes have been made in the surface earth temperature (T_o) and geothermal gradient (G_T) distributions since they are independent of the operation. The input distributions for QRA of CSS at 6,250 ft are shown in Table 6-7.

QRA was performed to generate the distribution of CSS at 6,250'. Output probability density distribution of CSS is shown in Fig. 6.9. Similar to other well sections, distribution of CSS is log-normal with mean value 5,645 psi, standard deviation 583 psi, and the 90% confidence interval from 4,903 psi to 6,787 psi. In contrast, the conventional gives CSS=4730 psi, thus underestimating CSS by 915 psi or 19.3%. Fig. 6.10 shows the sensitivity analysis of CSS at 6,250'. Contributions of v, α_T and $\mathbf{E}$ are greater than in the other well sections and remaining parameters are still insignificant, except for T_{inlet} and T_o.
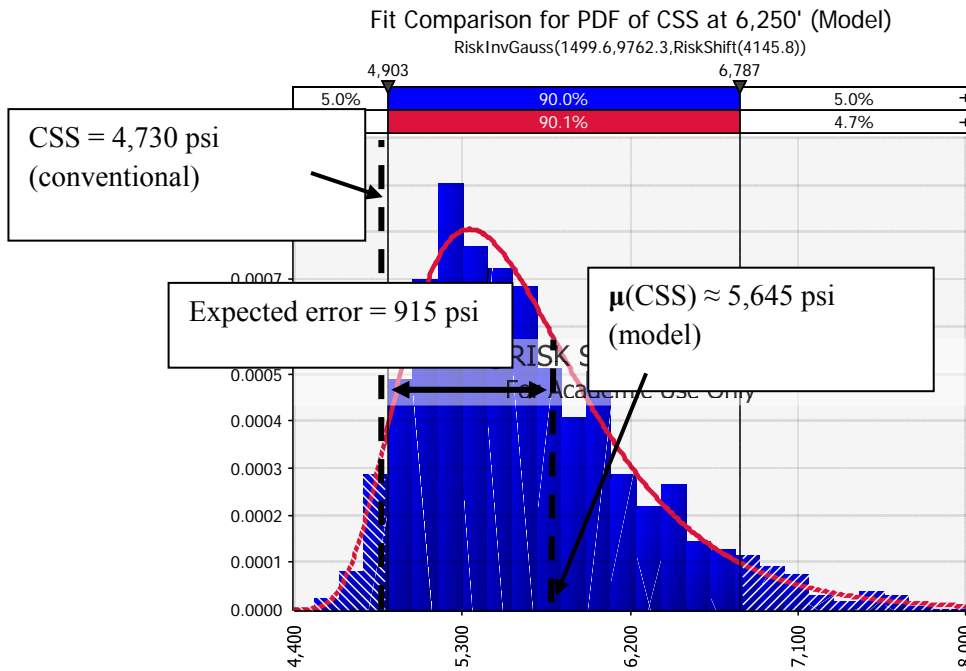
Fig. 6.9- PDF of CSS at 6,250 ft

The reason is that at shallower depths rock temperature is more dependent on the surface earth temperature.. Also, the subsurface mud volume in the well is small comparing to the surface volume that results in different mud cooling/heating cycles.
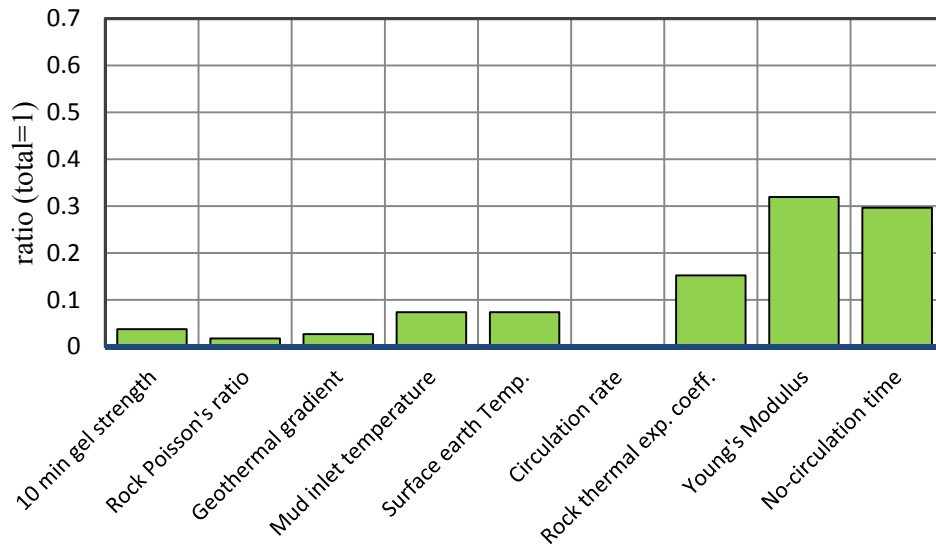
Fig. 6.10- Pareto plot of CSS sensitivity at 6,250 ft

6.2.2.4. Discussion

Several observations result from the application of QRA to estimate CSS in three sections of the Study Well. A considerable uncertainty of casing shoe strength, its sources and possible control are further discussed below. Applications of the new CSS model in Section 4.3.3 gives higher values of CSS than the conventional method that underestimates CSS. The degree of underestimation depends on the uncertainty of the CSS estimation from the new model demonstrated by PDF plots in Fig. 6.5, Fig. 6.7, and Fig. 6.9. The statistical spread is considerable with standard deviation up to 10% of the mean value. Moreover, the CSS distribution is log-normal with strong negative skewness even though the input parameters have symmetrical (nearly normal) distributions. The reason for this is the function describing the well temperature change during the non-circulating time (the change is described by a logarithmic function.) The PDF skewness indicates strong effect of temperature that contributes to mud gellation and thermal stress terms in eqn.4.6. As the casing shoe proves stronger than measured by conventional LOT analysis (that regards gellation and thermal effects) the thermal stress component supersedes the gellation effect

Thermal stress is controlled by thermal expansion coefficient (α_T), Young's modulus (**E**); and the time-dependent variable, mud temperature (T_{ws}). (T_{ws} is controlled by non-circulating time, Δt_s). The parameters α_T and **E** describe rock properties, and their uncertainty depends only on precision of geological data at hand. In contrast, Δt_s can be controlled. Therefore, a more detailed study of the dependency of CSS uncertainty to Δt_s is reported in the following section.

It is observed from Pareto plots that the effect of E on the CSS uncertainty decreases with depth. The reason is that the Δt_s effect becomes more dominant due to the mud-rock temperature differences increase as the well gets deeper – despite lower circulation rate. Hence, it can be concluded that the effects **E** and Δt_s oppose each other in contributing to the CSS uncertainty. (We have not found documented evidence of α_T change with depth.)

Availability of MWD tool could improve the precision (less uncertainty) of CSS measurement in a LOT as it would directly measure the bottom-hole pressure and temperature and accommodate for the discrepancy due gellation and mud compressibility. However, without the correction for the thermal stresses it would not determine the actual (static) value of CSS at the geothermal temperature. The correction brings about additional uncertainties to the CSS value. The overall precision of CSS could only be improved by keeping precise record of non-circulating time.

6.2.3. Significance of Probabilistic Approach

The uncertainty analysis of the Study Well above, using the probabilistic CSS model identified two parameters that mostly control dispersion of CSS values, Young's modulus and non-circulating time. The former (**E**) is a geological property widely varying for rocks due their heterogeneity. The latter (Δt_s) is an operational parameter that can be controlled and precisely reported thus reducing the error introduced by non-circulating time, gel strength and type of mud.

Statistical study was performed to investigate the effect of non-circulating time, mud type and thixotropy on CSS uncertainty using the probabilistic CSS model. Casing shoe at the bottom of the second intermediate hole (at 14,830 ft) of the Study Well was used in the study. Drilling data from this well section is summarized in Table 6-2 and input distributed parameters are listed in Table 6-3. In this study, all input parameters are kept constant, except for the parameter being investigated. The investigated parameter in each study, below, was modified hypothetically to illustrate its effect.

6.2.3.1. CSS Uncertainty Change with Non-circulating Time

As discussed, non-circulating time (Δt_s) is the only operational parameter that has significant impact on the CSS uncertainty. In this analysis, the distributions of the control parameters shown in Table 6-3 ('default'), except Δt_s, are used for the uncertainty analysis. The effect of Δt_s is analyzed by modifying the distribution of Δt_s hypothetically.

Firstly, the input distribution of Δt_s is entered as discrete uniform distribution, which is defined with a minimum and maximum value. This theoretical distribution is commonly used in engineering applications

when there is no information about the distribution of the parameter. Within its interval, no Δt_s values in particular are biased, thus any value of Δt_s has equal chance of being selected during the Monte Carlo experiments (corresponding to a probability value 0.00416 in this analysis).

The interval for is divided into finite number of equally spaced values, each of which has the same frequency of being selected, corresponding to an equal probability value 0.00416. By doing so we remove the uncertainty effect of Δt_s and emphasize contributions of other distributed parameters. Shown in Fig. 6.11 is the scatter plot of calculated CSS values vs. various values of Δt_s. Also there are plots of CSS calculated with the deterministic CSS model and using the conventional method.

Similar to deterministic study, in Sections 4.3.3 and 4.3.4 the discrepancy between the CSS P_{50} and the conventional method is initially high, and decreases rapidly with time. This is a result of mud temperature (T_{ws}) build-up after the circulation stops. After 60 minutes, the CSS (P_{50}) approaches the conventional CSS line, and its asymptote is about 400 psig greater than the conventional CSS value.
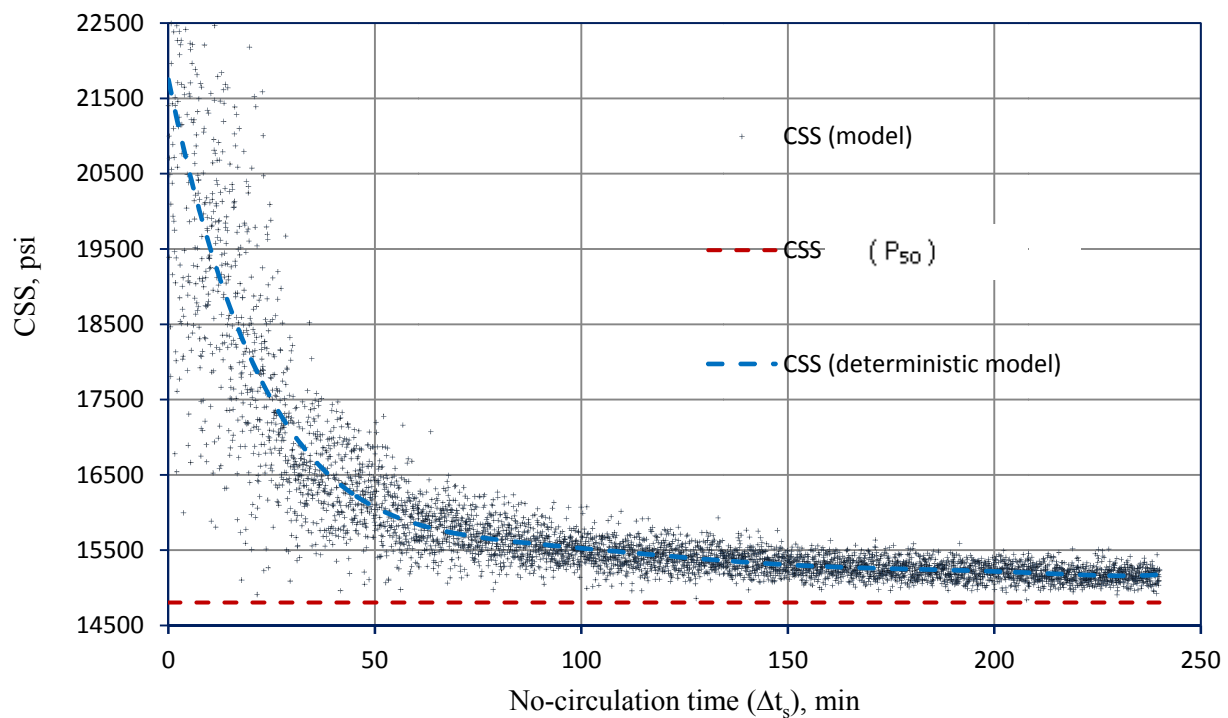
Fig. 6.11-Distribution of CSS as a function Δt_s

The difference stems from the mud compressibility effect that is disregarded by conventional model as discussed in Section 4.2.1. It is shown that the probabilistic CSS values are initially more dispersed and the dispersion reduces in time with decreasing discrepancy between CSS and conventional CSS. The

dispersion is caused by contribution of factors other than Δt_s to the thermal effects. This observations is consistant with results of the sensitivity analysis and Pareto plots above (See Fig. 6.6). Hence, further analysis of CSS vs. Δt_s was performed for discrete values of Δt_s with the same probability.

In this study, Δt_s was entered as binomial distribution, each Δt_s with equal probabilities. That is, Δt_s is not considered as a distributed parameter, but for each simulation it is assumed known with no uncertainty. Separate distributions of the CSS are simulated for each constant value of Δt_s. These empirical distributions are then best-fitted with log-normal theoretical distribution. Shown in Fig. 6.12 are the probability density distributions (PDF) of CSS at each non-circulating time (Δt_s). Included in the figure are plots P_{50} and CSS (conventional).

The PDF plots show that standard deviation of the CSS dispersion decreases significantly with non-circulating time, Δt_s. The result indicates that the uncertainty of CSS stems mostly from the thermal effects that reduces with the well temperature approaching geothermal gradient.
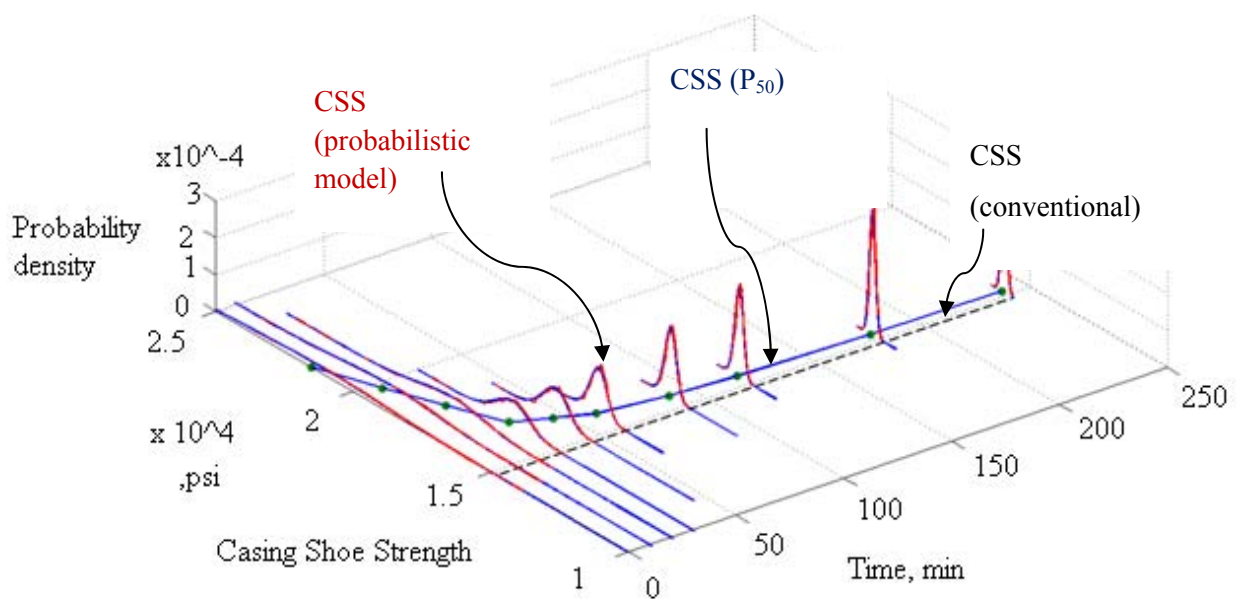
Fig. 6.12-Distributions of CSS (model) vs. Δt_s

As the wellbore temperature increases with time and the time's distribution is binomial the temperature is a statistical variable with its own distribution controlled by parameters of the transient temperature model in equations 4.33 through 4.39. Distribution of the wellbore temperatures calculated throughout the same simulation presented above, are presented separately to visualize the progress of temperature buildup in wellbore with non-circulating time. The input distributions are as presented in Table 6-3, except for the non-circulating time.
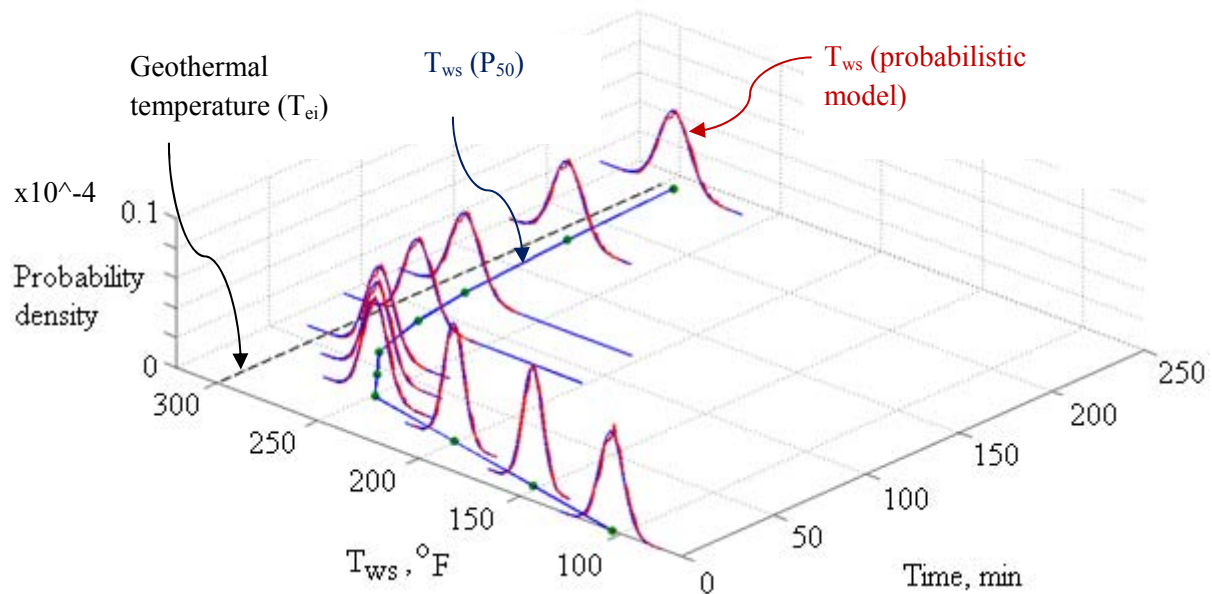
Fig. 6.13-Uncertainty of mud temperature vs. non-circulating time

Statistical distribution of wellbore temperature at various non-circulating times is shown in Fig. 6.13 together with the mode ($T_{ws\text{-}P50}$) and geothermal temperature. The results show that the uncertainty of T_{ws} does not change with Δt_s. Thus we conclude that the CSS uncertainty decrease in time is not caused by the temperature dispersion but solely results from the average temperature change ($T_{ws\text{-}P50}$).

6.2.3.2. CSS Uncertainty with Oil-Base and Water-Base Muds

Statistical analysis is made to compare CSS uncertainties vs. mud type. The Study Well's configuration is the same as in Table 6-3, except for the mud type and its thermal properties shown in Table 6-3. Mud type was hypothetically modified by replacing water base mud (WBM) with the same density (17.3 ppg) oil base mud (OBM). Then, CSS uncertainty model analysis was performed to generate PDF plots shown in Fig. 6.14.

The P_{50} values for WBM and OBM, 16,150 psi and 16,050 psi, respectively, are practically the same and there is no significant difference in the size of confidence interval although it is slightly smaller for WBM than for OBM. This is mainly due smaller correction of thermal stresses for OBM in eqn.4.6.

118
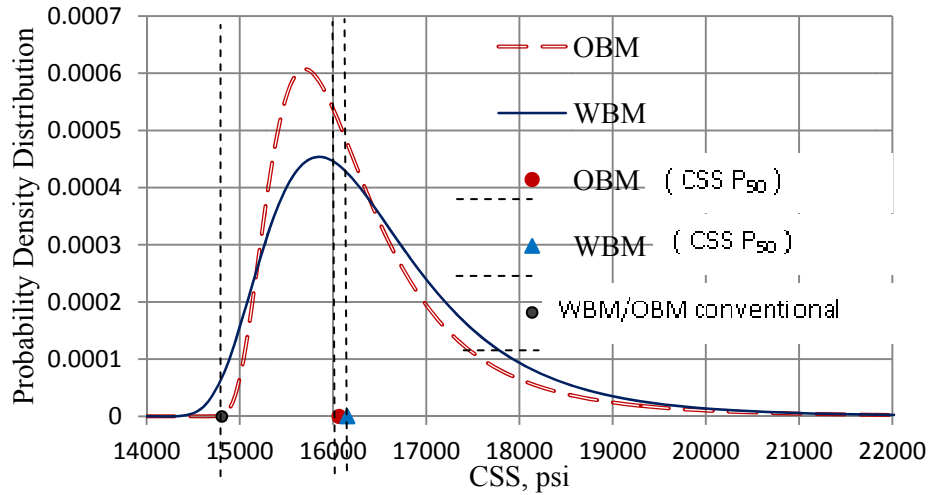
Fig. 6.14-Comparison of CSS probability distribution for oil base and water base mud

Note that the effect of mud type is due two factors in this analysis. Firstly, the CSS model does not consider the effect of temperature on gel strength for WBM. Secondly, the mud type only affects T_{ws} since WBM and OBM has different thermal properties, as discussed in Section 4.3.4. Recall that OBM heats up and cools down faster because solid content of the same density OBM is higher than that in WBM, and heat capacity of barite is around 4-fold smaller than that of water. In this analysis, the heat capacity of mud (c_{p-m}) was calculated 0.525 BTU/lb-^{o}F for WBM and 0.232 BTU/lb-^{o}F for OBM.
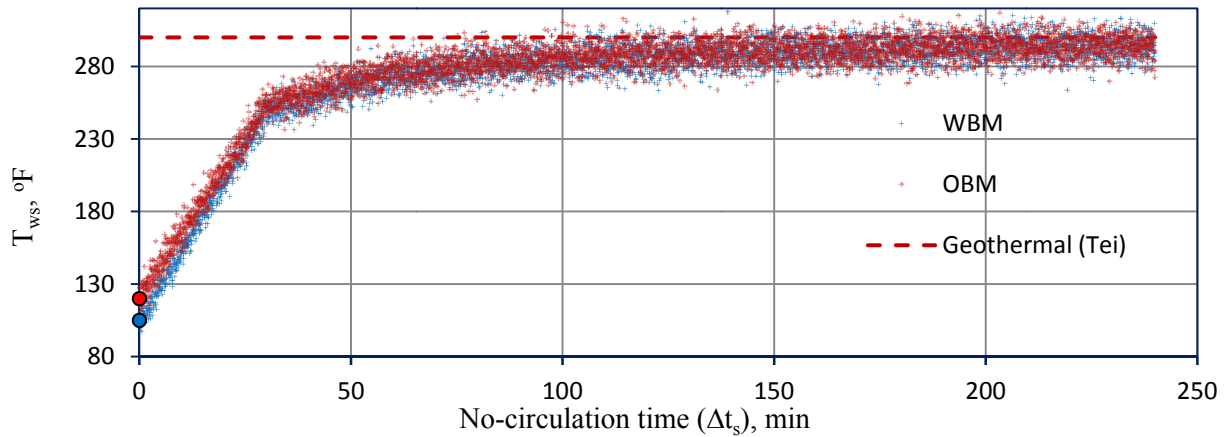
Fig. 6.15-Distribution of T_{ws} as a function of Δt_s – WBM and OBM

Thermal conductivity of mud (k_m) was calculated 0.725 BTU/ft-^{o}F-hr for WBM and 0.233 BTU/ft-^{o}F-hr for OBM. Since the mud type controls mud temperature, comparison of the distributions of T_{ws} of WBM and OBM was made to further analyze the difference due mud type- shown in Fig. 6.14.

The same simulation was repeated, except that the input Δt_s was entered as uniform discrete distribution from 0 to 240 min. The output distribution of T_{ws} vs. Δt_s was plotted, as shown in Fig. 6.15. There is some difference between initial temperature that disappears later as the values merge with geothermal temperature. The initial disparity is because mud type affects the steady state circulating temperature. The steady state circulating temperature (T_{ws} at Δt_s=0) is 105 ^{o}F for WBM and 120 ^{o}F for OBM. We conclude that mud type would affect CSS uncertainty very little – only due to the difference in wellbore temperature at the end of circulation prior to LOT.

6.2.3.3. Contribution of Mud Thixotropy to CSS Uncertainty

Another analysis is made to investigate the effect of thixotropy on CSS uncertainty using the probabilistic CSS model. The study well configuration is not changed and distributions of the model parameters are given in Table 6-3, except for the 10 min gel strength. $\tau_{gel-10min}$.
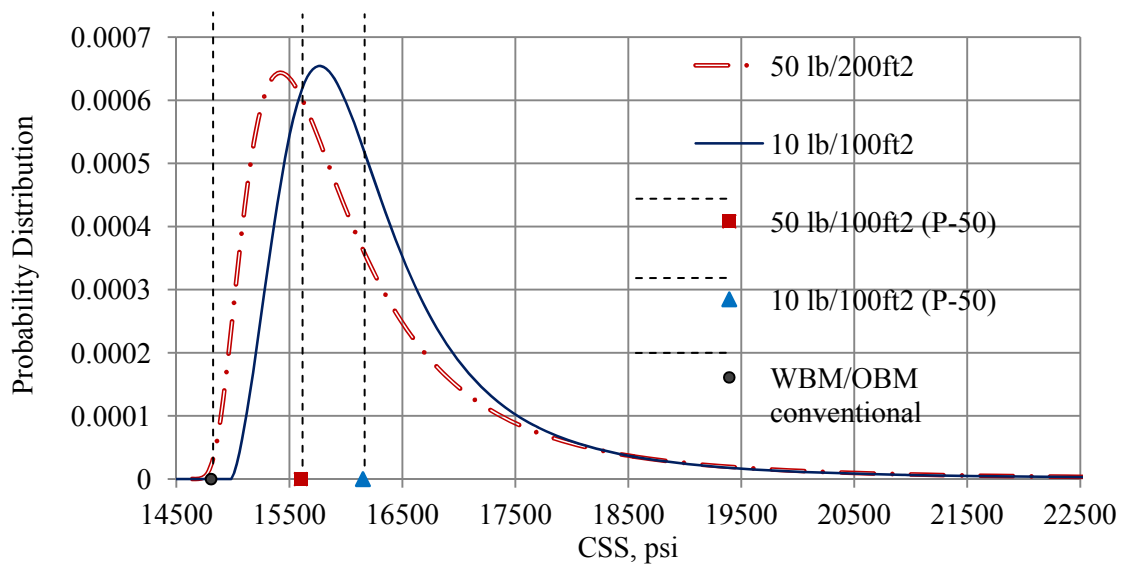
Fig. 6.16-Probability density distributions of CSS for flat and progressive gel strength

Instead of being normally distributed with mean value 12 lb/100 ft^2, gel strength is hypothetically modified as normal distribution with mean value 50 lb/100ft^2. A comparison of CSS's for flat (12 lb/100 ft^2) and progressive gel strength muds is shown in Fig. 6.16. The resulting PDF plot are little different which means that quite significant change of mud thixotropy has little effect on CSS uncertainty although it does significantly affect the average value of CSS, as shown in the next simulation.

A second simulation addresses the effect of flat and progressive gels on CSS uncertainty, and its average value. Again, Δt_s was assumed a uniform discrete distribution from 0 to 240 min. The resulting average

and scattered values of pressure loss due mud thixotropy are plotted in Fig. 6.17. The effect of progressive gellation of mud is significant as it may reduce the LOT pressure transition by 400 psi for the late LOTs. However, the statistical variation of the pressure seems little affected by gellation but it does increase in time.

The dispersion of P_{gel} is further analyzed. The simulation is performed for $\tau_{gel-10min}$=50 lb/100ft^2 by defining Δt_s as uniform binomial distribution. For each constant Δt_s value, separate simulation is run to generate $P_{gel}(\Delta t_s)$ distributions. The resulting P_{gel} distributions are plotted in Fig. 6.18.

The results show the dispersion of ΔP_{gel} increasing with time. Note that ΔP_{gel} value for Δt_s =0 is deterministic, since gel strength value is zero. Also, note that gellation is the only effect decreasing the magnitude of calculated CSS, regardless of Δt_s.
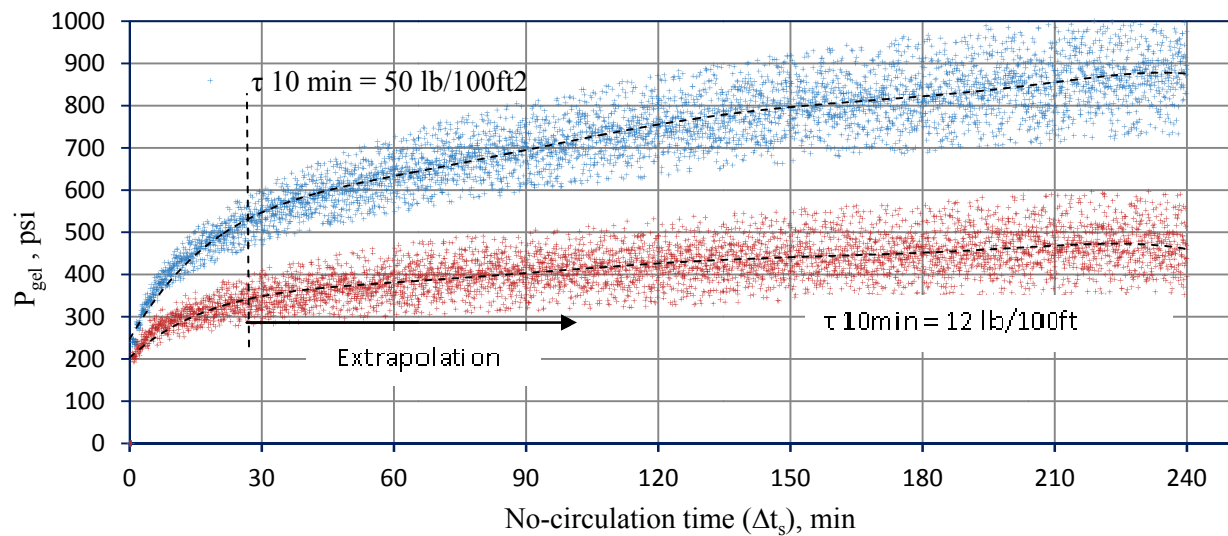
Fig. 6.17-Average and scattered values of pressure loss due flat and progressive gellation in time

Therefore, contribution of the gellation effect to improve analysis of CSS is only meaningful for late LOTs after long non-circulating times and drilling fluids with progressive gel strength. In all other cases, thermal effects would make most of contribution.
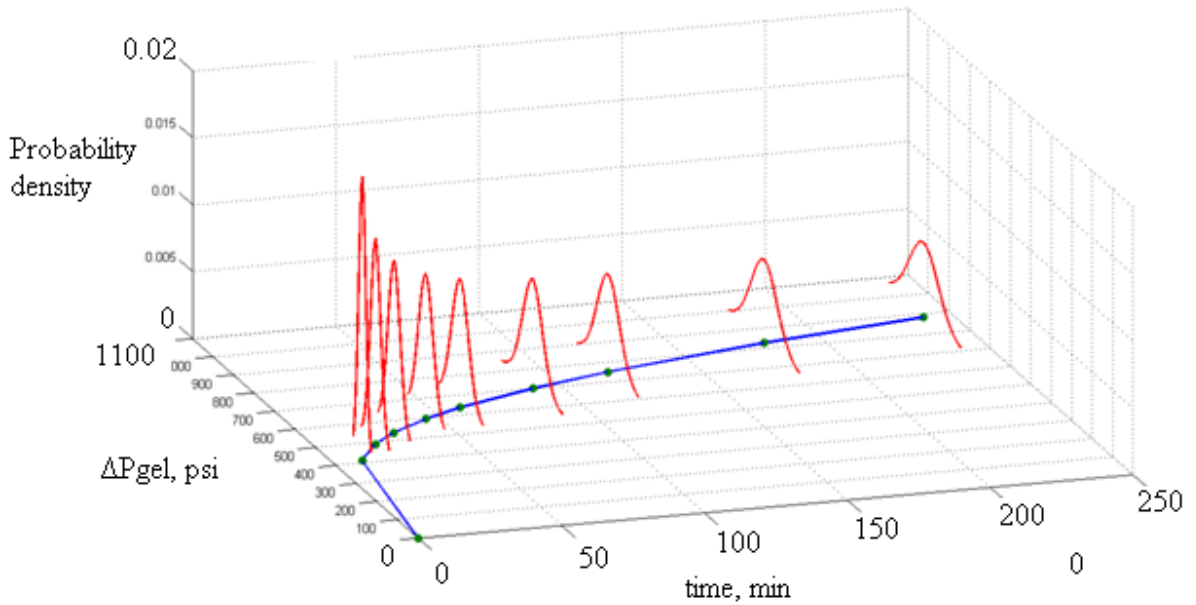
Fig. 6.18-Distributions of P_{gel} vs. Δt_s for mud with progressive gel strength

6.2.4. Summary of Probabilistic Assessment of CSS

Based on the quantitative risk analysis of casing shoe strength presented above, the following observations are made concerning precision/error of CSS determination:

1. Uncertainty of casing shoe strength value can be very significant – with 90 percent confidence interval reaching up to 25 percent of the calculated (average) value;

2. Regardless of depth, mud type or thixotropy, the CSS uncertainty PDF is negatively skewed and can be approximated by theoretical log-normal distribution. The log-normal pattern results from uncertain value of non-circulating time;

3. Uncertainty of CSS is controlled solely by thermal effects, formation Young's modulus (**E)** and and thermal expansion coefficient (α_T), and non-circulating time (Δt_s). The uncertainty could be greatly reduced if Δt_s was known and reported;

4. Contribution of Δt_s to CSS uncertainty increases with increasing depth, while the contribution of **E** decreases with depth;

5. Uncertainty of CSS decreases with increasing Δt_s. This is because most of the uncertainty is due thermal effects (term 4 in eqn.4.8), that contribute less to CSS for longer Δt_s. Thus, if non-circulating time is known, delayed LOT would render lesser error of CSS;

6. In this study, a characteristic 60-min non-circulating time was identified after which the CSS uncertainty is noticeably smaller. Thus, CSS estimation could be greatly improved by performing LOT after 60 minute static time;

7. Leak off test using water base mud (WBM) yields greater uncertainty of CSS than OBM. However, the difference is not significant. Thus, mud type does not have significant effect on CSS determination compared to E and Δt_s;

8. CSS estimation can be greatly improved by better estimation of Young's modulus of the rock below casing shoe.

6.3.   Probabilistic Assessment of Downhole Pressure due SCP

As discussed in section 5, subsurface failure of a well occurs if the down-pressure at the casing shoe (SCP_d) exceeds the casing shoe strength (CSS). SCP_d depends on the wellhead pressure (P_{csg}), and the hydrostatic pressure of the annular fluid in the annulus (P_{hyd}), as given by eqn.4.7. Sustained casing pressure transmission model is presented in section 5.1 to calculate SCP_d.

Quantitative risk analysis methodology was applied to the SCP_d model to determine the distribution of SCP_d values associated with the uncertainties of its model parameters. The distributed parameters of the probabilistic SCP_d model are summarized in Table 6-8.

Table 6-8-Experiment Matrix for SCP_d Uncertainty Study

	Exp 1	Exp 2	Exp 3
Annular mud density (ρ_m), ppg	8.35-17	9.4-17.5	8.35-14.7
Length of mud column (L_m), ft	270-10,020	9,900-10,350	5,200-10,200
10-minute gel strength ($\tau_{gel-10min}$), lb/100ft^2	1-107	3-30	13-67

As shown in Table 6-8, the input distributions of the SCP_d model is quite dispersed, i.e. with large difference between the minimum and maximum values. This is due to lack of knowledge of the annular fluid, since often the best estimate is the drilling mud left in the annulus during the cementing operation, disregarding possible alterations during life time of the well. Direct sampling or B-B test interpretation would provide valuable information about the annular fluid properties, however they are rarely performed. Yet, mud density is sufficient input for the software in Fig. 4.22 in Section 4.3 to run simulation of SCP_d.

Using probabilistic terminology the SCP$_d$ model in Section 4.2.1 and 4.2.2 can be described as,

$$\overline{E}\left(SCP_{\,d}\,\right) = \overline{E}\left(P_{\,csg}\, -\, \varDelta\,P_{\,gel}\, +\, P_{\,hyd}\,\right) \qquad 6.7$$

$$\overline{E}\left(\varDelta\,P_{\,gel}\,\right) = f_{\,1}\left[\overline{E}\left(\tau_{\,gel\,-10\,\,min}\,\right)\right] \qquad 6.8$$

$$\overline{E}\left(P_{\,hyd}\,\right) = f_{\,1}\left[\overline{E}\left(\rho_{\,m}\,\right), \overline{E}\left(L_{\,m}\,\right)\right] \qquad 6.9$$

where eqn.6.7 is modified eqn.4.7, eqn.6.8 is 4.19, and eqn.6.9 is 4.9.

The probabilistic SCP$_d$ model is examined in three theoretical experiments in Annulus B of the Study Well[1], as shown in Table 6-8. Schematic of the Study Well is shown in Fig. 3.22. Well-head pressure in Annulus B was assumed 4,168 psig to demonstrate a high-risk example. The depth and pressure of the gas reservoir is assumed unknown. The parameters that are constant throughout the experiments are listed in Table 6-9.

<div align="center">Table 6-9-Constant Parameters in SCP$_d$ Experiments</div>

Wellhead pressure, P$_{csg}$	4,168	psi
Cement sheath length, L$_c$	1,400	ft
Annulus geometry, d$_{ci}$, d$_{to}$	12.375 x 9.625	in
Depth to top of cement, D$_{TOC}$	10,385	in
Casing shoe strength, CSS [2]	11,120	psi

Aging time for the gel strength calculations using extrapolated thixotropy effect model (See section 4.2.2.3) was assumed 10 hours. The PDF models of the distributed parameters, ρ_m , L_m, and $\tau_{gel\text{-}10min}$ are assumed using the theoretical Perth distribution since they cannot take values lesser or greater than certain magnitudes (for example, L_m cannot extend above the surface or ρ_m cannot be smaller than 8 ppg). Perth distribution is defined for a minimum, maximum and most-likely values.

In Experiment 1, water base mud (WBM) with high inert solid content with highly polymeric liquid phase is assumed giving thermal stability of the mud vulnerable to high temperatures. (As discussed in section 5.1, at high temperatures exceeding the thermal stability of WBM, deterioration of the polymeric gel structure allows solid sagging [106].) In such case, the mud solids would settle on the bottom and the fluid

---

[1] In Section 6.2.2 we present detailed information including drilling, leak-off test, and geological data.
[2] CSS was calculated by the model presented in section 0.
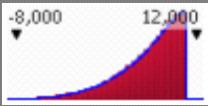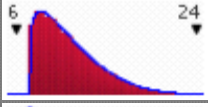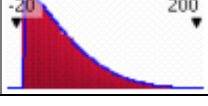
density would reduce to the density of water [118]. Besides, degradation of the polymers at high temperatures would result in partial loss of the gel structure. Moreover, for such mud in the annulus, a fast bleed-off followed by a gradual build-up during the B-B test would indicate a small gas cap, *i.e.* almost full annulus[1].

The minimum and maximum values of $\tau_{gel-10min}$, were set considering high likeliness of thermal degradation. The values of 1 and 107 lb/100ft^2 were set as the minimum and maximum, respectively and 5 lb/100ft^2 as the most-likely value for $\tau_{gel-10min}$.

Length of the mud column (L_m) was set considering the well configuration and high likeliness of annular fill-up. The minimum and maximum values were assumed 270 and 10,020 ft, respectively, and 9,900 ft was set as the most likely value. Input distribution of the mud density (ρ_m) was set between 8.35 and 17 ppg with a most likely value of 9 ppg, considering high likeliness of barite sag. The input distributions of the model parameters ρ_m, L_m, and $\tau_{gel-10min}$ are summarized in Table 6-10.

Table 6-10-Input distributions of parameters in Experiment 1

Performed By: kkinik1				
Parameter	Graph	5%	Most-Likely	95%
L_m	-8,000 12,000	270	9,900	10,020
ρ_m	6 24	8.35	9	17
$\tau_{gel-10min}$	-20 200	1	5	107

The output distribution of SCP$_d$ is shown in Fig. 6.19 together with best-fitted PDF of the theoretical normal distribution with mean value 6,627 psi and standard deviation 2,669 psi. The result shows a considerable dispersion of the SCP$_d$ values with 90% confidence interval being 128% of the mean value of 7,000 psi.

---

[1] Xu.R. et al. [17] identified characteristic bleed-off and build-up responses in B-B testing of SCP wells.
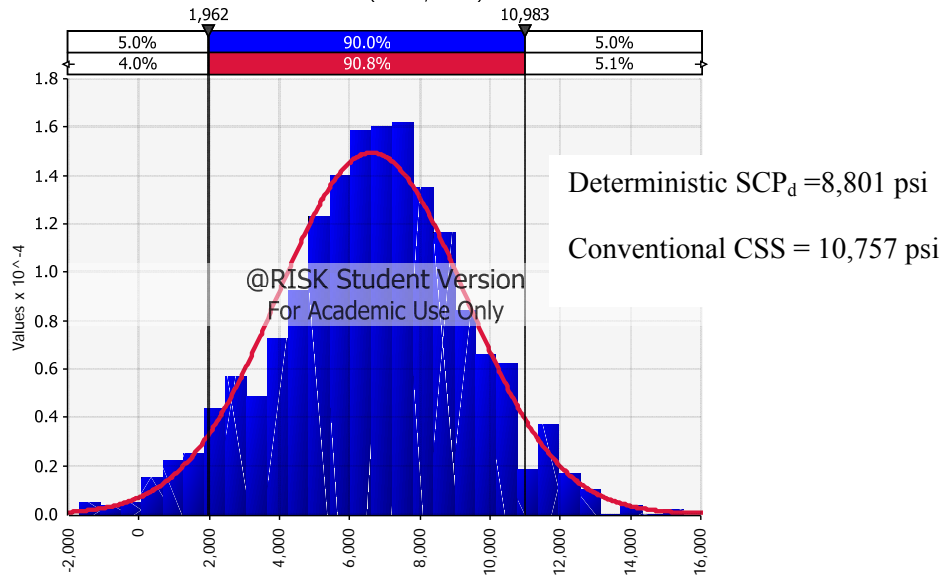
Fig. 6.19-Probabilistic SCP$_d$ - Experiment 1

Sensitivity of SCP$_d$ to its distributed model parameters has been analyzed. Fig. 6.20 shows Pareto plot of the parameters and their percent contribution to the SCP$_d$ variation. It shows 46% of the SCP$_d$ uncertainty is attributed to the mud length variation. It was observed that all three distributed parameters have noticeable effect on SCP$_d$ uncertainty and are statistically significant.
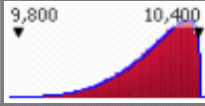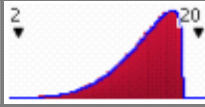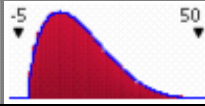
Fig. 6.20-Pareto plot of SCP$_d$ sensitivity to length, density and gel strength of mud- Experiment 1

In Experiment 2, oil base mud (OBM) is assumed in the annulus. As discussed in section 5.1, OBM is stable, at higher temperatures for long time without losing its properties [109]. Also, unlike extreme gellation during mud aging due bentonite flocculation (Exner *et al.*) [104], OBM is expected to maintain thixotrophic properties at higher temperatures because of sufficient concentration of organophilic clay [84].

The most likely value of $\tau_{gel-10min}$ is set 10 lb/100ft^2 with low permeability of progressive gellation. It is also assumed that B-B test was performed on the Annulus B, and the mud length is known better.

Table 6-11- Input distributions of the model parameters –Experiment 2

Performed By: kkinik1					
Parameter	Graph		5%	Most Likely	95%
L_m	9,800 — 10,400		9900	10000	10350
ρ_m	2 — 20		9.4	16.5	17.5
$\tau_{gel-10min}$	-5 — 50		3	10	30

Hence, a smaller range of for L_m was set from 9,000 to 10,350 ft. A most likely value of 16.5 ppg was set for ρ_m assuming that a sample of annular fluid was recovered from B-B testing. The distributed parameters of the probabilistic SCP_d model are listed in Table 6-11.

The output distribution of SCP_d is shown in Fig. 6.21. Also, the distribution was best fitted with the theoretical Beta-General distribution with mean value 11,687 psi and standard deviation 1,497 psi. The results show discrepancy between mean and mode, i.e. high probability of SCP_d greater than the average computed deterministically. Also, the 90% confidence interval is 42% fraction of the average value.

Deterministic SCP_d =11,730 psi

Conventional SCP_d = 10,757 psi

@RISK Student Version
For Academic Use Only
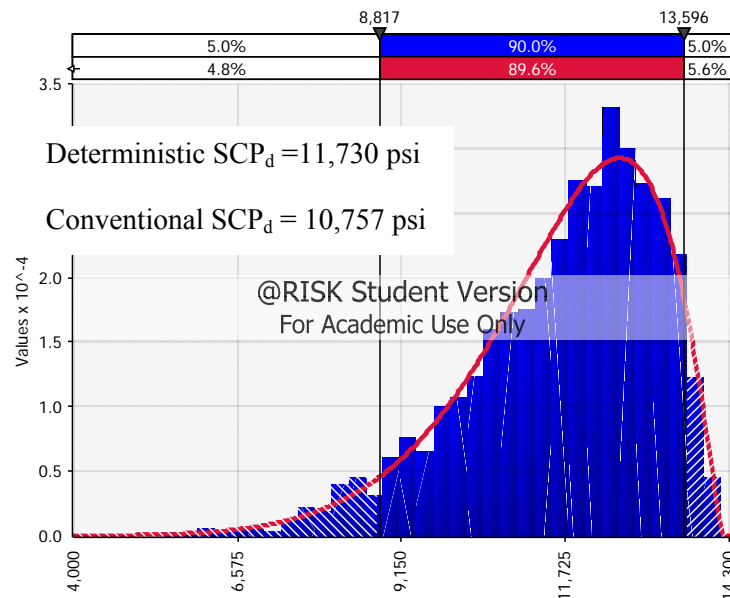
Fig. 6.21- Probabilistic SCP_d - Experiment 2

Sensitivity of SCP_d to its control parameters was also analyzed. Pareto plot of the distributed parameters is shown in Fig. 6.22. The effect of mud column length is relatively small, resulting from the better-known input value. Interestingly, the effects of other two parameters, density and gel strength, are very significant despite their small uncertainties. The strong effect of mud density results from the symmetry of its input value uncertainty.
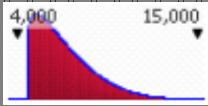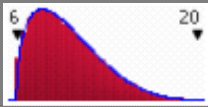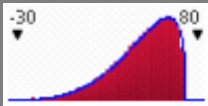
Fig. 6.22- Pareto plot of SCP_d sensitivity to length, density and gel strength of mud- Experiment 2

Experiment 2 demonstrates the improvement in SCP_d estimation due to excellent thermal stability and non-progressive gel properties of OBM (desired properties for all drilling fluids), As the two properties change little with time, hydrostatic pressure transmission in mature wells with SCP can be estimated better. Particularly, long term mud density reduction is critical for any predictions of subsurface consequences resulting from casing pressure.

In Experiment 3, WBM with low polymer concentration is assumed. In such a mud, the gel structure is formed mainly by the electro-chemical forces of reactive solids, that gives the mud greater thermal stability. However, despite its high strength, the gel structure is fragile, allowing slow static barite sag. (Saasen et al. [119] made experiments to relate viscoelasticity to static and dynamic barite sag potential. He suggested that the barite sag is initiated as the gravity force minus buoyancy force overcomes the gel strength times the surface area of a solid particle. He concluded that a high strength but fragile gel does not prevent barite sag. A fragile gel is the gel strength that quickly builds up at static conditions, but require small mechanical energy to be broken. A strong gel is the gel that requires greater shear stress to be applied for longer durations to be broken. A fragile gel behaves closer to the ideal viscoelastic respond of a fluid to shearing [68].). Thus, a low-density and high gel strength mud was assumed to occupy the annulus B. Also, it was assumed that no B-B tests have been performed in this annulus. Therefore, the length of the mud column is little known. A minimum value of 5,200 ft was set for L_m, assuming that the reservoir is abnormally pressured, i.e. greater than 0.465 psi/ft. The most likely value of 60 lb/100ft^2 was set for $\tau_{gel-10min}$ representing the high strength fragile mud thixotropy.

128

Table 6-12- Input distributions of the model parameters –Experiment 3

Performed By: kkinik1				
Parameter	Graph	5%	Most Likely	95%
L_m	4,000 ... 15,000	5200	6000	10200
ρ_m	6 ... 20	8.35	9	14.7
$\tau_{gel-10min}$	-30 ... 80	13	60	67

Shown in Fig. 6.23 is the SCP_d distribution resulting from the input distributions listed in Table 6-12. The PDF plot is a positively skewed. The distribution is best-fitted with the theoretical Log-Normal distribution having with mean value 6,220 psi and standard deviation 1,491 psi.

The Standard Error of Estimate (Standard deviation-mean ratio) is 24 percent and the 90% confidence interval is 73% fraction of the mean. Thus the SCP_d uncertainty is quite significant and the mean value computed from the determined model is likely to overestimate downhole pressure and its consequences.

Deterministic SCP_d =6,550 psi

Conventional SCP_d = 10,757 psi
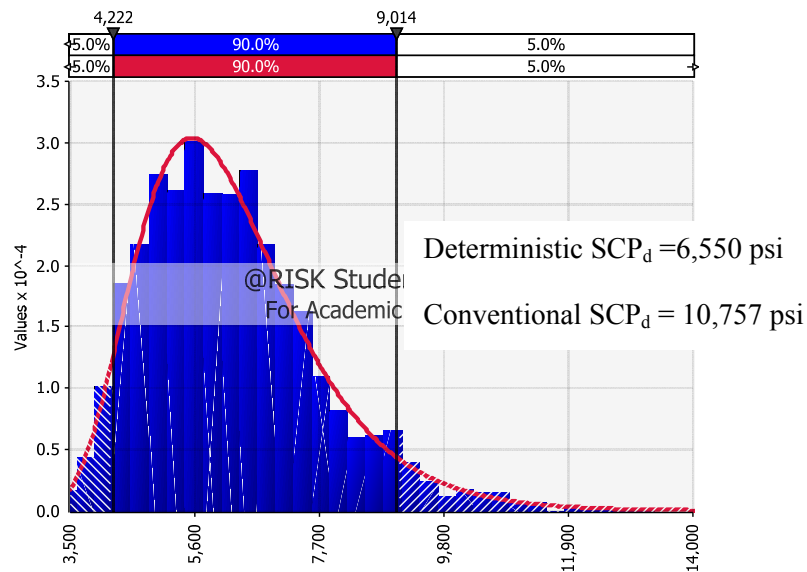
Fig. 6.23- Probabilistic SCP_d - Experiment 3

The sensitivity analysis of SCP_d to distributed input parameters using Pareto plot shows that all three parameters are significant. Unlike the other two scenarios (Experiments 1 and 2) all three parameters equally contribute to the precision of SCPd estimation. However the way they contribute is different.
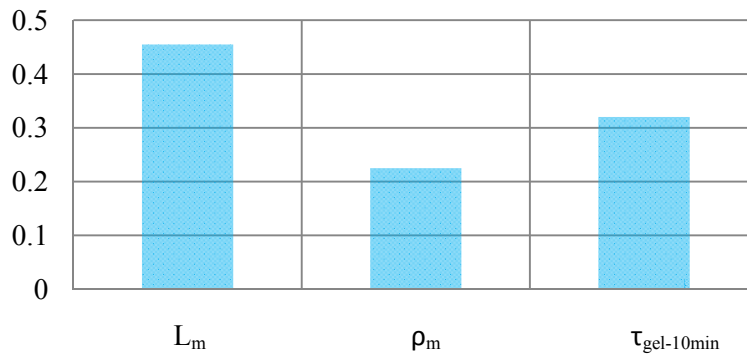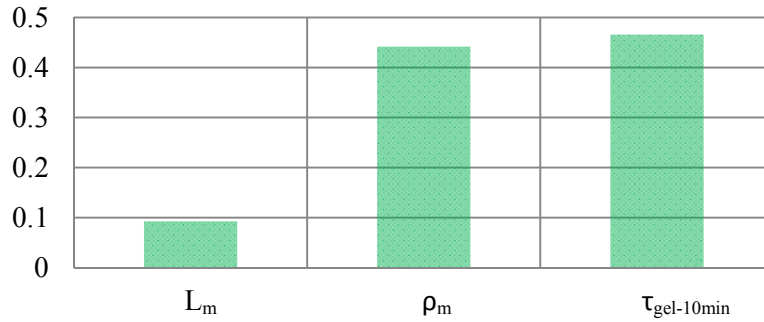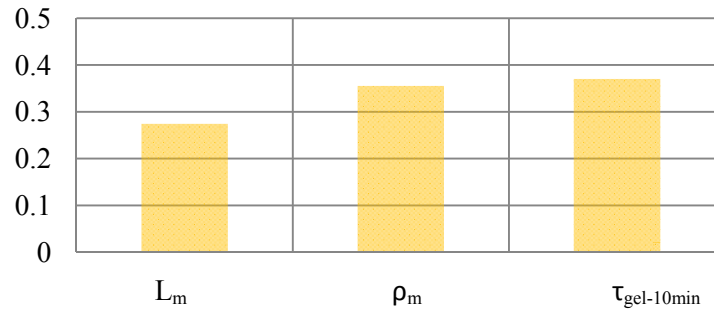
Fig. 6.24- Pareto plot of SCP_d sensitivity to length, density and gel strength of mud- Experiment 3

For the same value of SCPd at the surface highly progressive long-term gel strength reduces the transmission of the surface pressure downhole; so does the sagging of barite (due fragile gels) by causing decrease of the mud density in the annulus. A complete fill-up of annulus, on the other hand, would maximize downhole pressure.

The theoretical study, above, demonstrates the level of uncertainty of SCP_d for the recorded casing pressure. The following conclusions are made:

1. As SCP develops in mature producing wells, there is a significant level of uncertainty of estimated downhole pressure caused either by incomplete well drilling records and long term changes in the annular mud properties.

2. Variation of the estimated SCP_d values can be very significant with 90% confidence interval being 128% fraction of the average value and standard error of estimate from 24% to 38% depending upon the mud type and knowledge of the mud column length.

3. The SCP_d values predicted with the new deterministic model described in Section 5 may be either close to the most-likely value of SCP_d when PDF is normal, or would overestimate SCP_d when PDF is positively skewed, or would underestimate when PDF skewness is negative. Thus, prediction of SCP_d requires probabilistic assessment of skewness in addition to dispersion.

4. Accurate knowledge of mud column size is critical as it removes almost half of the downhole pressure uncertainty. An unknown mud column size would skew SCPd distribution to the right (negatively).

5. For the known surface casing pressure (SCP) and the size of mud column, ths SCPd uncertainty would result from time-dependent reduction of density (thermal degredation of WBM polymer mud, fragile gels) and thixotropy (progressive gels). Since both effects reduce bottom-hole pressure, the resulting SCPd distribution would be positively skewed.

130

6. Conventional approach to estimating SCP downhole (using mud density prior to cementing) would always result in overestimation with no clue on possible error.

6.4. Risk of Casing Shoe Failure

In Section 2, the mechanism and the critical conditions for well integrity failure at the wellhead, and at the casing shoe are described with equations 2.1 and 2.2, respectively. As discussed in Section 5, both failure mechanisms incorporate two individual elements, SCP (SCP_d) and casing shoe strength (CSS). In Sections 6.2 and 6.3 presented QRA methodology to describe these quantities as scholastic variables, and generate their probability density distributions associated with their uncertain input parameters. Quantitative assessment of the subsurface integrity loss, in this context, evaluates the load and failure elements conjunctively, and involves implementation of statistical methodology to calculate the resultant risk.

Ostebo *et al.* [120] outlined different types of risk and safety analysis methods to evaluate the safety of drilling operations associated with equipment failure. He presented Fault Tree Analysis (FTA) and Cause Consequence Analysis (CCA) techniques to define failure risk quantitatively, associated with the factors such as equipment reliability, human error and organizational factors, each defined as discrete frequencies. Klovning *et al.* [121] presented environmental risk assessment methodology based on design and operation data in a schematic manner.
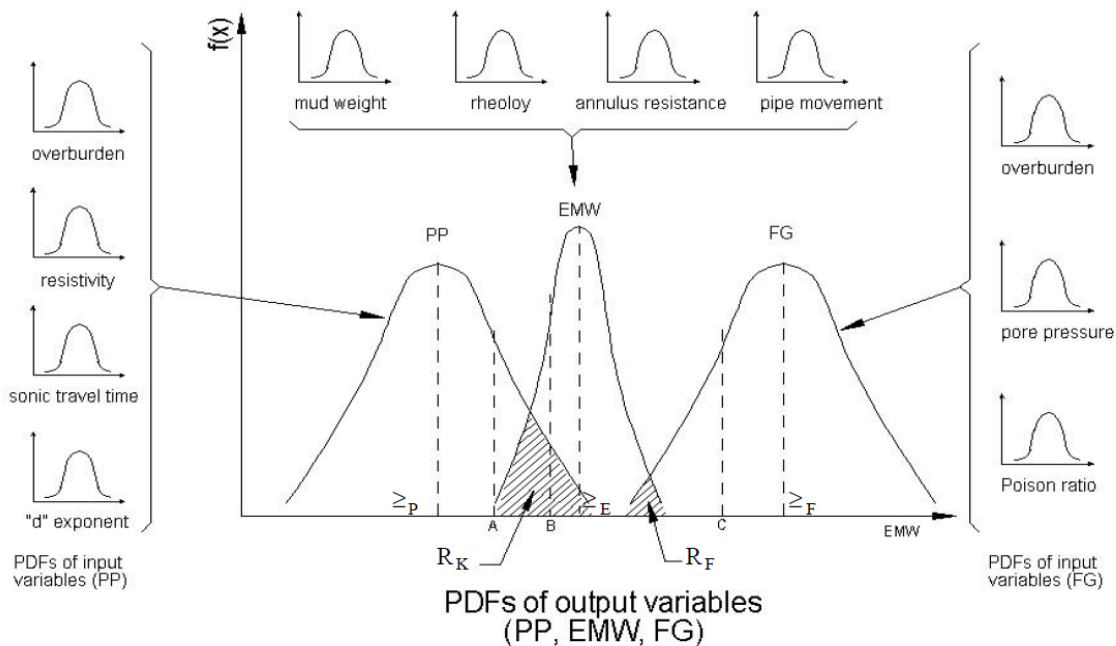
Fig. 6.25-Application of QRA to calculate the safe mud density window (Liang *et al.*,2002) [122]

Adams, *et al.* [123] used structural reliability approach to calculate risk-calibrated design factors to calculate the risk of blowout during drilling operation. Liang, *et al.* [122] applied QRA methodology to predict pore pressure and fracture gradients to determine the safe mud density window. As shown in Fig. 6.25, they described the uncertain model parameters as continuous probability densities to calculate the lower limit and upper limits for the mud density during drilling. Their study can be considered as a typical example of QRA application on wellbore integrity.They defined the risk of equivalent mud weight (EMW) to exceed the fracture gradient (FG) as,

$$R_F = P\left[\left(\mu_{EG}, \frac{\mu_{EG}}{\sqrt{\sigma_{EG}^2}}\right) \geq 0\right] \qquad 6.10$$

where the distributions if EMW and FG are described as normal distributions with a mean (μ) and variance (σ^2) as,

$\mu_{EG} = \mu_{EMW} - \mu_{FG}$

$\sigma_{EG}^2 = (\sigma_{EMW}^2 / n_1) + (\sigma_{FG}^2 / n_2)$

where n_1 and n_2 are the populations sizes of EMW and FG, respectively. The approach is a direct application of fundamental statistical methodology of hypothesis testing on an engineering problem to compute the risk of failure.

In this study, the mechanism of subsurface well integrity failure is considered as a similar load vs. strength mechanism, as discussed in Section 5 in detail. Calculation of risk of casing shoe failure considers the SCP_d and CSS's as two populations with known, but different means and standard deviations. The two models calculate the same measure (pressure) at the same point (casing shoe); however their calculation involves totally different operational set up, *i.e.* leak off test for the CSS and well-head pressure transmission during entire life of the well. Therefore, the two populations are considered independent. The Monte Carlo simulations performed in the QRA makes large numbers of statistical experiments, thus the central limit theorem suggests that the output samples obtained by the probabilistic CSS and SCP_d models represent their populations. This means that the sample variances approximate the population variance, allowing Z test statistics. Under these assumptions, the risk of CSS failure is calculated by one-tailed hypothesis testing on two population means, given as,

$H_O : \mu(SCP_d) = \mu(CSS)$

$H_A : \mu(SCP_d) > \mu(CSS)$

The risk is the probability value of the Z statistic of the difference between the means of the two independent populations, given as,

$$R_F = P\left[\left(\overline{SCP}_d - \overline{CSS}\right) > 0\right] \cong P\left[\left(\mu(SCP_d) - \mu(CSS)\right) > 0\right]$$ 6.11

One-tailed hypothesis testing was applied on the casing shoe of the three experiments presented in section 6.3. In Comparison 1, the CSS distribution calculated by the probabilistic CSS model in section 6.2.2.2 and the SCP_d distribution calculated by the probabilistic SCP_d model in section 6.3, Experiment 1 were considered. In Fig. 6.26 the distribution of the CSS shown in Fig. 6.7, and the distribution of SCP_d shown in Fig. 6.19 were plotted on the same graph.
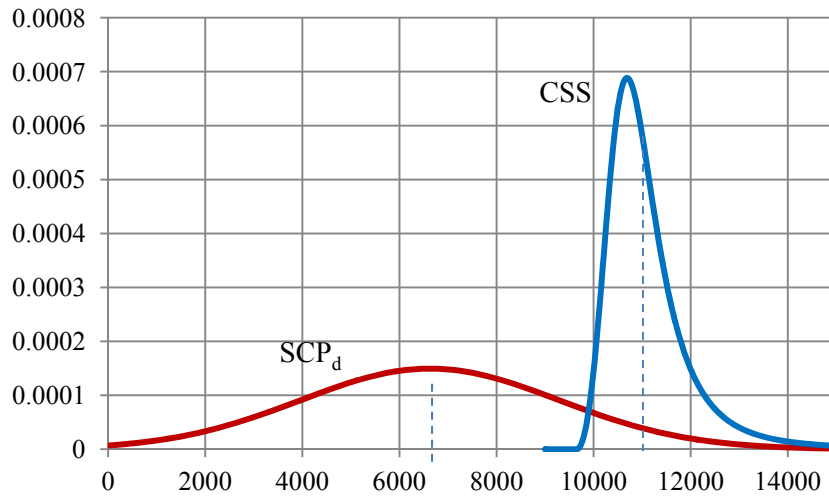
Fig. 6.26-Probability densities of SCP_d (Experiment 1) and CSS at 10,754 ft

The two distributions, as discussed, represent the probability distributions of the two elements of the failure mechanism. Distribution of SCP_d is observed to be more dispersed compared to that of CSS. That is, the model parameters of the SCP_d involve greater uncertainty due to measurement or interpretation limitations.

Shown in Fig. 6.27 is the cumulative density distribution (CDF) of the population of the difference of two individual populations, SCP_d and CSS, described as,

$$\overline{SCP}_d - \overline{CSS} \sim N\left(\mu_{SCP_d} - \mu_{CSS}, \frac{\sigma^2_{SCP_d}}{n_{SCP_d}} + \frac{\sigma^2_{CSS}}{n_{CSS}}\right)$$ 6.12

133

with the test statistics,

$$Z_{(\overline{SCP}_d - \overline{CSS})} = \frac{\overline{SCP}_d - \overline{CSS}}{\sqrt{\dfrac{\sigma^2_{SCP_d}}{n_{SCP_d}} + \dfrac{\sigma^2_{CSS}}{n_{CSS}}}} \qquad 6.13$$

Application of one-tailed hypothesis testing yielded 0.046 probability that the mean of the SCP_d is greater than the mean of CSS population, as shown in Fig. 6.27. In other words, the risk of subsurface failure is calculated 4.6%, which is considered statistically insignificant. This example shows that even though the expected value of the SCP_d is smaller than that of CSS, there is small risk of subsurface failure.
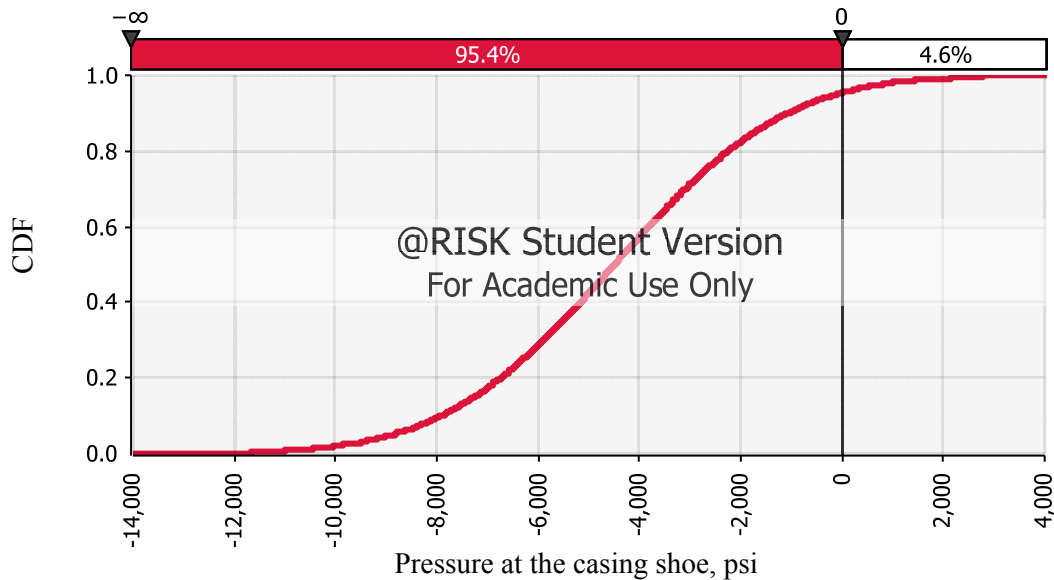
Fig. 6.27-CDF of the difference of two populations–(SCP_d-CSS) –Experiment 1

In Comparison 2, the CSS distribution calculated by the probabilistic CSS model in section 6.2.2.2 and the SCP_d distribution calculated by the probabilistic SCP_d model in section 6.3, Experiment 2 are considered. The two distributions are plotted on the same graph for comparison, as shown in Fig. 6.28.

As discussed in Section 6.3, Experiment 2 demonstrated a case of OBM in the annulus with high thermal stability and non-progressive gels. As shown in Fig. 6.28, the deterministic comparison of SCP_d and CSS (the population mean of SCP_d is 303 psi greater than that of CSS) would result in an arbitrary interpretation of predestined subsurface integrity failure. However, the QRA application suggests that there is significant risk of no-failure- 20.6%, as shown in Fig. 6.29.
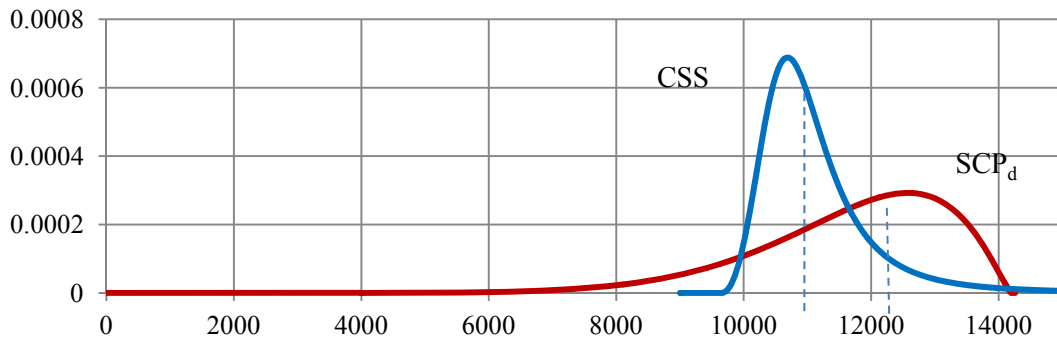
Fig. 6.28- Probability densities of SCP_d (Experiment 2) and CSS at 10,754 ft
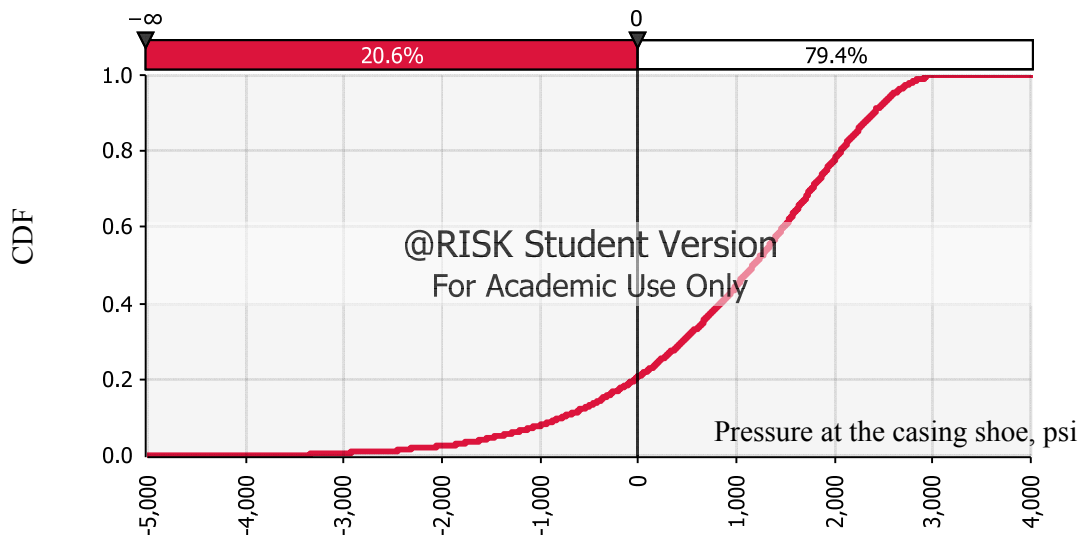
Fig. 6.29- CDF of the difference of two populations–$(SCP_d$-CSS) –Experiment 2

In Comparison 3, the CSS and SCP_d distributions shown in Fig. 6.23and Fig. 6.7, respectively, were compared, as shown in Fig. 6.30. As discussed in Section 6.3, Experiment 3 demonstrates the case for polymeric WBM with progressive gel strength in the annulus. As shown in Fig. 6.30, the deterministic comparison yields a 5,432 psi difference between SCP_d and CSS.

Application of QRA on the SCP_d and CSS yields small risk of failure, represented by the small intersection area restricted by the high end tail of the SCP_d and low end of the CSS distribution. Application of one-tailed hypothesis testing on the two populations yields 0.008 probability of SCP_d to exceed CSS, as shown in Fig. 6.31.
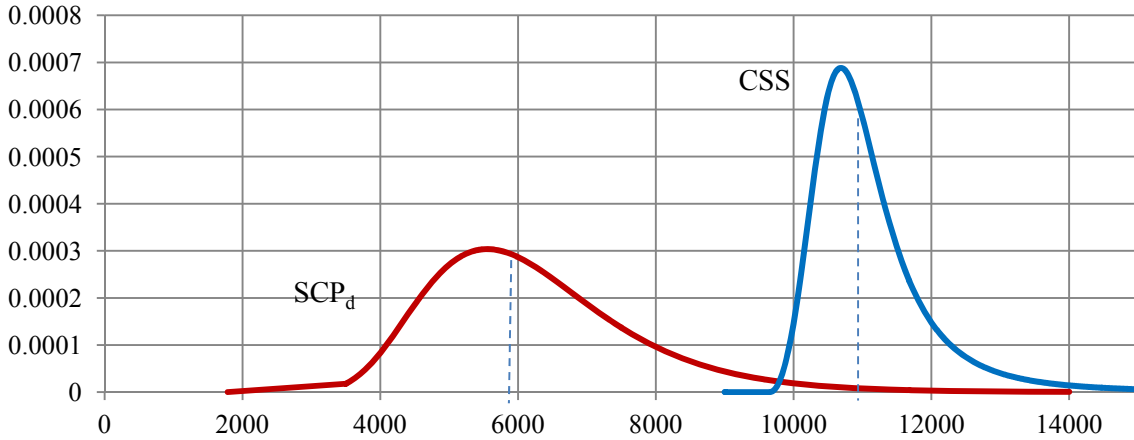
Fig. 6.30- Probability densities of SCP_d (Experiment 3) and CSS at 10,754 ft
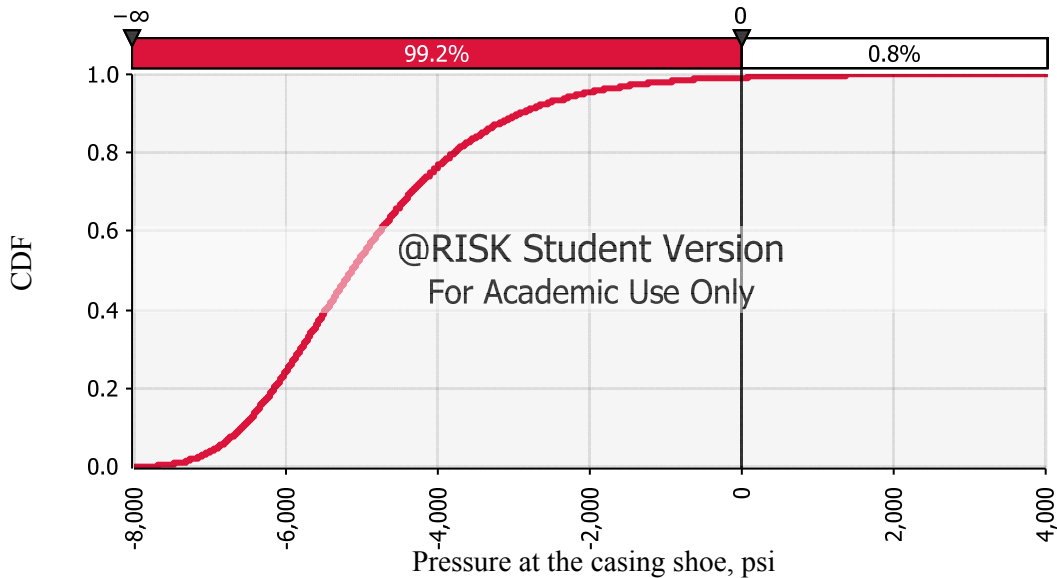
Fig. 6.31- CDF of the difference of two populations–(SCP_d-CSS) –Experiment 3

The comparisons of the SCP_d experiments with the CSS distribution at 10,740 ft presented above demonstrate three possible risk scenarios for the same annulus. It is observed that the dispersion and skewness of the SCP_d distribution controls the quantitative risk of subsurface failure. (CSS was observed to distribute always positively skewed, and its dispersion is controlled by non-circulating time during the leak-off test and Young's modulus of the rock being tested, as discussed in section 6.2.4.) The width of the input range and most likely values of ρ_m , L_m, and $\tau_{gel\text{-}10min}$ determine the subsurface failure risk. The observations in the three comparisons presented above are summarized in Table 6-13.

Table 6-13- Summary of the risk potential due input distributions

		L_m	ρ_m	$\tau_{gel-10min}$	calculated risk
Experiment 1	most likely value	high	low	low	low
	range	wide	wide	wide	
Experiment 2	most likely value	high	low	low	high
	range	narrow	wide	narrow	
Experiment 3	most likely value	low	low	high	negligible
	range	narrow	narrow	wide	

The analysis shows that knowledge of the length and density of the annular fluid column is critical for the risk assessment of subsurface well integrity failure. B-B test interpretation provides tool to analyze the pressure data that is readily available since well-head with SCP exceeding 100 psig are mandated to be regularly tested by the regulations [3]. Therefore, the probabilistic SCP_d model, in conjunction with B-B test interpretation, can be used as a QRA tool and allow the operators to focus on the most problematic annuli, reducing the overall operation costs and environmental risk. Note that the depth, reservoir pressure, and pressure rating of the casings play critical role on the subsurface risk. However, the Study Well demonstrates a typical example of a medium-depth fixed platform GOM, thus the conclusions made in this section have considerable applicability.

7. SUMMARY AND CONCLUSIONS

In this study, the risk of well integrity failure due sustained casing pressure has been evaluated considering different potential failure mechanisms - surface and subsurface. Comparison of failure mechanisms has been done and mathematical models have been developed to improve the reliability of the engineering calculations. Furthermore, the subsurface failure mechanism has been defined in statistical language to achieve the objectives of the study. The methodologies then have been tested on a GOM well, (Study Well) and substantial observations have been made. The discussions and conclusions, followed by a brief summary of the completed items can been listed as follows.

One of the main focuses of the study has been developing mathematical models and software to calculate the maximum gas emission rates from open end wells, and the casing shoe strength. Also, probabilistic approach is considered to apply quantitative risk assessment on the casing shoe strength, downhole pressure due SCP, and subsurface failure risk. Moreover, comparison of the critical well-head pressures causing surface and subsurface well integrity failure has been made. The critical values have been compared with the current regulatory criteria in two example wells (See Section 2).

Mathematical model and software for maximum gas emission rate (MER) from open ended SCP wells have been developed (See Section 3.3). The model applies linear flow of real gas through cement and two-phase modeling of gas flow through stagnant water base mud in annulus. The system performance is described as integrated cement top inflow and outflow mechanism. For the cement top outflow performance (CTOP), a new model has been proposed considering liquid unloading from annulus. The MER model has been tested on example well and effect of the control parameters have been investigated through theoretical experiments (See Section 3.3.3).

Mathematical model to calculate the casing shoe strength (CSS) has been developed (See Section 4.3). The model considers mud compressibility, effect of thixotropy on pressure transmission and thermally induced rock stresses. Also transient well temperature model has been implemented into the CSS model. Validation of each model component has been done by field data (See 4.2.1.2, 4.2.2.4, and 4.2.4.4). The model has been validated with PWD data with adequate accuracy (See Section 4.3.2). The model has been tested on Study Well to investigate the effects of mud compressibility, thixotropy and non-circulating time on CSS (See Section 4.3.3) and the results have been compared with the conventional CSS determination method (See Section 4.3.4).

Mathematical model to calculate the downhole pressure due SCP (SCP_d) has been developed (See Section 5.1). The model considers mud compressibility and thixotropy on the transmission of the surface pressure.

The model was applied on Study Well. Experiments on Study Well have been performed to illustrate the effect of the control parameters on SCP_d (See Section 5.2).

The CSS and SCP_d models have been described probabilistically (See Sections 6.2.1 and 6.3). The input parameters of both models have been described as scholastic variables and discussion on description of their distributions is presented. The probabilistic CSS model has been applied on Study Well's surface, upper and lower intermediate casing shoes (See Section 6.2.2). Also, significance of the system parameters has been investigated through theoretical experiments (See Section 6.2.3). The probabilistic SCP_d model has been tested on Study Well and theoretical experiments have been made to examine the effect of control parameters such as mud density, thixotropy and column length (See Section 6.3).

Quantitative risk analysis (QRA) methodology to determine the risk of subsurface well integrity failure has been presented. The method considers integrated probabilistic assessment of SCP_d and CSS using statistical hypothesis testing method (See Section 6.4). The method has been applied on Study Well and the risk of subsurface well integrity has been calculated quantitatively.

The following conclusions have been made throughout the study:

1. Solely the magnitude of the wellhead pressure (P_{csg}) does not fully describe the environmental risk of sustained casing pressure (SCP). Flow potential of the SCP well must also be considered. Also, wellhead pressure can constitute higher risk of integrity failure at the subsurface, i.e. at the casing shoe (See Table 2-1and Table 2-2).

2. For a SCP well having small leak size (cement sheath with low effective permeability), inflow performance of the cement controls the emission rate in case of a wellhead failure (See Fig. 3.25) . Even though P_{csg} is possibly high, the emission rate can be quite small (e.g. 0.067 MMscf/d from 1,200 md cement sheath).

3. For a SCP well having large leak size, length and density of the annular fluid column plays critical role in the resultant rate of gas emissions from failed wellhead (See Fig. 3.24). The proposed model should be used to calculate the actual flow potential to avoid overestimation of open end flow rate.

4. The ultimate casing shoe strength (CSS), which considers thermal equilibrium conditions, is almost always underestimated by the conventional interpretation of leak-off test (See Fig. 4.25 .

5. Progressive mud gellation causes overestimation, and mud compressibility causes underestimation of the bottomhole pressure (See eqn.4.8). Neglecting thermally effected rock stresses causes underestimation of the CSS (See Fig. 4.27, Fig. 4.28, and Fig. 4.29). The effect of mud thixotropy and compressibility

counteract, and the magnitude of the net underestimation is controlled by the thermal stresses (See Fig. 4.30).

6. Thermal stress depends on the borehole mud temperature, thus directly dependent to the non-circulating time period during a LOT. Performing the LOT immediately after ceasing the circulation would result in significant underestimation of the ultimate CSS.

7. Commonplace calculation of downhole pressure due SCP (SCP_d) neglects development of mud gellation over time in static conditions and mud density variation due mud aging (See Fig. 5.4and Fig. 5.5). SCP_d is mostly overestimated by the conventional method (See Fig. 5.3). The new methodology should be used to calculate the actual SCP_d.

8. The smallest SCP_d is created by a short column of low density mud with progressive gels. The largest SCP_d is created by a long column of high density mud with fragile gels.

9. Thermal stability of the annular fluid due mud aging plays critical role in the magnitude of SCP_d (See Section 5.1). If the mud maintains its thermal stability, gellation partially prevents the transmission of P_{csg} to the casing shoe. Else, if the thermal stability is lost, solids tend to sag reducing the mud density significantly. Therefore, in both cases the mud aging tries to reduce SCP_d.

10. The length and density of the mud in the annulus can be estimated by direct measuring or SCP test (B-B test) interpretation. However, mud thixotropy remains its uncertainty.

11. The ultimate CSS determined by LOT may involve significant uncertainty, with 90 percent confidence interval reaching up to quarter of the mean value (See Fig. 6.5).

12. The probability density distribution of the CSS follows a characteristic negatively skewed bell curve, which can be characterized by the theoretical log-normal distribution (See Fig. 6.11). The log-normal distribution is an indirect result of the model parameter, non circulating time (Δt_s).

13. CSS uncertainty is solely controlled by the rock's Young's modulus (**E**), thermal expansion coefficient (α_T) and non-circulating time (Δt_s). Sufficient period of non-circulating time before the LOT would noticeably reduce the uncertainty of CSS (See Fig. 6.6).

14. With increasing depth, CSS uncertainty increases while the contribution of Young's modulus decreases by depth (See Section 6.2.2).

15. With increasing Δt_s, CSS uncertainty decreases since most of the uncertainty is due thermal effects (See eqn.4.8). Therefore knowledge of Δt_s would yield in less error in CSS determination.

16. Regardless of depth, formation, and mud type, a characteristic 60 minute non-circulating time has been identified above which the uncertainty of CSS greatly is reduced due thermal equilibrium between the mud and the rock (See Sections 6.2.2 and 6.2.3).

17. CSS uncertainty for a WBM well is greater than that of an OBM since WBM cooling down and heating up of WBM requires more heat, resulting in greater error in CSS estimation (See Fig. 6.15).

18. Accuracy in the Young's modulus estimation would greatly reduce the CSS uncertainty since E is commonly the most uncertain rock parameter (See eqn.4.23).

19. Long term changes in mud properties due mud aging and incomplete well data result in noticeable uncertainty in estimated downhole pressures (SCP_d) in SCP wells (See Section 6.3).

20. The uncertainty of the SCP_d can be quite dispersed, with confidence interval exceeding 128 percent of its mean value and standard error of estimate from 24 to 38 percent depending upon the mud condition and length (See Section 6.3).

21. The SCP_d values predicted by the deterministic model presented in Section 5.1 may either be approximate to the most-likely SCP_d is the distribution of SCP_d is normal, or overestimate SCP_d if it is distributed positively skewed, or underestimate SCP_d if the skewness is negative. Therefore skewness of the SCP_d distribution is a key statistical measure in addition to the dispersion of the distribution.

22. Uncertainty in column length and/or density would result the SCP_d distribution be negatively skewed. An accurate knowledge of the mud column length and density would remove almost 50% of the SCP_d uncertainty.

23. For a known wellhead pressure at the surface, uncertainty of SCP_d is mainly due time dependent mud properties. Density reduction due to the loss of thermal stability (barite sag due deterioration of the polymers, and fragile gels) and thixotropy (development of progressive gels) results in reduction of SCP_d and its distribution be positively skewed (See Section 6.3).

24. Conventional approach using mud density prior to cementing does not provide any insight of the possible error in SCP_d estimation (See Section 6.4). Knowledge of the length and density of the annular fluid column is critical for the quantitative risk assessment (QRA). The probabilistic methodology presented here provides powerful tool for the risk assessment of subsurface well integrity failure due SCP.

REFERENCES

[1] API Recommended Practice 90, First Edition, "Annular Casing Pressure Management for Offshore Wells," August 2006.

[2] Stuart L. Scott, Wojciech Manowski Adam T. Bourgoyne, "A Review of Sustained Casing Pressure Occuring on the OCS," Mineral Management Services, MMS 2000.

[3] MMS 30 CFR Part 250, "Annular Casing Pressure Management for Offshore Wells," May 4, 2010.

[4] EUB Canadian Energy and Utilities Board, Jan, 2003.

[5] NORSOK Standard D-010, "Well Integrity in Drilling and Well Operations," 2004.

[6] API Recommended Practice 65 - Part2, "IsolatingPotential Flow Zones During Well Construction," American Petroleum Institute, May 2010.

[7] Henry L. Doherty, "Environmental Engineering for Exploration and Production Activities," SPE, Monograph Series Volume 18 1999.

[8] Wilson Jane Mary and D. Frederick Jesse: *Environmental Engineering for Exploration and Production Activities*, Monograph Volume 18 SPE Series, Ed.: SPE, 1999.

[9] Watson D., Brittenham T., and Moore P.: *Advanced Well Control*. Richardson, Texas: SPE Textbook Series, 2003.

[10] Stefan T. Orszulik, *Environmental Technology in the Oil Industry*.: Springer, 2008.

[11] Xu, R. and Wojtanowicz, A.K.: "Diagnostic Testing of Wells With Sustained Casing Pressure – An Analytical Approach," *Louisiana State University*, 2003.

[12] Rostami, S.A., "Comparison of Surface and Subsurface Well Integrity Failure Criteria," Louisiana State University, Baton Rouge, Class Assignment 2011.

[13] David, W.R., "Microannulus Leaks Repaired with Pressure-Activated Sealant," *SPE 91399*, 2004.

[14] Grace, R.D., *Advanced Blowout and Well Control*. Houston TX: Gulf Publishing, 1994.

[15] Stuart L. Scott , James B. Regg Adam T. Bourgoyne, "Sustained Casing Pressure in offshore Producing Wells," in *OTC 11029*, Houston, TX, 1999.

[16] U.S. Department of the Interior Minerals Management Services, "Investigation of Loss of Control Grand Isle Block 90, Well C-7ST OcS-G 4003," MMS/BOEMRE, New Orleans, MMS-2003-068, November 14, 2002.

[17] Rong Xu, "Analysis of Diagnostic Testing Of Sustained Casing Pressure In Wells," *LSU*

Dissertation, 2002.

[18] John W. Lee & Robert A. Wattenbarger, *Gas Reservoir Engineering*.: SPE Textbook Series, Vol. 5, 1996.

[19] API Recommended Practice 65- Part1, "Cementing Shallow Water Flow," American Petroleum Institute, 2003.

[20] Somei Nishikawa, Xu Rong Andrew Wojtanowicz, "Diagnosis And Remediation Of Sustained Casing Pressure In Wells," Louisiana State University, US Department of Interior Final Report 2001.

[21] Ahmadi, G., Smith, D.H. Nazridoust K., "New Friction Factor Correlation for Laminar Single Phase Flows through Rock Fractures," *J.Hydrol*, pp. 329, 315-328, 2006.

[22] Shengkai Duan, "Progressive Water-Oil Transition Zone to Transverse Dispersion Near the Well," Louisiana State University, Baton Rouge, Thesis Report 2009.

[23] AlHussaiyn, M., "The Flow of Real Gasses through Porous Media", Journal of Petroleum Technology," 1966.

[24] Amol A. , Jyesthtaraj B. Joshi Kulkarni, "Bubble Formation and Bubble Rise Velocity in Gas-Liquid Systems: A Review," *Ind. Eng. Chem. Res.* , pp. 44, 5873-5931, 2005.

[25] Ovadia Shoham, *Mechanistic Modelling of Gas-Liquid Two-Phase Flow in Pipes*. Tulsa, OK: SPE, 2006.

[26] Brill, J. P. and Mukherjee, H., *Multiphase Flow in Wells*. Richardson, TX: SPE, 1999.

[27] Ansari, A.M., et al., "A Compressive Mechanistic Model for Two-Phase Flow in Wellbores," *SPEPF*, vol. AIME, 297, p. 143;Trans, May 1994.

[28] Hasan, A.R. and Kabir, C.S., "A Study of multiphase Flow Behavior in Verticle Wells," *SPEPE*, pp. 263-285, May 1988.

[29] Caetano, E.F., Shoham, O., and Brill, J.P., "Upward Verticle Two-Phase Flow through an Annulus, Part I: Single-Phase Friction Factor, Taylor Bubble rise Velocity and Flow-Pattern Prediction," *J. Energy Res. Tech.*, pp. 114,1, Mar 1992.

[30] Barnea, Y.M., Dukler, A.E., and Taitel,D., "Modelling of Flow Pattern Transitions for Steady Upward Gas-Liquid Flow in Vertical Tubes," *AIChE J.*, vol. 26, p. 345, 1980.

[31] Haciislamoglu, M. and Langlinais, J., "Non-Newtonian Flow in Eccentric Annuli," *J.Energy Res. tech*, pp. 112,163, June 1990.

[32] Fernando S. Flores Avila, John Rogers Smith, Adam T. Bourgoyne, and Darryl Bourgoyne, "Experimental Evaluation of Control Fluid Fallback During Off-bottom Well Control: Effect of

Deviaton Angle," in *IADC/SPE 74568*, Dallas, TX, 2002.

[33] Kulkami, A. and Joshi, B., "Bubble Formation and Bubble Rise Velocity in Gas-Liquid Systems: A Review," *American Chemical Society*, 2005.

[34] Harmathy, T.Z., "Velocity of Large Drops and Bubbles in Media of Infinite or restricted Extend," *AIChE J.*, p. 6281, 1960.

[35] Rodrigue, D., "A general correlation for the rise velocity of single gas bubbles," *Can.J. Chem. Eng.* , pp. 82 (2),382-386, 2004.

[36] Akthar, M., "CFD Simulations for Continuous Flow of Bubbles through Gas-Liquid Columns: Application of VOF," 2007.

[37] Urseanu, M.I., "Scaling up bubble column reactors.," 2000.

[38] Zuber, N., and Hench, J., "Steady-State and Transient Void Fraction of Bubbling Systems and Their Operating Limits. Part 1: Steady State Operation," 1962.

[39] Luo, X., Zhang, J., Tsuchiya, K., and Fan, L.S., "On the rise velocity of bubbles in liquid-solid suspensions at elevated pressure and temperature," *Chem. Eng. Sci.*, pp. 52(21-22), 3693, 1997.

[40] Rader, D.W., Bourgoyne, A.T., and Ward, R.H., "Factors Affecting Bubble Rise Velocity of Gas Kicks," *Journal of Petroleum Engineering*, 1975.

[41] Dumitrescu, D.T., "Stromung and Einer Luftbluse in Senkrechten Rohr," *ZAAM* , pp. 139-149, 1943.

[42] Casariego, V., "Generation, Migration and Transportation of Gas Contaminated Regions of Drilling Fluid," 1987.

[43] Mark D. Zoback, *Reservoir Geomechanics*.: Cambridge University Press, 2007.

[44] Fairhurst, B.E. and Haimson, C., "Initiation and extension of Hydraulic Fractures in Rocks," *SPE Journal*, September 1967.

[45] Christopher D. Hawkes, et al., "Analysis if In-situ Stress Regime in the Alberta Basin, Canada, for Performance Assessment of CO2 Geological Sequstration Sites," in *Fourth Annual Conference on Carbon Capture and Sequstration DOE/NETL*, May 2005.

[46] Wojtanowicz, A.K. and Zhou, D., "Shallow Casing Shoe Integrity Interpretation Technique," in *IADC /SPE 67777*, Amsterdam, 2001.

[47] Eric Van Oort and Richard Vargo, "Improving Formation Evaluation Strength tests and Their Interpretation," in *SPE/IADC*, 2007.

[48] McMordie J., Bland W.C., and J.M. Hauser, "Effect of Temperature and Pressure on the Density of

Drilling Fluids," in *SPE Annual Technical Conference and exhibition*, New Orleans, 1982.

[49] Babu, D.R., "Effects of P-p-T Behaviour of Muds on Static Pressures during Deep Well Drilling - Part 2," *SPE Drilling& Completion*, p. 91, 1996.

[50] Mullen G. , Gonzales, Y. et al. Bland R., "HTHP Drilling Fluids Challenges," in *IADC/SPE*, Banghok, Thailand, 2006.

[51] Ekwere J.Peters and Martin E. Chenevert and Chunhai Zhang, "A Model for Predicting the Density of Oil-Base Muds at High Pressures and Temperatures," *SPE Drilling Engineering*, pp. 141-148, June 1990.

[52] Hoberock, L.L., Thomas, D.D. and Nickens, H.V., "Here's How Compressibility and Temperature Affect Bottom Hole Mud Pressure," *Oil & Gas Journal*, vol. 64, p. 159, March 1982.

[53] Thomas, D.C. and Nickens, H.V., and Hoberock L.L., "Bottom Hole Mud Pressure Variations Due to Compressibility and Thermal Effects," in *IADC Drilling Technology Conference*, Houston, TX, March, 1982.

[54] White, R.J., "Bottom Hole Pressure Reduction Due to Gas Cut Mud," *Society of Petroleum Engineers*, vol. volume 9, Number 7, pp. 774-G, July 1957.

[55] "Well Control Manual," Louisiana State University Dept. of Petroleum Engineering, Baton Rouge, LA, 2009.

[56] Patrick, L. and Bourgoyne, A., O'Bryan, Jr.,"Swelling of Oil Based Drilling Fluids Resulting From Dissolved Gas," *SPE Drilling Engineering*, pp. 149-155, June 1990.

[57] Standing, M.B., "Volumetric and Phase Behavior of Oil Field Hydrocarbon Systems," Richardson, TX, 1981.

[58] Huang, D.C., and VanSlyke, E.T.S., "Predicting Gas KIck Behavior in Oil Based Drilling Fluids Using a PC Based Dynamic Wellbore Model," *IADC/SPE 19972*, March 1990.

[59] Standing, M.B., "A Pressure-Volume-Temperature Correlation for Mixtures of California Oils and Gasses," *Drill. & Prod. Prac. API*, vol. 87, p. 275, 1947.

[60] McCain, W.D. Jr., *The Properties of Petroleum Fluids*. Tulsa, OK: Penn Well Publishing, 1990.

[61] Vasquez, M. and Beggs, H.D., "Correlation for Fluid Physical Property Prediction," *JPT*, pp. 968-70, June 1980.

[62] McCain, W.D. Jr., "Reservoir water Property Correlations State of Art," in *SPE 18573*, Richardson, TX.

[63] Meehan, D.N., "A Correlation for Water Compressibility," *Petroleum Engineer*, pp. pp. 25-126, November 1980.

[64] Dranchuk, P.M., and Abou-Kassem, J.H., "Calculation of Z Factors for Natural Gases Using Equation of State," *J. Cdn. Pet. Tech.*, pp. 34-36, July-Sep 1975.

[65] Adam T. Bourgoyne, Patrick L. O'Bryan, et al., "An Experimental Study of Gas Solubility in Oil Based Drilling Fluids," *SPE Drilling Engineering*, pp. 33-42, March 1988.

[66] Peters, E.J., Chenevert, M.E. , and Zhang, A., "A Model for Predicting the Density of Oil-Muds at High Pressures and Temperatures," *SPEDE*, vol. 58, pp. 45-47, June 1990.

[67] Rolv Rommetveit, Bjarne Aas, Helga Gjeraldstveit Knut S. Bjorkevoll, "Transient Gel Breaking Model For Critical Wells Applications with field Data Verification," in *IADC/SPE 79843*, Amsterdam, 2003.

[68] Jason Maxey, "Txitrophy and Yield Stress Behavior in Drilling Fluids," in *AADE-07NTCE-37*, Houston, TX, 2007.

[69] Terry Hemphill , William Gusler and Gregory Mullen William Dye, "Correlation of Ultra Low Shear Rate Viscosity and Dynamic Barite Sag in Invert Emulsion Drilling Fluids," in *SPE 56636*, Houston, TX, 1999.

[70] Herzhaft, B. and Ragouillaux, A., "How to Unify Low Shear Rate Rheology and Gel Properties of Drilling Muds: A Transient Rheological and Structural Model for Complex Well Applications," in *IADC/SPE*, Miami, FL, 2006.

[71] Thonhauser, G. and Zoellner, P., "Automated Real-Time Drilling Hydraulics Monitoring," in *IADC/SPE 140298*, Amsterdam, 2011.

[72] Negrao, C.O.R., Oliveira, G.M., and Franco, A.T., "Pressure Transmission in Gelled Drilling Fluids in Deepwater Environments," in *IADC/SPE 128859*, New Orleans, LA, 2010.

[73] Cheng, DC-H and Evans, F., "Phenomenological Characterization of the Rheological behavior of Inelastic Reversible Thixotrophic and Antithixotrophic Fluids," *Brit. J. Appl. Phys.*, vol. 16, pp. 1599-1617, 1965.

[74] Paulo R.S., and Eduardo, S.S. Dutra Mendes, "A Viscosity Function For Viscoplastic Liquids," *An. Trans. Nordic Rheo. Soc.*, vol. v.12, pp. 183-188, 2004.

[75] Peder, C.F., Mewis, J., and Moller, D.B., "Yield Stress and Thitrophy: on the Difficulty of Measuring Yield Stress and Thixotrophy," *Soft Marter*, vol. v.2, pp. 274-283, 2006.

[76] Andy Popplestone and Ahmadi Tehrani, "Modelling the Gelling Properties of Water Based Drilling Fluids," in *AADE-NTCE-12-02*, New Orleans, LA, 2009.

[77] Bartlett, L.E., "Effect of Temperature on the Flow Properties of Drilling Fluids," in *SPE 1816*, Dallas, 1967.

[78] Dahab, A.S., "Thermal stability of Drilling Fluids Prepared from Saudi Palygorskite," *JCPT*, 1991.

[79] Annis, M.R., "High-Temperature Flow Properties of Water Base Drilling FLuids," *Journal of Petroleum Technology*, p. 1074, May 1967.

[80] Adam T. Bourgoyne, *Applied Drilling Engineering*., 1986.

[81] Coffin, R.C., Byrd C.B., DeWolfe, R.V., "Less Toxic Oil Muds," in *SPE 11892*, Aberdeen, 1983.

[82] Frederick, F.B., Growcock, T.P., "Operational Limits of Synthetic Drilling Fluids," in *OTC 7579*, Houston, TX, 1994.

[83] Leal, R.A., Goncalves, R.A.F., Gandelman, J.T., et al. "Study of Gelation of Freezing Phenomena of Synthetic Drilling Fluids in UltradeepwaterEnvironments," in *IADC/SPE 105881*, Amsterdam, 2007.

[84] Politte, M.D. "Invert Oil Mud Rheology as a Function of Temperature and Pressure," in *SPE* , New Orleans, 1985.

[85] Gonzales T.K. Perkins, J.A. "Changes in Earth Stresses Around a Wellbore Caused by Radially Symterical Pressure and Temperature Gradients," *SPE 56th Annual Fall Technical Conference and Exhibition*, October 1981.

[86] Sauzay, V.M., Maury, J-M., "Borehole Instability: Case Histories, Rock Mechanics Approach and Results," in *SPE/IADC 16051*, New Orleans, March 1987.

[87] Joseph Schmidt, Carey Naquin , Scot Ellis Gregory Pepin, "Effect of Drilling Fluid Temperature on Fracture Gradient: Field Measurements and Model Predictions," in *ARMA/NARMS 04-527*, Houston, TX, 2004.

[88] Hettema, M.H.H., et al., "Analysis of Lost Circulation During Drilling in Cooled Formations," in *SPE 90442*, Houston, TX, 2004.

[89] Fjaer, R.M., et al., *Petroleum Related Rock Mechanics*, 2nd ed. New York: Elsevier, 2008.

[90] Charlez, Ph. A., *Rock Mechanics: Petroleum Applications*., 1997.

[91] Raymond, L.R. "Temperature Distribution in a Circulating Drilling Fluid," *JPT*, p. 333, 1969.

[92] Crawford, A.P., Paul Tragesser B., , et al. "A Method for Calculating Circulating Temperatures," *JPT*, 1966.

[93] Couch, H.H., Keller, C.C., et al. "Temperature Distribution in Circulating Mud Columns," *Society of Petroleum Engineers Journal*, pp. 23-30, 1971.

[94] Charles, S. and Samuel, C. Holmes, S., "Calculation of Circulating Mud Temperatures," *JPT*, p. 670, 1970.

[95] Manuel Eduardo , Benjamin Bloys, James, et al. Gonzales, "Increasing effective Fracture Gradients

by Managing Wellbore Temperatures," in *IADC/SPE 87217*, Dallas,TX, 2004.

[96] Cobb, W.L., Dowdle, W.M., "Static Formation Temperature From Well Logs - An Emprical Method," *JPT*, p. 1326, 1975.

[97] Hasan A.R., and Kabir, S.C., "Predicting Multiphase Flow Behavior in a Deviated well," *SPEPE*, p. 474, Nov 1988.

[98] Kabir, A.R., Hasan, C.S., "Static Reservoir Temperature Determination from Transient Data After Mud Circulation," 1994.

[99] Kabir, A.R. , Hasan, C.S., *Fluid Flow and Heat Transfer in Wellbores*. Richardson, TX: SPE , 2002.

[100] MI Swaco, *Drilling Fluids Handbook.*, 1998.

[101] Annis, M.R., "Retention of Synthetic Based Drilling Material on Cuttings Discharged to the GOM," API, Washington DC, 1997.

[102] Mohammed Shahjahan Ali, "The Effects of High Temperature and Aging on Water Based Drilling Fluids ," King Fahd University, Dhahran, M.Sc. Thesis 1990.

[103] Ashiru O.S., Shokoya, O.A., et al., "The rheology and corrosivity of water based drilling fluids under simulated downhole conditions," King Fahd University, Dhahran, 1997.

[104] Craft, J.D. and Exner, B.C., "Effects of Temperature on the Viscosity of Some Gulf Coast Drilling Muds," *Petroleum Transactions, AIME*, vol. Volume 103, pp. 112-116, 1933.

[105] Dejumo, F.A., and Makinde, A.D., "Modelling the effects of temperature and aging time on the rheological properties of drilling fluids," *Petroleum and Coal*, p. 1337, Nov 2010.

[106] Nicholas, N.A., and Andreas, C., et al., "Shear Rejuvenation, Aging and Shear Banding in Yield Stress Fluids," *Journal of Non-Newtonian Fluid Mechanics*, vol. Vol 158, no. 1-3, pp. 6-17, May 2009.

[107] Svoboda Charlie, "Optimizing High-Temperature Kill Pills: The Åsgard Experience," in *SPE/IADC*, Abu Dhabi, 1999.

[108] Bielewicz, D., Knez, D., AGH U. of Science and Technology S. Wysocki, "Environmental Biodegradation and Drilling Performance of Water-Based Polyampholyte Drilling Muds," in *SPE/EPA/DOE Exploration and Production Environmental Conference*, Cracow, Poland, 2005, pp. 95640-STU.

[109] Baumann, N.E., and Methven, R.,"Performance of Oil Muds at Higher Temperatures," , Amsterdam, Aug 1972, p. SPE/AIME.

[110] Peska, D., and Moos, P. et al., "Compressive wellbore stability analysis using quantitative risk assessment ," *Jour. Petrol. Sci. and Eng. Spec. Issue on Wellbore Stability*, vol. 38.B.S., no. Asdnoy

and S.Ong., pp. 97-109, 2003.

[111] Myers, T.R. , Haden, G.M., Wahl, E.L., and Sifferman, H.A., "Drill Cutting Transport in Full Scale Vertical Annuli," *JPT*, pp. 1295-1302, Nov 1974.

[112] Vutukuri, R., and Lama, V., *Handbook on mechanical Properties of Rock*. Clausthal, Germany: Trans Tech Publications, 1978.

[113] Balsch, C.J. and Pater, S. "Geomechanical Study of Bowland Shale Seismicity," Cuadrilla Resources Ltd., 2011.

[114] John R. Smith, "Diagnosis of Poor PDC Bit Performance in Deep Shales," Louisiana State University Department of Petroleum Engineering , Baton Rouge, PHD Dissertation 1998.

[115] Langlinais, G. and Altun, J. "Application of a New Model to Analyze Leakoff Tests," in *SPE 56761*, Houston, TX, 1999.

[116] Burke Lauri, "Comprehensive Database of Wellbore Temperatures and Drillign Mud Weight Pressures by Depth for Judge Digby Field, Louisiana," US Department of Interior, 2010.

[117] William, W., et al. Hines, *Probability and Statistics in Engineering and Management Science*. New York, USA: John Wiley & Sons, 1980.

[118] Arild Saasen, "Sag of Weight Materials in Oil Based Drilling Fluids," in *IADC/SPE 77190*, Jakarta, 2002.

[119] Liu, A., Marken, D., Sterii, C.D., Saasen, N., et al., "Prediction of Barite Sag Potential of Drilling fluids from Rheological Measurement," in *SPE/IADC Drilling Conference*, Amsterdam, 1995.

[120] Ostebo, R., et al. "Risk Analysis of Drilling and Well Operations," in *SPE/IADC 21952*, Amsterdam, 1991.

[121] Klovning, J et al. "Quantitative Environmental risk Analysis," in *SPE/IADC 30686*, Dallas, 1995.

[122] Liang, Q.J. at al. "Application of Quantitative Risk Analysis to Pore Pressure and Fracture Gradient Prediction," in *SPE/IADC 77354*, San Antonio, 2002.

[123] Adams, A.J et al. "Casing System Risk Analysis Using Structural Reliability," in *SPE/IADC*, Amsterdam, 1993.

[124] Thomas, P.B. and Baxendell R., "The Calculation of Pressure Gradient in High-Rate Flowing Wells," *JPT*, vol. AIME 222, p. 1023 Trans., October 1961.

[125] Govier, K., Fogarasi, G.W. and Aziz, M. "Pressure Drop in Wells Producing Oil and Gas," *J.Cdn. Pet. Tech.*, p. 11.38, Jul-Sep 1972.

[126] Reed, A.B. and Metzner, J.C. "Flow of Non-Newtonian Fluids-Correlation of the Laminar

Transition and Turbulent Flow Regions," *AlChE J.*, vol. 1, p. 434, 1955.

[127] Aziz, G.W. and Govier, K., *The Flow of Complex Mixtures in Pipes*. New York City: Van Nostrand Reinhold Co., 1972.

[128] Robinson, D.Y. and Peng, D.B. "A New Two Constant Equation of State," *Ind. & Eng. chem. Fund.*, vol. No.1, pp. 59-64, 1976.

[129] Lea, J.F.Jr., Turek, E.A., and Thomas D.C., "Gas Solubility in Oil Based Drilling Fluids:Effect on kick Detection," *JPT*, pp. 959-968, June 1984.

[130] Stalkup, F.I. Jr. "Miscible Displacement," *Monograph Series, SPE, Richardson, Texas*, vol. 41, p. 139, 1983.

[131] Beggs, H.D. "Oil System Correlations," in *Petroleum Engineering Handbook*. Richardson, TX: SPE, 1987, ch. Chap. 22.

[132] Peter Buckley, R.R. , and Ricardo A. Jardiolin Sorelle, "Mathematical Field Model Predicts Downhiole Density Changes in Static Drilling Fluids," in *SPE 11118*, New Orleans, 1982.

[133] Katz, M.B. and Standing, D.L. "Density of Natural Gases," *AIME*, vol. 146, pp. 140-149, 1942.

[134] Carmichael, R.S. *Handbook of Physical properties of Rocks*. Boca Raton, FL: CRC Press, 1982.

[135] Jizba, D. "Mechanical and Acoustical Properties of Sandstone and Shales," Stanford University, PHD Dissertation 1991.

[136] David, T.F. and Wong, C. et al. "The Transition from Brittle Faulting to Cataclastic Flow in Porous Sandstones: mechanical Deformation," *Journal of Geophysical Research*, pp. 102(B2), 3009-3025, 1997.

[137] Horsrud, P. "Estimating Mechanical Properties of Shale from Emprical Correlations," *SPE Drilling and Completion*, pp. 16(2), 68-73, 2001.

[138] Kwasniewski, M. "Laws of Brittle Failure and of B-D Transition in Sandstones. Rock at Great Depth," in *Proceedings ISRM-SPE International Symposium*, Elf Aquitaine, Pau, France, A.A. Balkema, 1989.

[139] Moses, P.L. "Geothermal Gradients," *Spring Meeting of the Southern District* , pp. 57-63, 1961.

[140] Robert B. Carpenter, et al., "Remediating Sustained casing Pressure by forming a Downhole Annular Seal with Low Melting Point Eutectic Metal," *SPE 87198*, 2004.

[141] Zoback, S.H. and Hickman, M.D., "The Interpretation of Hydraulic Fracturing Stress Measurements: Proceedings, Workshop on Hydraulic Stress Measurements," *National Academy Press*, no. Washington D.C., pp. 44-54, 1983.

[142] Hamed Soroush, "Importance of Geophisical Logging Data for Geomechanical Analysis," in *Well Engineering Center of Excellence, Weatherford Oil Tool*, Dubai, 2007.

[143] Richard Bircwood, Tom Bratton Donald Lee, "Leak off Test Interpreattion and Modelling with Application to Geomechanics," in *ARMA/NARMS*, Houston, TX, 2004.

[144] Willis M.K., and Hubbert, D.G., "Mechanics of Hydraulic Fracturing," *SPE-AIME*, vol. Trans. 210, pp. 153-168, 1957.
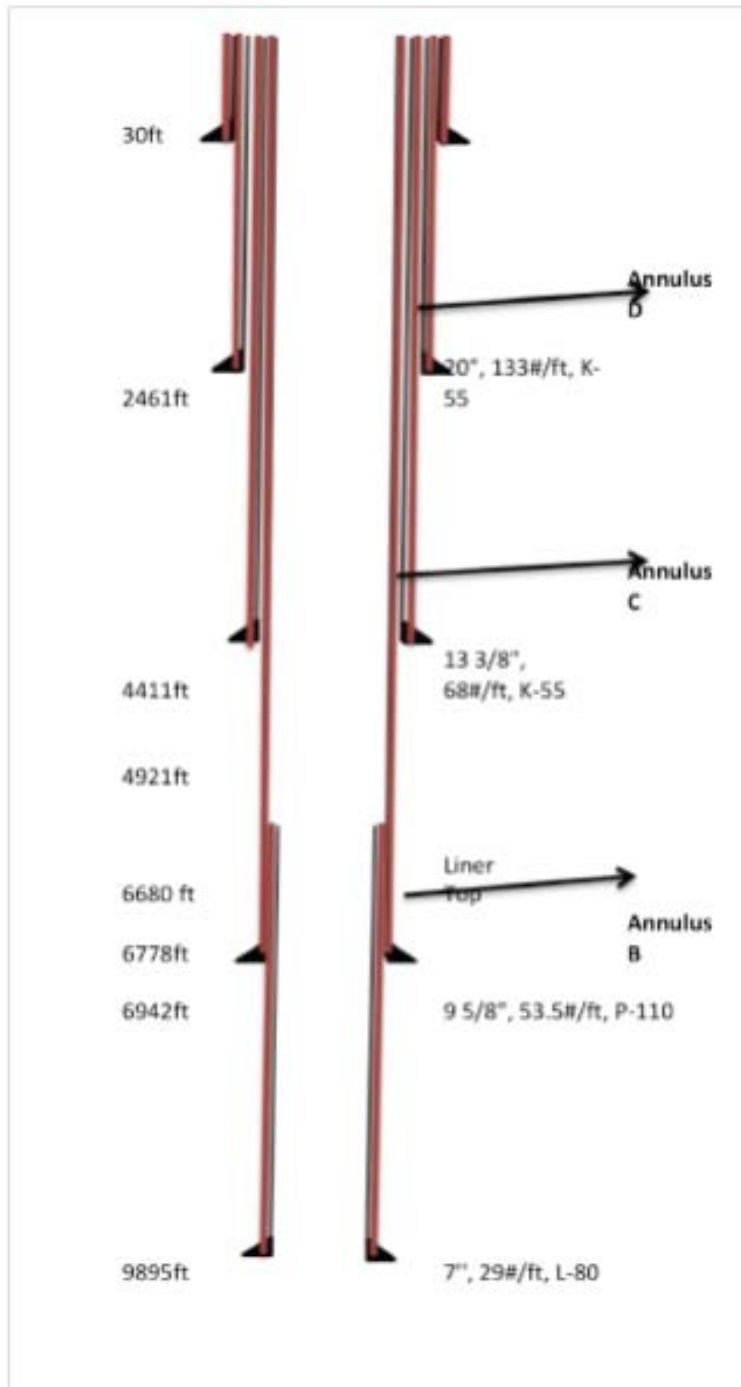
Fig.A.1-Well configuration of Well KH-9

Table-A.1- Well KH-9 leak off test data

Depth,ft	Density, ppg	P_{ff} , ppge	P_{ff}, psi	LOTsurface, psi	MAWOP
9895.0	17.6	20	10291	9301	4080.0
6942.3	14	18.5	6678	5984	2760.0
4110.9	10.5	15	3206	2795	1725.0
2460.6	9	10.5	1344	1097	918.0

Tabel-A.2--Well KH-9 drilling data

Depth	CSG Size	Drilling mud			Pressure Gradient		Cementing	
		Mud Type	Density, ppg	Fracture Grad , ppg	Pore Pressure, ppg	MW, ppg	TOC	
2460.6	20"	Gel/ Water	9	10.5	9	12.5	Lead to Surface	
4110.9	13 3/8"	NACL Polymer Glydril	10.5	15	12	14.6	Lead to Surface	
6942.3	9 5/8"	KCL Polymer Mud	14	18.5	14	15.5	Lead to Surface	
9895.0	7"	KCL Polymer Mud	17.6	20	18	18.5	195' in 9 5/8 CSG,169' above in	

Table.A.3-well KH-9 casing data

Casing Size	Shoe Depth(ft)	Wt #/ft	Grade	Conn	Collapse(psi)	Burst (psi)	Tension1000lbs	CSG PresTest
30"	+/- 10							N/A
20"	2461	133	K-55	BTC	1500	3060	2125	1000
13 3/8"	4111	68	K-55	BTC	1950	3450	1069	2800
9 5/8"	6942	53.5	P-110	NSCC	7930	10900	1710	8500
7"	9895	29	L-80	NSCC	7020	8160	676	6500

APPENDIX B. MATHEMATICAL MODEL FOR SCP TEST INTERPRETATION

Xu.R. et.al. [11] presented mathematical model that simulates the B-B test. The model requests the B-B test pressure vs. time data the control parameters are estimated by visually fitting the simulation plot to the data. The fitting is done manually by trial-and-error until a acceptable match is achieved. The control parameters are gas chamber volume, cement effective permeability, mud density, and reservoir pressure. The model assumes homogeneous mud density in the annulus, top of cement above the casing shoe, vertical well, water base mud and ignores thermal expansion.

It considers linear flow of the gas in cement, which relates the flow rate and pressure at the cement top to the annular permeability, gas source formation pressure and time. Gas migration in the mud column above the cement top is modeled as dispersed two-phase flow. The model assumes constant formation pressure, negligible gas density in the cement column, constant gas deviation factor, compressible mud column, steady-state gas flow at each time step of the iterative computation cycle. At each time step gas flow rate, q_g and pressure at the cement/mud interface, P_{TOC}, are computed iteratively. The iterative solution algorithm is shown in Fig.B.1

Upper boundary condition: needle valve, q_g and q_L.

Initial Condition: $F_g(z,0)$ and $P(z,0)$ Numerical Solution: $F_g(z,t)$ and P_{ws} in

Initial condition: $P(z,0)$ Analytical solution: P_{wf} in cement

Coupling criteria: $P_{ws}=P_{wf}$ for $q_c>0$ or $P_{ws}> P_{wf}$ for $q_c=0$

Lower boundary condition: P_f constant at formation
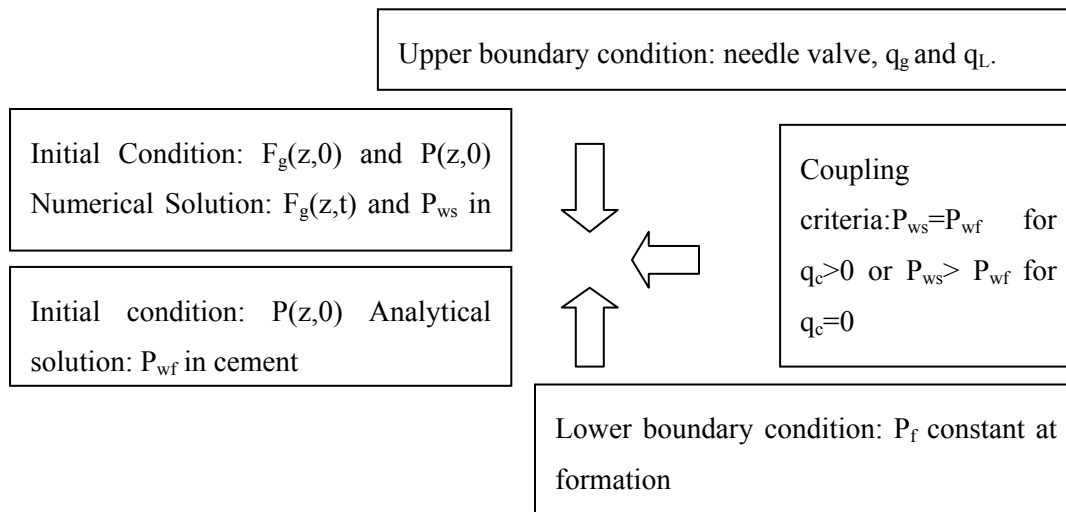
Fig.B.1-Coupling Procedure for Mathematical SCP

The model was also used to characterize bleed off and build up patterns since different control parameters dominate different stages of the B-B test. The bleed off period is controlled by the gas cap volume. An example simulation of the bleed off test is shown in Fig.B.2 (left). The 24 hour build up is controlled by the cement permeability, mud density and reservoir pressure. As shown in Fig.B.2 (right).
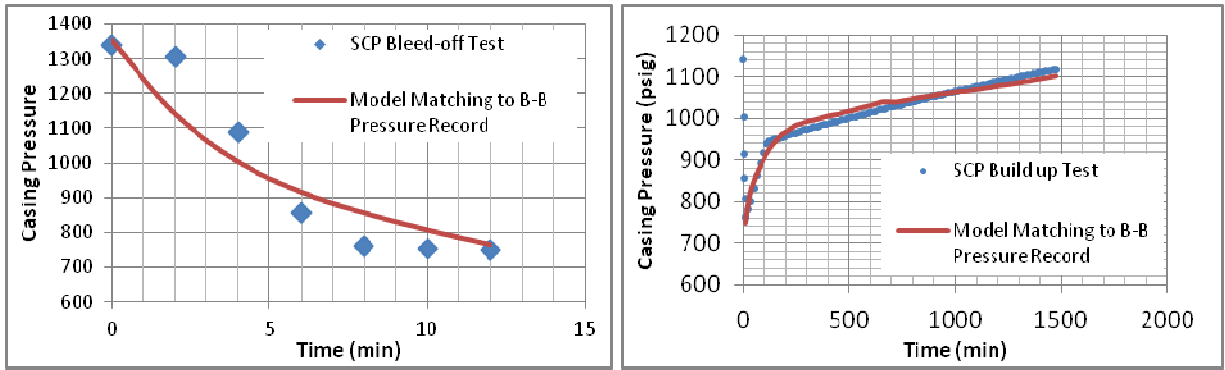
Fig.B.2- Matching of pressure bleed off and build up with SCP model

APPENDIX C. MECHANISTIC MODELING OF TWO-PHASE SLUG FLOW IN ANNULI

Majority of the correlations developed to calculate the pressure gradient based on the flow regime determined by pipe flow assumption, and implementing the hydraulic diameter concept into the calculations. Baxendell and Thomas [124] developed empirical correlations for two-phase flow, not considering flow regime variation or slippage. Aziz *et al.* [125] presented empirical correlation for pipe flow, which distinguishes the flow pattern by a map and considers slippage. Ansari *et al.* [27] presented mechanistic model for vertical flow in pipes.

For two-phase flow in annulus, Hasan and Kabir [97] presented mechanistic model. They compared liquid holdup values calculated by the mechanistic model for flow in concentric annulus with those measured by Caetano [29]. Flow regime transition is a strong function of flow geometry, *i.e.*, pipe diameter ratio and eccentricity as Hasan and Kabir [98] observed that with higher gas volume fractions, presence of inner pipe makes nose of the Taylor bubble sharper, increasing the rise its velocity, v_{TB}, linearly by,

$$v_{TB} = \left(0.345 + 0.1\frac{d_t}{d_c} \right)\sqrt{sin\,\theta}\,(1 + cos\,\theta)^{1.2}\sqrt{\frac{gd_c(\rho_L - \rho_g)}{\rho_L}} \qquad \text{C.1}$$

Caetao *et al.* [29] presented mechanistic model for vertical upward flow in concentric and fully eccentric annuli. Caetao *et al.* model is considered in this study for bubble and slug flow regimes. Mixture velocity is given as,

$$v_m = v_{SL} + v_{Sg} \qquad \text{C.2}$$

Taylor bubble velocity is given as,

$$v_{TB} = 1.2v_m + 0.345\sqrt{g(d_c + d_t)} \qquad \text{C.3}$$

Caetano *et al.* [29] assumed the liquid hold-up was constant at the bubble/slug transition, for concentric annulus $H_{LLS} = 0.80$, for eccentric annulus $H_{LLS} = 0.85$. Velocity in the liquid-slug zone is obtained by combining mass balance at the liquid/slug zone and slip velocity given as,

$$v_{LLS} = (v_{SL} + v_{Sg}) - 1.53\left[\frac{(\rho_L - \rho_g)g\sigma_L}{\rho_L^2} \right]^{\frac{1}{4}}(H_{LLS})^{\frac{1}{2}}(1 - H_{LLS}) \qquad \text{C.4}$$

For a known flow geometry and film thickness, δ, liquid holdup in the film zone for a fully developed Taylor bubble is given as,

$$H_{LTB} = \frac{4\delta(d_c - \delta)}{d_c^2 - d_t^2} \qquad \text{C.5}$$

Relationship between the film thickness and film velocity of a free falling film of liquid flowing downward and surrounding the Taylor bubble is given as,

$$v_{LTB} = \frac{\delta^{(1-C_M)c_M}}{\left\{C_K\left[\dfrac{\mu_L^2}{g(\rho_L - \rho_g)\rho_L}\right]^{\frac{1}{3}}\right\}^{\frac{1}{c_M}}} \frac{\mu_L}{4\rho_L}$$

C.6

where the indices C_K and C_M are a function of film zone flow regime, with a transition described by Reynold's Number given as,

$$N_{RE_{LTB}} = \frac{4\rho_L v_{LTB}\delta}{\mu_L}$$

C.7

$$C_K = \begin{cases} 0.9086 & \text{if } N_{RE_{LTB}} < 1{,}000 \\ 0.0682 & \text{if } N_{RE_{LTB}} > 1{,}000 \end{cases}$$

C.8

$$C_M = \begin{cases} 0.3333 & \text{if } N_{RE_{LTB}} < 1{,}000 \\ 0.6666 & \text{if } N_{RE_{LTB}} > 1{,}000 \end{cases}$$

C.9

Mass balance on liquid phases in slug and film zone must be satisfied for a film thickness, δ. Thus, iterative procedure on δ is necessary to solve for v_{LTB}, v_{LLS} and H_{LTB} for a known eccentricity, thus, H_{LLS}. Mass balance between $A\text{-}A`$ and $B\text{-}B`$ is given as,

$$(v_{TB} - v_{LLS})H_{LLS} = (v_{TB} + v_{LTB})H_{LTB}$$

C.10

Overall mass and volume balances assuming incompressible flow of liquid and gas within a slug unit yields,

$$\frac{L_{LS}}{L_{SU}} = \frac{v_{SL} + v_{LTB}H_{LTB}}{v_{LLS}H_{LLS} + v_{LTB}H_{LTB}}$$

C.11

The elevation component of the pressure gradient equation is given as,

$$\left(\frac{dP}{dL}\right)_{el_{z,i}} = \rho_{LS}g\left(\frac{L_{LS}}{L_{SU}}\right)$$

C.12

where the slip density for the gas/liquid mixture in the liquid slug is given as,

$$\rho_{LS} = \rho_L H_{LLS} + \rho_g(1 - H_{LLS})$$

C.13

and where L_{SU} is the slug-unit length, given as,

157

$$L_{SU} = L_{LF} + L_{LS}$$
<div align="right">C.14</div>

Since $\dfrac{L_{LS}}{L_{SU}}$ is known, L_{SU} can be solved from the superficial liquid velocity equation defined by overall mass balance in a slug unit is given as,

$$v_{SL} = v_{LLS}H_{LLS}\frac{L_{LS}}{L_{SU}} - v_{LTB}H_{LTB}\frac{L_{LF}}{L_{SU}}$$
<div align="right">C.15</div>

The friction component of the pressure gradient equation is given as,

$$\left(\frac{dP}{dL}\right)_{f_{z,i}} = \frac{2f'}{d_c - d_t}\rho_{LS}\left(v_{Sg} + v_{SL}\right)^2\left(\frac{L_{LS}}{L_{SU}}\right)$$
<div align="right">C.16</div>

where the fanning friction factor, f', is the Fanning friction factor for non-Newtonian flow in eccentric/concentric annuli configurations.

APPENDIX D. FRICTION FACTOR CALCULATION FOR NON-NEWTONIAN FLUID

D.1.   Turbulence Criterion

Bubble Flow. Reynold's number for two-phase bubble flow. The turbulence criterion is defined by Moody as 1500[26].

Reynold's number is given as,

$$N_{Re_{TP}} = \frac{\rho_{TP} v_m (d_c - d_t)}{\mu_{TP}}$$

D.1

where μ_{TP} is the two-phase viscosity, given as,

$$\mu_{TP} = \mu_L \lambda_L + \mu_g (1 - \lambda_L)$$

D.2

where μ_L is liquid apparent viscosity, given as,

$$\mu_L = K' \left(\frac{4n'}{3n'+1}\right)\left(\frac{8v_m}{0.816(d_c - d_t)}\right)^{n'-1}$$

D.3

and λ_L is the no-slip holdup, given as,

$$\lambda_L = \frac{v_{SL}}{v_{SL} + v_{Sg}}$$

D.4

Slug Flow. Corresponding two-phase Reynold's Number for slug flow given as,

$$N_{Re_{TP}} = \frac{\rho_{LS} v_m (d_c - d_t)}{\mu_{TP}}$$

D.5

Annular Flow. Reynold's number for single phase flow is given as,

$$N_{Re} = \frac{\rho_g v_g (d_c - d_t)}{\mu_g}$$

D.6

For laminar flow, friction factor is given as,

D.7

$$f' = C \cdot N_{RE}^n$$

where $n = -1$ and $C = 16$ for laminar flow. For turbulent flow, friction factor is given as,

$$\frac{1}{\sqrt{f}} = 1.74 - 2log\left(\frac{2\varepsilon}{d}\right) + \frac{18.7}{N_{RE}\sqrt{f}}$$

D.8

D.2. Non-Newtonian Laminar Flow in Eccentric Annulus

Haciislamoglu and Langlinais [31] developed numerical model for flow of yield power law fluids in concentric and eccentric annuli considering Metzner and Reed [126] generalized Reynold's number concept and narrow slot approximation, which estimates accurate friction factors for annulus pipe diameter ratios, *K*, greater than 0.3, where,

$$K = d_t / d_c \qquad \text{D.9}$$

For a yield power law fluid, *n'* is the flow behavior index and *K'* is the equivalent consistency index defined as a function of annulus pipe diameter ratio, given as,

$$K' = K \left(\frac{4n' + 2}{4n'} \right)^{n'} \qquad \text{D.10}$$

The relationship between true shear rate and apparent shear rate at the wall is given as,

$$\left(-\frac{dv}{dr} \right)_w = \frac{4n' + 2}{4n'} \frac{8v}{d_c - d_t} \qquad \text{D.11}$$

For laminar flow of non-Newtonian fluid in annulus, generalized Reynold's number thus is given as,

$$N_{Re_{M-R}} = \frac{\rho v^{2-n'} (d_c - d_t)^{n'}}{8^{n'-1} K'} \qquad \text{D.12}$$

Thus, friction factor is given as,

$$f' = \frac{16}{N_{Re_{M-R}}} \qquad \text{D.13}$$

Note that density and velocity parameters, ρ and *v*, are in generic form, which are replaced for the corresponding density and velocity values considered for bubble and slug flow during frictional pressure loss calculations.

For eccentric annuli, correlation parameter, *R*, developed by Haciislamoglu and Langlinais (1990) [31] is applied to calculate frictional losses for flow of non-Newtonian fluids in eccentric annulus, which predicts results with ±5% accuracy for eccentricities from 0 to 0.95, pipe diameter ratios from 0.35 to 0.9, and flow behavior indices, *n'*, from 0.4 to 1. Correlation parameter, *R*, is given as,

$$R = 1 - 0.072 \frac{e}{n'} \left(\frac{d_t}{d_c} \right)^{0.8454} - 0.015 e^2 \sqrt{n'} \left(\frac{d_t}{d_c} \right)^{0.1852} + 0.96 e^3 \sqrt{n} \left(\frac{d_t}{d_c} \right)^{0.2527} \qquad \text{D.14}$$

where eccentricity of the annulus, *e*, is expressed as a function of distance between pipe centers, given as,

$$e = \frac{2D_{BC}}{(d_c - d_t)} \qquad \text{D.15}$$

from 0 to 1, where d_c and d_t are inner diameter of outer pipe and outer diameter of the inner pipe, respectively, as shown in Fig.D.1
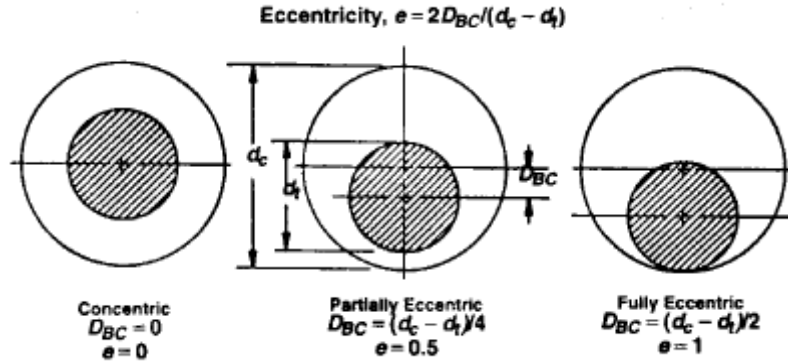

Fig.D.1-Eccentricity annuli configurations (Haciislamoglu *et al.*, 1990)[31]

For eccentric annuli, friction factor calculated for concentric annulus can be correlated with R, given as,

$$\left(f'\right)_{eccentric} = R \cdot \left(f'\right)_{concentric} \qquad \text{D.16}$$

D.3. Non-Newtonian Turbulent Flow in Eccentric Annulus

For turbulent flow of non-Newtonian fluid in eccentric annuli, there is no documented methodology. However, Brill and Mukherjee[26] suggested using Metzner Reed[126] generalized Reynold's number for a concentric annulus in the non-Newtonian pipe flow friction factor correlations.

Govier and Aziz[127] suggested methodology to calculate friction factor for power-law, pseudoplastic fluids in rough pipes, given as,

$$\sqrt{\frac{1}{f'}} = -4.0 \, log \left[\frac{10^{-\beta/2}}{N_{Re_{M-R}}^{1/n'} \left(4f'\right)^{(2-n')2n'}} + \frac{\varepsilon}{3.71d} \right] \qquad \text{D.17}$$

where,

$$\beta = 1.51^{1/n'} \left(\frac{0.707}{n'} + 2.12 \right) - \frac{4.015}{n'} - 1.057 \qquad \text{D.18}$$

161

APPENDIX E. PVT CORRELATIONS USED BY THE CSS MODEL AND SOFTWARE

E.1.   Oil and Synthetic Phase P-ρ-T Properties

Pressure-Density-Temperature P-ρ-T behavior of inverse emulsion drilling fluids have been well studied regarding hardship of kick detection and well control complications [9]. In addition to diesel and mineral oils, P-ρ-T properties of synthetic base fluids such as Linear Alpha Olefin (LAO), Ester, Paraffin and Internal Olefin (IO) have been studied to improve kick detection and control as well as equivalent circulating density (ECD) calculations. Accurate calculation of oil or synthetic base fluid densities at elevated temperatures and pressures requires computation of formation volume factor (B_o), bubble point pressure (P_b), solution gas oil ratio (R_{so}) and compressibility (c_o) as a function of temperature, pressure and dissolved gas.

E.1.1.   Gas Solubility in Oil and Synthetic Phase

Gas solubility is denoted as the solution gas oil ratio at bubble point pressure for an oil or synthetic phase and gas at certain temperature (R_{sob}). Peng-Robinson equation of state (EOS) model [128] has been widely used as the backbone of the P-ρ-T calculations for a wide range of oils. Thomas *et al.* [129] experimentally determined methane solubility in diesel oil at 100 to 60°F. O'Bryan *et al.* [65] performed a series of experiments with methane, carbon dioxide and ethane at temperatures 100 to 600 °F to estimate solubility and swelling properties of Diesel Oil No.2, and two commonly used mineral oils Conoco LVL and Exxon Chemicals Mentor 28. The following correlation is presented for methane, ethane and CO_2 solubility in Diesel Oil no. 2.

$$R_{sob} = \left(\frac{p}{aT^b} \right)^c$$

E.1

The correlation constants a, b and c are shown in Table E.1

Table E.1-Gas solubility correlation constants

Gas	Component	a	b
for Hydrocarbon	Diesel	1.922	0.2552
for CO_2	Diesel	0.059	0.7134

and constant C is calculated as for temperature, T (°F) [1] :

---

[1] Do not confuse with specific heat capacity, c_p

$$C_{HC-oil} = 0.3576 + 1.168\gamma_g + \left(0.0027 - 0.00492\gamma_g\right)T -$$
$$\left(4.51\cdot10^{-6} - 8.198\cdot10^{-6}\gamma_g\right)T^2$$
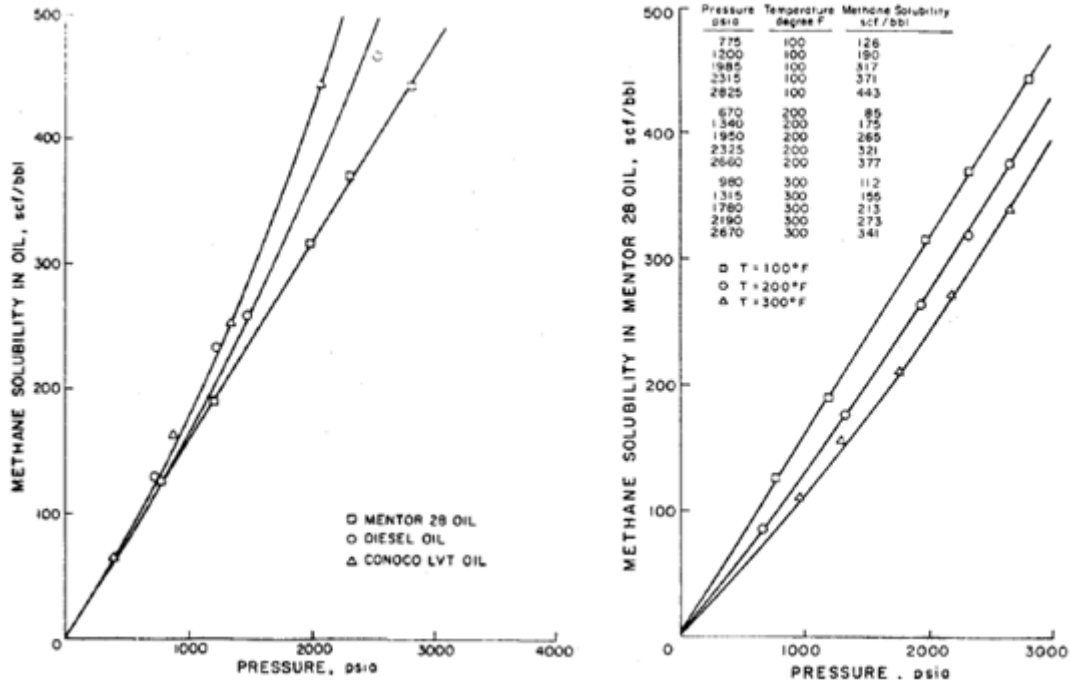$$C_{CO_2-oil} = 1.0$$

E.2

Fig.E.1- Methane solubility in Diesel oil and commonly used mineral oils (left), Methane solubility in mineral oil at various temperatures (right) [56]

Gas solubility somewhat linearly increases with pressure until a critical point for certain temperature, the miscibility pressure. At pressures above this methane and the oil become miscible at all portions, and solubility curves become vertical, as shown in Fig.E.1 (left). Stalkup [130] presented miscibility pressures for methane, ethane and CO_2 in Diesel Oil No.2 up to temperatures of 400 °F, as shown in Fig.E.1 (right). Calculation of the miscibility pressure is critical for kick detection during a well control operation since the downhole volume, and so the initial pit gain volume depend on the bottom hole vs. miscibility pressure of the continuous phase in conjunction with the oil content of the mud. Also, further calculation of formation volume factor, bubble point pressure and compressibility of oil and synthetic phase require gas solubility in oil, *i.e.* the value of solution gas at bubble point.
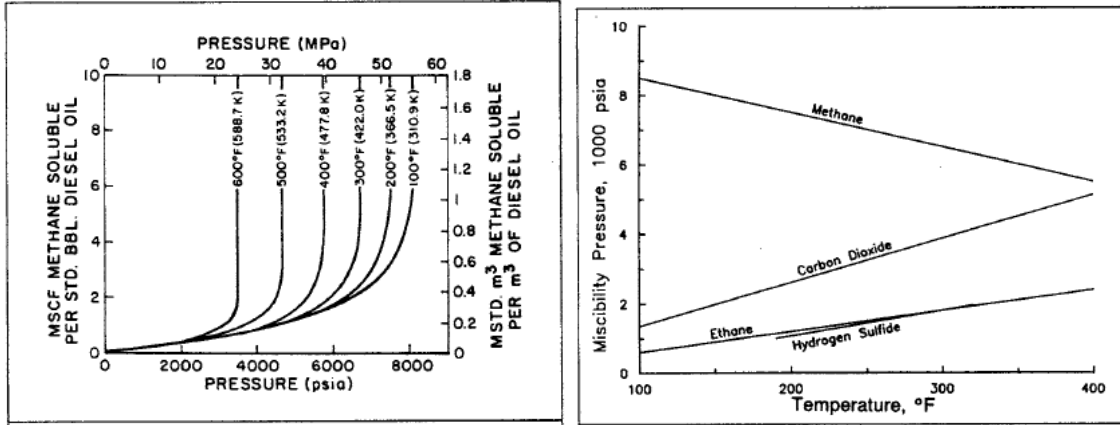
Fig.E.2-Solubility of methane in diesel oil at various temperatures (left) (O'Bryan *et al.*, 1989)[56], Miscibility Pressures for various gasses in diesel oil vs. Temperature (right) (Stalkap, 1983)[130]

Solubility of gas in water phase of the mud is presented in Section E.2. Moore *et al.* [9] showed that dissolved gas in the emulsifier component of the mud is small compared to that in oil phase, thus in this model it is neglected.

E.1.2. Oil Formation Volume Factor

Swelling of the drilling fluid is expressed by formation volume factor (B_o), which is the ratio of volume of mud plus dissolved gas at downhole conditions to its gas free volume at surface conditions. Major fraction of the oil and synthetic based mud is composed of the continuous phase, thus makes the greater contribution to the overall volume factor. O'Bryan *et al.* [56] experimentally tuned Peng-Robinson EOS [128] to estimate formation volume factor of oil phase for No.2 Diesel, Conoco LVT and Mentor 28 oils applicable to temperatures and pressures up to 400 ^{o}F and 20,000 psig, as shown in Fig.E.3.
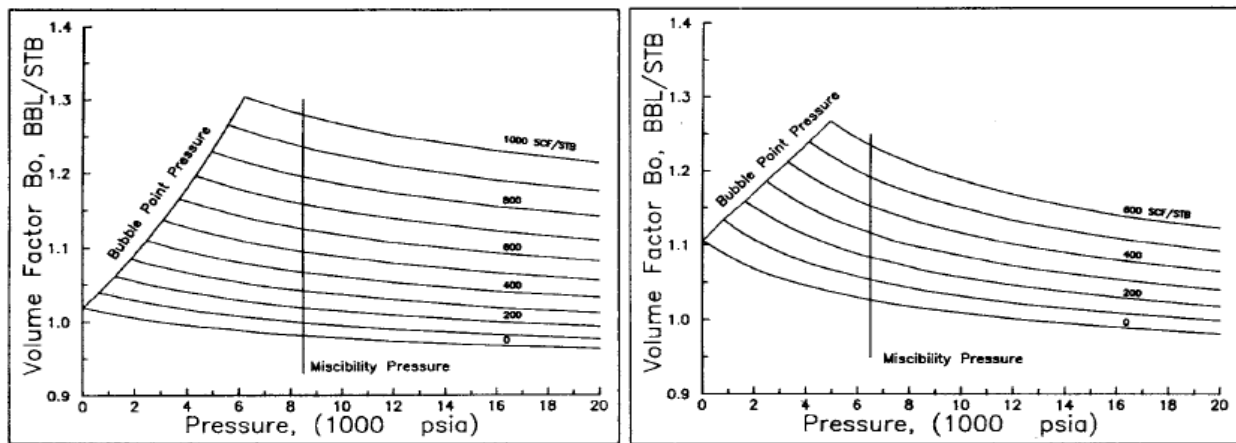

Fig.E.3- No.2 diesel oil FVF's with and without dissolved methane at 100 ^{o}F, No.2 diesel oil FVF's with and without dissolved methane at 300 ^{o}F [56]

Van Slyke *et al.* [58] presented correlation with regard to data from 9 ppg mineral oil mud samples with dissolved gas values up to 927 scf/Stb, as in equations below. The presented correlation provided good match with the method proposed by O'Bryan.

$$B_{ob} = \left(1.028 + \frac{T-150}{2000}\right) + \left[\left(2.15 + \left(\frac{T-150}{1000}\right)\right)^{P/1000} + 82\right] \cdot 10^{-1} P \qquad \text{E.3}$$

$$B_o = 1 + \left(\frac{R_{so}}{2600 - 4.5T}\right) - \left[\begin{array}{l}(5.1 \cdot 10^{-6} - 7 \cdot 10^{-9}(400 - T)) \\ + (3.8 \cdot 10^{-8} - 10^{-10}(400 - T)) \cdot R_{so}\end{array}\right] \qquad \text{E.4}$$

Standing [59], [57] presented formation volume factor correlation for reservoir oils with gravity from 16.5 to 63.8 °API, given by the equations below.

$$B_o = 0.9759 + 0.00012 \cdot F^{1.2} \qquad \text{E.5}$$
where

$$F = R_s \left(\gamma_g / \gamma_o\right)^{0.5} + 1.25 \cdot T_F \qquad \text{E.6}$$
$$130 < P_b < 7000 \text{ psia}$$
$$100 < T < 258 \text{ °F}$$
$$20 < R_{so} < 1425 \text{ scf/STB}$$
$$16.5 < \gamma_{API} < 63.8 \text{ °API}$$
$$0.59 < \gamma_g < 0.95 \text{ (air} = 1.0)$$
$$1.024 < B_o < 2.05 \text{ rb/STB}$$

Above bubble point pressure,

$$B_o = B_{ob} \cdot e^{[c_o (P_b - P)]} \qquad \text{E.7}$$

E.1.3. Oil Bubble Point Pressure

Standing [59], [57] also developed correlation to estimate the bubble point of reservoir oils for known dissolved gas at bubble point, R_{sob}. For reservoir oils, R_{sob} value can be determined from production history or laboratory PVT analysis. For The correlation is has proved adequate and is given by [131]:

$$P_b = \left(18 \cdot 10^{y_g}\right)\left(R_{sob} / \gamma_g\right)^{0.83} \qquad \text{E.8}$$
where T is in °F and y_g is

$$y_g = 0.00091 \cdot T - 0.0125 \gamma_{API} \qquad \text{E.9}$$

E.1.4. Oil Compressibility

McCain *et al.* [60] developed correlation for isothermal coefficient of oil compressibility for black oils below bubble point pressure for known R_{sob}.

$$ln(c_o) = -7.633 - 1.497\,ln(P) + 1.115\,ln(T+460) + 0.533\,ln(\gamma_{API}) + 0.184\,ln(R_{sob}) \qquad \text{E.10}$$

The correlation calculated the apparent compressibility coefficient for the liquid and dissolved gas jointly. The ranges of conditions the data is correlated is as follows.

$31 \cdot 10^{-6} < c_o < 6600 \cdot 10^{-6} \text{ psia}^{-1}$

$500 < P < 5300 \text{ psia}$

$763 < P_b < 5300 \text{ psia}$

$78 < T < 330 \text{ }^\circ F$

$15 < R_{so} < 1947 \text{ scf / Stb}$

$18 < \gamma_{API} < 52 \text{ }^\circ API$

$0.58 < \gamma_g < 1.2\,(\text{air} = 1.0))$

Vazquez-Begg's [61] can be used for pressures above bubble point pressure to estimate the isothermal oil compressibility for known R_{sob}.

$$c_o = \frac{-1433 + 5R_{sob} + 17.2(T) - 1180 \cdot \gamma_{gas} + 12.61 \cdot \gamma_{API}}{10^5 \cdot P} \qquad \text{E.11}$$

where T if in $^\circ F$ and γ_{API} is oil gravity is:

$$\gamma_{API} = \frac{141.5}{SG_{oil}} - 131.5 \qquad \text{E.12}$$

The correlation works adequate under the following ranges of conditions.

$126 < P < 9500 \text{ psig}$

$9.3 < R_{so} < 2199 \text{ scf / Stb}$

$1.006 < B_o < 2.226 \text{ rb / Stb}$

$15.3 < \gamma_{API} < 59.5 \text{ }^\circ API$

$0.511 < \gamma_g < 1.351\,(\text{air} = 1.0))$

E.1.5. Oil Density

Density of each component can be mathematically related to the its compressibility at elevated temperature and pressures.

$$\rho_o(P,T) = \frac{\rho_{surface}}{1 - c_o(P,T) \cdot \Delta P} \qquad \text{E.13}$$

Sorelle *et al.* [132] performed laboratory tests for Diesel Oil No.2 for temperatures 100 to 350 °F, and pressures up to 12,500 psig, and presented correlation for oil density calculation as a function which has been verified with a series of field measurements from 18,186 ft well.

$$\rho_o = 7.24032 - 2.84383 \cdot 10^{-3}\,T + 2.7566 \cdot 10^{-5}\left(P - P_0\right)$$

E.14

where P_0 is the pressure at reference conditions and T in °F.

CSS software uses compositional model to calculate oil density at elevated temperature and pressures.

E.2. Water P-ρ-T Calculations

E.2.1. Water Solution Gas Oil Ratio

McCain [62] developed correlation for estimating solution gas water ratio of pure water, which works adequate for temperatures 100 to 350 °F and pressures 1,000 to 10,000 psig.

$$R_{swp} = A + B \cdot P + C \cdot P^2$$

E.15

where solution gas water ratio of pure water, R_{swp} is in scf/Stb. The constants A, B and C are as follows:

E.16

$$A = 8.15839 - 6.12265 \cdot 10^{-2}\,T + 1.91663 \cdot 10^{-4}\,T^2 - 2.1654 \cdot 10^{-7}\,T^3$$

E.17

$$B = 1.01021 \cdot 10^{-2} - 7.44241 \cdot 10^{-5}\,T + 3.05553 \cdot 10^{-7}\,T^2 - 2.9488 \cdot 10^{-10}\,T^3$$

$$C = -10^{-7}\left(\begin{array}{l}9.02505 - 0.130237 \cdot T + 8.53425 \cdot 10^{-4}\,T^2 \\ -2.34122 \cdot 10^{-6}\,T^3 + 2.37049 \cdot 10^{-9}\,T^4\end{array}\right)$$

E.18

McCain also presented correlation for adjusting gas water ratio of pure water for salinity to estimate the gas water ratio of brines, which works adequate for temperatures 70 to 250 °F and salinities 0 to 30 weight%.

E.19

$$R_{sw}/R_{swp} = 10\,\hat{}\left(-0.08406555 \cdot T^{-0.285584}\right)$$

E.2.2. Water Formation Volume Factor

McCain [60] presented correlation for formation volume factor for reservoir waters for pressures up to 10,000 psig and temperatures 100 to 300 °F.

E.20

$$B_w = \left(1 + \Delta V_{wT}\right)\left(1 + \Delta V_{wP}\right)$$

where

$$\Delta V_{wT} = -1.00010 \cdot 10^{-2} + 1.33391 \cdot 10^{-4}\,T + 5.50654 \cdot 10^{-7}\,T^2 \qquad \text{E.21}$$

$$\Delta V_{wP} = -1.95301 \cdot 10^{-9}\,PT - 1.72834 \cdot 10^{-13}\,P^2 T \qquad \text{E.22}$$
$$- 3.58922 \cdot 10^{-7}\,P - 2.25341 \cdot 10^{-10}\,P^2$$

E.2.3. Water Compressibility

Meehan [63] presented correlation for estimating compressibility of formation brines.

$$C_{gfw} = 10^{-6} \cdot \left(A_1 + A_2 T + A_3 T^2 \right) \cdot \left(1 + 0.0089\,R_{spw} \right) \qquad \text{E.23}$$

$$A_1 = 3.8546 - 0.000134 \cdot P \qquad \text{E.24}$$

$$A_2 = -0.01052 + 4.77 \cdot 10^{-7} \cdot P \qquad \text{E.25}$$

$$A_3 = 3.9267 \cdot 10^{-5} - 8.8 \cdot 10^{-10} \cdot P \qquad \text{E.26}$$

$$C_w = R_{spw}\left(\left(-0.052 \cdot 0.00027 \cdot T + 1.14 \cdot 10^{-5}T^2 + 1.121 \cdot 10^{-8}T^3\right) \cdot salinity^{0.7} + 1\right) \qquad \text{E.27}$$

where T is in ^{o}F and salinity is the brine salinity in weight%.

E.2.4. Water Density

Density of water phase of the mud can be mathematically related to its compressibility at elevated pressures and temperatures.

$$\rho_w(P,T) = \frac{\rho_{surface}}{1 - c_w(P,T) \cdot \Delta P} \qquad \text{E.28}$$

Buckley *et al.* [132] presented correlation to estimate water density based on field measurements from 17.65 ppg WBM for temperatures to 176 ^{o}F.

$$\rho_w = 8.63186 - 3.31977 \cdot 10^{-3}\,T + 2.3717 \cdot 10^{-5}\left(P - P_0\right) \qquad \text{E.29}$$

where P_0 is the reference pressure and T in ^{o}F. CSS software uses compositional model to calculate water density at elevated temperature and pressures.

E.3. Gas PVT Properties

Standing and Katz [133] presented graphical correlation for the gas deviation factor and Dranchuk and Abou-Kassem [64] fitted EOS to their data which works adequate for a wide range of pressure (0.2<P_r<30) and temperature (1.0<T_r<3.0). Gas density, formation volume factor and compressibility can then be calculated using real gas law.

APPENDIX F. STUDY WELL WIRELINE LOG AND CORE DATA

In Study Well, open-hole wireline logging (DIL/LLS/LDT/CNL/GR) was run by Schlumberger from 14,843' to shoe at 10,740'. Summary of the formation characteristics from wireline log interpretation is shown in Table F.2. Sidewall cores also has been taken in this interval. Summary of the subsurface core data is shown in Table F.1. Miocene high illite shale (with Φ 1.2-3.8%, V_{sh} 42.1-84.6%, high quartz) was encountered until penetrating into relatively clean sandstone formation, into which casing shoe of 9-5/8" liner was set.

Table F.1- Subsurface Core Data from Study Well [114]

Sample Name	Depth (ft)	Mud weight (ppg)	Age	XRD mineralogy							
				Quartz	Feldspar	Calcite	Dolomite	Siderite	Pyrite	Halite	Barite
Mat.Is. Siltstone	13,078'	18	Miocene	56	6	28	0	trc	trc	0	
Mat.Is. Mudshale	13,086'	18	Miocene	41	3	7					
Mat.Is. Laminated Sandstone	13,659'	18	Miocene	41	5	16	0	0	trc	0	

Table F.2- Bit Performance and Formation Characteristics Data from wireline log in Study Well [114]

Formation type	Depth interval	ROP (fph)	Specific Energy (psi)	Force Ratio	V_{sh} %	LDT Eff porosity %	LDT/CNL Eff/Por %	LDT/CNL Tot Por %	Acoustic Travel Time (μs/ft)
Shale	13,460-95'	17.0	104,435	0.99	66.7	2.7	0.0	12.0	100
Shale	13,670-80'	15.4	197,889	2.03	52.9	3.8	0.0	12.0	95
Shale	14,320-45'	18.1	228,885	1.48	42.1	6.6	2.5	14.0	99
Shale	13,830-60'	29.4	201,303	1.95	84.6	1.2	1.5	12.0	97
Shale	13,265-95'	41.9	93,508	3.76	61.7	3.1	0.0	13.0	100
Shale	13,920-50'	46.7	81,709	2.99	57.1	3.4	0.0	12.0	99
Siltstone	13,315-30'	24.8	132,709	1.64	36.1	0.1	2.0	6.5	82
Siltstone	13,635-45'	22.3	170,868	2.60	30.8	1.5	2.0	8.0	72
Sandstone	13,535-60'	64.6	51,908	4.44	0.0	16.0	17.0	19.0	78
Shaly Sandstone	14,095-105'	42.9	79,827	1.79	11.8	8.1	6.0	12.0	78

APPENDIX G.ESTIMATION OF ROCK STRENGTH PARAMETERS

Estimation of rock strength parameters from geophysical logs commonly is done by relating travel time of compressional waves along the wellbore wall, expressed in μs/ft, density and porosity measurements. Lama and Vutukuri (1978) [112], Carmichael (1982) [134], Jizba (1991) [135], Wong, David *et al.* (1997) [136], Horsrud (2001) [137] and Kwasniewski (1989) [138] made laboratory testing on sandstone, siltstone, shale and dolomites to study the dependence of uniaxial compressive strength on the rock parameters Young's modulus (E), Poisson's ratio and porosity (Φ) [43]. The data from sandstone, shale and siltstone/dolomite are shown in the following figures. The data is considerably dispersed, however a reasonable margin can still be estimated.
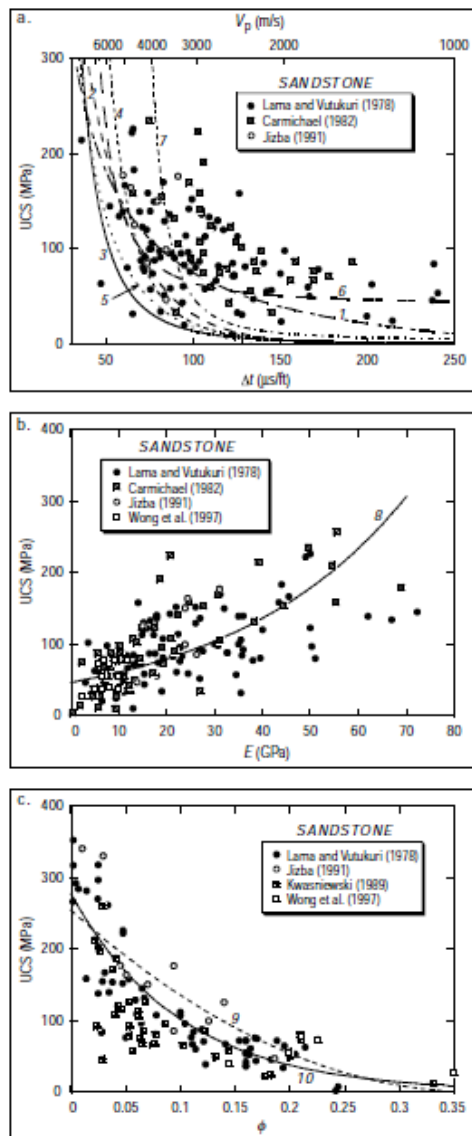

Fig.G.1-Data for estimation of rock strength from measurements in sandstones [43]
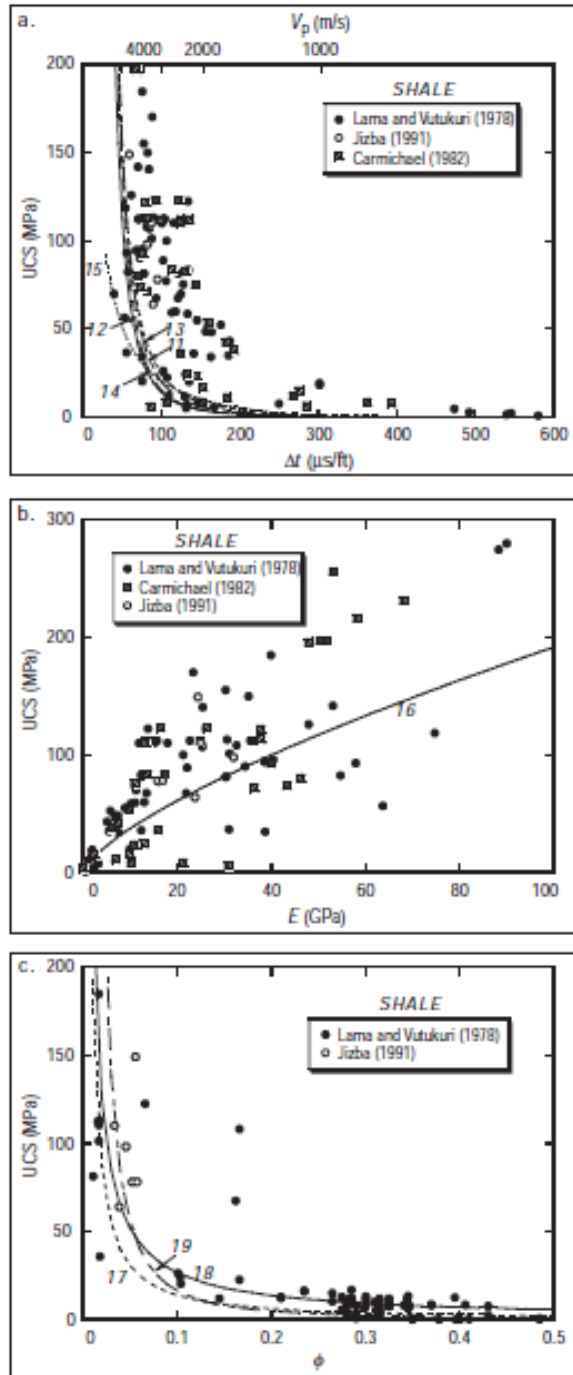
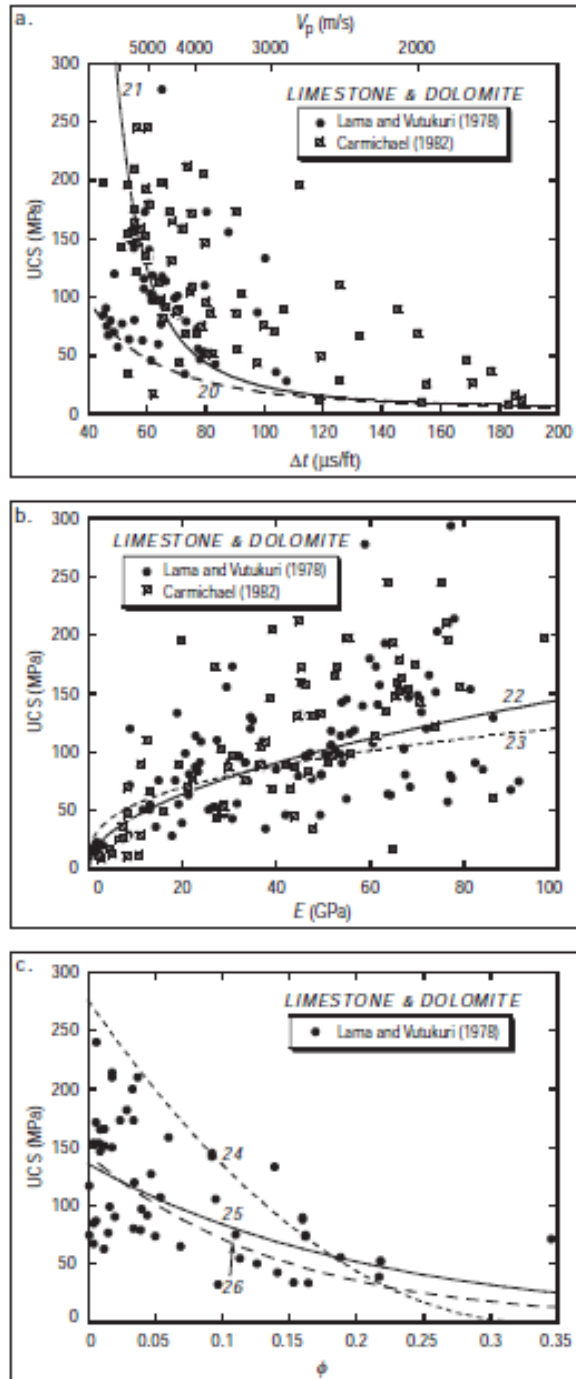Fig.G.2-Data for estimation of rock strength from measurements in shales [43]

Fig.G.3-Data for estimation of rock strength from measurements in limestone and dolomites [43]

APPENDIX H. ESTIMATION OF GEOTHERMAL GRADIENT FROM FIELD DATA

For the geothermal earth temperature profile, offset geophysical data is used to obtain the best estimate for the formation temperature at the leak off depth, T_{ei}. An example from Department of interior is shown in Fig.H.1.
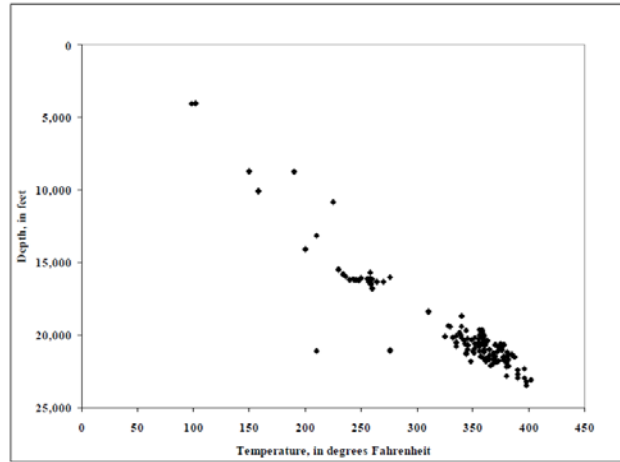

Fig.H.1-Temperature vs. Depth for the 108 study wellbores located in Judge Digby Field, Louisiana [139]

VITA

Koray Kinik was born in Ankara, Turkey.

He obtained a Bachelor of Science in Petroleum Engineering, Middle East Technical University, Ankara, Turkey, 2007.

He worked in Karkim Drilling Fluids, Ankara, Turkey from 2007 to 2009.

He then entered the Craft & Hawkins Department of Petroleum Engineering at Louisiana State University in the Fall 2009 to work towards a masters degree in petroleum engineering in April 2012.